ASTRONOMICAL INSTITUTE
SLOVAK ACADEMY OF SCIENCES

SPECIAL ISSUE

SPECTRAL LINE SHAPES IN ASTROPHYSICS AND RELATED ATOMIC DATA

CONTRIBUTIONS OF THE ASTRONOMICAL OBSERVATORY SKALNATÉ PLESO

• VOLUME LVI •

Number 1

January 2026.

Editorial Board

ISSN: 1336–0337 (on-line version)

CODEN: CAOPF8

Editorial Office: Astronomical Institute of the Slovak Academy of Sciences
SK - 059 60 Tatranská Lomnica, The Slovak Republic

CONTENTS

The Contributions of the Astronomical Observatory Skalnaté Pleso
are available in a full version
in the frame of ADS Abstract Service
and can be downloaded in a usual way from the URL address:

‘’http://adsabs.harvard.edu/article_service.html‘’

as well as from the web-site of
the Astronomical Institute of the Slovak Academy of Sciences
on the URL address:

‘’http://www.astro.sk/caosp/‘’

The journal is covered/indexed by:

Web of Science (WoS)

WoS Core Collection: Science Citation Index Expanded

SCOPUS

Index Copernicus International

SPECIAL ISSUE

SPECTRAL LINE SHAPES IN ASTROPHYSICS AND RELATED ATOMIC DATA

Edited by

Milan S. Dimitrijević, Paola Marziani, Djordje Savić
and Luka Č. Popović

Based on lectures presented at

15th Serbian Conference on
Spectral Line Shapes in Astrophysics

June 9 - 13, 2025, Niš, Serbia

Astronomical Observatory of Belgrade

http://servo.aob.rs/scslsa/

Scientific Organizing Committee

Milan S. Dimitrijević (Serbia), co-chair
Paola Marziani (Italy), co-chair
Alexei Moiseev (Russia)
Anjelka Kovačević (Serbia)
Dragana Ilić (Serbia)
Đorđe Savić (Serbia)
Evangelia Lyratzi (Greece)
Evencio Mediavilla (Spain)
Evgeny Stambulchik (Israel)
Gillian Peach (United Kingdom)
Jian-Min Wang (China)
Luka Č. Popović (Serbia)
Martin Gaskell (USA)
Robert Beuc (Croatia)
Roland Stamm (France)
Saša Simić (University of Kragujevac)
Sylvie Sahal-Bréchot (France)
Vladimir Srećković (Serbia)
Wolfram Kollatschny (Germany)

Local Organizing Committee

Đorđe Savić, chair
Slajana Knežević, secretary
Dragana Ilić
Milica Vučetić
Edi Bon

CONFERENCE PHOTO

LIST OF PARTICIPANTS

Amador-Portes Alfredo	Instituto Nacional de Astrofísica, Óptica y Electrónica, Puebla, Mexico
Andjelić Milica	Faculty of Mathematics - Department of Astronomy, University of Belgrade, Serbia
Arshinova Arina	Special Astrophysical Observatory, Russian Academy of Sciences, Russia
Bachir Amieur	University of Ghardaia, Algeria
Bianco Federica	University of Delaware, Newark, USA
Bon Edi	Astronomical Observatory, Belgrade, Serbia
Bon Nataša	Astronomical Observatory, Belgrade, Serbia
Caba Pineda Thara Rubi	Universidad Autónoma de Santo Domingo, Dominican Republic
Chakraborty Avinanda	National Institute for Astrophysics (INAF), Arcetri Astrophysical Observatory, Florence, Italy
Chelouche Doron	University of Haifa, Israel
Christova Magdalena	Department of Applied Physics, Technical University, Sofia, Bulgaria
Dalla Barba Benedetta	Università degli studi dell'Insubria, Como, Italy
Das Nandita	Faculty of Mathematics - Department of Astronomy, University of Belgrade, Serbia
Dimitrijević Milan	Astronomical Observatory, Belgrade, Serbia
Dojčinović Ivan	Faculty of Physics, University of Belgrade, Serbia
Farafontova Anastasiya	Institute of Astronomy of the RAS, Moscow, Russia
Fatović Marta	Dipartimento di Fisica ”Ettore Pancini”, Università di Napoli, Naples, Italy
Faycal Chouia	University of Ghardaia, Algeria
Fian Carina	Departamento de Astronomía y Astrofísica, Universidad de Valencia, Spain
Guerrero González Jonhatan Uriel	Instituto Nacional de Astrofísica, Óptica y Electrónica, Puebla, Mexico
Hannachi Ibtissem	University of Batna, Algeria
Houria Guerrida	Faculty of Mathematics and Matter Sciences, University of Kasdi Merbahn Ouargla, Algeria
Iacob Felix	Physics Faculty, West University of Timisoara, Romania
Ilić Dragana	Faculty of Mathematics - Department of Astronomy, University of Belgrade, Serbia
Jovanović Milena	Astronomical Observatory, Belgrade, Serbia
Karlica Mile	Astronomical Observatory, Belgrade, Serbia
Kirsanova Maria S.	Institute of Astronomy of the RAS, Moscow, Russia

Kneževic Sladjana	Astronomical Observatory, Belgrade, Serbia
Kostić Teodor	Astronomical Observatory, Belgrade, Serbia
Koubiti Mohammed	Aix-Marseille Université, France
Kovačević Andjelka B.	Faculty of Mathematics - Department of Astronomy, University of Belgrade, Serbia
Kovačević-Dojčinović Jelena	Astronomical Observatory, Belgrade, Serbia
Lalović Ana	Astronomical Observatory, Belgrade, Serbia
Lauwers Arno	Sterrenkundig Observatorium, Universiteit Gent, Belgium
Marčeta Mandić Sladjana	Astronomical Observatory, Belgrade, Serbia
Marziani Paola	National Institute for Astrophysics (INAF), Padua Astronomical Observatory, Padova, Italy
Meftah Mohammed Tayeb	Faculty of Mathematics and Matter Sciences, University of Kasdi Merbahn Ouargla, Algeria
Meštrić Uroš	Faculty of Mathematics - Department of Astronomy, University of Belgrade, Serbia
Mijović Djordje	Faculty of Mathematics - Department of Astronomy, University of Belgrade, Serbia
Milić Ivan	Faculty of Mathematics - Department of Astronomy, University of Belgrade, Serbia
Moiseev Alexei	Special Astrophysical Observatory, Russian Academy of Sciences, Russia
Mokadem Safia	University of Sciences and Technology Houari Boumediene, Algeria
Naddaf Mohammad Hassan	Institut d'Astrophysique et de Géophysique, Université de Liège, Belgium
Ochmann Martin	nstitut für Astrophysik und Geophysik, Universität Göttingen, Germany
Panda Swayamtrupta	International Gemini Observatory/NSF NOIRLab, La Serena Chile
Patiño Álvarez Víctor Manuel	Instituto Nacional de Astrofísica, Óptica y Electrónica, Puebla, Mexico
Petrushevska Tanja	Center for Astrophysics and Cosmology, University of Nova Gorica, Slovenia
Popović Luka	Astronomical Observatory, Belgrade, Serbia
Probst Malte Andrés	Institut für Astrophysik und Geophysik, Universität Göttingen, Germany
Pérez-Callejo Gabriel	Departamento de Física Teórica, Atómica y Óptica, Universidad de Valladolid, Spain
Rosato Joel	Aix-Marseille Université, France

Salvato Mara	Max-Planck-Institut für extraterrestrische Physik, Garching Germany
Savić Djordje	Astronomical Observatory, Belgrade, Serbia
Shakeri Soroush	Isfahan University of Technology, Iran
Shaliapina Liliia	St Petersburg State University, Russia
Shamsi Shoaib Jamal	Faculty of Mathematics - Department of Astronomy, University of Belgrade, Serbia
Simić Saša	Faculty of Sciences, University of Kragujevac, Serbia
Smirnova Aleksandrina	Special Astrophysical Observatory, Russian Academy of Sciences, Russia
Srećković Vladimir	Institute of Physics, Belgrade, Serbia
Stambulchik Evgeny	Faculty of Physics, Weizmann Institute of Science, Israel
Stamm Roland	Aix-Marseille Université, France
Tagliacozzo Daniele	Sterrenkundig Observatorium, Universiteit Gent, Belgium
Vujčić Veljko	Astronomical Observatory, Belgrade, Serbia
Yarovova Anastasiya	Lomonosov Moscow State University, Sternberg Astronomical Institute, Russia

PREFACE

The special issue of Contributions of the Astronomical Observatory Skalnaté Pleso: Spectral Line Shapes in Astrophysics and related Atomic Data focuses on research concerning the spectral line properties and the corresponding atomic and molecular data. Namely, the analysis of spectral lines, their widths, and, more generally, their shapes, is a powerful diagnostic tool for probing emitting/absorbing gas, enabling to use the observed spectra for analysis and modelling of various astrophysical objects from interstellar clouds of molecular and ionized hydrogen to neutron stars and quasars. It is well known, that atomic and molecular spectroscopy is a key method for plasma studies not only in astronomy but also for laboratory plasma, lasers and laser produced plasma, fusion research, atmospheric investigations, applied physics and industry. Therefore, interaction between astrophysicists and laboratory physicists who produce various atomic and molecular data and investigate spectra originating from different cosmic sources can provide a boost to our understanding of the Universe. Accordingly, stating from 1995 to 2025 we have organized 15 conferences on Spectral line shapes in astrophysics, in order to bring together astronomers and physicists from Serbia and other countries to review and present their current research.

In this Special Issue there are 15 selected papers written by participants of XV Serbian Conference on Spectral Line Shapes in Astrophysics, June 9-13, 2025, Niš, Serbia, where 65 colleagues from 19 countries attended. The particpants were from Algeria, Bangladesh, Belgium, Bulgaria, Chile, China, Dominican Republic, France, Germany, Iran, Israel, Italy, Mexico, Romania, Russia, Serbia, Slovenia, Spain, and USA. The conference sessions have been dedicated to *Databases and spectral line shapes from laboratory to space plasma, Spectral line shapes and astrophysical phenomena, Emission lines in active galaxies and nebulae, Spectral line phenomena in plasmas from diffuse to dense states, Spectral lines in astrophysical and laboratory plasma, Surveys and spectral line variability in extragalactic objects, Atomic parameters and spectral line shapes, Spectral line phenomena in extragalactic objects, Spectral line shapes in different space conditions, Spectral line research: new frontiers and Spectral line variability and other characteristics in AGNs.* More informations could be found on the official website of the conference: http://servo.aob.rs/scslsa/. All materials (programme, talks, presentations, photos, etc.) from the previous meetings are available at http://servo.aob.rs/eeditions/SCSLSA.php through Serbian Virtual Observatory (http://servo.aob.rs/scslsa/).

All papers, selected for this special issue, were subjected to a strict refereeing process. We are thankful to the reviewers for their valuable time to ensure the strict scientific standard of the articles.

Milan S. Dimitrijević, Paola Marziani, Djordje Savić and Luka Č. Popović
guest editors

Contrib. Astron. Obs. Skalnaté Pleso **56/1**, 15 – 30, (2026)
https://doi.org/10.31577/caosp.2026.56.1.15

Exploring the broad-line region of PKS 1510-089: Jet contributions and mass estimation

A. Amador-Portes[1], **A. García-Pérez**[1,2], **V. Chavushyan**[1] and **V.M. Patiño-Álvarez**[1,3]

[1] *Instituto Nacional de Astrofísica, Óptica y Electrónica, Luis Enrique Erro 1, Tonantzintla Puebla, México, C.P. 72840 (E-mail: alfreportess9730@gmail.com)*

[2] *Dipartimento di Fisica, Università degli Studi di Torino, via Pietro Giuria 1, I-10125 Torino, Italy*

[3] *Max-Planck-Institut für Radioastronomie, Auf dem Hügel 69, D-53121 Bonn, Germany*

Received: August 5, 2025.; Accepted: November 12, 2025.

Abstract.
PKS 1510-089, a highly active flat-spectrum radio quasar, known for its frequent flaring activity across the electromagnetic spectrum. We present a decade-long analysis of its flux variability in optical bands and γ-rays, focusing on the non-thermal dominance parameter, Hβ and Hγ lines, and the λ5100 Å continuum. We examine the Hβ flux and full width at half maximum (FWHM), along with the λ5100 Å continuum light curves to assess whether the primary source of continuum emission is the accretion disk or the jet during different activity periods. Our results highlight that jet emission dominates the continuum during flare-like episodes. We obtain an approximately 80 day delay between the Hβ and continuum emissions, which we interpret as the spatial separation between the optical emission region and the broad-line region (BLR). Near-zero delays between optical and near-infrared bands indicate co-spatial emission within the jet. Synchrotron self-Compton is identified as the dominant γ-ray mechanism during flares, supported by minimal delays with optical/NIR emission. A persistent anticorrelation between the Hβ FWHM and luminosity reveals a "breathing-BLR" effect, independent of whether ionization arises from the disk or jet. This relation also holds between Hβ FWHM and λ5100 Å luminosity during disk-dominated phases, suggesting that the emission line arises mostly from the canonical virialized BLR. Moreover, jet-related λ5100 Å flares coincide with Hβ flares, suggesting the jet base lies within the BLR. From 219 disk-dominated spectra, we estimate a mean black hole mass of $M_{BH} = (2.85 \pm 0.37) \times 10^8\ M_\odot$. This study sheds light on the jet-BLR connection in PKS 1510-089, enhancing our understanding of blazar emission.

Key words: active galactic nuclei (16) – galaxy jets (601) – emission line galaxies (459) – flat-spectrum radio quasars (2163) – supermassive black holes (1663)

1. Introduction

PKS 1510-089 (redshift $z = 0.361$; Burbidge & Kinman, 1966) is a flat-spectrum radio quasar (FSRQ), one of the most active and well-studied sources across the entire electromagnetic spectrum (e.g. Marscher et al., 2010; Rani et al., 2010; Aleksić et al., 2014; Fuhrmann et al., 2016; Prince et al., 2019; Yuan et al., 2023). The relativistic jet of PKS 1510-089 is oriented at an angle of roughly 3° to our line of sight (Homan et al., 2002), allowing the detection of knots with apparent superluminal velocities of up to $20c$ along the jet (Jorstad et al., 2005). The location of the γ-ray emission zone in this source remains uncertain. Some studies place it close to the supermassive black hole (SMBH), within the broad-line region (BLR) (e.g. Poutanen & Stern, 2010; Tavecchio et al., 2010; Brown, 2013), while others argue for a position further downstream, beyond the BLR and outside the central parsec (e.g. Tavecchio et al., 2010; Orienti et al., 2013; Dotson et al., 2015; H.E.S.S. Collaboration et al., 2021). This complicates the identification of the dominant γ-ray production mechanism. While combined external Compton (EC) and synchrotron self-Compton (SSC) scenarios are often invoked (Kataoka et al., 2008; D'Ammando et al., 2009; Castignani et al., 2017), purely EC or SSC models (Aleksić et al., 2014; H.E.S.S. Collaboration et al., 2021) and lepto-hadronic interpretations (Dzhatdoev et al., 2022) have also been proposed and cannot be completely ruled out.

Aharonian et al. (2023) showed that during 2021 to 2022, PKS 1510-089 remained in a low activity state, accompanied by a decline in optical polarization, with spectra consistent with emission from the accretion disk and BLR. In these epochs, Barnard et al. (2024) reported that the strength and width of emission features (Mg II λ2798 Å, Hδ, and Hγ) were stable, but their average EW increased. Furthermore, Podjed et al. (2024) found no polarized broad Hγ or Hβ emission, suggesting that these lines are intrinsically unpolarized. Estimates of the black hole mass (M_{BH}) in PKS 1510-089 span a range of values. Disk temperature profile modeling yields values of 5.40 and 2.40×10^8 M⊙ (Abdo et al., 2010; Castignani et al., 2017, respectively). Single-epoch spectra based on λ5100 Å continuum luminosity and Hβ full width at half maximum (FWHM) give values of 3.86 and 2.00×10^8 M⊙ (Oshlack et al., 2002; Xie et al., 2005, respectively), while reverberation mapping by Rakshit (2020) yields a mass of $5.71^{+0.62}_{-0.58} \times 10^7$ $M_{\odot}$.

This work summarizes the results in Amador-Portes et al. (2024b, 2025), where γ-ray variability alongside the fluxes of Hβ and Hγ, the Hβ FWHM, and the optical continuum flux at λ5100 Å were analyzed. Multi-wavelength light curves spanning ~ 10 years using cross-correlation analysis were used to probe time lags between bands and infer the locations and dominant mechanisms of different emission regions. We also studied correlations between $L_{\lambda5100}$ and $L_{\mathrm{H}\beta}$, as well as between FWHM Hβ and these luminosities. To assess the influence of the jet on BLR emission, we separated spectra based on the dominant continuum source, accretion disk or jet. For disk-dominated spectra, we estimated the MBH via single-epoch methods from $L_{\mathrm{H}\beta}$ and FWHM Hβ. Throughout this work, we adopt a cosmology with $H_0 = 71$ km s^{-1} Mpc^{-1}, $\Omega_\Lambda = 0.73$, and $\Omega_\mathrm{M} = 0.27$, corresponding to a luminosity distance of 1906.9 Mpc at $z = 0.361$.

2. Observations and data

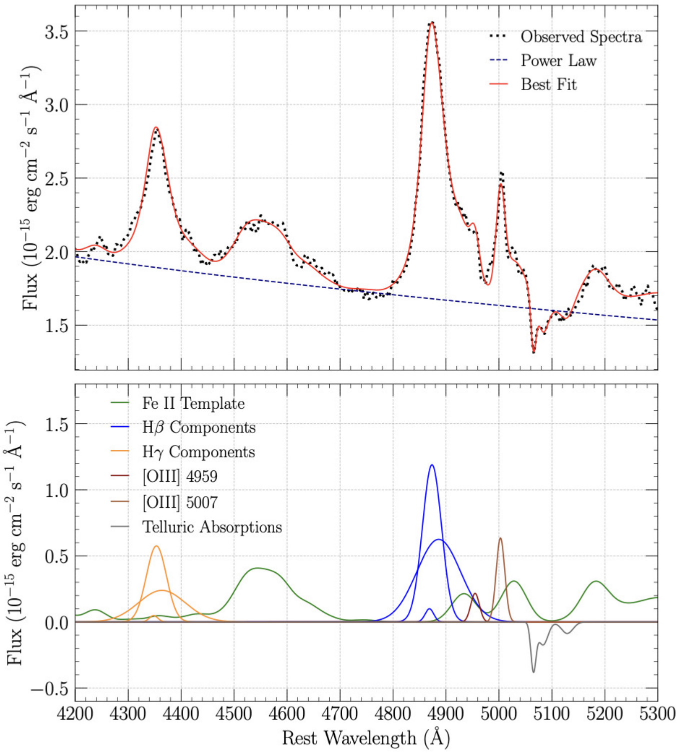

Figure 1. Example decomposition of the Hβ and Hγ emission lines from a spectrum observed at the Steward Observatory on April 10, 2018. Top panel: The rest-frame spectrum with the best-fit model overlaid. The continuum is represented by a power-law function. Bottom panel: The broad and narrow components used to fit Hβ and Hγ, along with the Fe II template, [O III] doublet, and telluric absorptions.

We analyzed γ-ray data ($0.1 - 300$ GeV) from the Fermi-LAT (Abdo et al., 2010) public archive[1] using `Fermitools version 2.0.8` to construct weekly light curves. The near-infrared (NIR) J-band data were obtained from the Small

---

[1] https://fermi.gsfc.nasa.gov/cgi-bin/ssc/LAT/LATDataQuery.cgi

and Moderate Aperture Research Telescope System (SMARTS; Bonning et al., 2012). Optical V-band data were retrieved from two sources, SMARTS and the Steward Observatory (SO). We obtained 34 optical spectra from the Observatorio Astrofísico Guillermo Haro (OAGH[2]), and 353 spectra from the SO as part of the Ground-based Observational Support of the Fermi Gamma-ray Space Telescope monitoring program at the University of Arizona[3]. The OAGH spectra, covers a wavelength range of 3800–7100 Å, while the SO spectra spans the wavelengths 4000–7500 Å. Details of the OAGH spectra data reduction is found in Amador-Portes et al. (2024b) and SO observational setup and data processing are provided in Smith et al. (2009).

The spectra were shifted to the rest frame and corrected for cosmological effects using the $(1+z)^3$ factor (Peterson, 1997). Galactic reddening was removed using the dust maps from Schlafly & Finkbeiner (2011) with $E(B-V) = 0.09$, adopting the reddening law of Cardelli et al. (1989) with $R_V = 3.1$. We extract the Hβ, Hγ, and λ5100 Å continuum fluxes through spectral decomposition. The local continuum was modeled with a power-law. Fe II multiplet emission between 4000–5500 Å was modeled using the template from Kovačević et al. (2010). Emission and absorption lines were fitted using the `astropy.modeling`[4] framework. The Hβ and Hγ lines were each fitted with three Gaussian components: narrow, broad, and very broad. An example of the spectral decomposition is shown in Figure 1.

Three sources of uncertainty were considered for the emission line flux measurements: i) Random error from spectral dispersion and signal-to-noise (S/N) ratio (Tresse et al., 1999); ii) uncertainties from Fe II subtraction (León-Tavares et al., 2013); and iii) a 10% contribution from flux calibration (Paul Smith private communication). The narrow Hβ contribution to the total profile was minimal, ranging from 5.2% at its lowest line flux to 1.5% at its highest line flux, smaller than the total Hβ flux uncertainty. Therefore, the total Hβ profile was used in all calculations. Given that the Hγ line is expected to behave similarly, its total profile flux was also adopted for the cross-correlation analysis.

We measured the FWHM from the sum of Gaussians used for the Hβ profile. The uncertainty in the observed FWHM arises from two sources: i) the random error due to spectral dispersion (~ 4 Å), and ii) the fitting error, estimated as the standard deviation between the fitted Gaussians and the observed spectrum. A correction by instrumental broadening was made for each slit width used in the SO observations, adopting the values from Amador-Portes et al. (2024a): 9.45 ± 2.70 Å for $3.''0$, 12.92 ± 3.69 Å for $4.''1$, and 16.07 ± 4.59 Å for $5.''1$. As the instrumental uncertainties dominate over S/N effects, the corrected FWHM was obtained via quadratic subtraction of the instrumental and observed profiles, with its uncertainty derived through standard error propagation.

---

[2] https://astro.inaoep.mx/observatorios/oagh/

[3] http://james.as.arizona.edu/~psmith/Fermi/

[4] https://docs.astropy.org/en/stable/modeling/index.html

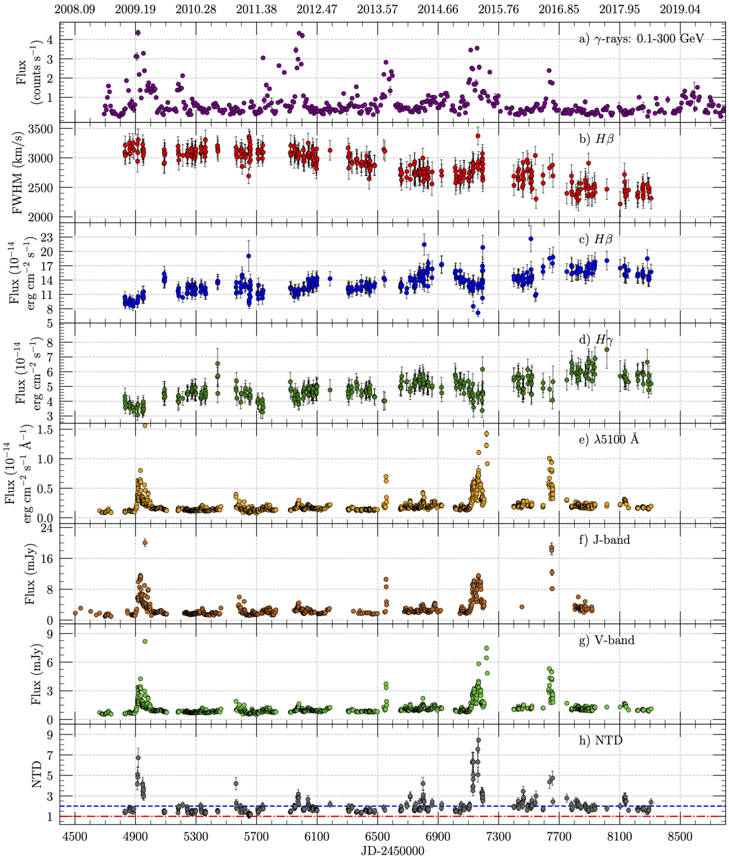

Figure 2. Multi-wavelength light curves. (a) γ-ray data from Fermi/LAT ($0.1-300$ GeV), (b) FWHM of the Hβ emission line, (c) Hβ emission line flux, (d) Hγ emission line flux, (e) λ5100 Å continuum flux, (f) V-band from SO and SMARTS, (g) J-band from SMARTS, and (h) NTD parameter. The red dash-dotted and blue dashed lines in panel (h) represent NTD$=1$ and NTD$=2$, respectively.

$$NTD = \frac{L_{obs}}{L_{pred}} \tag{1}$$

The NTD parameter (Shaw et al., 2012) was calculated following Equation 1, where $L_{\rm obs}$ is the observed continuum luminosity, and $L_{\rm pred}$ is the continuum luminosity predicted from the Hβ luminosity using the non-blazar relation of Greene & Ho (2005). The NTD parameter quantifies the relative non-thermal (jet) contribution to the total continuum emission in AGN. Following Patiño-Álvarez et al. (2016), NTD $=$ 1 indicates purely thermal emission from the accretion disk; 1 < NTD < 2 implies disk-dominated emission with a jet contribution; NTD = 2 corresponds to equal contributions from disk and jet; and NTD > 2 indicates jet-dominated emission. Thus, two regimes can be defined: Disk-Dominated (NTD < 2) and Jet-Dominated (NTD > 2). The light curves of the γ-rays, Hβ and λ5100 Å continuum fluxes along with the FWHM of Hβ and NTD are displayed in Figure 2.

3. Variability and correlations analysis

Table 1. Time lags between emission in different bands, and NTD values, obtained from cross-correlation analysis of the full light curves.

Light Curves	Delay (days)
5100 Åvs γ-rays	-6.8 ± 6.4
5100 Åvs Hβ	82.4 ± 6.1
5100 Åvs Hγ	87.7 ± 6.6
5100 Åvs J-band	0.0 ± 3.7
5100 Åvs NTD	0.1 ± 6.7
5100 Åvs V-band	0.2 ± 2.5
γ-rays vs NTD	6.0 ± 6.7
J-band vs γ-rays	-8.8 ± 6.4
J-band vs Hβ	81.8 ± 6.1
J-band vs NTD	-0.5 ± 6.7
V-band vs γ-rays	-9.0 ± 11.3
V-band vs Hβ	$78.9^{+14.9}_{-4.2}$
V-band vs J-band	0.0 ± 3.7
V-band vs NTD	0.6 ± 6.7

We conducted cross-correlations amongst all multi-wavelength light curves previously described. Three different methods were employed to ensure robustness: the interpolated cross-correlation function (ICCF; Gaskell & Sparke, 1986), the discrete cross-correlation function (DCCF; Edelson & Krolik, 1988), and the Z-transformed discrete cross-correlation function (ZDCF; Alexander, 1997). These methods followed the established protocols outlined in Patiño-Álvarez et al. (2013); Patiño-Álvarez et al. (2018), and Amaya-Almazán et al. (2022). Only time delays with correlation coefficients at above 99% significance,, and consistent across at least two of the three methods, were considered. Further details on significance levels can be found in Emmanoulopoulos et al. (2013) and Amaya-Almazán et al. (2022) The reported delays represent the average results obtained from either two or all three methods, depending on the case, with the reported uncertainty being the maximum uncertainty value among the three methods employed. Results of the cross-correlation analysis for the are summarized in Table 1.

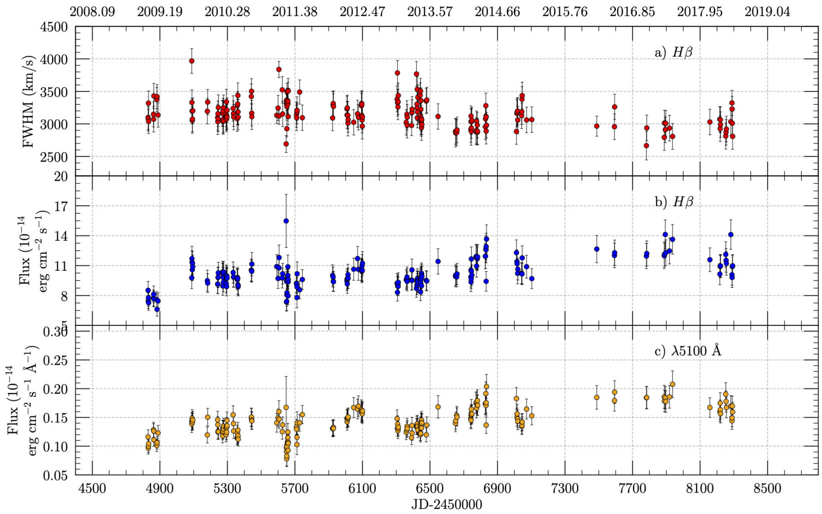

Figure 3. Spectroscopic light curves for the disk dominance regime. (a) FWHM of the Hβ emission line, (b) Hβ emission line flux, and (c) the λ5100 Å continuum flux.

Delays between the optical/NIR emissions (λ5100 Å continuum, J-band, V-band, and NTD) are consistent with zero, indicating quasi-simultaneous, co-spatial emission. Continuum variability is largely driven by flare-like episodes linked to strong jet activity, as shown by NTD values exceeding 2. Thus, the variability in the λ5100 Å continuum is predominantly powered by synchrotron emission from the jet. Given the co-spatiality, the V-band and J-band emissions during flares also arise primarily within the jet, confirming synchrotron radiation as the main driver of variability across these bands. The ~80-day delay between the continuum and emission lines likely reflects the light-travel time from the continuum source to the BLR. In addition, a cross-correlation analysis between the λ5100 Å continuum and Hβ light curves, separated by jet- and disk-dominated regimes (NTD+σ < 2) was performed. The results for these subsets did not reveal any significant correlation, indicating no physical delay between the light curves in separated regimes. In the jet dominance regime, the observed delays appeared to be spurious correlations. Conversely, in the disk dominance regime, we obtain inconclusive results, stemmed from the similarity in the light curves, characterized by prolonged periods of quiescence with minimal variability as shown in Figure 3. A detailed discussion of this inconclusive results is presented on Amador-Portes et al. (2024b).

Table 2. Pearson (ρ_P) and Spearman (ρ_S) correlation coefficients obtained for $L_{\lambda5100}$ versus $L_{H\beta}$ and $L_{H\beta}$ or $L_{\lambda5100}$ versus $FWHM_{H\beta}$ across various data sets: Full Set, Disk Dominance (DD), and Jet Dominance (JD). Corresponding p-values are displayed for each case.

Regime	ρ_P	p_v	ρ_S	p_v
		$L_{\lambda5100}$ vs $L_{H\beta}$		
Full Set	0.200	2.60×10^{-6}	0.450	6.0×10^{-21}
DD	0.800	6.90×10^{-59}	0.810	7.00×10^{-53}
JD	0.100	0.260	0.170	0.200
		$L_{\lambda5100}$ vs $FWHM_{H\beta}$		
Full Set	-0.187	2.09×10^{-4}	-0.450	2.27×10^{-20}
DD	-0.678	8.81×10^{-31}	-0.650	6.21×10^{-28}
JD	-0.104	0.395	-0.054	0.658
		$L_{H\beta}$ vs $FWHM_{H\beta}$		
Full Set	-0.650	9.34×10^{-48}	-0.683	1.72×10^{-54}
DD	-0.678	8.04×10^{-31}	-0.651	7.86×10^{-28}
JD	-0.575	2.33×10^{-7}	-0.630	6.59×10^{-9}

The delay of 7.0 ± 7.7 days between optical/NIR bands and γ-ray emission suggests that the optical emission region and the source of seed photons are quasi-cospatial. Since optical variability is jet-driven, delays between the optical light curves and other light curves will also trace jet activity during flares. The near-zero lag therefore indicates that optical/NIR and γ-ray emission regions are co-spatial within the jet. For the γ-ray energies detected by Fermi/LAT (0.1−300 GeV), the seed photons must be within the NIR-NUV range, corresponding to observable flux in the V-band, J-band, and λ5100 Å continuum. Given the quasi-cospatiality of optical/NIR and seed photon regions within the jet, SSC is favored as the dominant emission mechanism during flares, where γ-rays arise from synchrotron photons scattered by the same relativistic electrons. However, EC processes cannot be excluded, as both are expected to occur simultaneously.

We look for correlations in the logarithmic space between $FWHM_{H\beta}$, $L_{\lambda5100}$, and $L_{H\beta}$ for the entire dataset, as well as separately for the jet dominance and disk dominance regimes to picture the role of jet emission over the Hβ emission line (and thus the BLR). The correlations were conducted with the Pearson (ρ_P) and Spearman (ρ_S) correlation rank tests, Person or Spearman coefficients with values absolute below $|\rho| \leq 0.39$ are considered as a weak correlation, values between $0.40 \leq |\rho| \leq 0.59$ as a moderate correlation, and values greater than $|\rho| \geq 0.60$ as a strong correlation (positive or negative, given the case). All correlation coefficients are displayed in Table 2.

$$L_{\lambda5100} = 10^{44}\ \mathrm{erg\ s^{-1}} \left(\frac{L_{H\beta}}{(1.425 \pm 0.007) \times 10^{42}\ \mathrm{erg\ s^{-1}}} \right)^{-\frac{1}{1.133 \pm 0.005}} \tag{2}$$

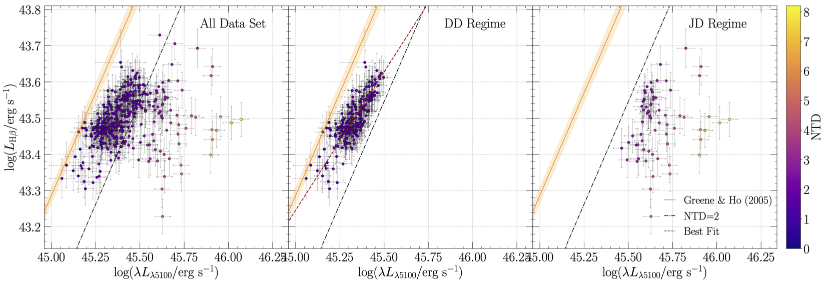

Figure 4. Variation of the Hβ emission-line luminosity compared to the $\lambda5100$ Å continuum luminosity. In all panels, the color bar indicates the NTD value for each observation. Left Panel: Full sample. Middle Panel: Disk dominance (DD) regime data. Right Panel: Jet dominance (JD) regime data. The dashed black line denotes the boundary between the regimes. The orange solid line and shaded area represent the Greene & Ho (2005) relation for a non-blazar sample and its uncertainty at 3σ. The dashed red line denotes the significant ($p_v < 0.05$) linear regression to the correspondent data.

The NTD parameter, defined as the ratio of observed to predicted continuum luminosity, with predictions based on the Hβ - continuum relation (Equation 2) from Greene & Ho 2005, was used to distinguish between jet- and disk-dominated states. Figure 4 shows this comparison, with NTD$=2$ marking the boundary. Across the full sample, correlations between continuum and Hβ luminosities were weak to moderate, and linear regression failed to yield a significant fit (as evidenced by their p-value[5], p_v of 1 to machine accuracy). For the linear regression, a p-value below 0.05 is considered statistically significant, indicating that the observed relationship is unlikely to have occurred by chance. To refine the analysis, we separated the data: 219 spectra (56.6%) in the disk-dominated regime, 17.8% in the jet-dominated regime, and 25.6% near the threshold. In the disk-dominated regime, a strong correlation was recovered, with a slope of $\beta = 0.76 \pm 0.05$ ($p_v \approx 0$) for the linear regression, consistent with a non-blazar AGN. In contrast, no significant correlation was found in the jet-dominated regime, indicating that line luminosities do not reliably track continuum variability when the jet dominates.

Across the full dataset, the Pearson test shows no correlation between $L_{\lambda5100}$ and FWHM$H\beta$, while the Spearman test reveals a moderate anti-correlation, indicating a monotonic but non-linear relationship; the linear regression does not accurately describe the data ($p_v = 0.620$). In the disk-dominated regime, strong correlations appear in both tests, with a regression slope $\beta = -0.360 \pm 0.034$ ($p_v \approx 0.0$), reflecting the “breathing-BLR” effect (Figure 5): as the ionizing

---

[5] The p-value represents the probability that our null hypothesis is true, which states there is no relationship between the model and the data.

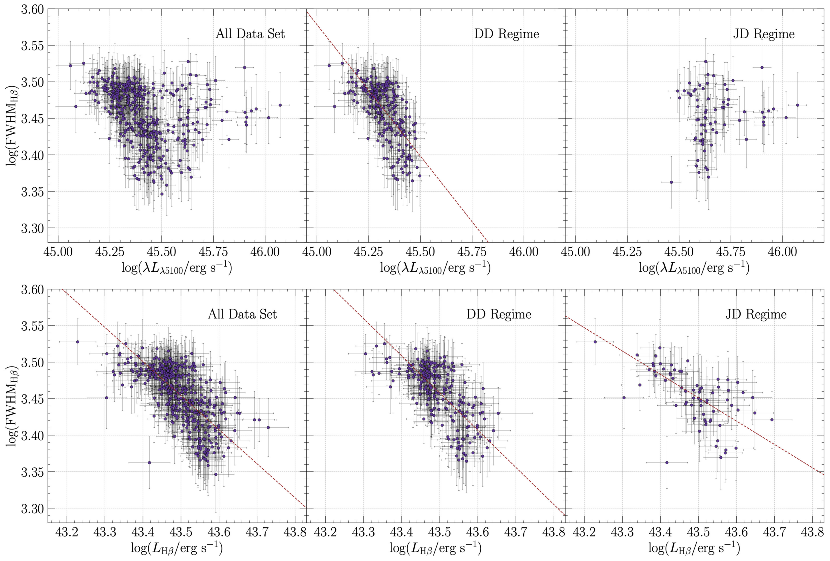

Figure 5. Top Row: Variation of the Hβ emission-line FWHM compared to the λ5100 Å continuum luminosity. Bottom Row: Variation of the Hβ emission-line FWHM compared to its luminosity. Left Column: Full sample. Middle Column: Disk dominance (DD) regime data set. Right Column: Jet dominance (JD) regime data set. Only linear regression fits with $p_v < 0.05$ are plotted, as red dashed lines, for the corresponding data.

continuum increases, the BLR radius expands due to clouds farther away being ionized, producing narrower Hβ profiles. In contrast, the jet-dominated regime shows no significant correlation, implying that the ionizing influence of the jet on the BLR is weaker compared to the accretion disk, thus insufficient to induce a similar dynamic response in the BLR. We find a strong anti-correlation between $L_{H\beta}$ and FWHM$_{H\beta}$ across all subsets, indicating that changes in Hβ luminosity similarly affect the BLR regardless of the ionizing source. Long-term trends over $\sim$ 10 years show that flux increases correspond to FWHM decreases. Linear regression is statistically significant for all subsets, with slopes $\beta = -0.467 \pm 0.032$ (full dataset), $\beta = -0.509 \pm 0.048$ (disk-dominated), and $\beta = -0.320 \pm 0.056$ (jet-dominated), all with $p_v < 0.002$.

The observed "breathing-BLR" effect, indicates that the photons driving the Hβ emission consistently originate from the canonical BLR, regardless of whether the dominant continuum source is the accretion disk or the jet. This rules out the contribution of any external BLR material. Based on these, we propose that the base of the jet, where the UV synchrotron emission is produced, resides within the canonical BLR. In this configuration, the jet emission directly impacts the Hβ line, reinforcing the idea that the canonical BLR remains the principal emission region even when the jet dominates the continuum. In Figure 6 we present a schematic illustration of the Jet-BLR system coupling and the different interactions between regions.

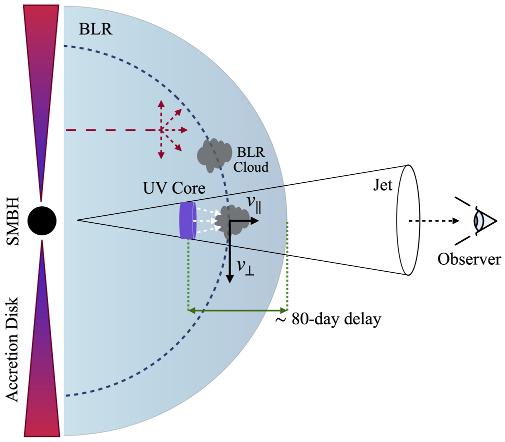

Figure 6. Schematic illustration of the Jet-BLR system suggested in this work (not to scale). The blue dashed curve represents the orbit of a BLR cloud around the SMBH with the parallel velocity component being low while crossing the jet section. BLR clouds in this region will be ionized by a contribution of UV flux from the accretion disk (red arrows) and from the jet (white arrows). The $\sim$ 80-day delay between the continuum emission and the Hβ emission line traces the distance between the continuum emission within the jet during flare-like events and the edge of the BLR.

4. Black hole mass estimation

The variability in this source is predominantly jet-driven. This complicates supermassive black hole mass (M_{BH}) estimates via reverberation mapping, since the measured delay in disk dominance regime yielded inconclusive results we could not use reverberation mapping. Given these limitations, we adopted single-epoch spectroscopic methods for M_{BH} estimation, applying Equation 3 from Greene & Ho (2005) to 192 spectra in the disk-dominated regime. FWHM$_{H\beta}$ is corrected for instrumental broadening. From this set of data points, we estimated a weighted mean mass for the supermassive black hole (M_{BH}). The resulting value is $M_{BH} = 2.85 \pm 0.37 \times 10^{8}\ M_{\odot}$, with the uncertainty derived from the standard deviation of this set.

$$M_{\rm BH} = (3.6 \pm 0.2) \times 10^6 \left(\frac{L_{H\beta}}{10^{42}\ {\rm erg/s}} \right)^{0.56\pm0.02} \left(\frac{FWHM_{H\beta}}{10^3\ {\rm km/s}} \right)^2 M_\odot \qquad (3)$$

5. Summary and results

Delays between optical/IR emissions are consistent with zero, indicating nearly simultaneous, co-spatial regions. Continuum variability is driven by flares, suggesting that optical and NIR emissions mainly arise from synchrotron processes in the jet. The 7.0 ± 7.7-day lag between optical/IR and γ-rays indicates a close spatial link, with seed photons for inverse Compton emission originating from jet-produced optical/NIR flux. SSC is suspected to be the dominant γ-ray emission process during flare-like events, but further analysis needs to be made. Cross-correlations across the full dataset between the λ5100 Å continuum and the Hβ and Hγ emission line fluxes revealed a delay of approximately 80 ± 6 days. This delay reflects the separation between the continuum emission region and the BLR, and cannot be interpreted as the size of a virialized BLR. Instead, it likely traces the distance between the edge of the BLR and the continuum source associated with the jet during flare-like events. In the disk-dominated regime, the results were inconclusive, a behavior attributed to the prevalence of quiescent periods with minimal variability.

The λ5100 Å continuum and Hβ luminosities show a weak positive correlation across the full dataset, diverging from the non-blazar relation at NTD>2. In the disk dominance regime, the correlation strengthens (Pearson $= 0.80$, Spearman $= 0.79$), indicating that the emission line closely follows the continuum, as in non-blazar AGNs. A consistent anti-correlation between $L_{H\beta}$ and FWHM$_{H\beta}$ across all datasets reflects the "breathing-BLR" effect. These results suggest that the BLR responds similarly to ionizing flux from both the accretion disk and the jet, supporting a scenario where the jet base is embedded within the canonical BLR.

Single-epoch spectra were employed to estimate M_{BH} in the disk dominance regime, using the scaling relation proposed by Greene & Ho (2005). A robust M_{BH} value of $2.85 \pm 0.37 \times 10^8\, M_\odot$ was derived exclusively from spectra spanning approximately a decade within the disk dominance regime. This approach minimized jet contamination and short-term variability potentially associated with jets. However, for this object, the jet does not significantly impact the M_{BH} estimated, as seen from the analysis of the complete spectra set for this particular source.

Acknowledgements. A.A.-P. and A. G.-P. gratefully acknowledges the support received from the SECIHTI (Secretaria de Ciencias, Humanidades, Tecnología e Inovación) program for their Ph.D. studies. This work was made possible thanks to the generous assistance provided by the Max Planck Institute for Radio Astronomy (MPIfR) - Mexico Max Planck Partner Group led by V.M.P.-A. Data from the Steward Observatory spectropolarimetric monitoring project were used. This program is supported by Fermi Guest Investigator grants NNX08AW56G, NNX09AU10G, NNX12AO93G, and NNX15AU81G. This publication is based on data collected at the Observatorio Astrofísico Guillermo Haro (OAGH), Cananea, Sonora, Mexico, operated by the Instituto Nacional de Astrofísica, Óptica y Electrónica (INAOE). Funding for the OAGH has been provided by SECIHTI.

References

Abdo, A. A., Ackermann, M., Agudo, I., et al., FERMI LARGE AREA TELESCOPE AND MULTI-WAVELENGTH OBSERVATIONS OF THE FLARING ACTIVITY OF PKS 1510-089 BETWEEN 2008 SEPTEMBER AND 2009 JUNE. 2010, *The Astrophysical Journal*, **721**, 1425, DOI:10.1088/0004-637X/721/2/1425

Aharonian, F., Benkhali, F. A., Aschersleben, J., et al., The Vanishing of the Primary Emission Region in PKS 1510–089. 2023, *The Astrophysical Journal Letters*, **952**, L38, DOI:10.3847/2041-8213/ace3c0

Aleksić, J., Ansoldi, S., Antonelli, L. A., et al., MAGIC gamma-ray and multi-frequency observations of flat spectrum radio quasar PKS 1510-089 in early 2012. 2014, *A&A*, **569**, A46, DOI:10.1051/0004-6361/201423484

Alexander, T., Is AGN Variability Correlated with Other AGN Properties?—ZDCF Analysis of Small Samples of Sparse Light Curves. 1997, in *Astronomical Time Series*, ed. D. Maoz, A. Sternberg, & E. M. Leibowitz (Dordrecht: Springer Netherlands), 163–166

Amador-Portes, A., Chavushyan, V., & Patiño-Álvarez, V. M., Instrumental Broadening of the SPOL Spectropolarimeter at the University of Arizona. 2024a, *Revista Mexicana de Astronomia y Astrofisica*, **60**, 317, DOI:10.22201/ia.01851101p.2024.60.02.09

Amador-Portes, A., Chavushyan, V., Patiño-Álvarez, V. M., & Ramón-Valdés, J., Unveiling the Emission Mechanisms of Blazar PKS 1510-089. II. Jet-BLR Connection and Black Hole Mass Estimation. 2025, *Astrophysical Journal*, **979**, 227, DOI:10.3847/1538-4357/ada38b

Amador-Portes, A., García-Pérez, A., Chavushyan, V., & Patiño-Álvarez, V. M., Unveiling the Emission Mechanisms of Blazar PKS 1510-089. I. Multiwavelength Variability. 2024b, *Astrophysical Journal*, **977**, 178, DOI:10.3847/1538-4357/ad8ddd

Amaya-Almazán, R. A., Chavushyan, V., & Patiño-Álvarez, V. M., Multiwavelength Analysis and the C iv λ 1549 Å Emission Line Behavior From 2008 to 2020 of FSRQ B2 1633+382. 2022, *The Astrophysical Journal*, **929**, 14, DOI:10.3847/1538-4357/ac5741

Barnard, J., van Soelen, B., Acharya, S., et al., The optical spectropolarimetric behaviour of a selection of high-energy blazars. 2024, *Monthly Notices of the RAS*, **532**, 1991, DOI:10.1093/mnras/stae1576

Bonning, E., Urry, C. M., Bailyn, C., et al., SMARTS OPTICAL AND INFRARED MONITORING OF 12 GAMMA-RAY BRIGHT BLAZARS. 2012, *The Astrophysical Journal*, **756**, 13, `DOI:10.1088/0004-637X/756/1/13`

Brown, A. M., Locating the γ-ray emission region of the flat spectrum radio quasar PKS 1510-089. 2013, *Monthly Notices of the RAS*, **431**, 824, `DOI:10.1093/mnras/stt218`

Burbidge, E. M. & Kinman, T. D., Redshifts of Fourteen Quasi-Stellar Radio Sources. 1966, *Astrophysical Journal*, **145**, 654, `DOI:10.1086/148808`

Cardelli, J. A., Clayton, G. C., & Mathis, J. S., The Relationship between Infrared, Optical, and Ultraviolet Extinction. 1989, *Astrophysical Journal*, **345**, 245, `DOI:10.1086/167900`

Castignani, G., Pian, E., Belloni, T. M., et al., Multiwavelength variability study and search for periodicity of PKS 1510-089. 2017, *A&A*, **601**, A30, `DOI:10.1051/0004-6361/201629775`

D'Ammando, F., Pucella, G., Raiteri, C. M., et al., AGILE detection of a rapid flare from the blazar PKS 1510-089 during the GASP-WEBT monitoring*. 2009, *A&A*, **508**, 181, `DOI:10.1051/0004-6361/200912560`

Dotson, A., Georganopoulos, M., Meyer, E. T., & McCann, K., On the Location of the 2009 GeV Flares of Blazar PKS 1510-089. 2015, *Astrophysical Journal*, **809**, 164, `DOI:10.1088/0004-637X/809/2/164`

Dzhatdoev, T. A., Khalikov, E. V., Latypova, V. S., Podlesnyi, E. I., & Vaiman, I. A., Modeling the persistent low-state gamma-ray emission of the PKS 1510-089 blazar with electromagnetic cascades initiated in hadronuclear interactions. 2022, *Monthly Notices of the Royal Astronomical Society*, **515**, 5242, `DOI:10.1093/mnras/stac2094`

Edelson, R. A. & Krolik, J. H., The Discrete Correlation Function: A New Method for Analyzing Unevenly Sampled Variability Data. 1988, *Astrophysical Journal*, **333**, 646, `DOI:10.1086/166773`

Emmanoulopoulos, D., McHardy, I. M., & Papadakis, I. E., Generating artificial light curves: revisited and updated. 2013, *Monthly Notices of the RAS*, **433**, 907, `DOI:10.1093/mnras/stt764`

Fuhrmann, L., Angelakis, E., Zensus, J. A., et al., The F-GAMMA programme: multi-frequency study of active galactic nuclei in the Fermi era. Programme description and the first 2.5 years of monitoring. 2016, *Astronomy and Astrophysics*, **596**, A45, `DOI:10.1051/0004-6361/201528034`

Gaskell, C. M. & Sparke, L. S., Line Variations in Quasars and Seyfert Galaxies. 1986, *Astrophysical Journal*, **305**, 175, `DOI:10.1086/164238`

Greene, J. E. & Ho, L. C., Estimating Black Hole Masses in Active Galaxies Using the Hα Emission Line. 2005, *The Astrophysical Journal*, **630**, 122, `DOI:10.1086/431897`

H.E.S.S. Collaboration, Abdalla, H., Adam, R., et al., H.E.S.S. and MAGIC observations of a sudden cessation of a very-high-energy flare in PKS 1510-089 in May 2016. 2021, *A&A*, **648**, A23, `DOI:10.1051/0004-6361/202038949`

Homan, D. C., Wardle, J. F. C., Cheung, C. C., Roberts, D. H., & Attridge, J. M., PKS 1510–089: A Head-on View of a Relativistic Jet. 2002, *The Astrophysical Journal*, **580**, 742, `DOI:10.1086/343894`

Jorstad, S. G., Marscher, A. P., Lister, M. L., et al., Polarimetric Observations of 15 Active Galactic Nuclei at High Frequencies: Jet Kinematics from Bimonthly Monitoring with the Very Long Baseline Array. 2005, *Astronomical Journal*, **130**, 1418, `DOI:10.1086/444593`

Kataoka, J., Madejski, G., Sikora, M., et al., Multiwavelength Observations of the Powerful Gamma-Ray Quasar PKS 1510–089: Clues on the Jet Composition. 2008, *The Astrophysical Journal*, **672**, 787, `DOI:10.1086/523093`

Kovačević, J., Popović, L. Č., & Dimitrijević, M. S., Analysis of Optical Fe II Emission in a Sample of Active Galactic Nucleus Spectra. 2010, *Astrophysical Journal, Supplement*, **189**, 15, `DOI:10.1088/0067-0049/189/1/15`

León-Tavares, J., Chavushyan, V., Patiño-Álvarez, V. M., et al., Flare-like Variability of the Mg II λ2800 Emission Line in the γ-ray Blazar 3C 454.3. 2013, *The Astrophysical Journal Letters*, **763**, L36, `DOI:10.1088/2041-8205/763/2/L36`

Marscher, A. P., Jorstad, S. G., Larionov, V. M., et al., PROBING THE INNER JET OF THE QUASAR PKS 1510-089 WITH MULTI-WAVEBAND MONITORING DURING STRONG GAMMA-RAY ACTIVITY. 2010, *The Astrophysical Journal Letters*, **710**, L126, `DOI:10.1088/2041-8205/710/2/L126`

Orienti, M., Koyama, S., D'Ammando, F., et al., Radio and γ-ray follow-up of the exceptionally high-activity state of PKS 1510-089 in 2011. 2013, *Monthly Notices of the RAS*, **428**, 2418, `DOI:10.1093/mnras/sts201`

Oshlack, A. Y. K. N., Webster, R. L., & Whiting, M. T., Black Hole Mass Estimates of Radio-selected Quasars. 2002, *The Astrophysical Journal*, **576**, 81, `DOI:10.1086/341729`

Patiño-Álvarez, V. M., Carramiñana, A., Carrasco, L., & Chavushyan, V., A Multiwavelength Cross-Correlation Variability Study of Fermi-LAT Blazars. 2013, in *4th Fermi Symposium, eConf Proceedings C121028*, Monterey, CA, 0–6, 4th Fermi Symposium, eConf Proceedings C121028, 6 pages, 2 figures.

Patiño-Álvarez, V. M., Torrealba, J., Chavushyan, V., et al., Baldwin Effect and Additional BLR Component in AGN with Superluminal Jets. 2016, *Frontiers in Astronomy and Space Sciences*, **3**, 19, `DOI:10.3389/fspas.2016.00019`

Patiño-Álvarez, V. M., Fernandes, S., Chavushyan, V., et al., Multiwavelength photometric and spectropolarimetric analysis of the FSRQ 3C 279. 2018, *Monthly Notices of the Royal Astronomical Society*, **479**, 2037, `DOI:10.1093/mnras/sty1497`, _eprint: https://academic.oup.com/mnras/article-pdf/479/2/2037/25142034/sty1497.pdf

Peterson, B. M. 1997, *An Introduction to Active Galactic Nuclei*

Podjed, S. A., Hickox, R. C., Isler, J. C., Böttcher, M., & Schutte, H. M., Optical Spectropolarimetric Variability Properties in Blazars PKS 0637–75 and PKS 1510–089. 2024, *Astrophysical Journal*, **968**, 130, `DOI:10.3847/1538-4357/ad4111`

Poutanen, J. & Stern, B., GeV Breaks in Blazars as a Result of Gamma-ray Absorption Within the Broad-line Region. 2010, *Astrophysical Journal, Letters*, **717**, L118, `DOI:10.1088/2041-8205/717/2/L118`

Prince, R., Gupta, N., & Nalewajko, K., Two-zone Emission Modeling of PKS 1510-089 during the High State of 2015. 2019, *The Astrophysical Journal*, **883**, 137, `DOI:10.3847/1538-4357/ab3afa`

Rakshit, S., Broad line region and black hole mass of PKS 1510-089 from spectroscopic reverberation mapping. 2020, *A&A*, **642**, A59, `DOI:10.1051/0004-6361/202038324`

Rani, B., Gupta, A. C., Strigachev, A., et al., Short-term flux and colour variations in low-energy peaked blazars. 2010, *Monthly Notices of the RAS*, **404**, 1992, `DOI:10.1111/j.1365-2966.2010.16419.x`

Schlafly, E. F. & Finkbeiner, D. P., Measuring Reddening with Sloan Digital Sky Survey Stellar Spectra and Recalibrating SFD. 2011, *Astrophysical Journal*, **737**, 103, `DOI:10.1088/0004-637X/737/2/103`

Shaw, M. S., Romani, R. W., Cotter, G., et al., SPECTROSCOPY OF BROAD-LINE BLAZARS FROM 1LAC. 2012, *The Astrophysical Journal*, **748**, 49, `DOI:10.1088/0004-637X/748/1/49`

Smith, P. S., Montiel, E., Rightley, S., et al., Coordinated Fermi/Optical Monitoring of Blazars and the Great 2009 September Gamma-ray Flare of 3C 454.3. 2009, in *Fermi Symposium, eConf Proceedings C091122*, Washington, D.C, 0–6, 2009 Fermi Symposium, eConf Proceedings C091122, 6 pages, 2 figures.

Tavecchio, F., Ghisellini, G., Bonnoli, G., & Ghirlanda, G., Constraining the location of the emitting region in Fermi blazars through rapid γ-ray variability. 2010, *Monthly Notices of the RAS*, **405**, L94, `DOI:10.1111/j.1745-3933.2010.00867.x`

Tresse, L., Maddox, S., Loveday, J., & Singleton, C., Spectral analysis of the Stromlo-APM Survey — I. Spectral properties of galaxies. 1999, *Monthly Notices of the Royal Astronomical Society*, **310**, 262, `DOI:10.1046/j.1365-8711.1999.02977.x`

Xie, G. Z., Liu, H. T., Cha, G. W., et al., Spectrophotometry and Photometry for Five Blazars and Their Central Black Hole Masses. 2005, *Astronomical Journal*, **130**, 2506, `DOI:10.1086/497163`

Yuan, Q., Kushwaha, P., Gupta, A. C., et al., Multiwavelength Temporal Variability of the Blazar PKS 1510-089. 2023, *Astrophysical Journal*, **953**, 47, `DOI:10.3847/1538-4357/acdd74`

Contrib. Astron. Obs. Skalnaté Pleso **56/1**, 31 – 42, (2026)
https://doi.org/10.31577/caosp.2026.56.1.31

Green Bean galaxies and the fading echoes of AGN activity

A. Arshinova[1], **K. Sanderson**[2] **and A. Moiseev**[1,3]

[1] *Special Astrophysical Observatory, Russian Academy of Sciences, Nizhny Arkhyz 369167, Russia*
(E-mail: arina.arshinova@gmail.com)

[2] *Department of Astronomy, New Mexico State University, Las Cruces, NM 88033, USA*

[3] *Space Research Institute Russian Academy of Sciences, 84/32 Profsouznaya str., Moscow, 117997, Russian*

Received: October 20, 2025; Accepted: October 28, 2025

Abstract. Green Bean is a rare type of galaxy which represents a short-lived phase in the life cycle of active galactic nuclei (AGN), characterised by large-scale, powerful ionised clouds in the circumgalactic medium. Recent studies demonstrate that these extended ionised structures may reflect fading signatures of past AGN activity, often manifested in the form of large-scale ionisation cones. The analysis of their observational properties provides unique constraints on AGN lifetimes, feedback mechanisms, and transitions between radiative and kinetic modes of activity. In this paper we announce the first results of the project dedicated to the long-slit spectroscopic and scanning Fabry-Perot interferometric observations of Green Bean galaxies at the Russian 6-m telescope with SCORPIO-2 multi-mode instrument. We describe the data reduction and spectral fitting procedures that allow one to characterise ionisation conditions in extended gaseous regions of the galaxy SDSSJ095100.54+051026.7.

Key words: galaxies: active – galaxies: evolution – galaxies: ISM – galaxies: nuclei – techniques: spectroscopic

1. Introduction

Active Galactic Nuclei (AGN) represent a critical transitional stage in galaxy evolution, where supermassive black holes undergo intense but temporary phases of accretion. While extremely luminous, their true significance lies in this fleeting yet transformative period – a key link in understanding how galaxies and their central black holes co-evolve. Although estimates of the duration of the active phase vary and are subject to debate, they have been determined in recent years using a variety of ‘galactic archaeology’ methods (Morganti, 2017a, and references therein). In some radio-loud AGNs, extended relic structures can be identified, marking the decline of past activity and characterised by steep radio spectra and specific morphological features (Morganti, 2024). These relics typically trace AGN activity cycles on timescales of $\sim 10^6$–10^8 yr, reflecting the gradual fading of synchrotron-emitting plasma. Similarly, in the optical domain, extended photoionised nebulae (ionisation cones) are observed, providing clues to the timescales of their activity. Such structures often extend up to 3–50 kpc, corresponding to light-travel timescales of $\sim 10^4$–10^5 yr, while the recombination timescales of the ionised gas are much shorter (see Section 6.5 Schirmer et al., 2016), thereby probing much more recent phases of AGN activity.

These indicators of fading activity are typically studied separately for radio-loud and radio-quiet AGNs, with links to different accretion rates — either low or high, approaching the Eddington limit – or to kinetic and radiative forms of activity, respectively (Mullaney et al., 2013; Kukreti & Morganti, 2024). Recent multi-wavelength studies of nearby AGNs have revealed rare instances of galactic nuclei transitioning between kinetic and radiative regimes, or vice versa (Harvey et al., 2023; Moiseev et al., 2025). While a comprehensive theoretical explanation for this behaviour is still lacking, some models suggest that the influence of the nucleus on the interstellar medium during the earlier active phase of the galaxy plays a critical role (Morganti, 2017b; Ciotti et al., 2017).

'Green Bean' galaxies (GBGs), thought to be remnants of quasar ionisation, are extended ionised clouds detected in the SDSS sky survey at redshifts up to $z \sim 0.6$ (Schirmer et al., 2013). While these systems were originally characterised primarily by their extended emission-line regions, recent work has demonstrated that they can also host extended radio structures, including jet-induced lobes on scales of hundreds of kiloparsecs (Sanderson et al., 2024). Moreover, the same study revealed that the radio jets are at least 6 Myr old, and estimate of the ionisation balance indicates that the central activity has faded over the past 0.15 Myr. The ability to probe these accretion and radiative fading timescales makes GBGs ideal laboratories for studying changes in AGN activity, with Hanny's Voorwerp (Lintott et al., 2009) representing a well-studied example in the local Universe. Motivated by this, we have initiated observations of the ionised gas in GBGs already known to host extended radio structures, in order to probe whether the ionisation, kinematics, and spatial extent of the ionised gas correlate with the relic radio morphology, and to characterise the current evolutionary state of the AGN. As part of this program, we use long-slit (LS) spectroscopy and scanning Fabry–Perot interferometry (FPI) to obtain spatially resolved spectroscopic information on the extended emission-line regions. In this paper we present the first results for SDSS J095100.54+051026.7, selected as a pilot target because it shows clearly separated, spatially extended ionised clouds visible already in the photometric data.

This paper is structured as follows. In Section 2 we describe the observations and the reduction procedure. Section 3 presents the analysis of the long-slit and FPI data, including the emission-line fitting, kinematics, and diagnostic diagrams. Section 4 summarises the main results.

2. Observation and data reduction

As a pilot study, we focus here on the GBG candidate SDSS J095100.54+051026.7 (hereafter GP 117) at $z = 0.24072$, selected from our sample of visually green galaxies originally identified by participants of the Radio Galaxy Zoo project (Banfield et al., 2015). To explore its properties, we obtained LS spectroscopy and scanning FPI, which together allow us to probe the spatial distribution and kinematics of the ionised gas. The details of the observational setup are summarised in Table 1. The following subsections describe the observations and the data reduction procedures. The accepted spatial scale in this work is based on a flat ΛCDM cosmology with $H_0 = 70$ km s^{-1} Mpc^{-1}, $\Omega_{\rm m} = 0.3$, and $\Omega_\Lambda = 0.7$. The conversion between angular and physical scales was performed using the `astropy.cosmology` package (Astropy Collaboration et al., 2013). At the redshift of GP 117 ($z = 0.24072 \pm 0.00014$) as measured from the centroid positions of the Hα, Hβ, [O III], [N II], and [S II] emission lines in our long-slit spectrum, this corresponds to a spatial scale of 3.8 kpc arcsec^{-1}.

Table 1. Log of GP 117 observations at the 6-m telescope.

Data set	Date	T$_{exp}$, s	FOV	Seeing, ″	$\Delta\lambda$ Å	FWHM Å
			LS spectroscopy			
SCORPIO-2 PA=72°	2025 Jan 20	7200	$1'' \times 6.8'$	1.7	3500–8500	7
			FPI data			
SCORPIO-2	2025 Mar 07	3330	$6.8' \times 6.8'$	2.3	6170–6300	13

2.1. Long-slit spectroscopy

We conducted long-slit spectroscopy using SCORPIO-2 multi-mode focal reducer (Afanasiev & Moiseev, 2011) installed in the prime focus of the BTA 6-m telescope of Special Astrophysical Observatory of Russian Academy of Science (SAO RAS).

Individual exposures were 600 s each, with a total exposure of 7200 s. The slit was positioned at PA=72°, as shown in Fig. 1 (top left). The observations were carried out on 2025 January 20. The log of observations with other parameters (spectral range – $\Delta\lambda$, spectral resolution – FWHM, field-of-view – FOV) are given in Tab. 1.

The primary reduction of the long-slit spectra was performed using the custom `longwid` pipeline (designed for SCORPIO-1,2) operating in the IDL environment. The reduction followed a standard sequence of steps to calibrate the data and extract 2D spectra.

The process began with the creation of master calibration frames: a master bias was constructed from multiple zero-exposure frames to model the bias readout level, and a master flat-field was produced by system of LEDs (Afanasiev et al., 2017), providing stable and reproducible illumination for correcting variations of pixel-to-pixel sensitivity, optics transmission and non-uniformity of the slit width.

Wavelength calibration was performed by constructing a master He–Ne–Ar lamp frame from multiple comparison exposures and fitting a polynomial to positions of identified lines, which was then applied to each science frame.

Science frames were subsequently corrected for the curvature of spectral lines across the detector, ensuring that each wavelength aligned along a constant spatial column. The geometric correction was derived from the He–Ne–Ar lamp calibration frames by tracing the positions of comparison lines along the slit and modelling their curvature to construct a distortion map, which was then applied to the science frames using a two-dimensional warping transformation. The frames were then divided by the normalized master flat to apply flat-fielding. The geometric distortions related with aberrations of SCORPIO-2 optics and misalignment between CCD chip horizontal axis and direction of dispersion were modelled and corrected using a 13-point test pattern (13-dot mask) observed during the same run. This allowed for the precise rectification of the spectra.

The night sky background was modelled and subtracted by fitting a fifth-order polynomial to the spatial profile at each wavelength column in regions of the slit devoid of astronomical sources. Following sky subtraction, residual cosmic ray hits were identified and removed with standard algorithms based on sigma-clipping algorithm applied to multiple exposures, as described for the CCD261-84 detector (see Sec. 9 in Afanasieva et al., 2023). Residual cosmic rays were manually masked when necessary.

Finally, the data were flux-calibrated. Spectrophotometric standard star Feige 56 was observed at a close zenith distance before the object to minimize the effects of atmospheric extinction variations. A sensitivity function was derived by comparing the extracted spectrum of the standard star to its absolute flux table. This function was applied to the science target to produce a final spectrum in absolute flux units [$\mathrm{erg\,s^{-1}\,cm^{2}\,\AA^{-1}}$].

In parallel with the spectroscopic reduction, Poisson noise and readout noise were estimated from the raw frames. These measurements were then propagated to construct error frames, allowing proper error propagation throughout the subsequent data reduction steps.

From the long-slit data, we extracted one spectrum from the central region (hereafter C) and two from the extended emission-line regions located to the East and West of the nucleus (E and W components, respectively). The extraction areas were chosen to match the regions of enhanced [O III] emission visible in the two-dimensional spectrum. The stellar population fitting was performed only for the central spectrum, while the emission-line analysis was carried out for all three components (Section 3.1).

2.2. 3D spectroscopy with scanning FPI

3D spectroscopic observations in the [O III]$\lambda5007$ emission line were performed with at the 6-m telescope with the SCORPIO-2 instrument in the scanning FPI mode having field of view 6.8×6.8 arcmin (Tab. 1) with the scale $0.39''$per px. We used the low spectral resolution FPI20 that is usually employed as a tunable filter for mapping emission lines in various extended objects with MaNGaL photometer at the 1-m and 2.5-m telescopes (Moiseev et al., 2020). This FPI works in the order interference ~ 20 (at 6560 Å) and has a spectral resolution FWHM ≈ 13Å ($\sim 780\,\mathrm{km\,s^{-1}}$ in the [O III]). Of course, this resolution is too low for detailed analysis of lines shape, however it is enough to study the gas kinematics if the amplitude of velocity changes exceeds $50\,\mathrm{km\,s^{-1}}$, as it was shown in our previous research dedicated to Teacup AGN (Moiseev & Ikhsanova, 2023).

In contrast to 'classical' observations with a high spectral resolution at which the full range between adjacent interference orders was scanned (Moiseev, 2021, and references therein), with low-resolution FPI20 we selected only 8 spectral channels for observations with the following wavelengths: 0, ±8, ±16, ±24Å relative to 6201Å. This central wavelength corresponds to the [O III]$\lambda5007$ emission line redshifted by the systemic velocity of the galactic nucleus, and +100Å for the continuum emission. We sequentially switched corresponding gap between FPI plates (below – 'channel') with individual exposures 90 s per frame. In total we collect 3–6 frames in each channel, because only frames with the best seeing values were selected for the final analysis. The medium band filter (central wavelength – 6271 Å, FWHM = 250 Å) isolated the required spectral range with a single peak of FPI transmission (see Fig. 1 in Moiseev et al., 2020).

Internal calibration included the exposures of the following sources: (i) continuous spectrum halogen lamp for creating a flat-field in the same channels as in the galaxy observations; (ii) the same He-Ne-Ar lamp as in the LS mode (Sec. 2.1) scanned in the full working spectral range.

The first steps of data reduction were performed using custom developed IDL package `diwid`, specialized for reduction of direct images and MaNGaL data (Moiseev et al., 2020).

The reduction process began with the application of standard calibrations: subtraction of a master bias frame and division by a normalized master flat-field frame to correct for pixel-to-pixel sensitivity variations. Cosmic ray hits in individual frames were removed using `L.A.COSMIC` program based on Laplacian edge detection (van Dokkum, 2001).

Subsequent steps involved the spatial alignment of all frames. This was achieved by matching the positions of foreground stars across individual exposures, and applying corresponding shifts to ensure precise registration throughout the data cube. Details obtained from stellar photometry were used to reject frames with poor seeing value, or with subsected excess of atmospheric extinction.

Individual exposures were then combined into data cube according to their channel numbers. Remaining cosmic ray hits were removed during the stacking process using a sigma-clipping technique.

Further data reduction steps were based on algorithms from our IDL package for FPI data reduction `ifpwid` (see references and description in Moiseev, 2021). The foreground air-glow emission were subtracted in the each data cube channel using a polynomial approximation of sky emission in a polar coordinate system in areas free from stars and contribution from galaxies. This procedure is important because the wavelength in the observed frames changes with radius (see Fig. 4 in Moiseev, 2021). The correction on variations of atmospheric extinction from channel to channel were performed using photometry of stars with 2D Moffat function. Then the astrometric calibration was performed via the astrometry.net[1] online service (Lang et al., 2010) and rotated to the custom orientation 'North is up, East is to the left'.

Emission lines in the cube of bias-subtracted frames illuminated by He-Ne-Ar calibration lamps were fitted by Lorentz profile. Based on the fitting results we created a Λ-cube having the same size as the object's data cube. The values in the Λ-cube correspond to wavelength of each pixel in the object's data cube (Moiseev, 2015). In other words, a non-linear wavelength scale were created for each spaxel in field-of-view. Based on this wavelength calibration [O III] emission line was fitted with Voigt function that gives a good approximation of a FPI spectrum. The fitting results are images in the [O III] flux and line-of-sight velocity field shown in Fig. 1 (bottom). Regions on the presented maps with signal-to-noise $S/N \leq 3$ were masked.

To flux-calibrate the data, the spectrophotometric standard BD+33d2642 was observed in the same instrumental configuration and atmospheric conditions. The identical reduction procedure was applied to the standard star observations. The calibration to the energetic units [$\mathrm{erg\,s^{-1}\,cm^2}$] per pixel or arcsec^2 was performed similar with MaNGaL data as desribed in (Moiseev et al., 2020). The instrumental response curve was derived by comparing the observed and tabulated fluxes of the standard star, after correcting for atmospheric extinction, and was subsequently applied to the object.

3. Data analysis

The combined use of long-slit spectroscopy and FPI mapping provides a methodology for the spatially resolved analysis of the ionized gas in GP 117.

---

[1] http://astrometry.net/

3.1. Stellar population subtraction and emission-line fitting

A crucial step in the analysis of spectra of galaxies with weak or fading AGN signatures is the separation of stellar and gaseous contributions in the central regions, where the host galaxy continuum can significantly dominate. To account for the stellar population, we employed the `pPXF` (penalized pixel-fitting) package (Cappellari, 2017), fitting the observed spectra with the eMILES stellar population synthesis (SPS) models (Vazdekis et al., 2016), without including an AGN component. Although the nuclear contribution is relatively weak, consistent with a fading or low-luminosity AGN scenario, the emission lines in the nuclear spectrum are still noticeable. Therefore, the stellar continuum fitting was performed iteratively: the strongest emission-line regions were first masked, followed by the fitting of the absorption features and subsequent refinement of the emission-line model until convergence was reached. This approach ensures a reliable subtraction of the absorption features, particularly those affecting the Balmer lines. The resulting luminosity-weighted stellar age and metallicity for this object are $\langle Age \rangle = 12.6 \pm 0.5\, Gyr$ and $\langle[\mathrm{M/H}]\rangle = -0.40 \pm 0.05$, respectively.

After continuum subtraction, the residual emission-line spectra were fitted with Gaussian profiles using the standard `python` library `scipy`. From this fitting, we derived the radial velocities and line fluxes for each emission line, which are essential for constructing diagnostic diagrams that distinguish between different ionisation mechanisms and trace the fading signatures of AGN activity (see Fig. 2).

3.2. Spatially Resolved Kinematics

The long-slit spectra provide the primary data for kinematic analysis. Velocities were derived by fitting Gaussian profiles to the main emission lines after subtraction of the stellar continuum. The line-of-sight velocity distribution shown in Fig. 1 (top right). Furthermore, the [O III] velocity field was reconstructed from the FPI data cube by fitting the [O III] line profile in each spatial element with a Voigt function, producing the two-dimensional map of line-of-sight velocities (Fig. 1) (bottom right). A more comprehensive interpretation of the kinematics will be addressed in a forthcoming study, where we will combine these data with a larger sample and additional multiwavelength observations.

3.3. Excitation and Ionization Conditions

The primary tool for diagnosing the mechanisms powering the ionized gas (e.g., star formation vs. active galactic nuclei) is the analysis of emission-line ratios.

BPT Diagnostics: From the long-slit spectra, we measure the fluxes of key diagnostic lines ([O III]λ5007, Hβ, Hα, [N II]λ6583) at various positions. These ratios are plotted on standard Baldwin-Phillips-Terlevich (BPT) diagrams (Baldwin et al., 1981) in Fig. 2. The central region (C) of the galaxy lies within the LINER area of the diagram. The observed emission-line widths (~330–400 km/s)

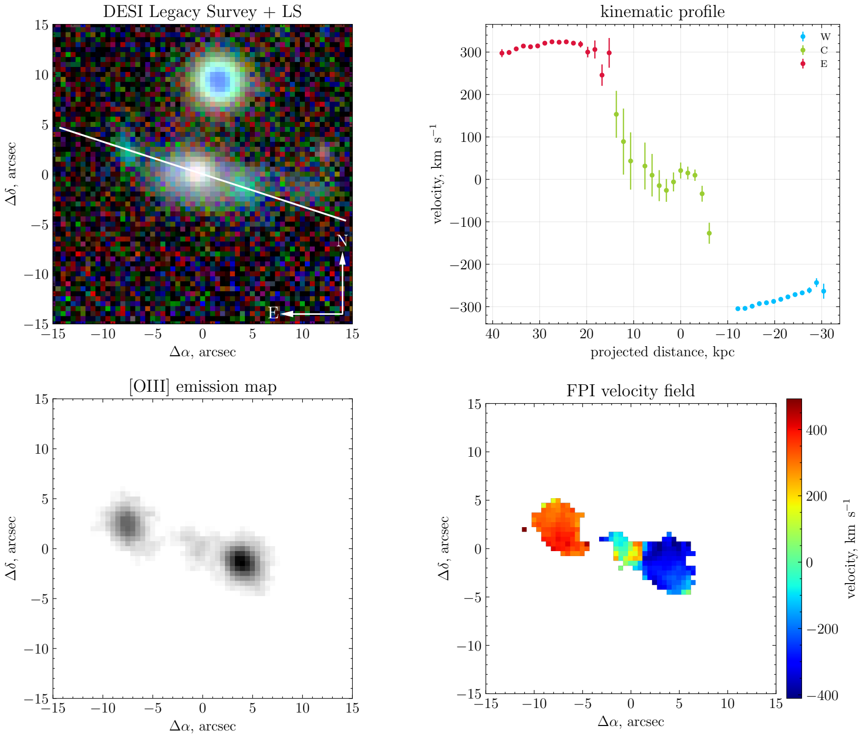

Figure 1. *(Top left:)* Optical image from the DESI Legacy Survey. The white line indicates the position of the LS at PA = 72°, used for the spectroscopic observations. *(Top right:)* Line-of-sight velocity distribution derived from the long-slit spectroscopic data. Velocity distribution corrected for the systemic velocity $v_{sys} = 71567\,km\,s^{-1}$. The green symbols represent the stellar-population-subtracted gas component in the central galactic region, while the red and blue symbols trace the velocity and its measurement errors in the extended clouds on either side of the galaxy.
(Bottom:) Maps obtained from Voigt fitting of FPI spectra: flux map in the [O III]λ5007 emission line *(left)* and corresponding line-of-sight velocity field *(right)*.

show no evidence for the extremely broad profiles expected from strong shock ionization. While some local kinematic disturbances may be present, photoionization by the AGN appears to be the dominant excitation mechanism. Meanwhile, the extended ionised clouds (W and E) exhibit systematically higher ionisation, which is indicative of a previous phase of AGN activity.

Helium Line Analysis: For the He II, emission line in the long-slit spectra, we construct a helium diagnostic diagram (He II/Hβ, vs. [N II]λ6583/Hα) (Shirazi & Brinchmann, 2012) to probe the ionising source and the physical conditions of the gas (Fig. 2). Notably, He II emission is detected predominantly in the extended ionised clouds, while it is absent in the central region, highlighting that the hard ionising radiation from the AGN primarily affects the outer regions.

These results confirm the presence of large-scale ionised clouds surrounding GP 117, which were previously only suspected based on photometric data. The [O III]λ5007 emission extends up to $\sim$ 40 kpc from the nucleus, as seen from both the line-of-sight velocity curve and the [O III] flux map (Fig. 1) (right panels).

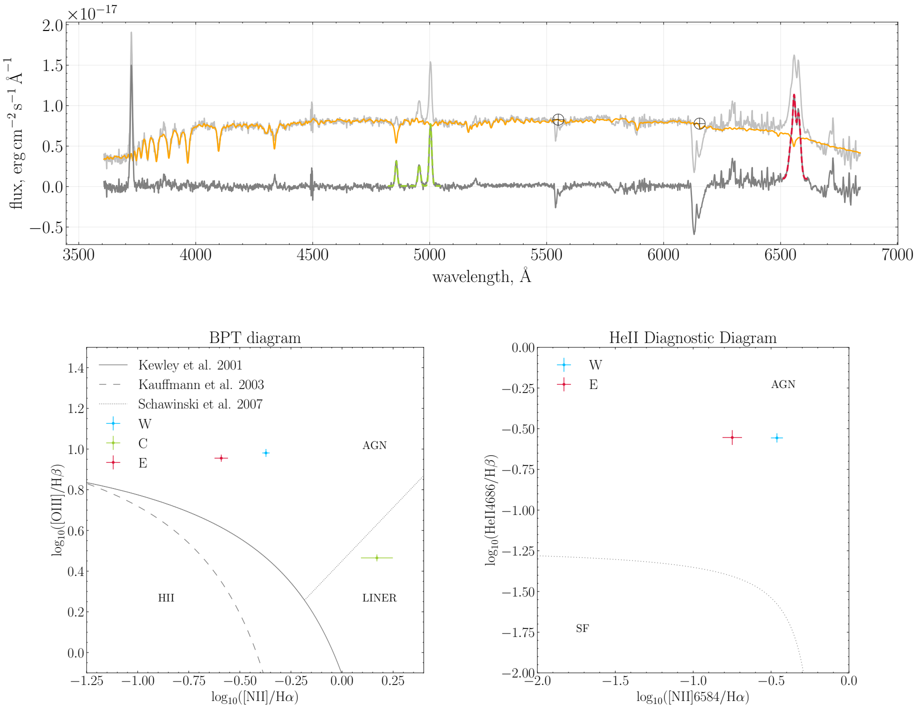

Figure 2. *(Top):* Nuclear spectrum of GP 117. The observed SCORPIO-2 spectrum is shown in light gray, the stellar population model - in orange. The dark gray line corresponds to the residual spectrum after subtracting the stellar continuum. The green dashed and red dashed lines represent Gaussian fits to the [O III]+Hβ and [N II]+Hα emission lines, respectively. Telluric absorption lines are marked with the $\oplus$ symbol at the corresponding wavelengths.
(Bottom left): Standard [O III]λ5007/Hβ vs. [N II]λ6583/Hα (BPT) diagram. The solid and dashed curves represent the separation lines between different ionization sources (Kewley et al., 2001; Kauffmann et al., 2003; Schawinski et al., 2007).
(Bottom right): He II/Hβ vs. [N II]λ6583/Hα diagram (Shirazi & Brinchmann, 2012). The green point marks the central galactic region, while the red and blue points show the integrated line ratios for the extended clouds.

4. Conclusions

In this work, we present a pilot study of the Green Bean galaxy GP 117 (SDSS J095100.54+051026.7), based on new long-slit and 3D spectroscopic observations obtained with the SCORPIO-2 spectrograph at the 6-m Russian telescope. These data provide the first spectroscopic confirmation of the large-scale ionised clouds in this system, allowing us to characterise their ionisation state and kinematics in detail. The [O III]λ5007 emission is traced up to ~ 40 kpc from the nucleus on each side, confirming the presence of extended high-ionisation gas previously suspected only from imaging data.

The properties of these ionised clouds show similarities to other systems with extended high-ionisation emission, such as Hanny's Voorwerp in the local Universe (Lintott et al., 2009) and several Green Bean galaxies analysed previously (Schirmer et al., 2016). In these objects, bright [O III] emission on tens-of-kiloparsec scales and enhanced ionisation away from the nucleus have been reported as common features. Although the physical interpretation of such structures varies across individual cases, GP 117 exhibits ionisation characteristics and spatial morphology comparable to those seen in these previously studied systems.

To quantify these properties, we modelled the stellar population using the `pPXF` package with eMILES templates to subtract the host galaxy continuum in the central regions, allowing reliable recovery of emission-line fluxes. Gaussian fitting of the emission lines then provided kinematic parameters and fluxes for key diagnostic features, enabling the construction of classical and extended diagnostic diagrams. Resolved emission-line ratio maps and spatially resolved kinematics suggest a radiative fading scenario in GP 117, and our next step is to combine this optical analysis with radio observations to gain a deeper understanding of the evolutionary status of GP 117 and related systems.

Acknowledgements. This study was supported by the Russian Science Foundation, project no. 25-12-00129 'Study of activity cycles of galactic nuclei'. The observational data were obtained with the 6-m telescope of the Special Astrophysical Observatory of the Russian Academy of Sciences carried out with the financial support of the Ministry of Science and Higher Education of the Russian Federation. The renovation of the telescope equipment is currently provided within the national project "Science and Universities".

References

Afanasiev, V. L., Amirkhanyan, V. R., Moiseev, A. V., Uklein, R. I., & Perepelitsyn, A. E., SCORPIO-2 guiding and calibration system in the prime focus of the 6-m telescope. 2017, *Astrophysical Bulletin*, **72**, 458, DOI:10.1134/S1990341317040095

Afanasiev, V. L. & Moiseev, A. V., Scorpio on the 6 m Telescope: Current State and Perspectives for Spectroscopy of Galactic and Extragalactic Objects. 2011, *Baltic Astronomy*, **20**, 363, `DOI:10.1515/astro-2017-0305`

Afanasieva, I., Murzin, V., Ardilanov, V., et al., Astronomical Camera Based on a CCD261-84 Detector with Increased Sensitivity in the Near-Infrared. 2023, *Photonics*, **10**, 774, `DOI:10.3390/photonics10070774`

Astropy Collaboration, Robitaille, T. P., Tollerud, E. J., et al., Astropy: A community Python package for astronomy. 2013, *Astronomy and Astrophysics*, **558**, A33, `DOI:10.1051/0004-6361/201322068`

Baldwin, J. A., Phillips, M. M., & Terlevich, R., Classification parameters for the emission-line spectra of extragalactic objects. 1981, *Publications of the ASP*, **93**, 5, `DOI:10.1086/130766`

Banfield, J. K., Wong, O. I., Willett, K. W., et al., Radio Galaxy Zoo: host galaxies and radio morphologies derived from visual inspection. 2015, *Monthly Notices of the RAS*, **453**, 2326, `DOI:10.1093/mnras/stv1688`

Cappellari, M., Improving the full spectrum fitting method: accurate convolution with Gauss-Hermite functions. 2017, *Monthly Notices of the RAS*, **466**, 798, `DOI:10.1093/mnras/stw3020`

Ciotti, L., Pellegrini, S., Negri, A., & Ostriker, J. P., The Effect of the AGN Feedback on the Interstellar Medium of Early-Type Galaxies:2D Hydrodynamical Simulations of the Low-Rotation Case. 2017, *Astrophysical Journal*, **835**, 15, `DOI:10.3847/1538-4357/835/1/15`

Harvey, T., Maksym, W. P., Keel, W., et al., Signatures of feedback in the spectacular extended emission region of NGC 5972. 2023, *Monthly Notices of the RAS*, **526**, 4174, `DOI:10.1093/mnras/stad2989`

Kauffmann, G., Heckman, T. M., Tremonti, C., et al., The host galaxies of active galactic nuclei. 2003, *Monthly Notices of the RAS*, **346**, 1055, `DOI:10.1111/j.1365-2966.2003.07154.x`

Kewley, L. J., Dopita, M. A., Sutherland, R. S., Heisler, C. A., & Trevena, J., Theoretical Modeling of Starburst Galaxies. 2001, *Astrophysical Journal*, **556**, 121, `DOI:10.1086/321545`

Kukreti, P. & Morganti, R., Connecting the radio AGN life cycle to feedback: Ionised gas is more disturbed in young radio AGN. 2024, *Astronomy and Astrophysics*, **690**, A140, `DOI:10.1051/0004-6361/202450454`

Lang, D., Hogg, D. W., Mierle, K., Blanton, M., & Roweis, S., Astrometry.net: Blind Astrometric Calibration of Arbitrary Astronomical Images. 2010, *Astronomical Journal*, **139**, 1782, `DOI:10.1088/0004-6256/139/5/1782`

Lintott, C. J., Schawinski, K., Keel, W., et al., Galaxy Zoo: 'Hanny's Voorwerp', a quasar light echo? 2009, *Monthly Notices of the RAS*, **399**, 129, `DOI:10.1111/j.1365-2966.2009.15299.x`

Moiseev, A., Arshinova, A., & Smirnova, A., Archaeology of galactic nuclei activity. 2025, *Phys. Usp.*, **68**, accepted, `DOI:10.3367/UFNr.2025.03.040022`

Moiseev, A., Perepelitsyn, A., & Oparin, D., Mapper of Narrow Galaxy Lines (MaNGaL): new tunable filter imager for Caucasian telescopes. 2020, *Experimental Astronomy*, **50**, 199, `DOI:10.1007/s10686-020-09672-x`

Moiseev, A. V., Reduction of CCD observations made with a scanning Fabry–Perot interferometer. III. Wavelength scale refinement. 2015, *Astrophysical Bulletin*, **70**, 494, `DOI:10.1134/S1990341315040112`

Moiseev, A. V., Scanning Fabry–Perot Interferometer of the 6-m SAO RAS Telescope. 2021, *Astrophysical Bulletin*, **76**, 316, `DOI:10.1134/S1990341321030081`

Moiseev, A. V. & Ikhsanova, A. I., Gas and Stars in the Teacup Quasar Looking with the 6-m Telescope. 2023, *Universe*, **9**, 66, `DOI:10.3390/universe9020066`

Morganti, R., Archaeology of active galaxies across the electromagnetic spectrum. 2017a, *Nature Astronomy*, **1**, 596, `DOI:10.1038/s41550-017-0223-0`

Morganti, R., The many routes to AGN feedback. 2017b, *Frontiers in Astronomy and Space Sciences*, **4**, 42, `DOI:10.3389/fspas.2017.00042`

Morganti, R., What Have We Learned about the Life Cycle of Radio Galaxies from New Radio Surveys. 2024, *Galaxies*, **12**, 11, `DOI:10.3390/galaxies12020011`

Mullaney, J. R., Alexander, D. M., Fine, S., et al., Narrow-line region gas kinematics of 24 264 optically selected AGN: the radio connection. 2013, *Monthly Notices of the RAS*, **433**, 622, `DOI:10.1093/mnras/stt751`

Sanderson, K. N., Kapińska, A. D., Prescott, M. K. M., et al., Signatures of Active Galactic Nucleus Feedback Modes: A Green Bean Galaxy with 150 kpc Jet-induced Radio Emission. 2024, *Astrophysical Journal*, **971**, 20, `DOI:10.3847/1538-4357/ad50a8`

Schawinski, K., Thomas, D., Sarzi, M., et al., Observational evidence for AGN feedback in early-type galaxies. 2007, *Monthly Notices of the RAS*, **382**, 1415, `DOI:10.1111/j.1365-2966.2007.12487.x`

Schirmer, M., Diaz, R., Holhjem, K., Levenson, N. A., & Winge, C., A Sample of Seyfert-2 Galaxies with Ultraluminous Galaxy-wide Narrow-line Regions: Quasar Light Echoes? 2013, *Astrophysical Journal*, **763**, 60, `DOI:10.1088/0004-637X/763/1/60`

Schirmer, M., Malhotra, S., Levenson, N. A., et al., About AGN ionization echoes, thermal echoes and ionization deficits in low-redshift Lyα blobs. 2016, *Monthly Notices of the RAS*, **463**, 1554, `DOI:10.1093/mnras/stw1819`

Shirazi, M. & Brinchmann, J., Strongly star forming galaxies in the local Universe with nebular He IIλ4686 emission. 2012, *Monthly Notices of the RAS*, **421**, 1043, `DOI:10.1111/j.1365-2966.2012.20439.x`

van Dokkum, P. G., Cosmic-Ray Rejection by Laplacian Edge Detection. 2001, *Publications of the ASP*, **113**, 1420, `DOI:10.1086/323894`

Vazdekis, A., Koleva, M., Ricciardelli, E., Röck, B., & Falcón-Barroso, J., UV-extended E-MILES stellar population models: young components in massive early-type galaxies. 2016, *Monthly Notices of the RAS*, **463**, 3409, `DOI:10.1093/mnras/stw2231`

Contrib. Astron. Obs. Skalnaté Pleso **56/1**, 43 – 51, (2026)
https://doi.org/10.31577/caosp.2026.56.1.43

Insights into jet–NLR energetics in PMN J0948+0022

B. Dalla Barba[1,2,3], **L. Foschini**[2], **M. Berton**[3], **A. Lähteenmäki**[4,5], **M. Tornikoski**[4], **E. Sani**[3], **L. Crepaldi**[6,7], **E. Congiu**[3], **G. Venturi**[8,9], **W.J. Hon**[10] and **A. Vietri**[11,6]

[1] *Universitá degli studi dell'Insubria, Via Valleggio 11, Como 22100, Italy*
[2] *Osservatorio Astronomico di Brera, Istituto Nazionale di Astrofisica (INAF), Via E. Bianchi 46, Merate (LC) 23807, Italy*
[3] *European Southern Observatory (ESO), Alonso de Córdova 3107, Vitacura Santiago, Chile*
[4] *Aalto University Metsähovi Radio Observatory, Metsähovintie 114, FI-02540 Kylmälä, Finland*
[5] *Aalto University Department of Electronics and Nanoengineering, P.O. Box 15500, FI-00076 AALTO, Finland*
[6] *Dipartimento di Fisica e Astronomia "G. Galilei", Università degli studi di Padova, Vicolo dell'Osservatorio 3, Padova 35122, Italy*
[7] *Osservatorio Astronomico di Cagliari, Istituto Nazionale di Astrofisica (INAF), Via della Scienza 5, 09047 Selargius, Italy*
[8] *Scuola Normale Superiore, Piazza dei Cavalieri 7, Pisa 56126, Italy*
[9] *Osservatorio Astrofisico di Arcetri, Istituto Nazionale di Astrofisica (INAF), Largo E. Fermi 5, Firenze 50125, Italy*
[10] *School of Physics, University of Melbourne, Parkville, Victoria 3010, Australia*
[11] *Osservatorio Astronomico di Padova, Istituto Nazionale di Astrofisica (INAF), Vicolo dell'Osservatorio 5, 35122 Padova, Italy (E-mail: benedetta.dallabarba@inaf.it)*

Received: July 21, 2025; Accepted: November 5, 2025

Abstract. The analysis of the optical spectra of PMN J0948+0022 showed significant variations in the spectral lines that, when combined with the *Fermi* $\gamma-$ray light curve and radio observations reported by other authors, were interpreted as the result of interactions between the relativistic jet and the narrow-line region (NLR). In this work, we present order-of-magnitude calculations of the energetics associated with this proposed jet-NLR interaction. We demonstrate that the observed outflows are capable of absorbing a fraction of the jet energy and converting it into kinetic energy. This mechanism provides a natural explanation for the optical spectral variability recorded with the X-shooter and Multi-Unit Spectroscopic Explorer (MUSE) instruments. Our results support the scenario in which feedback from the relativistic jet can dynamically influence the circumnuclear gas, offering new insights into the coupling between jets and the NLR in $\gamma-$ray-emitting narrow-line Seyfert 1 galaxies.

Key words: Seyfert galaxies – individual: PMN J0948+0022 – optical spectroscopy

1. Introduction

Among active galactic nuclei (AGN), narrow-line Seyfert 1 galaxies (NLS1s) represent a peculiar class of objects. NLS1s are spectroscopically classified sources with relatively narrow Hβ, faint [O III]λ5007, and often strong Fe II multiplets (Osterbrock & Pogge, 1985; Goodrich, 1989). The importance of these sources lies in their nature as young or rejuvenated quasars (Mathur, 2000), potentially representing the progenitors of more evolved quasars (Berton et al., 2016, 2017, 2025). A small fraction of NLS1s show relativistic jet emission, which in some cases makes the sources detectable at γ-rays (γ-NLS1s). The first example of such a source is PMN J0948+0022 ($z = 0.585$; Williams et al. 2002; Zhou et al. 2003; Ahn et al. 2012; Foschini et al. 2010). To date, about two dozen γ-NLS1s have been identified (e.g., Foschini et al. 2022), and their number is steadily increasing.

In Dalla Barba et al. (2025) (hereafter referred to as DB25), we analyzed the optical spectral variations of PMN J0948+0022, focusing on the Hβ and [O III]$\lambda\lambda$4959, 5007 emission lines. We detected variability in the [O III]λ5007 core flux, in its outflow component, and in the outflow velocity. Based on intermediate-resolution ($R = \lambda/\Delta\lambda \sim 6500 - 2500$) X-shooter (2017-12-17) and Multi-Unit Spectroscopic Explorer (MUSE) spectra (between 2022-11-24 and 2023-03-08, the analyzed spectrum combines data from all epochs), we proposed a reclassification of this source from a NLS1 to an intermediate Seyfert, characterized by a composite profile for the Balmer lines. We suggested that the X-shooter and MUSE Hβ profiles are not due to a geometrical effect of partial obscuration, but rather to the interaction of the relativistic jet with the narrow-line region (NLR). This interaction was previously suggested by Doi et al. (2019) from the study of the radio component of the jet. The authors found a jet-shape change at a distance of $\sim$100-400 pc from the center, compatible with our estimate of the distance of the outflow ($D_{out} \sim$ 130-220 pc). From this, we proposed that the jet impacted the outflowing bubble, producing both the observed shape variation of the jet and the release of part of its energy into the surrounding NLR, which in turn generated the observed optical spectral variations.

In this work, we extend the study presented in DB25, focusing on the energetics of the jet-NLR interaction. These are back-of-the-envelope calculations, meant to provide an order-of-magnitude estimate of the process. The paper is organized as follows: Section 2 presents the physical conditions and energetics of the NLR; Section 3 describes the energetics of the jet from γ-ray and radio data; Section 4 discusses the results and conclusions. Throughout the manuscript we assume a standard ΛCDM cosmology with H_0=73.3 km s^{-1} Mpc^{-1}, Ω_m=0.3, and Ω_Λ=0.7 (Riess et al., 2022).

2. NLR and outflow properties

In general, from line ratios such as [O II] and [S II] we can estimate the electron density (n_e) and temperature (T_e) of the gas in the NLR. Given the X-shooter and MUSE spectral coverage, [S II] lines are not present in both PMN J0948+0022 spectra. For this reason, we assumed a typical $T_e \sim 10^4$ K (Osterbrock & Ferland, 2006) and calculated the electron density from the [O II]$\lambda\lambda$3726,3729 lines using `PyNeb` (Luridiana et al., 2013, 2015), a Python tool to compute emission line emissivities from recombination and collisionally excited lines (in our case we used only collisionally excited lines). The [O II] line fluxes from DB25 are reported in Table 2. The results, expressed as the median values obtained from N=5000 iterations with initial values inside the error bars of the observed fluxes, are: $n_{e,X} \sim 170$ cm^{-3} and $n_{e,M} \sim 260$ cm^{-3}, for the X-shooter and MUSE cases, respectively.

From the calculated n_e and the [O III]λ5007 luminosity of the outflow (L^{out}_{5007}), we can estimate the mass of the outflow (M_{out}). The L^{out}_{5007} parameter was obtained from $L^{out}_{5007} = 4\pi d_L^2 F^{out}_{5007}$, where d_L is the luminosity distance and F^{out}_{5007} is the observed flux of the outflowing component in [O III] (see again Table 2). M_{out} is then calculated using the relation from Komossa et al. (2018):

$$M_{out} = 67.4 \times 10^7 \left(\frac{L^{out}_{5007}}{10^{42}\,\mathrm{erg\,s^{-1}}}\right)\left(\frac{n_e}{100\,\mathrm{cm^{-3}}}\right)^{-1} M_\odot \tag{1}$$

where we re-scaled by a factor 10 the relation to use the [O III] luminosity instead of the Hβ one, as suggested by Komossa et al. (2018). For the two cases, the results are: $M_{out,X} \sim 8.6 \cdot 10^7\ M_\odot$ and $M_{out,M} \sim 3.9 \cdot 10^7\ M_\odot$.

Following the same reasoning presented in Blustin et al. (2005) and Venturi et al. (2023), the mass outflow rate through a spherical surface of radius r subtended by a solid angle Ω, with covering factor CF, is $\dot{M}_{out} = \Omega r^2 \rho v_{out} \cdot CF$. If the outflowing mass M_{out} is contained in a thin shell of radial thickness R_{out}, its volume is approximately $V \simeq \Omega r^2 R_{out}$ and therefore:

$$\begin{aligned} \dot{M}_{out} &\sim \Omega r^2 \frac{M_{out}}{V} v_{out} \cdot CF \sim \cancel{\Omega} \frac{M_{out}}{\cancel{\Omega r^2} R_{out}} \cancel{r^2} v_{out} \cdot CF \sim \\ &\sim \frac{M_{out}}{R_{out}} v_{out} \cdot CF \sim \frac{M_{out}}{D_{out} \cdot \cancel{0.1}} v_{out} \cdot \cancel{0.1} \end{aligned} \tag{2}$$

assuming roughly constant density and velocity across the shell, we have adopted a reference covering factor $CF \sim 0.1$ and an outflow distance from the center of $D_{out} \sim R_{out}/0.1 \sim 173$ pc (see the mean value reported in Table 2). In the D_{out} expression, we have further assumed a conical shape for the jet. Finally, the kinetic power of the outflow is:

$$\dot{E}_{kin} = \frac{1}{2}\dot{M}_{out}v_{out}^2 = P_{out} \tag{3}$$

The resulting estimates for the two cases are $P_{out,X} \sim 8.8 \cdot 10^{42}$ erg s^{-1} and $P_{out,M} \sim 14 \cdot 10^{42}$ erg s^{-1}.
If we instead assume electron temperatures in the range $T_e = (5 - 20) \cdot 10^4$ K (Osterbrock & Ferland, 2006), the resulting densities are $n_{e,X} \sim 120 - 210$ cm^{-3} and $n_{e,M} \sim 190 - 320$ cm^{-3}. The corresponding outflow powers are $P_{out,X} \sim (7.0 - 12) \cdot 10^{42}$ erg s^{-1} and $P_{out,M} \sim (12 - 19) \cdot 10^{42}$ erg s^{-1}. In all cases, these variations do not affect the conclusions.

3. Jet power

3.1. γ-ray component

We calculated the radiative power of the jet ($P_{\gamma,\mathrm{rad}}$) from *Fermi* data obtained in epochs nearly simultaneous with the X-shooter and MUSE observations. For X-shooter, we used the photon flux from 2017-12-30, while for MUSE we calculated the mean value of the *Fermi* datapoints over the interval 2022-12-04 to 2023-02-02. We multiplied the photon flux (F_γ, reported in Table 2) by the photon mean energy, using 1 GeV as reference for the conversion, and then obtained the flux in erg s^{-1} cm^{-2}. We calculated the corresponding luminosity (L_γ) using:

$$L_\gamma = 4\pi d_L^2 \frac{F_\gamma}{(1+z)^{1-\alpha_\gamma}} \tag{4}$$

where α_γ is the spectral index in the γ-rays obtained from the *Fermi* light-curve repository (see Table 2). With the luminosity, we then calculated $P_{\gamma,rad}$ using the equation from Maraschi & Tavecchio (2003):

$$P_{\gamma,rad} = \Gamma^2 \frac{L_\gamma}{\delta^4} \tag{5}$$

where Γ is the bulk Lorentz factor and δ the corresponding Doppler factor. As reported in Table 2, we can assume two possible values for these quantities, which lead to four different results. Here we report only the two mean values: $P_{\gamma,\mathrm{rad},X} \sim 2.5 \times 10^{44}$ erg s^{-1} and $P_{\gamma,\mathrm{rad},M} \sim 2.4 \times 10^{44}$ erg s^{-1}. Finally, we assume that the kinetic power is ten times the radiative one, see Table 1 for $P_{\gamma,kin}$.

3.2. Radio component

For the radio component, we can use the relation presented in Foschini et al. (2024) to obtain kinetic ($P_{radio,kin}$) power of the jet:

$$P_{radio,kin} = 3.9 \times 10^{44} \left(\frac{S_\nu d_L^2}{1+z} \right)^{\frac{12}{17}} \text{ erg s}^{-1} \tag{6}$$

where S_ν is the radio flux density in Jy (see Table 2). The radio data were taken from the monitoring of the source performed by the Metsähovi Radio Observatory at 37 GHz. For the X-shooter epoch we used the flux averaged between 2017-12-06 and 2017-12-22, and for the MUSE epochs the flux averaged between 2022-12-02 and 2023-03-06. The results are: $P_{radio,kin,X} \sim 4.8 \cdot 10^{44}$ erg s^{-1} and $P_{radio,kin,M} \sim 7.3 \cdot 10^{44}$ erg s^{-1}.

4. Discussion and conclusions

From the values reported in reported Table 1, we can compare the kinetic powers of the outflow with those of the jet in its $\gamma-$ray and radio components. Specifically, we find that the outflow kinetic power constitutes a small but non-negligible fraction of the jet power in both epochs. The respective ratios, listed in Table 1, indicate that approximately 0.35%-1.9% of the jet power has been deposited into the outflow in both epochs. This further supports the scenario proposed in DB25, where we suggested that the observed variations in the outflow properties (in terms of flux and velocity) could result from the interaction between the jet and the NLR. In turn, these variations in the outflow kinetic power would likely be driven by changes in the jet state and energetics.

Table 1. Summary of the kinetic powers and of the ratios between the outflow power and the $\gamma-$ray and radio jet powers ($R_{out,\gamma}$ and $R_{out,radio}$, respectively).

Epoch	P_{out} **[erg s^{-1}]**	$P_{\gamma,kin}$ **[erg s^{-1}]**	$P_{radio,kin}$ **[erg s^{-1}]**	$R_{out,\gamma}$	$R_{out,radio}$
X-shooter	$8.8 \cdot 10^{42}$	$2.5 \cdot 10^{45}$	$4.8 \cdot 10^{44}$	0.35%	0.55%
MUSE	$14 \cdot 10^{42}$	$2.4 \cdot 10^{45}$	$7.3 \cdot 10^{44}$	0.58%	1.9%

These results support a scenario in which the relativistic jet deposits part of its energy into the surrounding environment – specifically, the NLR – producing the observed variations in the optical spectra, particularly in the [O III]λ5007 outflow properties. This hypothesis is also supported by the radio study of Doi et al. 2019. Our optical spectroscopic analysis (DB25) provides a crucial link between these radio observations and the optical data, linking changes in jet morphology with the variability observed in both the optical band and the γ-rays. The order-of-magnitude calculations presented here provide further evidence that, from an energetic perspective, the jet-NLR interaction can account for the observed optical spectral variations. Together, these findings reinforce the notion that the interplay between the relativistic jet and the circumnuclear gas significantly influences both the kinematics and energetics of the NLR in $\gamma-$NLS1 galaxies. Similar results have been reported by other authors, who observed variability in spectral features associated with jet activity. Examples include variable Mg II lines (e.g., León-Tavares et al. 2013; Berton et al. 2018; Yang et al. 2020) and changes in the broad Hβ component (Hon et al., 2023).

In conclusion, this analysis, combined with the results reported in DB25, underscores the importance of a multi-wavelength approach to the study of AGN, particularly for jetted sources. The combination of multi-epoch optical spectroscopy, radio observations, and $\gamma-$ray monitoring is essential for a better understanding of the mechanisms driving the interplay between jet emission and the AGN environment.

Acknowledgements. B.D.B. thank the organizers of the 15th Serbian Conference on Spectral Line Shapes in Astrophysics for the contributed talk. G.V. acknowledges support from the European Union (ERC, WINGS, 101040227). This publication makes use of data obtained at Metsähovi Radio Observatory, operated by Aalto University in Finland.

References

Abdollahi, S., Ajello, M., Baldini, L., et al., The Fermi-LAT Lightcurve Repository. 2023, *Astrophysical Journal, Supplement*, **265**, 31, `DOI:10.3847/1538-4365/acbb6a`

Ahn, C. P., Alexandroff, R., Allende Prieto, C., et al., The Ninth Data Release of the Sloan Digital Sky Survey: First Spectroscopic Data from the SDSS-III Baryon Oscillation Spectroscopic Survey. 2012, *Astrophysical Journal, Supplement*, **203**, 21, `DOI:10.1088/0067-0049/203/2/21`

Berton, M., Foschini, L., Caccianiga, A., et al., An orientation-based unification of young jetted active galactic nuclei: the case of 3C 286. 2017, *Frontiers in Astronomy and Space Sciences*, **4**, 8, `DOI:10.3389/fspas.2017.00008`

Berton, M., Foschini, L., Ciroi, S., et al., [O III] line properties in two samples of radio-emitting narrow-line Seyfert 1 galaxies. 2016, *Astronomy and Astrophysics*, **591**, A88, `DOI:10.1051/0004-6361/201527056`

Berton, M., Järvelä, E., Tortosa, A., & Mazzucchelli, C., How similar are narrow-line Seyfert 1 galaxies and high-z type 1 AGN? 2025, *arXiv e-prints*, arXiv:2509.03576, `DOI:10.48550/arXiv.2509.03576`

Berton, M., Liao, N. H., La Mura, G., et al., The flat-spectrum radio quasar 3C 345 from the high to the low emission state. 2018, *Astronomy and Astrophysics*, **614**, A148, `DOI:10.1051/0004-6361/201731625`

Blustin, A. J., Page, M. J., Fuerst, S. V., Branduardi-Raymont, G., & Ashton, C. E., The nature and origin of Seyfert warm absorbers. 2005, *Astronomy and Astrophysics*, **431**, 111, `DOI:10.1051/0004-6361:20041775`

Dalla Barba, B., Berton, M., Foschini, L., et al., Interaction of the relativistic jet and the narrow-line region of PMN J0948+0022. 2025, *Astronomy and Astrophysics*, **698**, A320, `DOI:10.1051/0004-6361/202452421`

Doi, A., Nakahara, S., Nakamura, M., et al., Radio jet structures at ∼100 pc and larger scales of the γ-ray-emitting narrow-line Seyfert 1 galaxy PMN J0948+0022. 2019, *Monthly Notices of the RAS*, **487**, 640, `DOI:10.1093/mnras/stz1290`

Foschini, L., Angelakis, E., Fuhrmann, L., et al., Radio-to-γ-ray monitoring of the narrow-line Seyfert 1 galaxy PMN J0948 + 0022 from 2008 to 2011. 2012, *Astronomy and Astrophysics*, **548**, A106, `DOI:10.1051/0004-6361/201220225`

Foschini, L., Dalla Barba, B., Tornikoski, M., et al., The Power of Relativistic Jets: A Comparative Study. 2024, *Universe*, **10**, 156, `DOI:10.3390/universe10040156`

Foschini, L., Fermi/Lat Collaboration, Ghisellini, G., et al., Fermi/LAT Discovery of Gamma-Ray Emission from a Relativistic Jet in the Narrow-Line Seyfert 1 Quasar PMN J0948+0022. 2010, in Astronomical Society of the Pacific Conference Series, Vol. **427**, *Accretion and Ejection in AGN: a Global View*, ed. L. Maraschi, G. Ghisellini, R. Della Ceca, & F. Tavecchio, 243–248

Foschini, L., Lister, M. L., Andernach, H., et al., A New Sample of Gamma-Ray Emitting Jetted Active Galactic Nuclei. 2022, *Universe*, **8**, 587, `DOI:10.3390/universe8110587`

Goodrich, R. W., Spectropolarimetry of "Narrow-Line" Seyfert 1 Galaxies. 1989, *Astrophysical Journal*, **342**, 224, `DOI:10.1086/167586`

Hon, W., Berton, M., Sani, E., et al., A redshifted excess in the broad emission lines after the flare of the γ-ray narrow-line Seyfert 1 PKS 2004−447. 2023, *Astronomy and Astrophysics*, **672**, L14, `DOI:10.1051/0004-6361/202245184`

Komossa, S., Xu, D. W., & Wagner, A. Y., Extreme gaseous outflows in radio-loud narrow-line Seyfert 1 galaxies. 2018, *Monthly Notices of the RAS*, **477**, 5115, `DOI:10.1093/mnras/sty901`

León-Tavares, J., Chavushyan, V., Patiño-Álvarez, V., et al., Flare-like Variability of the Mg II λ2800 Emission Line in the Γ-Ray Blazar 3C 454.3. 2013, *Astrophysical Journal, Letters*, **763**, L36, `DOI:10.1088/2041-8205/763/2/L36`

Luridiana, V., Morisset, C., & Shaw, R. A. 2013, PyNeb: Analysis of emission lines, Astrophysics Source Code Library, record ascl:1304.021

Luridiana, V., Morisset, C., & Shaw, R. A., PyNeb: a new tool for analyzing emission lines. I. Code description and validation of results. 2015, *Astronomy and Astrophysics*, **573**, A42, `DOI:10.1051/0004-6361/201323152`

Maraschi, L. & Tavecchio, F., The Jet-Disk Connection and Blazar Unification. 2003, *Astrophysical Journal*, **593**, 667, `DOI:10.1086/342118`

Mathur, S., Narrow-line Seyfert 1 galaxies and the evolution of galaxies and active galaxies. 2000, *Monthly Notices of the RAS*, **314**, L17, `DOI:10.1046/j.1365-8711.2000.03530.x`

Osterbrock, D. E. & Ferland, G. J. 2006, *Astrophysics of gaseous nebulae and active galactic nuclei* (University Science Books)

Osterbrock, D. E. & Pogge, R. W., The spectra of narrow-line Seyfert 1 galaxies. 1985, *Astrophysical Journal*, **297**, 166, `DOI:10.1086/163513`

Riess, A. G., Yuan, W., Macri, L. M., et al., A Comprehensive Measurement of the Local Value of the Hubble Constant with 1 km s^{-1} Mpc^{-1} Uncertainty from the Hubble Space Telescope and the SH0ES Team. 2022, *Astrophysical Journal, Letters*, **934**, L7, `DOI:10.3847/2041-8213/ac5c5b`

Venturi, G., Treister, E., Finlez, C., et al., Complex AGN feedback in the Teacup galaxy. A powerful ionised galactic outflow, jet-ISM interaction, and evidence for AGN-triggered star formation in a giant bubble. 2023, *Astronomy and Astrophysics*, **678**, A127, `DOI:10.1051/0004-6361/202347375`

Williams, R. J., Pogge, R. W., & Mathur, S., Narrow-line Seyfert 1 Galaxies from the Sloan Digital Sky Survey Early Data Release. 2002, *Astronomical Journal*, **124**, 3042, `DOI:10.1086/344765`

Yang, Q., Shen, Y., Chen, Y.-C., et al., Spectral variability of a sample of extreme variability quasars and implications for the Mg II broad-line region. 2020, *Monthly Notices of the RAS*, **493**, 5773, `DOI:10.1093/mnras/staa645`

Zhou, H.-Y., Wang, T.-G., Dong, X.-B., Zhou, Y.-Y., & Li, C., SDSS J094857.3+002225: A Very Radio Loud, Narrow-Line Quasar with Relativistic Jets? 2003, *Astrophysical Journal*, **584**, 147, `DOI:10.1086/345523`

A. Useful quantities

Table 2. List of the quantities involved in the calculations. References: *F*LCR) *Fermi* light-curve repository (Abdollahi et al., 2023), F12) Foschini et al. (2012), *Mets*) Metsähovi Radio Observatory data.

Quantity	**Symbol(s)**	**Value(s)**	**Units**	**Reference**
Luminosity distance	d_L	3.2	Gpc	Redshift
Outflow distance	D_{out}	130/220 → 170	pc	DB25
X-shooter [O II]λ3726 flux	$F_{3726,X}$	$(3.0 \pm 0.6) \times 10^{-17}$	erg s^{-1} cm^2	DB25
X-shooter [O II]λ3729 flux	$F_{3729,X}$	$(4.3 \pm 0.4) \times 10^{-17}$	erg s^{-1} cm^2	DB25
MUSE [O II]λ3726 flux	$F_{3726,M}$	$(8.4 \pm 0.6) \times 10^{-17}$	erg s^{-1} cm^2	DB25
MUSE [O II]λ3729 flux	$F_{3729,M}$	$(9.9 \pm 0.6) \times 10^{-17}$	erg s^{-1} cm^2	DB25
Fermi flux in the X-shooter epoch	$F_{\gamma,X}$	4.0×10^{-8}	ph s^{-1} cm^2	*F*LCR
Fermi flux in the MUSE epochs	$F_{\gamma,M}$	3.8×10^{-8}	ph s^{-1} cm^2	*F*LCR
X-shooter [O III]λ5007 outflow luminosity	$L^{out}_{5007,X}$	2.1×10^{41}	erg s^{-1}	DB25
MUSE [O III]λ5007 outflow luminosity	$L^{out}_{5007,M}$	1.5×10^{41}	erg s^{-1}	DB25
Radio flux density close to the X-shooter epoch	$S_{\nu,X}$	0.20	Jy	*Mets*
Radio flux density close to the MUSE epochs	$S_{\nu,M}$	0.37	Jy	*Mets*
X-shooter [O III]λ5007 outflow velocity	$v_{out,X}$	380	km s^{-1}	DB25
MUSE [O III]λ5007 outflow velocity	$v_{out,M}$	580	km s^{-1}	DB25
Fermi spectral index	α_γ	2.5	-	*F*LCR
Bulk Lorentz factor (two cases)	$\Gamma_{1,2}$	11/16	-	F12
Doppler factor (two cases)	$\delta_{1,2}$	17/19	-	F12

Contrib. Astron. Obs. Skalnaté Pleso **56/1**, 52 – 68, (2026)
https://doi.org/10.31577/caosp.2026.56.1.52

On the Stark broadening of N V spectral lines

M.S. Dimitrijević[1,2], **M.D. Christova**[3] **and S. Sahal-Bréchot**[2]

[1] *Astronomical Observatory, Volgina 7, 11060 Belgrade, Serbia,*
(E-mail: mdimitrijevic@aob.rs)

[2] *Sorbonne Université, Observatoire de Paris, Université PSL, CNRS, LUX,*
F-92190, Meudon, France

[3] *Department of Applied Physics, Technical University of Sofia, 1000 Sofia,*
Bulgaria

Received: August 24, 2025; Accepted: October 30, 2025

Abstract. Stark full widths at half intensity maximum (FWHM) and shifts, for spectral lines within 29 N V multiplets, have been calculated for collisions with α particles, B III, B IV, B V and B VI ions, employing the semiclassica perturbation method. The obtained data are of particular interest for proton-boron fusion experiments where boron nitride (BN) targets are used.

Key words: Stark broadening – N V – spectral lines – line profiles – proton-boron fusion

1. Introduction

Data on Stark broadening are useful in many research fields, like for diagnostics, modeling and investigation of different plasmas in astrophysics, laboratory, fusion, industry, technology, etc. Last years, many efforts are directed to the fusion using proton-boron thermonuclear reaction. Its particular advantage (Belloni & Batani, 2022) is that there is no radioactive species and neutrons in the reaction. Namely, neutrons, produced, for example, in deuterium tritium reaction, induce activation of the environment surrounding the fuel. Contrary, the proton-boron fusion produces three alpha particles and releases about 8.7 MeV of energy. Since this fusion is clean, because there is no induced radioactivity, α-particle generation during proton-boron fusion, could be a valuable source for medical and industrial applications (see for example Yoon et al. (2014); Giuffrida et al. (2016); Cirrone et al. (2018)). We note as well, that Schollmeier et al. (2022), underline that a boron-nitride (BN) nanotube target is more efficient in comparison with regular foils and nanostructured targets, used in previous experiments. Since in order to optimize the fusion yield, a plasma diagnostic is needed (see e.g. Ref. (Hegelich et al., 2023)), the corresponding Stark broadening data for N V spectral lines are useful for investigation and diagnostics of such plasma.

Our intention in this work is to calculate Stark broadening parameters for 29 N V multiplets, in the case of collisions with alpha particles and B III, B

IV, B V and B VI ions, in order to obtain the data of interest for proton-boron fusion investigations with BN targets.

2. Theory

The usede here semiclassical perturbation theory (Sahal-Bréchot, 1969a,b; Sahal-Bréchot, Dimitrijević, & Ben Nessib, 2014) has been described in detail in above mentioned references, and shortly, in many other papers, so that only basic formulas, enabling to understand the theory used for calculations, will be shown.

The full width at half maximum (FWHM - W) and shift (d) of an isolated spectral line of a non-hydrogenic ion is given as:

$$W = N \int v f(v) dv \left(\sum_{i' \neq i} \sigma_{ii'}(v) + \sum_{f' \neq f} \sigma_{ff'}(v) + \sigma_{el} \right)$$

$$d = N \int v f(v) dv \int_{R_3}^{R_D} 2\pi \rho d\rho \sin(2\varphi_p). \tag{1}$$

where i and f denote the initial and final level of the corresponding transition; i' and f' are perturbing levels; N perturber density; v perturber velocity, and $f(v)$ is the Maxwellian distribution of perturber velocities. The inelastic cross sections $\sigma_{kk'}(v)$, $k = i, f$ are presented here by an integration of the transition probability $P_{kk'}(\rho, v)$, over the impact parameter ρ as:

$$\sum_{k' \neq k} \sigma_{kk'}(v) = \frac{1}{2}\pi R_1^2 + \int_{R_1}^{R_D} 2\pi \rho d\rho \sum_{k' \neq k} P_{kk'}(\rho, v). \tag{2}$$

The cross section for elastic collisions is given as:

$$\sigma_{el} = 2\pi R_2^2 + \int_{R_2}^{R_D} 2\pi \rho d\rho \sin^2 \delta,$$

$$\delta = (\varphi_p^2 + \varphi_q^2)^{\frac{1}{2}}. \tag{3}$$

Here, δ denotes the phase shift with components φ_p (r^{-4}) and φ_q (r^{-3}), describing contributions due to polarization and quadrupole potentials, respectively. The method of symmetrization and calculation of cut-off parameters R_1, R_2, R_3, and the Debye cut-off R_D is explained in Sahal-Bréchot (1969b).

Table 1. This table gives B III-, and B IV-impact broadening parameters for N V multiplets (doublets), Stark FWHM W and shift d, expressed in Å. Calculated wavelength of the transitions (in Å) and parameter C are also given. This parameter, when divided with the corresponding Stark width, gives an estimate for the maximal pertuber density for which the line may be treated as isolated. Results are for perturber density of 10^{15} cm^{-3} and temperatures are from 50 000 K to 1 000 000 K. A positive shift is towards the red part of the spectrum. An asterisk before a value indicates that this value is on the limit of validity of the impact approximation.

		B III		B IV	
TRANSITION	T[K]	W[Å]	d[Å]	W[Å]	d[Å]
N V 2S-2P	50000.	0.250E-06	-0.528E-06	0.254E-06	-0.793E-06
1240.2 Å	80000.	0.513E-06	-0.829E-06	0.548E-06	-0.126E-05
C=0.12E+19	100000.	0.703E-06	-0.101E-05	0.782E-06	-0.155E-05
	200000.	0.158E-05	-0.171E-05	0.197E-05	-0.269E-05
	500000.	0.304E-05	-0.271E-05	0.433E-05	-0.443E-05
	1000000.	0.402E-05	-0.333E-05	0.620E-05	-0.559E-05
N V 2S-3P	50000.	0.234E-06	0.279E-06	0.293E-06	0.439E-06
209.3 Å	80000.	0.364E-06	0.371E-06	0.500E-06	0.604E-06
C=0.29E+16	100000.	0.415E-06	0.409E-06	0.594E-06	0.671E-06
	200000.	0.631E-06	0.546E-06	0.960E-06	0.921E-06
	500000.	0.843E-06	0.690E-06	0.135E-05	0.117E-05
	1000000.	0.101E-05	0.814E-06	0.160E-05	0.137E-05
N V 2S-4P	50000.	0.110E-05	0.117E-05	0.159E-05	0.192E-05
162.6 Å	80000.	0.148E-05	0.139E-05	0.227E-05	0.234E-05
C=0.73E+15	100000.	0.159E-05	0.147E-05	0.252E-05	0.248E-05
	200000.	0.197E-05	0.175E-05	0.324E-05	0.298E-05
	500000.	0.249E-05	0.212E-05	0.420E-05	0.364E-05
	1000000.	0.284E-05	0.243E-05	0.511E-05	0.434E-05
N V 2S-5P	50000.	0.347E-05	0.330E-05	0.556E-05	0.557E-05
147.4 Å	80000.	0.411E-05	0.375E-05	0.667E-05	0.634E-05
C=0.31E+15	100000.	0.439E-05	0.394E-05	0.711E-05	0.669E-05
	200000.	0.544E-05	0.468E-05	0.863E-05	0.805E-05
	500000.	0.644E-05	0.550E-05	0.113E-04	0.974E-05
	1000000.	0.740E-05	0.664E-05	0.133E-04	0.107E-04
N V 2P-3S	50000.	0.145E-06	0.401E-06	0.192E-06	0.631E-06
266.3 Å	80000.	0.299E-06	0.541E-06	0.412E-06	0.875E-06
C=0.15E+17	100000.	0.369E-06	0.594E-06	0.568E-06	0.980E-06
	200000.	0.673E-06	0.805E-06	0.102E-05	0.135E-05
	500000.	0.102E-05	0.102E-05	0.166E-05	0.173E-05
	1000000.	0.127E-05	0.119E-05	0.216E-05	0.204E-05
N V 2P-4S	50000.	0.727E-06	0.116E-05	0.115E-05	0.188E-05
190.2 Å	80000.	0.113E-05	0.142E-05	0.171E-05	0.237E-05
C=0.32E+16	100000.	0.132E-05	0.150E-05	0.209E-05	0.256E-05
	200000.	0.175E-05	0.181E-05	0.294E-05	0.308E-05
	500000.	0.238E-05	0.221E-05	0.408E-05	0.378E-05
	1000000.	0.289E-05	0.263E-05	0.470E-05	0.433E-05

Table 1. Continued.

		B III		B IV	
TRANSITION	T[K]	W[Å]	d[Å]	W[Å]	d[Å]
N V 2P-5S	50000.	0.265E-05	0.307E-05	0.414E-05	0.519E-05
168.6 Å	80000.	0.325E-05	0.349E-05	0.538E-05	0.592E-05
C=0.13E+16	100000.	0.358E-05	0.370E-05	0.587E-05	0.622E-05
	200000.	0.445E-05	0.432E-05	0.751E-05	0.745E-05
	500000.	0.572E-05	0.529E-05	0.991E-05	0.883E-05
	1000000.	0.667E-05	0.603E-05	0.112E-04	0.103E-04
N V 2P-3D	50000.	0.186E-06	-0.287E-06	0.228E-06	-0.449E-06
247.7 Å	80000.	0.319E-06	-0.393E-06	0.417E-06	-0.629E-06
C=0.40E+16	100000.	0.378E-06	-0.435E-06	0.539E-06	-0.716E-06
	200000.	0.615E-06	-0.596E-06	0.907E-06	-0.990E-06
	500000.	0.852E-06	-0.755E-06	0.137E-05	-0.129E-05
	1000000.	0.104E-05	-0.909E-06	0.171E-05	-0.152E-05
N V 2P-4D	50000.	0.533E-05	0.580E-05	0.874E-05	0.974E-05
186.1 Å	80000.	0.649E-05	0.653E-05	0.106E-04	0.111E-04
C=0.88E+14	100000.	0.701E-05	0.702E-05	0.113E-04	0.118E-04
	200000.	0.878E-05	0.813E-05	0.150E-04	0.141E-04
	500000.	0.108E-04	0.969E-05	0.205E-04	0.166E-04
	1000000.	0.141E-04	0.112E-04	0.225E-04	0.182E-04
N V 2P-5D	50000.	0.282E-04	0.273E-04	*0.468E-04	*0.468E-04
166.9 Å	80000.	0.338E-04	0.309E-04	*0.550E-04	*0.518E-04
C=0.21E+14	100000.	0.361E-04	0.320E-04	*0.616E-04	*0.531E-04
	200000.	0.436E-04	0.371E-04	0.670E-04	0.613E-04
	500000.	0.507E-04	0.408E-04	0.941E-04	0.703E-04
	1000000.	0.563E-04	0.500E-04	0.981E-04	0.753E-04
N V 3S-3P	50000.	0.888E-04	0.269E-04	0.102E-03	0.408E-04
4610.9 Å	80000.	0.131E-03	0.400E-04	0.160E-03	0.620E-04
C=0.14E+19	100000.	0.149E-03	0.467E-04	0.192E-03	0.736E-04
	200000.	0.209E-03	0.687E-04	0.284E-03	0.113E-03
	500000.	0.255E-03	0.971E-04	0.372E-03	0.165E-03
	1000000.	0.288E-03	0.116E-03	0.426E-03	0.198E-03
N V 3S-4P	50000.	0.158E-04	0.165E-04	0.226E-04	0.269E-04
628.8 Å	80000.	0.211E-04	0.196E-04	0.323E-04	0.331E-04
C=0.11E+17	100000.	0.228E-04	0.207E-04	0.363E-04	0.351E-04
	200000.	0.287E-04	0.248E-04	0.463E-04	0.420E-04
	500000.	0.378E-04	0.300E-04	0.592E-04	0.519E-04
	1000000.	0.407E-04	0.346E-04	0.701E-04	0.610E-04
N V 3S-5P	50000.	0.321E-04	0.304E-04	0.516E-04	0.515E-04
450.1 Å	80000.	0.381E-04	0.347E-04	0.616E-04	0.585E-04
C=0.28E+16	100000.	0.408E-04	0.364E-04	0.660E-04	0.616E-04
	200000.	0.501E-04	0.431E-04	0.791E-04	0.739E-04
	500000.	0.596E-04	0.512E-04	0.103E-03	0.900E-04
	1000000.	0.675E-04	0.614E-04	0.121E-03	0.100E-03

Table 1. Continued.

		B III		B IV	
TRANSITION	T[K]	W[Å]	d[Å]	W[Å]	d[Å]
N V 3P-4S	50000.	0.113E-04	0.171E-04	0.177E-04	0.279E-04
778.0 Å	80000.	0.172E-04	0.212E-04	0.256E-04	0.351E-04
C=0.40E+17	100000.	0.203E-04	0.226E-04	0.314E-04	0.382E-04
	200000.	0.267E-04	0.272E-04	0.444E-04	0.457E-04
	500000.	0.367E-04	0.337E-04	0.596E-04	0.583E-04
	1000000.	0.435E-04	0.387E-04	0.758E-04	0.657E-04
N V 3P-5S	50000.	0.239E-04	0.275E-04	0.371E-04	0.465E-04
510.0 Å	80000.	0.291E-04	0.312E-04	0.479E-04	0.529E-04
C=0.12E+17	100000.	0.318E-04	0.332E-04	0.529E-04	0.557E-04
	200000.	0.403E-04	0.389E-04	0.674E-04	0.671E-04
	500000.	0.519E-04	0.471E-04	0.908E-04	0.798E-04
	1000000.	0.587E-04	0.539E-04	0.982E-04	0.914E-04
N V 3P-3D	50000.	0.200E-02	-0.239E-02	0.251E-02	-0.376E-02
15148.3 Å	80000.	0.281E-02	-0.300E-02	0.408E-02	-0.491E-02
C=0.15E+20	100000.	0.333E-02	-0.336E-02	0.472E-02	-0.547E-02
	200000.	0.474E-02	-0.422E-02	0.752E-02	-0.716E-02
	500000.	0.633E-02	-0.541E-02	0.101E-01	-0.915E-02
	1000000.	0.789E-02	-0.616E-02	0.122E-01	-0.105E-01
N V 3P-4D	50000.	0.775E-04	0.844E-04	0.128E-03	0.142E-03
713.8 Å	80000.	0.950E-04	0.952E-04	0.155E-03	0.162E-03
C=0.13E+16	100000.	0.101E-03	0.102E-03	0.166E-03	0.170E-03
	200000.	0.127E-03	0.118E-03	0.217E-03	0.206E-03
	500000.	0.159E-03	0.142E-03	0.294E-03	0.244E-03
	1000000.	0.207E-03	0.164E-03	0.329E-03	0.268E-03
N V 3P-5D	50000.	0.248E-03	0.240E-03	*0.411E-03	*0.412E-03
495.3 Å	80000.	0.297E-03	0.272E-03	*0.485E-03	*0.455E-03
C=0.19E+15	100000.	0.318E-03	0.281E-03	*0.543E-03	*0.468E-03
	200000.	0.383E-03	0.326E-03	0.589E-03	0.539E-03
	500000.	0.447E-03	0.359E-03	0.826E-03	0.619E-03
	1000000.	0.496E-03	0.439E-03	0.864E-03	0.663E-03
N V 3D-4P	50000.	0.259E-04	0.273E-04	0.376E-04	0.448E-04
764.9 Å	80000.	0.345E-04	0.322E-04	0.533E-04	0.544E-04
C=0.16E+17	100000.	0.372E-04	0.341E-04	0.588E-04	0.573E-04
	200000.	0.462E-04	0.412E-04	0.742E-04	0.688E-04
	500000.	0.582E-04	0.498E-04	0.943E-04	0.854E-04
	1000000.	0.652E-04	0.573E-04	0.122E-03	0.982E-04
N V 3D-5P	50000.	0.392E-03	0.359E-03	0.624E-03	0.608E-03
1583.6 Å	80000.	0.460E-03	0.406E-03	0.739E-03	0.691E-03
C=0.35E+17	100000.	0.498E-03	0.432E-03	0.804E-03	0.734E-03
	200000.	0.607E-03	0.508E-03	0.973E-03	0.857E-03
	500000.	0.696E-03	0.589E-03	0.121E-02	0.105E-02
	1000000.	0.772E-03	0.698E-03	0.140E-02	0.120E-02

Table 1. Continued.

		B III		B IV	
TRANSITION	T[K]	W[Å]	d[Å]	W[Å]	d[Å]
N V 3D-4F	50000.	0.702E-04	-0.779E-04	0.116E-03	-0.133E-03
747.6 Å	80000.	0.871E-04	-0.886E-04	0.141E-03	-0.150E-03
C=0.14E+16	100000.	0.939E-04	-0.940E-04	0.154E-03	-0.160E-03
	200000.	0.119E-03	-0.111E-03	0.197E-03	-0.187E-03
	500000.	0.152E-03	-0.128E-03	0.260E-03	-0.227E-03
	1000000.	0.174E-03	-0.149E-03	0.300E-03	-0.260E-03
N V 4S-4P	50000.	0.357E-02	0.243E-02	0.490E-02	0.398E-02
11345.1 Å	80000.	0.468E-02	0.304E-02	0.651E-02	0.500E-02
C=0.36E+19	100000.	0.507E-02	0.334E-02	0.739E-02	0.554E-02
	200000.	0.612E-02	0.403E-02	0.931E-02	0.683E-02
	500000.	0.735E-02	0.499E-02	0.118E-01	0.862E-02
	1000000.	0.843E-02	0.586E-02	0.138E-01	0.101E-01
N V 4S-5P	50000.	0.286E-03	0.267E-03	0.459E-03	0.455E-03
1389.6 Å	80000.	0.341E-03	0.304E-03	0.541E-03	0.513E-03
C=0.27E+17	100000.	0.365E-03	0.322E-03	0.586E-03	0.546E-03
	200000.	0.444E-03	0.379E-03	0.726E-03	0.643E-03
	500000.	0.523E-03	0.435E-03	0.915E-03	0.787E-03
	1000000.	0.576E-03	0.510E-03	0.100E-02	0.881E-03
N V 4P-5S	50000.	0.218E-03	0.244E-03	0.328E-03	0.406E-03
1702.9 Å	80000.	0.274E-03	0.277E-03	0.435E-03	0.464E-03
C=0.80E+17	100000.	0.295E-03	0.293E-03	0.486E-03	0.495E-03
	200000.	0.372E-03	0.347E-03	0.607E-03	0.592E-03
	500000.	0.479E-03	0.416E-03	0.794E-03	0.713E-03
	1000000.	0.541E-03	0.478E-03	0.985E-03	0.833E-03
N V 4P-4D	50000.	0.183	0.193	0.299	0.328
36239.8 Å	80000.	0.221	0.220	0.364	0.372
C=0.33E+19	100000.	0.241	0.232	0.398	0.393
	200000.	0.304	0.274	0.484	0.461
	500000.	0.376	0.323	0.634	0.568
	1000000.	0.443	0.382	0.788	0.639
N V 4P-5D	50000.	0.242E-02	0.234E-02	*0.397E-02	*0.400E-02
1549.1 Å	80000.	0.286E-02	0.265E-02	*0.471E-02	*0.442E-02
C=0.18E+16	100000.	0.307E-02	0.274E-02	*0.529E-02	*0.457E-02
	200000.	0.370E-02	0.316E-02	0.569E-02	0.522E-02
	500000.	0.441E-02	0.348E-02	0.796E-02	0.601E-02
	1000000.	0.478E-02	0.427E-02	0.846E-02	0.647E-02
N V 4D-5P	50000.	0.260E-03	-0.987E-04	0.358E-03	-0.159E-03
1655.9 Å	80000.	0.290E-03	-0.119E-03	0.418E-03	-0.199E-03
C=0.69E+16	100000.	0.304E-03	-0.126E-03	0.441E-03	-0.214E-03
	200000.	0.357E-03	-0.153E-03	0.516E-03	-0.255E-03
	500000.	0.437E-03	-0.191E-03	0.627E-03	-0.318E-03
	1000000.	0.501E-03	-0.206E-03	0.720E-03	-0.364E-03

Table 1. Continued.

		B III		B IV	
TRANSITION	T[K]	W[Å]	d[Å]	W[Å]	d[Å]
N V 5S-5P	50000.	0.537E-01	0.399E-01	0.783E-01	0.663E-01
22592.2 Å	80000.	0.615E-01	0.453E-01	0.936E-01	0.758E-01
C=0.72E+19	100000.	0.654E-01	0.479E-01	0.101	0.810E-01
	200000.	0.780E-01	0.575E-01	0.123	0.967E-01
	500000.	0.967E-01	0.698E-01	0.155	0.118
	1000000.	0.102	0.778E-01	0.179	0.137
N V 5P-5D	50000.	4.93	4.76	*7.99	*8.03
71174.4 Å	80000.	5.53	5.36	9.54	8.99
C=0.39E+19	100000.	6.15	5.61	10.5	9.45
	200000.	7.47	6.49	11.8	10.4
	500000.	8.78	7.23	16.4	12.4
	1000000.	9.41	8.25	17.9	13.0

3. Results and discussion

In this paper, Stark broadening parameters, full width at half intensity maximum (FWHM - W) and shift (d), have been calculated by empoying the semi-classical perturbation theory (Sahal-Bréchot, 1969a,b; Sahal-Bréchot, Dimitrijević, & Ben Nessib, 2014),

The perturber density is 10^{15} cm^{-3} and temperatures 50 000 K, 80 000 K, 100 000 K, 200 000 K, 500 000 K, and 1 000 000 K. The energy levels of N V ion, which are needed to perform the present calculations, are from Moore (1993) and Kramida et al. (2021).

The Stark Full Widths at Half intensity Maximum (FWHM) and shifts for 29 N V multiplets broadened by collisions with B III and B IV ions are presented in Table 1, the corresponding results for broadening by collisions with B V and B VI ions in Table 2, while the Stark widths (FWHM) and shifts due to collisions with alpha particles are in Table 3.

We draw attention that the wavelengths given in the Tables 1-3 are calculated from atomic energy levels, so that they are not always identical with wavelengths in NIST databases (Kramida et al., 2021).

The perturber density is 10^{15} cm^{-3} and temperatures 50 000 K, 80 000 K, 100 000 K, 200 000 K, 500 000 K, and 1 000 000 K. The energy levels of N V ion, which are needed to perform the present calculations, are from Moore (1993) and Kramida et al. (2021).

Dividing the quantity C (Dimitrijević & Sahal-Bréchot, 1984), which is given in Tables, by the corresponding width (W), one can obtain the maximal perturber density when one can assume that the line is isolated.

Table 2. Same as in Table 1 but for B V-, and B VI-impact broadening of N V spectral lines.

		B V		B VI	
TRANSITION	T[K]	W[Å]	d[Å]	W[Å]	d[Å]
N V 2S-2P	50000.	0.256E-06	-0.106E-05	0.257E-06	-0.132E-05
1240.2 Å	80000.	0.566E-06	-0.168E-05	0.577E-06	-0.211E-05
C=0.12E+19	100000.	0.826E-06	-0.208E-05	0.854E-06	-0.261E-05
	200000.	0.232E-05	-0.372E-05	0.263E-05	-0.477E-05
	500000.	0.556E-05	-0.628E-05	0.671E-05	-0.816E-05
	1000000.	0.858E-05	-0.812E-05	0.110E-04	-0.109E-04
N V 2S-3P	50000.	0.339E-06	0.604E-06	0.369E-06	0.768E-06
209.3 Å	80000.	0.606E-06	0.845E-06	0.685E-06	0.108E-05
C=0.29E+16	100000.	0.767E-06	0.956E-06	0.906E-06	0.125E-05
	200000.	0.126E-05	0.132E-05	0.155E-05	0.173E-05
	500000.	0.187E-05	0.170E-05	0.244E-05	0.227E-05
	1000000.	0.231E-05	0.204E-05	0.298E-05	0.272E-05
N V 2S-4P	50000.	0.206E-05	0.269E-05	0.259E-05	0.353E-05
162.6 Å	80000.	0.300E-05	0.336E-05	0.373E-05	0.444E-05
C=0.73E+15	100000.	0.350E-05	0.361E-05	0.443E-05	0.482E-05
	200000.	0.453E-05	0.431E-05	0.592E-05	0.578E-05
	500000.	0.610E-05	0.540E-05	0.803E-05	0.734E-05
	1000000.	0.711E-05	0.620E-05	0.955E-05	0.822E-05
N V 2S-5P	50000.	0.771E-05	0.815E-05	0.972E-05	0.108E-04
147.4 Å	80000.	0.942E-05	0.922E-05	0.121E-04	0.124E-04
C=0.31E+15	100000.	0.102E-04	0.974E-05	0.132E-04	0.130E-04
	200000.	0.128E-04	0.117E-04	0.167E-04	0.157E-04
	500000.	0.155E-04	0.139E-04	0.218E-04	0.186E-04
	1000000.	0.187E-04	0.160E-04	0.237E-04	0.214E-04
N V 2P-3S	50000.	0.221E-06	0.864E-06	0.244E-06	0.110E-05
266.3 Å	80000.	0.497E-06	0.121E-05	0.589E-06	0.155E-05
C=0.15E+17	100000.	0.721E-06	0.139E-05	0.863E-06	0.181E-05
	200000.	0.137E-05	0.193E-05	0.173E-05	0.252E-05
	500000.	0.237E-05	0.251E-05	0.313E-05	0.334E-05
	1000000.	0.305E-05	0.299E-05	0.408E-05	0.399E-05
N V 2P-4S	50000.	0.156E-05	0.268E-05	0.192E-05	0.353E-05
190.2 Å	80000.	0.229E-05	0.335E-05	0.293E-05	0.441E-05
C=0.32E+16	100000.	0.283E-05	0.369E-05	0.357E-05	0.487E-05
	200000.	0.414E-05	0.445E-05	0.550E-05	0.594E-05
	500000.	0.571E-05	0.552E-05	0.763E-05	0.756E-05
	1000000.	0.682E-05	0.642E-05	0.942E-05	0.857E-05
N V 2P-5S	50000.	0.555E-05	0.746E-05	0.701E-05	0.985E-05
168.6 Å	80000.	0.759E-05	0.848E-05	0.101E-04	0.113E-04
C=0.13E+16	100000.	0.849E-05	0.901E-05	0.112E-04	0.121E-04
	200000.	0.109E-04	0.109E-04	0.145E-04	0.145E-04
	500000.	0.145E-04	0.129E-04	0.195E-04	0.177E-04
	1000000.	0.176E-04	0.146E-04	0.228E-04	0.208E-04

Table 2. Continued.

		B V		B VI	
TRANSITION	T[K]	W[Å]	d[Å]	W[Å]	d[Å]
N V 2P-3D	50000.	0.253E-06	-0.611E-06	0.273E-06	-0.773E-06
247.7 Å	80000.	0.491E-06	-0.866E-06	0.569E-06	-0.111E-05
C=0.40E+16	100000.	0.668E-06	-0.101E-05	0.770E-06	-0.130E-05
	200000.	0.118E-05	-0.140E-05	0.147E-05	-0.185E-05
	500000.	0.192E-05	-0.186E-05	0.253E-05	-0.249E-05
	1000000.	0.246E-05	-0.221E-05	0.315E-05	-0.294E-05
N V 2P-4D	50000.	0.123E-04	0.142E-04	0.157E-04	0.190E-04
186.1 Å	80000.	0.151E-04	0.161E-04	0.200E-04	0.215E-04
C=0.88E+14	100000.	0.165E-04	0.171E-04	0.219E-04	0.230E-04
	200000.	0.212E-04	0.200E-04	0.274E-04	0.271E-04
	500000.	0.270E-04	0.247E-04	0.359E-04	0.324E-04
	1000000.	0.316E-04	0.274E-04	0.429E-04	0.369E-04
N V 2P-5D	50000.	*0.677E-04	*0.672E-04	*0.886E-04	*0.895E-04
166.9 Å	80000.	*0.795E-04	*0.768E-04	*0.105E-03	*0.100E-03
C=0.21E+14	100000.	*0.829E-04	*0.783E-04	*0.114E-03	*0.106E-03
	200000.	*0.107E-03	*0.918E-04	*0.136E-03	*0.124E-03
	500000.	0.131E-03	0.109E-03	*0.164E-03	*0.151E-03
	1000000.	0.161E-03	0.114E-03	*0.205E-03	*0.165E-03
N V 3S-3P	50000.	0.109E-03	0.546E-04	0.114E-03	0.685E-04
4610.9 Å	80000.	0.182E-03	0.840E-04	0.198E-03	0.106E-03
C=0.14E+19	100000.	0.221E-03	0.101E-03	0.246E-03	0.129E-03
	200000.	0.345E-03	0.161E-03	0.404E-03	0.209E-03
	500000.	0.484E-03	0.240E-03	0.598E-03	0.319E-03
	1000000.	0.564E-03	0.288E-03	0.700E-03	0.383E-03
N V 3S-4P	50000.	0.294E-04	0.378E-04	0.369E-04	0.497E-04
628.8 Å	80000.	0.426E-04	0.474E-04	0.523E-04	0.624E-04
C=0.11E+17	100000.	0.498E-04	0.512E-04	0.626E-04	0.681E-04
	200000.	0.651E-04	0.613E-04	0.850E-04	0.818E-04
	500000.	0.862E-04	0.762E-04	0.111E-03	0.104E-03
	1000000.	0.999E-04	0.876E-04	0.139E-03	0.119E-03
N V 3S-5P	50000.	0.711E-04	0.752E-04	0.897E-04	0.100E-03
450.1 Å	80000.	0.868E-04	0.851E-04	0.112E-03	0.114E-03
C=0.28E+16	100000.	0.943E-04	0.901E-04	0.122E-03	0.120E-03
	200000.	0.118E-03	0.108E-03	0.153E-03	0.145E-03
	500000.	0.145E-03	0.128E-03	0.204E-03	0.173E-03
	1000000.	0.169E-03	0.148E-03	0.218E-03	0.196E-03
N V 3P-4S	50000.	0.234E-04	0.398E-04	0.280E-04	0.521E-04
778.0 Å	80000.	0.347E-04	0.497E-04	0.432E-04	0.653E-04
C=0.40E+17	100000.	0.420E-04	0.547E-04	0.526E-04	0.724E-04
	200000.	0.635E-04	0.665E-04	0.831E-04	0.893E-04
	500000.	0.877E-04	0.845E-04	0.115E-03	0.113E-03
	1000000.	0.107E-03	0.963E-04	0.142E-03	0.132E-03

Table 2. Continued.

		B V		B VI	
TRANSITION	T[K]	W[Å]	d[Å]	W[Å]	d[Å]
N V 3P-5S	50000.	0.497E-04	0.667E-04	0.625E-04	0.882E-04
510.0 Å	80000.	0.684E-04	0.761E-04	0.901E-04	0.101E-03
C=0.12E+17	100000.	0.762E-04	0.810E-04	0.100E-03	0.109E-03
	200000.	0.966E-04	0.976E-04	0.128E-03	0.130E-03
	500000.	0.129E-03	0.118E-03	0.172E-03	0.161E-03
	1000000.	0.163E-03	0.133E-03	0.206E-03	0.186E-03
N V 3P-3D	50000.	0.299E-02	-0.519E-02	0.342E-02	-0.666E-02
15148.3 Å	80000.	0.528E-02	-0.701E-02	0.625E-02	-0.914E-02
C=0.15E+20	100000.	0.613E-02	-0.769E-02	0.766E-02	-0.101E-01
	200000.	0.103E-01	-0.104E-01	0.129E-01	-0.139E-01
	500000.	0.145E-01	-0.132E-01	0.186E-01	-0.176E-01
	1000000.	0.177E-01	-0.155E-01	0.226E-01	-0.211E-01
N V 3P-4D	50000.	0.178E-03	0.207E-03	0.228E-03	0.277E-03
713.8 Å	80000.	0.220E-03	0.233E-03	0.292E-03	0.313E-03
C=0.13E+16	100000.	0.241E-03	0.249E-03	0.316E-03	0.333E-03
	200000.	0.312E-03	0.291E-03	0.403E-03	0.393E-03
	500000.	0.390E-03	0.357E-03	0.522E-03	0.469E-03
	1000000.	0.464E-03	0.400E-03	0.625E-03	0.540E-03
N V 3P-5D	50000.	*0.596E-03	*0.591E-03	*0.780E-03	*0.787E-03
495.3 Å	80000.	*0.700E-03	*0.676E-03	*0.920E-03	*0.881E-03
C=0.19E+15	100000.	*0.731E-03	*0.689E-03	*0.999E-03	*0.936E-03
	200000.	*0.945E-03	*0.807E-03	*0.119E-02	*0.109E-02
	500000.	0.115E-02	0.961E-03	*0.144E-02	*0.133E-02
	1000000.	0.142E-02	0.100E-02	*0.180E-02	*0.144E-02
N V 3D-4P	50000.	0.484E-04	0.628E-04	0.607E-04	0.822E-04
764.9 Å	80000.	0.707E-04	0.784E-04	0.880E-04	0.103E-03
C=0.16E+17	100000.	0.816E-04	0.837E-04	0.104E-03	0.112E-03
	200000.	0.106E-03	0.101E-03	0.138E-03	0.135E-03
	500000.	0.141E-03	0.125E-03	0.192E-03	0.170E-03
	1000000.	0.162E-03	0.144E-03	0.217E-03	0.189E-03
N V 3D-5P	50000.	0.854E-03	0.886E-03	0.107E-02	0.118E-02
1583.6 Å	80000.	0.104E-02	0.100E-02	0.134E-02	0.133E-02
C=0.35E+17	100000.	0.113E-02	0.107E-02	0.147E-02	0.142E-02
	200000.	0.137E-02	0.126E-02	0.181E-02	0.168E-02
	500000.	0.173E-02	0.150E-02	0.232E-02	0.207E-02
	1000000.	0.202E-02	0.172E-02	0.259E-02	0.224E-02
N V 3D-4F	50000.	0.158E-03	-0.193E-03	0.200E-03	-0.256E-03
747.6 Å	80000.	0.203E-03	-0.218E-03	0.265E-03	-0.291E-03
C=0.14E+16	100000.	0.220E-03	-0.232E-03	0.292E-03	-0.310E-03
	200000.	0.283E-03	-0.274E-03	0.372E-03	-0.365E-03
	500000.	0.369E-03	-0.326E-03	0.487E-03	-0.451E-03
	1000000.	0.444E-03	-0.377E-03	0.591E-03	-0.484E-03

Table 2. Continued.

		B V		B VI	
TRANSITION	T[K]	W[Å]	d[Å]	W[Å]	d[Å]
N V 4S-4P	50000.	0.603E-02	0.560E-02	0.695E-02	0.722E-02
11345.1 Å	80000.	0.815E-02	0.701E-02	0.968E-02	0.915E-02
C=0.36E+19	100000.	0.939E-02	0.783E-02	0.114E-01	0.103E-01
	200000.	0.125E-01	0.981E-02	0.159E-01	0.131E-01
	500000.	0.164E-01	0.125E-01	0.210E-01	0.167E-01
	1000000.	0.186E-01	0.140E-01	0.249E-01	0.199E-01
N V 4S-5P	50000.	0.625E-03	0.661E-03	0.784E-03	0.878E-03
1389.6 Å	80000.	0.770E-03	0.747E-03	0.991E-03	0.996E-03
C=0.27E+17	100000.	0.824E-03	0.793E-03	0.108E-02	0.106E-02
	200000.	0.104E-02	0.942E-03	0.135E-02	0.125E-02
	500000.	0.130E-02	0.112E-02	0.169E-02	0.154E-02
	1000000.	0.150E-02	0.130E-02	0.205E-02	0.167E-02
N V 4P-5S	50000.	0.432E-03	0.578E-03	0.547E-03	0.757E-03
1702.9 Å	80000.	0.618E-03	0.673E-03	0.801E-03	0.902E-03
C=0.80E+17	100000.	0.675E-03	0.716E-03	0.885E-03	0.952E-03
	200000.	0.889E-03	0.860E-03	0.116E-02	0.114E-02
	500000.	0.113E-02	0.104E-02	0.160E-02	0.138E-02
	1000000.	0.127E-02	0.123E-02	0.173E-02	0.159E-02
N V 4P-4D	50000.	0.411	0.477	0.519	0.635
36239.8 Å	80000.	0.515	0.539	0.665	0.720
C=0.33E+19	100000.	0.562	0.572	0.739	0.762
	200000.	0.707	0.687	0.923	0.914
	500000.	0.907	0.817	1.25	1.12
	1000000.	1.09	0.932	1.38	1.24
N V 4P-5D	50000.	*0.583E-02	*0.574E-02	*0.762E-02	*0.763E-02
1549.1 Å	80000.	*0.671E-02	*0.657E-02	*0.901E-02	*0.852E-02
C=0.18E+16	100000.	*0.709E-02	*0.670E-02	*0.970E-02	*0.908E-02
	200000.	*0.920E-02	*0.790E-02	*0.114E-01	*0.106E-01
	500000.	0.113E-01	0.936E-02	*0.138E-01	*0.129E-01
	1000000.	0.139E-01	0.975E-02	*0.178E-01	*0.137E-01
N V 4D-5P	50000.	0.442E-03	-0.226E-03	0.514E-03	-0.298E-03
1655.9 Å	80000.	0.546E-03	-0.284E-03	0.664E-03	-0.372E-03
C=0.69E+16	100000.	0.575E-03	-0.309E-03	0.712E-03	-0.410E-03
	200000.	0.679E-03	-0.370E-03	0.847E-03	-0.493E-03
	500000.	0.842E-03	-0.471E-03	0.104E-02	-0.619E-03
	1000000.	0.965E-03	-0.529E-03	0.119E-02	-0.707E-03
N V 5S-5P	50000.	0.100	0.938E-01	0.123	0.124
22592.2 Å	80000.	0.128	0.111	0.164	0.148
C=0.72E+19	100000.	0.139	0.118	0.174	0.155
	200000.	0.168	0.141	0.220	0.188
	500000.	0.211	0.171	0.288	0.234
	1000000.	0.230	0.195	0.311	0.253

Table 2. Continued.

TRANSITION	T[K]	B V W[Å]	d[Å]	B VI W[Å]	d[Å]
N V 5P-5D	50000.	*11.8	*11.7	*15.6	*15.6
71174.4 Å	80000.	*13.3	*13.3	*18.5	*17.5
C=0.39E+19	100000.	*14.8	*13.7	*19.6	*18.3
	200000.	*17.9	*16.0	*23.0	*21.1
	500000.	21.5	19.0	*26.8	*25.6
	1000000.	28.0	20.1	*37.7	*28.2

The validity of impact approximation has been checked for all results presented in Tables 1-3. This is done by calculating the value of NV, where V is the collision volume and N the perturber density. If $NV< 0.1$, the impact approximation is valid. When the violation of impact approximation is more or less tolerable, for $0.1<NV\leq 0.5$ we put an asterisk before the corresponding Stark broadening parameter in order to draw attention that this value is on the limit of validity of impact approximation.

We note that the data on broadening by collisions with electrons, protons and ionized helium can be found in Dimitrijevic & Sahal-Brechot (1992), while in Blagojević et al. (1999) and Dimitrijevic (1999), data on the broadening of N V by collisions with N III, N IV, N V, N VI, and N VII ions, has been reported for 3s ^{2}S - 3p ^{2}P^o transition.

The widths and shifts from Tables 1-3 can be used to obtain the line profile $F(\omega)$ (where ω is angular frequency), using the expression:

$$F(\omega) = \frac{W/(2\pi)}{(\omega - \omega_{if} - d)^2 + (W/2)^2}. \qquad (4)$$

Here

$$\omega_{if} = \frac{E_i - E_f}{\hbar}$$

where E_i, E_f are the energies of initial and final atomic energy level, respectively.

4. Conclusions

We have used here the impact semiclassical perturbation theory (Sahal-Bréchot, 1969a,b; Sahal-Bréchot, Dimitrijević, & Ben Nessib, 2014) for the calculation of Stark broadening parameters, widths (FWHM) and shifts, for 29 multiplets of fourtly charged nitrogen ion (N V). The results are presented for broadening due to collisions of N V with α particles, B III, B IV, B V and B VI ions. The obtained results are useful for proton-boron fusion, because one of the targets used in such

Table 3. Same as in Table 1 but for the broadening of N V spectral lines by collisions with α particles.

		α particles				
TRANSIT.	T[10^4K]	W[Å]	d[Å]	TRANSIT.	W[Å]	d[Å]
N V 2S-2P	5.	0.181E-06	-0.528E-06	N V 2P-3D	0.158E-06	-0.298E-06
1240.2 Å	8.	0.388E-06	-0.836E-06	247.7 Å	0.286E-06	-0.416E-06
	10.	0.549E-06	-0.103E-05		0.365E-06	-0.471E-06
	20.	0.135E-05	-0.178E-05		0.607E-06	-0.649E-06
	50.	0.290E-05	-0.291E-05		0.913E-06	-0.838E-06
	100.	0.410E-05	-0.364E-05		0.114E-05	-0.101E-05
N V 2S-3P	5.	0.202E-06	0.290E-06	N V 2P-4D	0.578E-05	0.637E-05
209.3 Å	8.	0.339E-06	0.398E-06	186.1 Å	0.717E-05	0.728E-05
	10.	0.399E-06	0.440E-06		0.780E-05	0.773E-05
	20.	0.642E-06	0.603E-06		0.101E-04	0.898E-05
	50.	0.884E-06	0.765E-06		0.138E-04	0.103E-04
	100.	0.108E-05	0.919E-06		0.156E-04	0.122E-04
N V 2S-4P	5.	0.107E-05	0.126E-05	N V 2P-5D	0.316E-04	0.305E-04
162.6 Å	8.	0.151E-05	0.153E-05	166.9 Å	0.372E-04	0.339E-04
	10.	0.167E-05	0.162E-05		0.385E-04	0.345E-04
	20.	0.210E-05	0.194E-05		0.465E-04	0.398E-04
	50.	0.268E-05	0.241E-05		0.636E-04	0.452E-04
	100.	0.347E-05	0.276E-05		0.716E-04	0.502E-04
N V 2S-5P	5.	0.368E-05	0.365E-05	N V 3S-3P	0.712E-04	0.271E-04
147.4 Å	8.	0.436E-05	0.414E-05	4610.9 Å	0.111E-03	0.412E-04
	10.	0.471E-05	0.438E-05		0.132E-03	0.487E-04
	20.	0.584E-05	0.529E-05		0.193E-03	0.740E-04
	50.	0.774E-05	0.633E-05		0.251E-03	0.107E-03
	100.	0.844E-05	0.696E-05		0.289E-03	0.128E-03
N V 2P-3S	5.	0.131E-06	0.417E-06	N V 3S-4P	0.152E-04	0.177E-04
266.3 Å	8.	0.280E-06	0.577E-06	628.8 Å	0.215E-04	0.217E-04
	10.	0.379E-06	0.642E-06		0.238E-04	0.229E-04
	20.	0.682E-06	0.884E-06		0.304E-04	0.276E-04
	50.	0.109E-05	0.113E-05		0.400E-04	0.339E-04
	100.	0.138E-05	0.132E-05		0.479E-04	0.401E-04
N V 2P-4S	5.	0.754E-06	0.124E-05	N V 3S-5P	0.340E-04	0.337E-04
190.2 Å	8.	0.114E-05	0.155E-05	450.1 Å	0.404E-04	0.382E-04
	10.	0.139E-05	0.167E-05		0.437E-04	0.405E-04
	20.	0.193E-05	0.200E-05		0.536E-04	0.487E-04
	50.	0.262E-05	0.249E-05		0.709E-04	0.590E-04
	100.	0.308E-05	0.284E-05		0.772E-04	0.641E-04
N V 2P-5S	5.	0.274E-05	0.340E-05	N V 3P-4S	0.117E-04	0.183E-04
168.6 Å	8.	0.356E-05	0.385E-05	778.0 Å	0.172E-04	0.231E-04
	10.	0.385E-05	0.408E-05		0.209E-04	0.250E-04
	20.	0.494E-05	0.485E-05		0.290E-04	0.300E-04
	50.	0.641E-05	0.576E-05		0.399E-04	0.381E-04
	100.	0.741E-05	0.668E-05		0.481E-04	0.425E-04

Table 3. Continued.

		α particles				
TRANSIT.	T[10^4K]	W[Å]	d[Å]	TRANSIT.	W[Å]	d[Å]
N V 3P-5S	5.	0.246E-04	0.305E-04	N V 4S-4P	0.332E-02	0.262E-02
510.0 Å	8.	0.319E-04	0.346E-04	11345.1 Å	0.439E-02	0.329E-02
	10.	0.346E-04	0.366E-04		0.496E-02	0.363E-02
	20.	0.445E-04	0.435E-04		0.614E-02	0.444E-02
	50.	0.576E-04	0.519E-04		0.779E-02	0.558E-02
	100.	0.657E-04	0.596E-04		0.925E-02	0.651E-02
N V 3P-3D	5.	0.172E-02	-0.249E-02	N V 4S-5P	0.303E-03	0.297E-03
15148.3 Å	8.	0.274E-02	-0.323E-02	1389.6 Å	0.361E-03	0.337E-03
	10.	0.319E-02	-0.361E-02		0.391E-03	0.357E-03
	20.	0.493E-02	-0.466E-02		0.471E-03	0.417E-03
	50.	0.683E-02	-0.597E-02		0.592E-03	0.509E-03
	100.	0.829E-02	-0.692E-02		0.703E-03	0.584E-03
N V 3P-4D	5.	0.842E-04	0.928E-04	N V 4P-5S	0.218E-03	0.266E-03
713.8 Å	8.	0.104E-03	0.106E-03	1702.9 Å	0.287E-03	0.303E-03
	10.	0.113E-03	0.113E-03		0.319E-03	0.322E-03
	20.	0.149E-03	0.131E-03		0.405E-03	0.389E-03
	50.	0.206E-03	0.151E-03		0.533E-03	0.459E-03
	100.	0.227E-03	0.174E-03		0.646E-03	0.521E-03
N V 3P-5D	5.	0.278E-03	0.268E-03	N V 4P-4D	0.197	0.214
495.3 Å	8.	0.327E-03	0.299E-03	36239.8 Å	0.242	0.243
	10.	0.339E-03	0.303E-03		0.262	0.258
	20.	0.410E-03	0.350E-03		0.333	0.309
	50.	0.560E-03	0.398E-03		0.461	0.372
	100.	0.632E-03	0.441E-03		0.574	0.404
N V 3D-4P	5.	0.253E-04	0.295E-04	N V 4P-5D	0.270E-02	0.261E-02
764.9 Å	8.	0.355E-04	0.357E-04	1549.1 Å	0.317E-02	0.290E-02
	10.	0.388E-04	0.375E-04		0.334E-02	0.293E-02
	20.	0.499E-04	0.456E-04		0.396E-02	0.340E-02
	50.	0.650E-04	0.570E-04		0.547E-02	0.382E-02
	100.	0.805E-04	0.614E-04		0.612E-02	0.426E-02
N V 3D-5P	5.	0.412E-03	0.396E-03	N V 4D-5P	0.245E-03	-0.105E-03
1583.6 Å	8.	0.490E-03	0.451E-03	1655.9 Å	0.287E-03	-0.131E-03
	10.	0.524E-03	0.475E-03		0.306E-03	-0.140E-03
	20.	0.625E-03	0.568E-03		0.374E-03	-0.167E-03
	50.	0.813E-03	0.692E-03		0.493E-03	-0.208E-03
	100.	0.960E-03	0.770E-03		0.636E-03	-0.241E-03
N V 3D-4F	5.	0.768E-04	-0.867E-04	N V 5S-5P	0.526E-01	0.435E-01
747.6 Å	8.	0.950E-04	-0.984E-04	22592.2 Å	0.621E-01	0.496E-01
	10.	0.105E-03	-0.104E-03		0.669E-01	0.530E-01
	20.	0.131E-03	-0.122E-03		0.803E-01	0.632E-01
	50.	0.178E-03	-0.150E-03		0.101	0.764E-01
	100.	0.230E-03	-0.169E-03		0.120	0.887E-01

Table 3. Continued.

		α particles	
TRANSIT.	T[10^4K]	W[Å]	d[Å]
N V 5P-5D	5.	5.38	5.29
71174.4 Å	8.	6.40	5.86
	10.	7.18	6.03
	20.	8.03	6.91
	50.	11.7	7.96
	100.	13.0	8.50

experiments is made of boron nitride (BN). Consequently, the broadening of spectral lines of fourthly charged nitrogen ion by collisions with different boron ions is useful for diagnostics of the created boron-nitrogen plasma and for its optimization, modeling and investigation. The presented Stark broadening parameters will be included later in STARK-B database (http://stark-b.obspm.fr/ - Sahal-Bréchot et al. (2015)), which is also a part of Virtual Atomic and Molecular Data Center (VAMDC) (http://www.vamdc.org/ - Dubernet et al. (2010, 2016); Albert et al. (2020)).

Acknowledgements. This work has been supported with a STSM visit grant for MSD within the framework of COST Action CA21128-PROBONO ”PROton BOron Nuclear fusion: from energy production to medical applicatiOns”, supported by COST (European Cooperation in Science and Technology `www.cost.eu`). Thanks also to Technical University of Sofia for the provided help.

References

Albert, D., Antony, B. K., Ba, Y. A., et al., A Decade with VAMDC: Results and Ambitions. 2020, *Atoms*, **8**, 76, `DOI:10.3390/atoms8040076`

Belloni, F. & Batani, K., Multiplication Processes in High-Density H-^{11}B Fusion Fuel. 2022, *Laser and Particle Beams*, **2022**, e11, `DOI:10.1155/2022/3952779`

Blagojević, B., Popović, M. V., Konjević, & Dimitrijević, M. S., Stark Broadening Parameters of Analogous Spectral Lines Along the Lithium and Beryllium Isoelectronic Sequences. 1999, *Journal of Quantitiative Spectroscopy and Radiative Transfer*, **61**, 361, `DOI:10.1016/S0022-4073(98)00002-8`

Cirrone, G. A. P., Manti, L., Margarone, D., et al., First experimental proof of Proton Boron Capture Therapy (PBCT) to enhance proton therapy effectiveness. 2018, *Scientific Reports*, **8**, 1141, `DOI:10.1038/s41598-018-19258-5`

Dimitrijevic, M. S., Stark Broadening Data Tables for Some Analogous Spectral Lines Along li and be Isoelectronic Sequences. 1999, *Serbian Astronomical Journal*, **159**, 65

Dimitrijević, M. S. & Sahal-Bréchot, S., Stark broadening of neutral helium lines. 1984, *Journal of Quantitiative Spectroscopy and Radiative Transfer*, **31**, 301, DOI:10.1016/0022-4073(84)90092-X

Dimitrijevic, M. S. & Sahal-Brechot, S., Stark broadening of spectral lines of multicharged ions of astrophysical interest. IV - N V lines. 1992, *Astronomy and Astrophysics, Supplement*, **95**, 109

Dubernet, M. L., Antony, B. K., Ba, Y. A., et al., The virtual atomic and molecular data centre (VAMDC) consortium. 2016, *Journal of Physics B Atomic Molecular Physics*, **49**, 074003, DOI:10.1088/0953-4075/49/7/074003

Dubernet, M. L., Boudon, V., Culhane, J. L., et al., Virtual atomic and molecular data centre. 2010, *Journal of Quantitiative Spectroscopy and Radiative Transfer*, **111**, 2151, DOI:10.1016/j.jqsrt.2010.05.004

Giuffrida, L., Margarone, D., Cirrone, G. A. P., et al., Prompt gamma ray diagnostics and enhanced hadron-therapy using neutron-free nuclear reactions. 2016, *AIP Advances*, **6**, 105204, DOI:10.1063/1.4965254

Hegelich, B. M., Labun, L., Labun, O. Z., Mehlhorn, T. A., & Batani, D., Photon and Neutron Production as In Situ Diagnostics of Proton-Boron Fusion. 2023, *Laser and Particle Beams*, **2023**, e7

Kramida, A., Yu. Ralchenko, Reader, J., & and NIST ASD Team. 2021, NIST Atomic Spectra Database (ver. 5.9), [Online]. Available: `https://physics.nist.gov/asd` [2022, September 7]. National Institute of Standards and Technology, Gaithersburg, MD.

Moore, C. E. 1993, *Tables of Spectra of Hydrogen, Carbon, Nitrogen, and Oxygen Atoms and Ions*

Sahal-Bréchot, S., Impact Theory of the Broadening and Shift of Spectral Lines due to Electrons and Ions in a Plasma. 1969a, *Astronomy and Astrophysics*, **1**, 91

Sahal-Bréchot, S., Impact Theory of the Broadening and Shift of Spectral Lines due to Electrons and Ions in a Plasma (Continued). 1969b, *Astronomy and Astrophysics*, **2**, 322

Sahal-Bréchot, S., Dimitrijević, M., & Ben Nessib, N., Widths and Shifts of Isolated Lines of Neutral and Ionized Atoms Perturbed by Collisions With Electrons and Ions: An Outline of the Semiclassical Perturbation (SCP) Method and of the Approximations Used for the Calculations. 2014, *Atoms*, **2**, 225, DOI:10.3390/atoms2020225

Sahal-Bréchot, S., Dimitrijević, M. S., Moreau, N., & Ben Nessib, N., The STARK-B database VAMDC node: a repository for spectral line broadening and shifts due to collisions with charged particles. 2015, *Physica Scripta*, **90**, 054008, DOI:10.1088/0031-8949/90/5/054008

Schollmeier, M. S., Shirvanyan, V., Capper, C., et al., Investigation of Proton Beam-Driven Fusion Reactions Generated by an Ultra-Short Petawatt-Scale Laser Pulse. 2022, *Laser and Particle Beams*, **2022**, e4, DOI:10.1155/2022/2404263

Yoon, D.-K., Jung, J.-Y., & Suh, T. S., Application of proton boron fusion reaction to radiation therapy: A Monte Carlo simulation study. 2014, *Applied Physics Letters*, **105**, 223507, `DOI:10.1063/1.4903345`

Contrib. Astron. Obs. Skalnaté Pleso **56/1**, 69 – 74, (2026)
https://doi.org/10.31577/caosp.2026.56.1.69

Probing rotation in quasars using microlensing-induced line profile distortions

C. Fian

INAF – Osservatorio Astronomico di Trieste, via G.B. Tiepolo, 11, I-34143 Trieste, Italy, (E-mail: carina.fian@inaf.it)

Received: August 30, 2025; Accepted: November 19, 2025

Abstract. We present a novel method to derive rotation curves of the inner broad-line region (BLR) of lensed quasars with light-day spatial resolution. The approach exploits microlensing distortions of the broad emission lines (BELs), where the strength of the effect in the line wings traces the size of the emitting region at different velocities. We analyze the high-ionization lines Si IV and C IV in five gravitationally lensed quasars, measuring microlensing amplitudes across several velocity bins. Bayesian inference yields emission-region sizes, which we confront with a Keplerian disk model. We find a smooth, monotonic increase in microlensing with velocity, and the derived velocity–size relations are consistent with disk-like rotation. These results provide the first direct evidence for Keplerian motion in the innermost BLR of quasars.

Key words: Gravitational lensing: micro – quasars: emission lines

1. Introduction

Direct evidence on the kinematics of the broad emission line (BEL) regions in quasars is still limited. The observed line profiles cannot usually be linked unambiguously to specific motions, although a two-component model has often been invoked: line wings arising from the accretion disk and the line core from a more isotropic component (Fian et al., 2023). Separating these contributions, however, is challenging, and most studies rely on virial estimates that mainly probe the core of the lines (Kaspi et al., 2021). Several methods have been proposed to explore the inner broad-line region (BLR) kinematics, such as velocity-resolved reverberation mapping (De Rosa et al., 2018; Bentz et al., 2023) and spectro-astrometry with GRAVITY@VLTI (Gravity Collaboration et al., 2018). These techniques have revealed complex results and are usually limited to nearby active galactic nuclei with spatial resolutions of tens of light-days. Gravitational microlensing provides an alternative probe. It is sensitive to source size on light-day scales and can thus map the emission regions of quasars at cosmological distances. While previous microlensing studies have focused on entire emission lines, strong microlensing distortions in the wings of some systems allow us to resolve the line profile into velocity bins. This enables the construction of experimental kinematic curves that relate velocity to emitting-region size. Here, we investigate the microlensing response in the high-ionization lines Si IV and C IV for five lensed quasars (SDSS J1001+5027, SDSS J1004+4112, HE 1104˘1805, SDSS J1206+4332, and SDSS J1339+1310). By comparing the observed microlensing signatures with predictions from a Keplerian disk model, we constrain the kinematics of the innermost BLR and test the hypothesis of disk-like rotation.

2. Data and observations

We compiled rest-frame ultraviolet spectra of gravitationally lensed quasars selected for clear microlensing signatures in the wings of the high-ionization lines Si IV $\lambda1397$ and/or C IV $\lambda1549$. Additional criteria required multi-epoch observations and sufficient signal-to-noise ratio in the relevant spectral range. The sample consists of one quadruply lensed quasar, SDSS J1004+4112 ($z = 1.734$), and four doubles: SDSS J1001+5027 ($z = 1.838$), HE 1104–1805 ($z = 2.319$), SDSS J1206+4332 ($z = 1.789$), and SDSS J1339+1310 ($z = 2.243$). The fully reduced spectra, collected from the literature, span multiple epochs over several years: six epochs for SDSS J1001+5027 (2003–2016), 21 epochs for SDSS J1004+4112 (2003–2018), seven epochs for HE 1104˘1805 (1993–2016), two epochs for SDSS J1206+4332 (2004, 2016), and eight epochs for SDSS J1339+1310 (2007–2017). For SDSS J1004+4112, only images A and B were used, since the long delays of images C and D (~ 2 and ~ 4.5 years; Muñoz et al. 2022) might mix intrinsic variability with microlensing.

3. Methodology

For each quasar image, we first subtracted the local continuum by fitting a straight line to adjacent regions free of emission features. The line cores, expected to be largely unaffected by microlensing (Fian et al., 2018), were used as a reference: we normalized the cores of images A and B to remove macro-magnification and extinction effects (Guerras et al., 2013). Average normalized profiles were then constructed, and splines were fitted to the wings most susceptible to microlensing. Microlensing signatures were detected as follows: in SDSS J1001+5027, a modest enhancement of image B in the red C IV wing (blue wing excluded due to absorption); in SDSS J1004+4112, strong distortions with a magnified blue wing and demagnified red wing in image A (Hutsemékers et al., 2023; Fian et al., 2024b); in SDSS J1206+4332 and SDSS J1339+1310, strong magnification of image B in the red wings of both lines (Goicoechea & Shalyapin, 2016; Fian et al., 2021, 2024c), plus additional blue-wing magnification in SDSS J1206+4332; and in HE 1104–1805, modest magnification of the red wings in image A (Fian et al., 2021). To quantify differential microlensing across velocities, we computed flux ratios between spline fits of the image pairs in 500 km s^{-1} bins, converted them into magnitudes, and sampled velocities between 3000–8000 km s^{-1}, yielding 11 independent measurements per line.

4. Microlensing simulations

To model microlensing of spatially extended sources, we employed the Fast Multipole Method–Inverse Polygon Mapping algorithm (FMM–IPM; Jiménez-Vicente & Mediavilla 2022), which combines the FMM approach for ray deflections with the IPM method for map generation. For each quasar image, we produced 3000×3000 pixel^2 magnification maps covering 100×100 Einstein radii^2, with a resolution of 0.30–0.40 light-days per pixel depending on the Einstein radius R_E. Stars of mass $0.3\,M_\odot$ were randomly distributed across the lens plane. The quasar emission regions were modeled with circular Gaussian profiles, $I(R) \propto \exp(-R^2/2r_s^2)$, convolved with the magnification maps. The relevant parameter is the half-light radius ($R_{1/2} = 1.18, r_s$), which largely determines microlensing results irrespective of the detailed brightness profile (Mortonson et al., 2005). Differential microlensing in the line wings between lensed images was used to infer emission-region sizes and thus probe BLR kinematics. Probabilities were computed by randomly placing the Gaussian sources on the maps and comparing the simulated and observed microlensing signals, following Guerras et al. (2013) and Fian et al. (2018, 2021).

5. Results and discussion

We examined microlensing magnification across velocity bins in the wings of Si IV and C IV, where contamination from other lines is minimal. This approach allows us to probe emission regions from several tens of light-days down to sub-light-day scales. A clear monotonic increase in microlensing with velocity is observed, consistent with high-velocity gas originating from more compact regions. A second key result is the agreement between velocity curves obtained from different wings or different lines in the same object, confirming the robustness of the method. We also find systematic asymmetries between red and blue wings: one wing may be magnified while the other is de-magnified, indicating that although both originate from similar-sized regions, they are not co-spatial. Finally, in several quasars (e.g., SDSS J1001+5027 and HE 1104˘1805) the velocity–size curves closely follow the expected Keplerian trend. In other systems, the curves flatten at high velocities, where size estimates are less reliable due to broad probability distributions. These deviations are within uncertainties and do not contradict the Keplerian hypothesis. Figure 1 illustrates the velocity-resolved microlensing signatures for one representative system in our sample. To improve statistical significance, we combined the velocity curves of all systems, scaling to a mean mass of $M_{\rm BH} \sin^2 i = 2.9 \times 10^7 M_\odot$. The stacked curve follows near-Keplerian motion over 3000–5500 km s^{-1}, with mild flattening at higher velocities, where uncertainties increase. Overall, the results provide strong evidence for Keplerian rotation in the innermost BLR, directly linking this region to the accretion disk structure. A detailed discussion of these results is presented in Fian et al. (2024a).

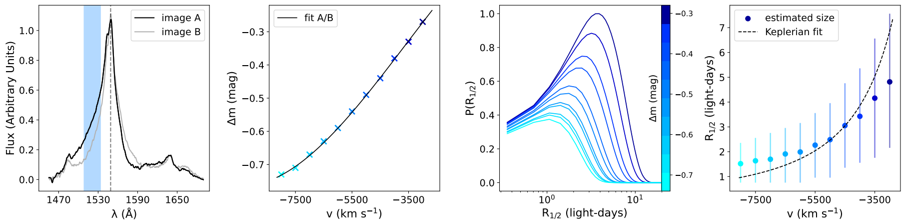

Figure 1. Kinematic responses to microlensing for SDSS J1004+4112. The left panel shows the average C IV line profiles for images A (black) and B (gray). The middle panels illustrate the magnitude differences between the images in the line wing and the probability density functions of the emitting region size. The rightmost panel displays the estimated sizes of different kinematic regions as a function of velocity, along with a Keplerian fit (dashed black line).

6. Conclusions

We obtained velocity-resolved microlensing magnification curves for the wings of the C IV and Si IV BELs in five lensed quasars. By linking microlensing strength to emitting-region size in each velocity bin, we derived velocity–size relations that reveal a smooth increase in magnification with velocity, consistent with high-velocity gas arising from more compact regions. We find strong consistency between curves obtained from red and blue wings of the same line, as well as from different lines in the same object, supporting the robustness of the method. Both individual systems and the composite curve align well with the predictions of a Keplerian disk, directly connecting the innermost BLR with the accretion disk structure. This represents the first direct evidence that the BLR follows Keplerian rotation over radii of $\sim$ 5˘20 light-days. Most notably, gravitational microlensing achieves an unprecedented spatial resolution - in some cases below one light-day - making it a uniquely powerful probe of quasar inner kinematics.

References

Bentz, M. C., Markham, M., Rosborough, S., et al., Velocity-resolved Reverberation Mapping of NGC 3227. 2023, *Astrophysical Journal*, **959**, 25, `DOI:10.3847/1538-4357/ad08b8`

De Rosa, G., Fausnaugh, M. M., Grier, C. J., et al., Velocity-resolved Reverberation Mapping of Five Bright Seyfert 1 Galaxies. 2018, *Astrophysical Journal*, **866**, 133, `DOI:10.3847/1538-4357/aadd11`

Fian, C., Guerras, E., Mediavilla, E., et al., Microlensing and Intrinsic Variability of the Broad Emission Lines of Lensed Quasars. 2018, *Astrophysical Journal*, **859**, 50, `DOI:10.3847/1538-4357/aabc0d`

Fian, C., Jiménez-Vicente, J., Mediavilla, E., et al., First Direct Evidence for Keplerian Rotation in Quasar Inner Broad-line Regions. 2024a, *Astrophysical Journal, Letters*, **972**, L7, `DOI:10.3847/2041-8213/ad654d`

Fian, C., Mediavilla, E., Motta, V., et al., Microlensing of the broad emission lines in 27 gravitationally lensed quasars. Broad line region structure and kinematics. 2021, *Astronomy and Astrophysics*, **653**, A109, `DOI:10.1051/0004-6361/202039829`

Fian, C., Muñoz, J. A., Forés-Toribio, R., et al., Probing the structure of the lensed quasar SDSS J1004+4112 through microlensing analysis of spectroscopic data. 2024b, *Astronomy and Astrophysics*, **682**, A57, `DOI:10.1051/0004-6361/202347382`

Fian, C., Muñoz, J. A., Jiménez-Vicente, J., et al., Revealing the inner workings of the lensed quasar SDSS J1339+1310: Insights from microlensing analysis. 2024c, *Astronomy and Astrophysics*, **689**, A129, `DOI:10.1051/0004-6361/202450151`

Fian, C., Muñoz, J. A., Mediavilla, E., et al., Revealing the structure of the lensed quasar Q 0957+561. III. Constraints on the size of the broad-line region. 2023, *Astronomy and Astrophysics*, **678**, A108, `DOI:10.1051/0004-6361/202140975`

Goicoechea, L. J. & Shalyapin, V. N., Gravitational lens system SDSS J1339+1310: microlensing factory and time delay. 2016, *Astronomy and Astrophysics*, **596**, A77, `DOI:10.1051/0004-6361/201628790`

Gravity Collaboration, Sturm, E., Dexter, J., et al., Spatially resolved rotation of the broad-line region of a quasar at sub-parsec scale. 2018, *Nature*, **563**, 657, `DOI:10.1038/s41586-018-0731-9`

Guerras, E., Mediavilla, E., Jimenez-Vicente, J., et al., Microlensing of Quasar Broad Emission Lines: Constraints on Broad Line Region Size. 2013, *Astrophysical Journal*, **764**, 160, `DOI:10.1088/0004-637X/764/2/160`

Hutsemékers, D., Sluse, D., Savić, Đ., & Richards, G. T., Microlensing of the broad emission line region in the lensed quasar J1004+4112. 2023, *Astronomy and Astrophysics*, **672**, A45, `DOI:10.1051/0004-6361/202245490`

Jiménez-Vicente, J. & Mediavilla, E., Fast Multipole Method for Gravitational Lensing: Application to High-magnification Quasar Microlensing. 2022, *Astrophysical Journal*, **941**, 80, `DOI:10.3847/1538-4357/ac9e59`

Kaspi, S., Brandt, W. N., Maoz, D., et al., Taking a Long Look: A Two-decade Reverberation Mapping Study of High-luminosity Quasars. 2021, *Astrophysical Journal*, **915**, 129, `DOI:10.3847/1538-4357/ac00aa`

Mortonson, M. J., Schechter, P. L., & Wambsganss, J., Size Is Everything: Universal Features of Quasar Microlensing with Extended Sources. 2005, *Astrophysical Journal*, **628**, 594, `DOI:10.1086/431195`

Muñoz, J. A., Kochanek, C. S., Fohlmeister, J., et al., The Longest Delay: A 14.5 yr Campaign to Determine the Third Time Delay in the Lensing Cluster SDSS J1004+4112. 2022, *Astrophysical Journal*, **937**, 34, DOI:10.3847/1538-4357/ac8877

Contrib. Astron. Obs. Skalnaté Pleso **56/1**, 75 – 86, (2026)
https://doi.org/10.31577/caosp.2026.56.1.75

Exploring emission line variability and jet-broad line region interaction in the blazar TON 599

Jonhatan U. Guerrero-González[1], **Vahram Chavushyan**[1] and **Víctor M. Patiño-Álvarez**[1,2]

[1] *Instituto Nacional de Astrofísica, Óptica y Electrónica (INAOE), Luis Enrique Erro #1, Tonantzintla, Puebla, México, C.P. 72840*

[2] *Max-Planck-Institut für Radioastronomie, Auf dem Hügel 69, D-53121 Bonn, Germany*

Received: September 26, 2025; Accepted: November 20, 2025

Abstract. Blazars, a highly variable Active Galactic Nuclei (AGNs) subclass, provide a unique opportunity to explore the physical processes within their relativistic jets and emission regions. In this study, we investigate the multiwavelength variability of the blazar TON 599, a Flat Spectrum Radio Quasar (FSRQ), with a particular emphasis on its emission line behavior. We focus on the Mg II λ2798 Å emission line, a key tracer of the ionized gas in the broad-line region (BLR), and its role in jet-induced variability. In addition to optical emission lines, we analyze gamma-rays (0.1–300 GeV), X-rays (0.2–10 keV), optical continuum (λ3000 Å), optical polarization, and millimeter-wavelength light curves. Three cross-correlation methods are employed to investigate temporal relationships between the emission line and continuum across various wavelengths. Using the Non-Thermal Dominance (NTD) parameter, our analysis confirms that synchrotron emission dominates the continuum during active states, highlighting the jet's primary role in the observed variability. The Mg II emission line exhibits quasi-simultaneous variability with the optical continuum, suggesting photoionization driven by the jet's non-thermal radiation. Additionally, the minimal time lag between gamma-ray and optical/near-ultraviolet emissions supports a synchrotron self-Compton origin for the most variable component of the gamma-ray emission. These findings highlight the importance of emission line variability and multiwavelength observations in constraining the interaction between jets and the BLR in blazars. The results contribute to a deeper understanding of AGN emission mechanisms and the complex interplay between jets and their surrounding environments.

1. Introduction

Supermassive black holes (SMBHs) reside at the centers of most galaxies, and those with high accretion rates give rise to Active Galactic Nuclei (AGN) (Urry & Padovani, 1995). A remarkable subclass of AGN is represented by blazars, whose relativistic jets are aligned close to our line of sight. They are powerful radio sources, characterized by extreme variability across the entire electromagnetic spectrum, with timescales ranging from years to minutes. Blazars provide a unique laboratory for studying physical conditions that cannot be reproduced on Earth.

Blazars are commonly divided into two subclasses: BL Lacertae objects (BL Lacs) and Flat Spectrum Radio Quasars (FSRQs). In particular, FSRQs tend to show broad optical emission lines (e.g., Hβ, Mg II, C IV) in addition to a non-thermal continuum (Urry & Padovani, 1995; Véron-Cetty & Véron, 2000). By contrast, BL Lacs are characterized by optical spectra dominated by a nearly featureless non-thermal continuum with very weak or absent emission lines (Stickel et al., 1991).

Within this context, this work focuses on the blazar TON 599 ($z = 0.725$; Hewett & Wild 2010), classified as an FSRQ. We investigate its multifrequency variability, including gamma rays (0.1–300 GeV), X-rays (0.2–10 keV), the UV spectral continuum (3000 Å), the Mg II λ2798 Å emission line, optical polarization (5000–7000 Å), and 1 mm emissions. Cross-correlation analysis is employed to explore connections among these bands. This study provides new insights into the multifrequency emission processes of TON 599 and contributes to a broader understanding of blazar-type AGN.

2. Object of study

The blazar TON 599 is classified as a Flat Spectrum Radio Quasar (FSRQ) due to its strong broad line emission and small viewing angle, making it one of the most variable types of AGN (Wills et al., 1983; Prince, 2019; Hallum et al., 2022).

Originally discovered in the 1950s by Iriarte & Chavira (1957), TON 599 was included in a catalog of more than 800 "blue stars" identified near the North Galactic Pole, as part of an observational program carried out with the Tonantzintla Schmidt Camera, in Puebla, Mexico. Since then, this source has been extensively monitored by multiple facilities, yielding a rich multi-band archive and numerous publications that consistently confirm its strong variability across different wavelengths.

Figure 1 shows the original identification chart of TON 599 together with its UV/optical spectrum, illustrating both the historical context of its discovery and the spectral features that define it as an FSRQ.

3. Methodology

The observations analyzed in this work span multiple wavelengths. Gamma-ray data were obtained from *Fermi*-LAT, while X-ray data were taken from the *Swift-XRT Monitoring of Fermi-LAT Sources of Interest*. Optical spectra

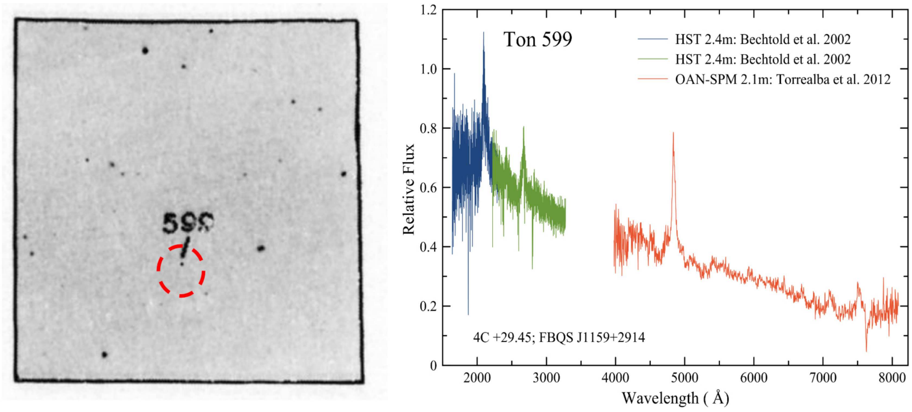

Figure 1. Left: Identification chart of TON 599 (Iriarte & Chavira, 1957). Right: Observed frame UV/Optical spectrum of TON 599 (Bechtold et al., 2002; Torrealba et al., 2012)

were retrieved from the database of the Ground-Based Observational Program associated with the *Fermi* Gamma-ray Space Telescope at the University of Arizona, and 1 mm observations were collected from the Submillimeter Array (SMA) database.

In total, 196 spectra of TON 599 were compiled, of which two were discarded due to low signal-to-noise ratio. For each remaining spectrum, a fitting procedure was performed on the Mg II $\lambda2798$ Å emission line using multi-component models. The continuum was fitted with a power-law function, the Fe II emission in the UV was modeled with empirical templates (Vestergaard & Wilkes, 2001), and the Mg II line itself was decomposed into broad and narrow components with Gaussian profiles (see Figure 2 for an example of the fitting procedure). This approach allowed us to reliably characterize the spectral features of TON 599.

From these fits we derived integrated fluxes, line and continuum luminosities, and subsequently physical parameters such as the Non-Thermal Dominance (NTD), which are discussed in the following section.

4. Non-thermal dominance parameter: NTD

The non-thermal dominance (NTD) parameter, introduced by Shaw et al. (2012), quantifies the contribution of the relativistic jet to the optical/UV continuum and is defined as:

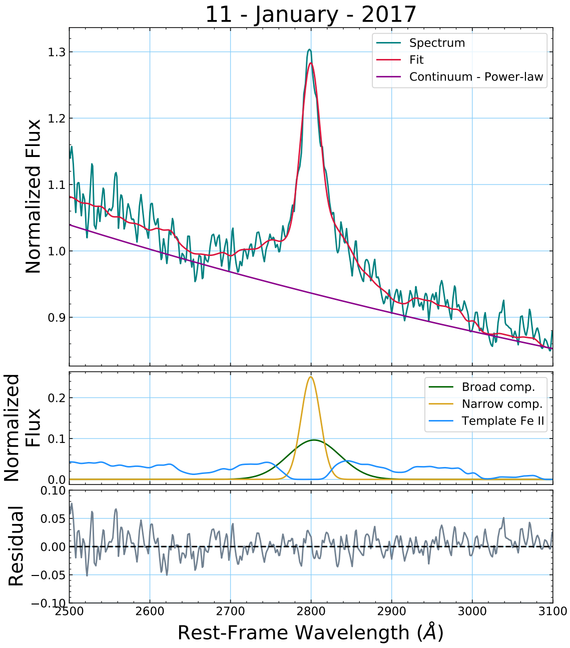

Figure 2. Example of a TON 599 spectrum (January 2017, Steward Observatory) showing the multi-component fit and residuals.

$$NTD = \frac{L_{obs}}{L_{pred}}, \tag{1}$$

where L_{obs} is the observed luminosity and L_{pred} is the predicted luminosity inferred from emission lines in non-blazar AGNs. Since broad emission lines trace the accretion disk power (i.e. L_{pred}=L_{disk}), Patiño Álvarez et al. (2016) reformulated NTD as:

$$NTD = 1 + \frac{L_{jet}}{L_{disk}}, \quad NTD \geq 1, \tag{2}$$

which allows different regimes to be identified: $NTD = 1$ (only disk emission), $1 < NTD < 2$ (disk-dominated), $NTD = 2$ (equal contributions from disk and jet), and $NTD > 2$ (jet-dominated).

The value of L_{pred} was obtained from the empirical relation between L_{MgII} and $L_{3000\,\text{Å}}$ derived from a sample of $\sim 40{,}000$ radio-quiet AGN (Patiño-Álvarez et al., 2025) :

$$\log L_{MgII} = (0.826 \pm 0.025) \log \lambda L_{\lambda 3000} + (6.057 \pm 1.164). \tag{3}$$

Here, L_{MgII} was measured from the integrated flux of the emission line, while L_{obs} was derived from the continuum flux at 3000 Å, both calculated using a luminosity distance of $D_L = 4445.5$ Mpc ($z = 0.725$).

In addition, single-epoch black hole mass estimates were obtained using standard virial relations based on the Mg II emission line luminosity and the 3000 Å continuum (Kong et al., 2006; Vestergaard & Peterson, 2006; Shen et al., 2011). These methods assume that the Broad Line Region (BLR) is virialized and that the continuum is primarily powered by the accretion disk.

For jet-dominated sources such as TON 599, however, the continuum can be significantly contaminated by non-thermal emission, which may lead to systematic overestimations of $M_{\rm BH}$. Since the Mg II emission line is expected to be less affected by this contamination, mass estimates derived from L_{MgII} are considered more reliable in these cases. Figure 3 shows the relation between L_{MgII} and $L_{3000\,\text{Å}}$ for TON 599, where deviations from the empirical trend directly reflect the increasing jet contribution and its impact on black hole mass determinations.

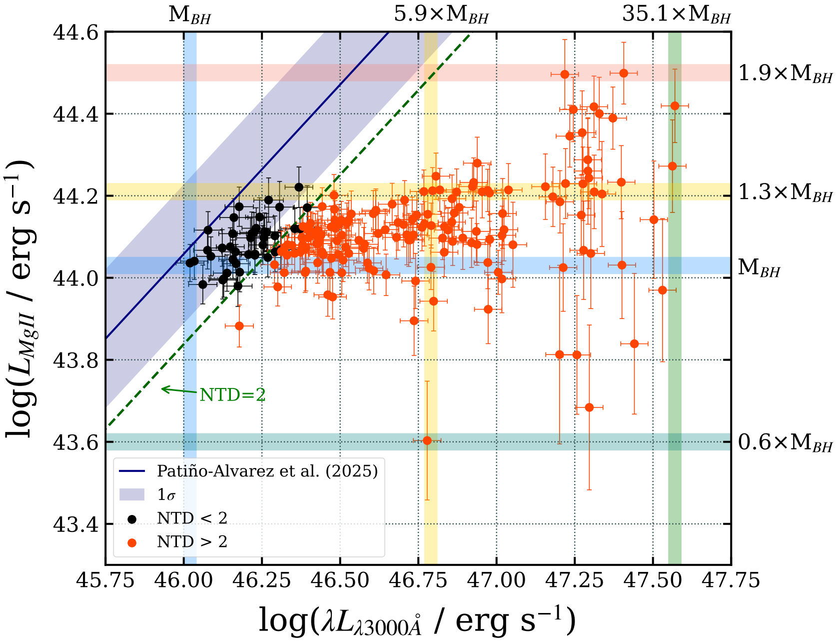

Figure 3. Variations in the Mg II emission line luminosity versus the continuum luminosity at 3000 Å for TON 599. The right and top axes show overestimations and underestimations of the black hole mass when calculated using single-epoch techniques, using the continuum and emission line luminosity, respectively.

5. Cross-correlation analysis

To investigate possible time lags between the continuum and emission line variability, we applied cross-correlation functions (CCFs) using three complementary approaches: the interpolated CCF (Gaskell & Sparke, 1986), the discrete CCF (Edelson & Krolik, 1988), and the Z-transformed DCF (Alexander, 1997), all incorporating non-stationarity corrections (Patiño-Álvarez et al., 2013; Amaya-Almazán et al., 2022).

The statistical significance of the correlations was evaluated through Monte Carlo simulations (Timmer & Koenig, 1995; Emmanoulopoulos et al., 2013), with confidence levels at 90, 95, and 99% (grey lines in Figure 4). In this work, we adopt the 99% level as the threshold for reliable correlations. Employing multiple CCF methods enhances robustness by mitigating the effects of interpolation gaps, spurious peaks, and aliasing, among other caveats the data might present.

As an illustrative example, Figure 4 presents the results of the cross-correlation between the gamma-ray and 3000 Å light curves using the three methods, illustrating both the consistency of the techniques and the regions where significant correlations are detected. In this figure, we see that the ICCF does not exceed the 99% confidence level, whereas the DCCF and ZDCF show a significant correlation within the same lag range. This difference stems from the ICCF's sensitivity to interpolation and irregular sampling. Therefore, for this specific case we consider the detection supported by DCCF/ZDCF to be more reliable.

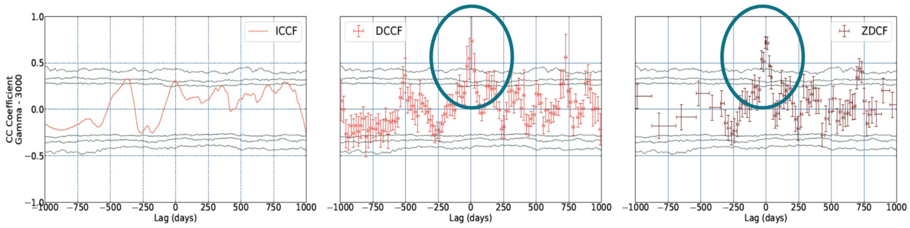

Figure 4. Example of the cross-correlation functions; in this case between the gamma-ray and 3000 Å light curves using three methods. Left: interpolated cross-correlation function (ICCF); middle: discrete cross-correlation function (DCCF); right: Z-transformed discrete correlation function (ZDCF).

6. Results

The results presented below are derived from a joint analysis of the multi-frequency light curves and the cross-correlations between bands. In particular, the cross-correlations provide information on the time lags between different wavelength bands of the electromagnetic spectrum, which may be related to distances between emitting regions, provided that factors such as the jet viewing angle and the wavelengths involved are taken into account.

Figure 5 shows the multi-frequency light curves of TON 599, including *Fermi*-LAT γ rays (0.1–300 GeV), *Swift*-XRT X rays (0.3–10 keV), optical data from the *Steward Observatory* (4000–7000 Å in the observer's frame), comprising the rest-frame 3000 Å continuum, the Mg II λ2798 Å line flux, V-band photometry, the polarization degree, and the polarization angle (measured between 5000 and 7000 Å), SMA 1 mm emission, and the Non-Thermal Dominance (NTD) curve computed from the 3000 Å continuum and the Mg II line.

Consistent with the cross-correlation analysis, the V band and the 3000 Å continuum vary quasi-simultaneously, with contemporaneous rises and declines in Figure 5 (panels c,e). The NTD in panel (i) increases over the same intervals to values above 2 (black dashed line), indicating enhanced jet contribution. The γ-ray activity (panel a) rises during the main optical/NUV events, in agreement with the significant correlations recovered by the discrete and Z-transformed discrete correlation functions. The Mg II λ2798 Å emission line (panel d) exhibits flux enhancements that coincide with optical/NUV high states, consistent with near-zero lags found for the line–continuum pairs.

By contrast, some bands do not show clear correlations. The X-ray coverage (panel b) is limited and does not sample the strongest optical/NUV outbursts, which restricts any association. The 1 mm emission (panel f) traces longer variability timescales and lacks dense sampling during the short optical/NUV flares, reducing the expected cross-correlation signal. The polarization degree and polarization angle (panels g–h) show variability but no consistent temporal relation with the other bands in this dataset. Finally, the γ-ray–Mg II correlation is inconclusive, mainly due to cadence and sampling differences between the high-energy and emission line light curves.

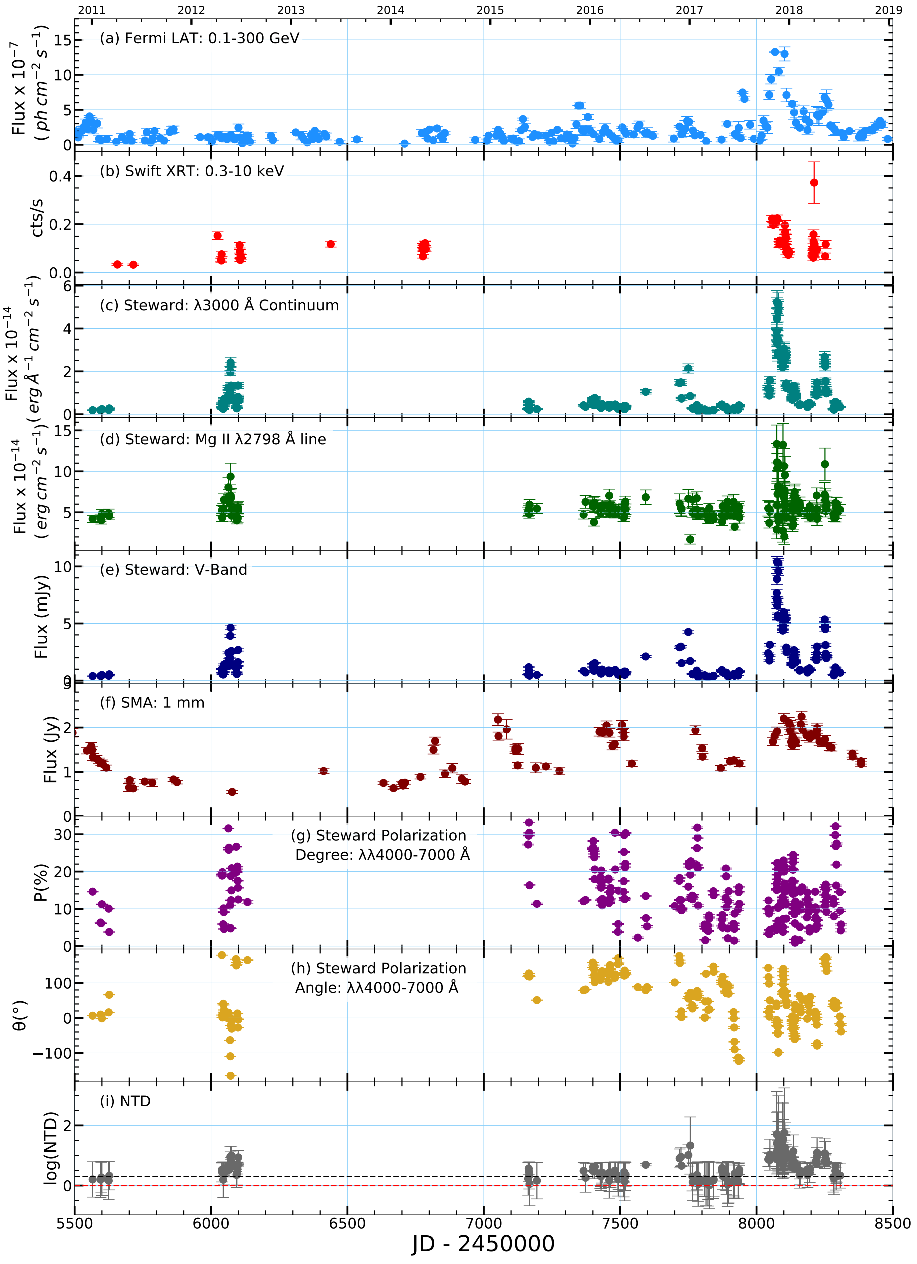

Figure 5. Multifrequency Light Curves for TON 599.

7. Conclusions

The cross-correlation analysis and multifrequency monitoring of TON 599 allow us to identify several key results regarding the connection between the jet, the optical/UV continuum, the emission lines, and the high-energy emission. These findings can be summarized as follows:

1. The cross-correlations between the V band, the 3000 Å continuum, and the NTD are consistent with zero lag. This indicates co-spatiality among the optical/NUV emissions, with the main variability in NTD arising from the jet. The similar variability patterns observed in both the V band and the 3000 Å continuum support the interpretation that these bands are dominated by synchrotron radiation from the jet.

2. The correlations between the optical/NUV bands and gamma rays suggest that the seed photon population is dominated by synchrotron emission, and that the gamma-ray variability is mainly produced by the Synchrotron Self-Compton (SSC) process during high states of the source. This finding that SSC dominates challenges the standard external Compton scenario and has implications for jet models and Spectral Energy Distribution (SED) studies.

3. Cross-correlations between the optical/NUV bands and the Mg II λ2798 Å emission line also yield a zero lag. The temporal coincidence of line flares with optical/NUV variability implies that the line-emitting gas is being ionized by synchrotron radiation from the jet, in addition to the accretion disk.

4. The observed relation between continuum and line luminosities deviates from expectations for a radio-quiet BLR, indicating that the emission line is not solely ionized by the accretion disk. As a result, black hole mass estimates based on single-epoch methods should preferentially use epochs when the continuum is disk-dominated to obtain more realistic values.

Overall, TON 599 demonstrates that optical/NUV synchrotron emission drives both γ–ray SSC variability and Mg II ionization, revealing a strong interplay between the relativistic jet and the BLR. This challenges canonical reverberation mapping assumptions and adds further evidence, consistent with sources such as 3C 454.3 (León-Tavares et al., 2013; Amaya-Almazán et al., 2021), 3C 279 (Patiño-Álvarez et al., 2018), and CTA 102 (Chavushyan et al., 2020), that BLR gas can be directly influenced by jets.

The case of TON 599 highlights how jet–BLR interactions significantly impact both variability patterns and black hole mass determinations in FSRQs. Future efforts should focus on short-timescale flares, testing the NTD threshold across different bands, refining Mg II-based mass estimates with improved instrumental corrections, and extending this methodology to a larger sample of blazars (Massaro et al., 2015).

Acknowledgements. This work has been supported by the SECIHTI program during my doctoral studies. Support was also provided by the MPIfR-Mexico Max Planck Partner Group, led by Dr. Víctor Manuel Patiño Álvarez, whose significant contribution to this research is greatly appreciated.

References

Alexander, T., Is AGN Variability Correlated with Other AGN Properties? ZDCF Analysis of Small Samples of Sparse Light Curves. 1997, in Astrophysics and Space Science Library, Vol. **218**, *Astronomical Time Series*, ed. D. Maoz, A. Sternberg, & E. M. Leibowitz, 163

Amaya-Almazán, R. A., Chavushyan, V., & Patiño-Álvarez, V. M., Multiwavelength Analysis and the Difference in the Behavior of the Spectral Features during the 2010 and 2014 Flaring Periods of the Blazar 3C 454.3. 2021, *Astrophysical Journal*, **906**, 5, `DOI:10.3847/1538-4357/abc689`

Amaya-Almazán, R. A., Chavushyan, V., & Patiño-Álvarez, V. M., Multiwavelength Analysis and the C IV λ1549 Å Emission Line Behavior From 2008 to 2020 of FSRQ B2 1633+382. 2022, *Astrophysical Journal*, **929**, 14, `DOI:10.3847/1538-4357/ac5741`

Bechtold, J., Dobrzycki, A., Wilden, B., et al., A Uniform Analysis of the Lyα Forest at z = 0-5. III. Hubble Space Telescope Faint Object Spectrograph Spectral Atlas. 2002, *Astrophysical Journal, Supplement*, **140**, 143, `DOI:10.1086/342489`

Chavushyan, V., Patiño-Álvarez, V. M., Amaya-Almazán, R. A., & Carrasco, L., Flare-like Variability of the Mg II λ2798 Å Emission Line and UV Fe II Band in the Blazar CTA 102. 2020, *Astrophysical Journal*, **891**, 68, `DOI:10.3847/1538-4357/ab6ef6`

Edelson, R. A. & Krolik, J. H., The Discrete Correlation Function: A New Method for Analyzing Unevenly Sampled Variability Data. 1988, *Astrophysical Journal*, **333**, 646, `DOI:10.1086/166773`

Emmanoulopoulos, D., McHardy, I. M., & Papadakis, I. E., Generating artificial light curves: revisited and updated. 2013, *Monthly Notices of the RAS*, **433**, 907, `DOI:10.1093/mnras/stt764`

Gaskell, C. M. & Sparke, L. S., Line Variations in Quasars and Seyfert Galaxies. 1986, *Astrophysical Journal*, **305**, 175, `DOI:10.1086/164238`

Hallum, M. K., Jorstad, S. G., Larionov, V. M., et al., Emission-line Variability during a Nonthermal Outburst in the Gamma-Ray Bright Quasar 1156+295. 2022, *Astrophysical Journal*, **926**, 180, `DOI:10.3847/1538-4357/ac4710`

Hewett, P. C. & Wild, V., Improved redshifts for SDSS quasar spectra. 2010, *Monthly Notices of the RAS*, **405**, 2302, `DOI:10.1111/j.1365-2966.2010.16648.x`

Iriarte, B. & Chavira, E., Estrellas Azules en el Casquete Galactico NorteEstrellas Azules en el Casquete Galactico NorteBlue Stars in the North Galactic Cap. 1957, *Boletin de los Observatorios Tonantzintla y Tacubaya*, **2**, 3

Kong, M.-Z., Wu, X.-B., Wang, R., & Han, J.-L., Estimating Black Hole Masses of AGNs using Ultraviolet Emission Line Properties. 2006, *Chinese Journal of Astronomy and Astrophysics*, **6**, 396, DOI:10.1088/1009-9271/6/4/02

León-Tavares, J., Chavushyan, V., Patiño-Álvarez, V., et al., Flare-like Variability of the Mg II λ2800 Emission Line in the Γ-Ray Blazar 3C 454.3. 2013, *Astrophysical Journal, Letters*, **763**, L36, DOI:10.1088/2041-8205/763/2/L36

Massaro, E., Maselli, A., Leto, C., et al., The 5th edition of the Roma-BZCAT. A short presentation. 2015, *Astrophysics and Space Science*, **357**, 75, DOI:10.1007/s10509-015-2254-2

Patiño-Álvarez, V., Carramiñana, A., Carrasco, L., & Chavushyan, V., A Multiwavelength Cross-Correlation Variability Study of Fermi-LAT Blazars. 2013, *arXiv e-prints*, arXiv:1303.1898, DOI:10.48550/arXiv.1303.1898

Patiño Álvarez, V., Torrealba, J., Chavushyan, V., et al., Baldwin Effect and Additional BLR Component in AGN with Superluminal Jets. 2016, *Frontiers in Astronomy and Space Sciences*, **3**, 19, DOI:10.3389/fspas.2016.00019

Patiño-Álvarez, V. M., Fernandes, S., Chavushyan, V., et al., Multiwavelength photometric and spectropolarimetric analysis of the FSRQ 3C 279. 2018, *Monthly Notices of the RAS*, **479**, 2037, DOI:10.1093/mnras/sty1497

Patiño-Álvarez, V. M., Guerrero-González, J. U., Chavushyan, V., et al., The Relationship Between Emission Line and Continuum Luminosity and the Baldwin Effect in Blazars. I. The Case of the Mg II λ2798 Å Emission Line. 2025, *arXiv e-prints*, arXiv:2511.15695, DOI:10.48550/arXiv.2511.15695

Prince, R., Multi-frequency Variability Study of Ton 599 during the High Activity of 2017. 2019, *Astrophysical Journal*, **871**, 101, DOI:10.3847/1538-4357/aaf475

Shaw, M. S., Romani, R. W., Cotter, G., et al., Spectroscopy of Broad-line Blazars from 1LAC. 2012, *Astrophysical Journal*, **748**, 49, DOI:10.1088/0004-637X/748/1/49

Shen, Y., Richards, G. T., Strauss, M. A., et al., A Catalog of Quasar Properties from Sloan Digital Sky Survey Data Release 7. 2011, *Astrophysical Journal, Supplement*, **194**, 45, DOI:10.1088/0067-0049/194/2/45

Stickel, M., Padovani, P., Urry, C. M., Fried, J. W., & Kuehr, H., The Complete Sample of 1 Jansky BL Lacertae Objects. I. Summary Properties. 1991, *Astrophysical Journal*, **374**, 431, DOI:10.1086/170133

Timmer, J. & Koenig, M., On generating power law noise. 1995, *Astronomy and Astrophysics*, **300**, 707

Torrealba, J., Chavushyan, V., Cruz-González, I., et al., Optical Spectroscopic Atlas of the MOJAVE/2cm AGN Sample. 2012, *Revista Mexicana de Astronomia y Astrofisica*, **48**, 9, DOI:10.48550/arXiv.1107.3416

Urry, C. M. & Padovani, P., Unified Schemes for Radio-Loud Active Galactic Nuclei. 1995, *Publications of the ASP*, **107**, 803, DOI:10.1086/133630

Véron-Cetty, M. P. & Véron, P., The emission line spectrum of active galactic nuclei and the unifying scheme. 2000, *Astronomy and Astrophysics Reviews*, **10**, 81, `DOI:10.1007/s001590000006`

Vestergaard, M. & Peterson, B. M., Determining Central Black Hole Masses in Distant Active Galaxies and Quasars. II. Improved Optical and UV Scaling Relationships. 2006, *Astrophysical Journal*, **641**, 689, `DOI:10.1086/500572`

Vestergaard, M. & Wilkes, B. J., An Empirical Ultraviolet Template for Iron Emission in Quasars as Derived from I Zwicky 1. 2001, *Astrophysical Journal, Supplement*, **134**, 1, `DOI:10.1086/320357`

Wills, B. J., Pollock, J. T., Aller, H. D., et al., The QSO 1156+295 : a multifrequency study of recent activity. 1983, *Astrophysical Journal*, **274**, 62, `DOI:10.1086/161426`

Contrib. Astron. Obs. Skalnaté Pleso **56/1**, 87 – 101, (2026)
https://doi.org/10.31577/caosp.2026.56.1.87

Evidence for a stratified accretion disk wind in AGN

P. Marziani[1], E. Bon[2], S. Panda[3], N. Bon[2], A. Del Olmo[4], A. Deconto-Machado[4,5], K. Garnica[6] and D. Dultzin[6]

[1] *INAF, Astronomical Observatory of Padua, Italy (E-mail: Paola.marziani@inaf.it)*
[2] *Belgrade Astronomical Observatory, Serbia*
[3] *International Gemini Observatory, NSF NOIRLab, La Serena, Chile*
[4] *IAA-CSIC, Granada, Spain*
[5] *IASF-INAF, Milan, Italy*
[6] *IA-UNAM, Mexico City, Mexico*

Received: September 24, 2025; Accepted: October 30, 2025

Abstract. We present observational evidence supporting the presence of a stratified accretion disk wind in active galactic nuclei (AGN), based on multi-wavelength spectroscopic analysis of broad and narrow emission lines. The diversity in emission line profiles, ionization potentials, and kinematic signatures suggests a structured outflow emerging from the accretion disk, with different zones contributing to specific spectral features. High-ionization lines (e.g., CIV λ1549) exhibit strong blueshifts and asymmetric profiles indicative of fast, inner winds, while low-ionization lines (e.g., Hβ, MgII λ 2800) show more symmetric profiles consistent with predominant emission from slower, denser regions farther out, although exhibiting systematic blueshifts in quasars radiating at high Eddington ratios. The intermediate ionization lines (e.g., AlIIIλ1860) present a situation that is intermediate in terms of shift amplitudes, although in several super-Eddington candidates radial outflow velocity may reach values comparable to the ones of the high ionization lines. These results are consistent with radiatively driven wind models featuring radial stratification. We made preliminary photoionization modeling assuming unabsorbed radiation emitted from the corona and the hotter disk regions emission or absorbed by a layer of gas. Our findings provide new constraints on the geometry and physical conditions of AGN winds, providing clear evidence in favor of stratified wind emission.

Key words: Supermassive black holes (1663) – Active galactic nuclei (16) – Quasars (1319) – Spectroscopy (1558) – Photoionization (2060)

1. Introduction

The concept of a quasar ”main sequence” (MS) emerged from the landmark work of Boroson & Green (1992), who identified a strong anti-correlation between the relative strength of FeIIλ4570 emission and the full width at half maximum (FWHM) of the broad Hβ line. This relation, commonly expressed through the parameter $R_{\rm FeII}$= FeIIλ4570/Hβ, was first hinted at in earlier works (e.g., Gaskell 1985 and has since been confirmed and extended in a large number of studies (Sulentic et al., 2000a,b; Shen & Ho, 2014; Rakshit et al., 2020; Wu & Shen, 2022). The MS framework provides a powerful tool for organizing the remarkable diversity of type-1 active galactic nuclei (AGN) spectroscopic properties.

Within this scheme, type-1 AGN can be broadly separated into two main populations: Population A and Population B (Sulentic et al., 2000a, 2002, 2011). Population A sources, characterized by narrower Hβ profiles (FWHM $<$ 4000 km s^{-1}), are generally associated with high accretion rates relative to the Eddington limit, while Population B sources (FWHM $>$ 4000 km s^{-1}) are typically lower Eddington ratio ($L/L_{\rm Edd}$, where $L_{\rm Edd}$ is the Eddington luminosity) systems. A small subset, on the order of $\sim$ 10% of the population, represents "extreme" Population A sources ($R_{\rm FeII}$$>$ 1), which are widely interpreted as candidates for super-Eddington accretion (Wang et al., 2013; Marziani & Sulentic, 2014; Du et al., 2018; Panda & Marziani, 2023; Panda, 2024; Marziani et al., 2025).

The MS is thought to be primarily driven by the Eddington ratio $L/L_{\rm Edd}$ (Marziani et al., 2001; Boroson, 2002; Shen & Ho, 2014; Sun & Shen, 2015; Panda et al., 2019), with orientation effects also playing a significant role in shaping the observed diversity. Black hole mass effects, concomitant with viewing angle effects, become relevant when AGN samples cover a wide range in luminosity (Marziani et al., 2018a; Naddaf et al., 2025). The organization of type-1 AGN properties across the MS has been extensively studied at multiple wavelengths, most prominently within the so-called 4D Eigenvector 1 (4DE1) parameter space introduced by Sulentic et al. (2000c). This framework combines optical, UV, and X-ray measures to capture the multidimensional diversity of quasars, while also providing a physical interpretation in terms of accretion physics and geometry (see Fraix-Burnet et al. 2017 for a summary).

Large surveys, such as the Sloan Digital Sky Survey (SDSS, York et al. 2000), have provided further statistical foundation for these studies. For instance, Zamfir et al. (2010) analyzed ≈470 quasars at $z < 0.7$ with average bolometric luminosities $\log L \sim 45.5$ erg/s, confirming the prevalence of the MS trends and strengthening the case for $L/L_{\rm Edd}$ as a primary driver. More recently, refinements in spectral analysis and improved databases have continued to reinforce this picture (e.g., Shen & Ho 2014; Wu & Shen 2022).

In summary, the quasar main sequence organizes type-1 AGN along a continuum of properties primarily governed by Eddington ratio and orientation. At one end of the sequence lie the extreme Population A sources, with the largest FeII strengths and the highest inferred $L/L_{\rm Edd}$ values, plausibly representing systems accreting at or above the Eddington limit. These sources provide critical laboratories for understanding black hole growth under extreme conditions and the broader role of AGN feedback in galaxy evolution (Marziani et al., 2025). Luminosity and black hole mass ($M_{\rm BH}$) effects appear in sample covering large ranges in luminosity and mass. They can be reconduced to two effects: an increase in the amplitude of shifts with respect to the rest frame observed mainly in high-ionization lines (e.g., Marziani et al., 2016), and a prominent redward asymmetries associated with very massive black holes (Marziani et al., 2009; Marziani, 2023).

In this paper, we first present a brief summary of three recent works dealing with the observations of outflows as diagnosed from the shifts with respect to the rest frame, namely the prototypical CIVλ1549 high-ionization line, the intermediate ionization emission AlIIIλ1860, and the low ionization line of MgIIλ2800 (Sections 2, 3). The three lines are all unresolved doublets associated with the resonance transition $^2P_{\frac{1}{2},\frac{3}{2}} \rightarrow ^2 S_{\frac{1}{2}}$, with parent ionic species of different ionization potential, from $\approx$ 50 eV (CIV) to $\approx$ 25 eV (AlIII) and $\approx$ 15 eV (MgII). We afterwards attempt to explain the observational results by photoionization models focused on the sectors of the MS where the larger amplitude blueshifts are found, namely Population A and extreme Population A (Section 4).

2. CIVλ1549 Shifts and outflows along the quasar main sequence

Systematic blueshifts of the high-ionization CIVλ1549 emission line provide one of the clearest observational signatures of quasar outflows. Early evidence for such features in composite spectra of radio-quiet quasars was strengthened by HST/FOS studies (Marziani et al., 1996; Corbin & Boroson, 1996; Sulentic et al., 2007; Marziani et al., 2010; Leighly & Moore, 2004; Richards et al., 2011; Sulentic et al., 2007; Marziani et al., 2010; Sulentic et al., 2017). These analyses showed that CIV profiles can be decomposed into at least two components: a virialized, symmetric, and generally unshifted component (well represented by a Lorentzian in Population A sources), and a blue-shifted component that is naturally interpreted as emission from an outflowing wind. The latter is best modeled with a skewed Gaussian profile and becomes increasingly prominent at high $R_{\rm FeII}$ values, i.e., in extreme Population A quasars.

Population trends are striking at low z: large blueshifts of $v_{\rm r} < -1000$ km s^{-1} are observed almost exclusively in Population A sources, particularly those with FWHM(Hβ) $<$ 4000 km s^{-1} and strong FeII emission ($R_{\rm FeII} > 1$; Zamfir et al. 2010; Marziani et al. 2010; Richards et al. 2011). In contrast, Population B quasars rarely show strong CIV blueshifts (if we exclude very high luminosity sources), reinforcing the link between high $L/L_{\rm Edd}$ and the presence of radiatively driven winds.

At higher luminosities, large blueshifts persist. Near-infrared spectroscopy of 52 Hamburg–ESO quasars with $1 \lesssim z \lesssim 3$ and $\log L > 47$ erg/s (HE main sequence, HEMS sample) confirmed that strong CIV blueshifts are associated with high Eddington ratios rather than simply high black hole masses or luminosities

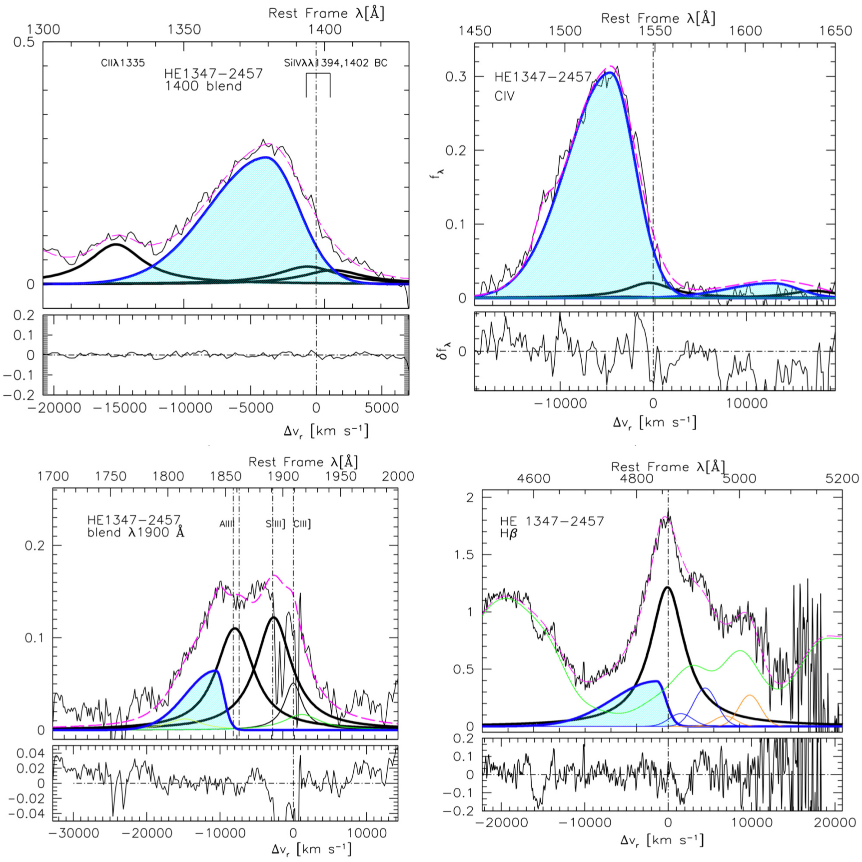

Figure 1. The continuum subtracted spectrum of the luminous Hamburg ESO Main Sequence (HEMS) quasar HE1347-2457, with an emphasis on the outflowing components of SiIVλ1397+OIV]λ1402, CIVλ1549, AlIIIλ1860, Hβ (cyan-shaded components).

(Marziani et al., 2018b; Richards et al., 2011; Giustini & Proga, 2019; Deconto-Machado et al., 2023, 2024). When viewed in the L/L_{Edd}–L and L/L_{Edd}–M_{BH} planes, blueshift amplitude is most clearly organized by accretion state, with Population A objects (above $L/L_{\mathrm{Edd}} \approx 0.2$) being wind-dominated (Marziani et al., 2016).

There is, however, a trend between outflow velocity and luminosity (Marziani et al., 2016; Sulentic et al., 2017). The scaling of outflow velocity with luminosity further supports a radiative-driving mechanism. Weak but consistent correlations ($v \propto L^{0.25}$) are in line with predictions from radiation-driven disk-wind models (Murray et al., 1995; Laor & Brandt, 2002; Proga, 2007b,a). Pop. B at high luminosity also show large blueshifts, up to a few thousands km s^{-1} (Sulentic et al., 2017). There is evidence of Pop. B outflows at luminosity lower than $\log L \sim 47$ erg/s (e.g., Richards et al. 2011; Marziani et al. 2022a). Since Pop. B shifts at low luminosity remain of small amplitude and difficult to measure, the considerations presented in this paper are meant for Pop. A and extreme Pop. A only.

An example of powerful wind-dominated quasar of the HEMS survey is shown in Fig. 1: the profiles of high ionization lines such as CIVand SiIVλ1397+ OIV]λ1402 are dominated by blueshifted emission associated with the outflows. In this rather extreme cases, the outflows also significantly affect Hβ and the AlIIIλ1860 lines. While the bolometric luminosity sets the available radiative power, it is the Eddington ratio that regulates the efficiency of wind launching and explains the prevalence of large blueshifts in high-$L/L_{\rm Edd}$ sources.

Taken together, the restrictions of large CIV blueshifts to Population A and extreme Population A sources reinforces the interpretation of the quasar main sequence as primarily driven by $L/L_{\rm Edd}$, with CIV outflows providing a direct tracer of radiative wind activity in the broad-line region.

3. Intermediate- and low-ionization lines: AlIIIλ1860 and MgIIλ2800

While the most dramatic blueshifts are observed in high-ionization lines such as CIV, intermediate- and low-ionization species also show systematic kinematic signatures that can provide complementary insights into quasar outflows.

3.1. AlIIIλ1860

The AlIIIλ1860 doublet, with intermediate ionization potential, generally shows only modest outflow signatures compared to CIV. Statistical analyses reveal that AlIIIλ1860 blueshifts are correlated with those of CIV but with a much shallower slope (≈0.1), indicating a less prominent wind contribution (Marziani et al., 2022b; Buendia-Rios et al., 2023). Quantitatively, the median centroid shift of AlIIIλ1860 follows the relation $c(\frac{1}{2})(\text{AlIII}) \approx (0.11 \pm 0.03)\ c(\frac{1}{2})(\text{CIV}) + (50 \pm 70)\ \text{km}\,\text{s}^{-1}$ (Marziani et al., 2022b), consistent with a weaker kinematic response of the intermediate-ionization gas. However, in the most extreme Population A quasars ($R_{\rm FeII} \gtrsim 1$), AlIII can display large blueshifts and asymmetric profiles comparable in strength to those of CIV, suggesting that under super-Eddington conditions the wind dominates across a broader ionization range.

3.2. MgIIλ2800

The MgIIλ2800 resonance doublet, one of the most widely used virial estimators of black hole mass (Marziani et al., 2013a), is typically far less affected by outflows (Trakhtenbrot & Netzer, 2012). Most quasars show symmetric and only weakly shifted MgII profiles. Nonetheless, careful spectral analysis has revealed subtle displacements of the line core, along with FWHM increases of a few hundred km s^{-1}, in the highest $L/L_{\rm Edd}$ extreme Pop. A sources (Marziani et al., 2013b). These modest but systematic shifts indicate that even low-ionization gas can participate in winds under conditions of extreme accretion.

Following Popović et al. (2019), MgIIλ2800 shows Lorentzian MgII profiles and also signatures of outflow, but these are present only in part of the line and not in every source, as already noted by Marziani et al. (2013a). Popović et al. (2019) argue that MgII consists of two kinematic pieces": (i) a core that behaves similarly to Hβ and appears virialized, and (ii) an additional "fountain-like" component, with motions roughly perpendicular to the disc, which produces the very broad wings and can reach shifts of a few thousand km s^{-1}. This second component may be associated with a photoionized "bowl" connecting the outer accretion disc and the inner torus (Goad et al., 2012), a configuration that is also consistent with a failed, radiatively accelerated, dusty wind (Czerny & Hryniewicz, 2011; Czerny et al., 2017; Naddaf et al., 2025). Since the fountain component does not correlate with the virial broadening estimators, it is interpreted as due to outflows/inflows rather than rotation.

This configuration can explain the Lorentzian wings of MgIIλ2800. It is, however, not intended to account for the net blueshift of the MgII line core reported by Marziani et al. (2013b) for the highest $L/L_{\rm Edd}$ sources. Those blueshifts are more naturally explained by a systematic line displacement, analogous to what is observed in CIVλ1549, although with a smaller amplitude.

3.3. Ionization potential and the hierarchy of shifts

In extreme Pop. A quasars, v(AlIII) $\approx 0.3\ v$(CIV) (and in some cases they are almost equal), while v(MgII) $\approx 0.1\ v$(CIV) (Marziani et al., 2013b; Buendia-Rios et al., 2025). The comparative behavior of CIVλ1549, AlIIIλ1860, and MgIIλ2800 therefore points to a simple trend: the higher the ionization potential of the line, the larger the blueshift. High-ionization lines such as CIV (IP $\approx$ 47.9 eV) show the largest shifts, often > -1000 km s^{-1} in extreme Pop. A sources. Intermediate-ionization AlIII (IP $\approx$ 28.4 eV) usually shows smaller shifts, but in the most extreme Pop. A quasars its outflow signature can approach that of CIV. In contrast, the low-ionization MgII doublet (IP $\approx$ 15 eV) shows only modest shifts, typically $\sim$10% of the CIVλ1549 amplitude (Marziani et al., 2013b, 2022b; Buendia-Rios et al., 2023, 2025). This ionization-stratified sequence matches the expectations of disk–wind models, in which the highest-ionization gas traces the fastest parts of the flow, while lower-ionization lines form deeper in the broad-line region, where motions are more nearly virial.

This stratification follows naturally if the high-ionization gas occupies the more accelerated layers of a radiatively driven disk wind close to the continuum source, whereas lower-ionization species arise farther out in the BLR (Murray et al., 1995; Proga, 2007b). In this picture, extreme Population A quasars lie in the regime where radiation pressure not only controls the dynamics of the highest-ionization gas but also has a measurable impact on intermediate- and even low-ionization lines.

4. Spectral energy distributions of high accretors and photoionization simulations

The interpretation of outflow signatures in high-accretion quasars requires a realistic description of their spectral energy distributions (SEDs). Recent works have established that quasars with high Eddington ratios ($L/L_{\rm Edd} \gtrsim 1$) and extreme FeII emission ($R_{\rm FeII} \gtrsim 1$) exhibit consistent and distinctive SEDs (Jin et al., 2012; Marziani & Sulentic, 2014; Ferland et al., 2020; Panda & Marziani, 2023; Garnica et al., 2025). We utilized the median SED derived from a sample of ≈150 low-redshift Pop. xA quasars (Garnica et al., 2025) as well as the high $L/L_{\rm Edd}$ SED from Jin et al. (2012), and we assume that the line emitting gas is exposed either to the unobscured continuum or continuum absorbed by a hot, dense layer of gas at $r \approx 200 r_{\rm g}$ (for $\approx 10^8$ $M_\odot$; $\log N_{\rm H} = 10^{23}$ cm^{-2}; $\log n_{\rm H} = 10^{11}$ cm^{-3}). A lower black hole mass 10^7 $M_\odot$ appropriate for NLSy1s would require a different, "harder" SED.

4.1. Radiatively driven outflows

Photoionization simulations highlight the conditions under which radiatively driven winds can be launched. Outflows are possible at relatively low column densities ($N_{\rm c} \approx 10^{21}$ cm^{-2}), where radiative acceleration exceeds gravity. The requirement that the force multiplier $M > 2$ translates into the condition M $(L/L_{\rm Edd}) > 1$ (see also Ferland et al., 2009; Netzer & Marziani, 2010). At higher column densities ($N_{\rm c} \approx 10^{24}$ cm^{-2}; Ferland & Persson 1989; Panda et al. 2020; Panda 2021), radiation fails to overcome gravity, and the gas remains bound. These results confirm that outflow efficiency is intimately tied to the accretion state and gas structure in the inner broad-line region.

4.2. Predicted emission luminosities and line ratios

The simulations further predict the radial stratification of outflow emission. CIVλ1549 emission is favored at smaller radii, AlIIIλ1860 at intermediate radii, and MgII at larger distances, reflecting both ionization potential and gas density conditions. The luminosities (L(CIV), L(AlIII), L(MgII)) define a narrow "corridor" of optimal ionization parameter where strong emission can be sustained (Fig. 2). The continuum luminosity at $\lambda = 3000$ Å has been assumed to be $\lambda L_\lambda(3000\text{Å}) \approx 4.2 \cdot 10^{44}$ erg/s. The hatched parts identify areas of the parameter plane where radiation forces are insufficient to drive an outflow; dark blue parts are regions where line emission is exceedingly low. The case shown here refers to a partially-absorbed high $L/L_{\rm Edd}$ Jin et al. (2012) continuum, with the absorber located at $r \approx 200 r_{\rm g}$. Due to the relative proximity of the

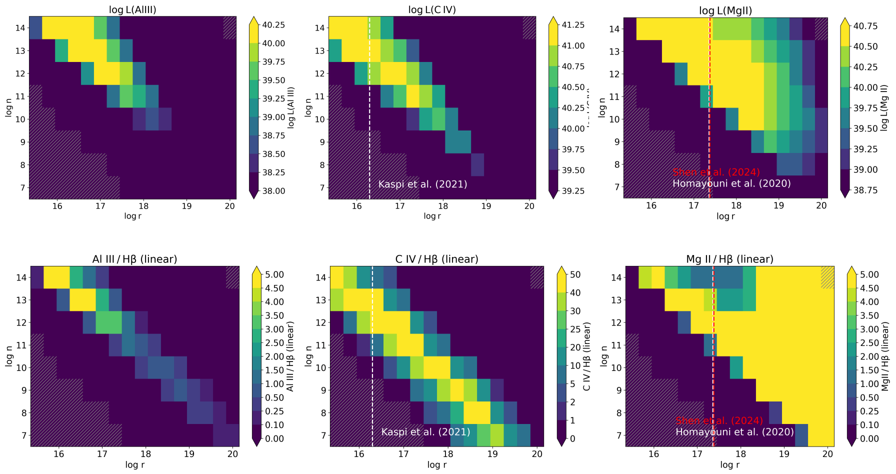

Figure 2. Behavior of line luminosity (top row) and intensity ratios with Hβ (bottom), for CIVλ1549, AlIIIλ1860, and MgIIλ2800 as a function of hydrogen density and radius, for a 10^8 solar masses black hole. The white vertical lines identify the radii measured according to the scaling laws of Kaspi et al. (2021) for CIVλ1549 and Homayouni et al. (2020); Shen et al. (2024) for MgIIλ2800.

absorber relative to the central continuum source, the absorbing gas remains hot and producing significant absorption only in the range between 1 and 10 keV. A fully unabsorbed Jin et al. (2012) continuum would give rise to similar trends.

The corridor peak, if considered at fixed density, is displaced toward larger radii for AlIII, and even more so for MgII with respect to CIV (top row of Fig. 2), as schematically emphasized in Fig. 3. Outside the corridor for CIV and AlIII emission, for radii smaller than the ones of the corridor, over-ionization suppresses line production, a behavior consistent with the observed weakness of CIVλ1549 in extreme Pop. A quasars (Kaspi et al., 2021). For larger radii, under-ionization depresses the emission of both CIVλ1549 and AlIIIλ1860. The behavior of MgIIλ2800 is different: strong emission and large MgIIλ2800/Hβ radii are possible over a wide range of radii that are however larger than the ones where AlIIIλ1860 and CIVλ1549 are maximized.

Predicted line ratios also provide critical tests (bottom panels of Fig. 2). For instance, `CLOUDY` simulations reproduce observed CIVλ1549/Hβ ratios $>$ 10–20

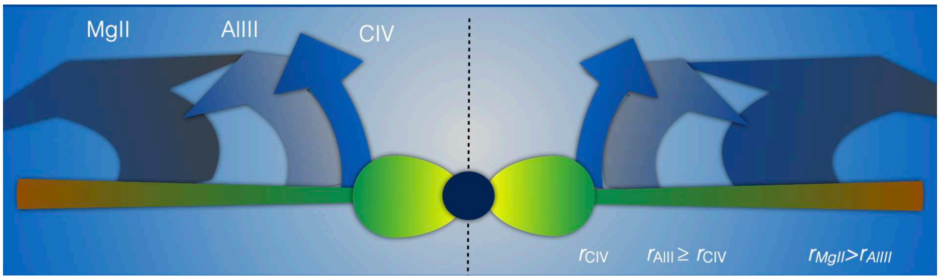

Figure 3. Sketch illustrating the differences in launching radii for the radiatively driven-wind emitting CIVλ1549, AlIIIλ1860, MgIIλ2800. The accretion disk around the central black hole is assumed to have an inner, puffed-up and optically thick region sustained by radiation pressure, as well as an outer thin, optically thick region. The various elements are not drawn to scale.

only under specific combinations of density and ionization, while MgIIλ2800/Hβ ratios match those measured in large quasar samples (Homayouni et al., 2022; Prince et al., 2023). The photoionization model therefore not only explains the ionization-dependent hierarchy of blueshifts (CIVλ1549 $>$ AlIIIλ1860 $>$ MgIIλ2800) but also constrains the physical conditions under which these outflows form.

5. Conclusions

Our analysis of emission-line shifts along the quasar main sequence reinforces the view that radiatively driven outflows are a ubiquitous feature of type-1 AGN. Outflow signatures are present even in single-epoch spectra, and they become dominant in high-ionization lines at high Eddington ratios and, more generally, at the highest luminosities ($L \gtrsim 10^{47}$ erg s^{-1}).

In terms of accretion mode, Pop. A AGN satisfying the criterion $L/L_{\mathrm{Edd}} > 0.1 - 0.2$ could be defined as black hole with an inner optically thick, geometrically thick region (c.f., Giustini & Proga, 2019). Among Population A sources, the amplitude of line blueshifts decreases systematically with ionization potential, from CIVλ1549 (C^{3+}) to AlIIIλ1860 and down to MgIIλ2800. While CIVλ1549 blueshifts can exceed several thousand km s^{-1}, MgIIλ2800 shows only subtle but measurable shifts, detectable mainly in extreme Pop. A quasars.

These trends are consistent with an ionization-stratified broad-line region, where higher ionization lines originate closer to the black hole in regions more directly exposed to radiation pressure (Figure 3).

Photoionization simulations with realistic high-accretor SEDs demonstrate that outflows can be launched over a wide range of radii if the column density remains low ($N_\mathrm{c} \approx 10^{21}$ cm^{-2}), whereas dense gas ($N_\mathrm{c} \approx 10^{24}$ cm^{-2}) remains gravitationally bound. These models reproduce both the hierarchy of shift amplitudes (CIV > AlIII > MgII) and the reverberation-mapped radii of CIVλ1549 and MgIIλ2800 (Homayouni et al., 2020; Khadka et al., 2021; Cao et al., 2022; Shen et al., 2024), providing a physically consistent picture that links SED shape, BLR stratification, and wind dynamics.

Acknowledgements.

S. P. is supported by the international Gemini Observatory, a program of NSF NOIRLab, which is managed by the Association of Universities for Research in Astronomy (AURA) under a cooperative agreement with the U.S. National Science Foundation, on behalf of the Gemini partnership of Argentina, Brazil, Canada, Chile, the Republic of Korea, and the United States of America. A. del Olmo and A. Deconto-Machado acknowledge financial support from the grant PID2022-140871NB-C21 funded by MCIN/AEI/10.13039/501100011033 and by 'ERDF A way of making Europe', and through the Center of Excelence Severo Ochoa grant CEX2021- 515001131-S of the IAA funded by MCIN/AEI/10.13039/501100011033.

References

Boroson, T. A., Black Hole Mass and Eddington Ratio as Drivers for the Observable Properties of Radio-loud and Radio-quiet QSOs. 2002, *ApJ*, **565**, 78, `DOI:HEmain10.1086/324486`

Boroson, T. A. & Green, R. F., The Emission-Line Properties of Low-Redshift Quasi-stellar Objects. 1992, *ApJS*, **80**, 109, `DOI:10.1086/191661`

Buendia-Rios, T. M., Marziani, P., Negrete, C. A., & Dultzin, D., Large Binocular Telescope infrared observations of candidate super-Eddington quasars. 2025, *MNRAS*, **540**, 562, `DOI:10.1093/mnras/staf694`

Buendia-Rios, T. M., Negrete, C. A., Marziani, P., & Dultzin, D., Statistical analysis of Al III and C III] emission lines as virial black hole mass estimators in quasars. 2023, *A&Ap*, **669**, A135, `DOI:10.1051/0004-6361/202244177`

Cao, S., Zajaček, M., Panda, S., et al., Standardizing reverberation-measured C IV time-lag quasars, and using them with standardized Mg II quasars to constrain cosmological parameters. 2022, *MNRAS*, **516**, 1721, `DOI:10.1093/mnras/stac2325`

Corbin, M. R. & Boroson, T. A., Combined Ultraviolet and Optical Spectra of 48 Low-Redshift QSOs and the Relation of the Continuum and Emission-Line Properties. 1996, *ApJS*, **107**, 69, `DOI:10.1086/192355`

Czerny, B. & Hryniewicz, K., The origin of the broad line region in active galactic nuclei. 2011, *A&Ap*, **525**, L8, `DOI:10.1051/0004-6361/201016025`

Czerny, B., Li, Y.-R., Hryniewicz, K., et al., Failed Radiatively Accelerated Dusty Outflow Model of the Broad Line Region in Active Galactic Nuclei. I. Analytical Solution. 2017, *ApJ*, **846**, 154, `DOI:10.3847/1538-4357/aa8810`

Deconto-Machado, A., del Olmo, A., & Marziani, P., Exploring the links between quasar winds and radio emission along the main sequence at high redshift. 2024, *A&Ap*, **691**, A15, `DOI:10.1051/0004-6361/202449976`

Deconto-Machado, A., del Olmo Orozco, A., Marziani, P., Perea, J., & Stirpe, G. M., High-redshift quasars along the main sequence. 2023, *A&Ap*, **669**, A83, `DOI:10.1051/0004-6361/202243801`

Du, P., Zhang, Z.-X., Wang, K., et al., Supermassive Black Holes with High Accretion Rates in Active Galactic Nuclei. IX. 10 New Observations of Reverberation Mapping and Shortened Hβ Lags. 2018, *ApJ*, **856**, 6, `DOI:10.3847/1538-4357/aaae6b`

Ferland, G. J., Done, C., Jin, C., Landt, H., & Ward, M. J., State-of-the-art AGN SEDs for photoionization models: BLR predictions confront the observations. 2020, *MNRAS*, **494**, 5917, `DOI:10.1093/mnras/staa1207`

Ferland, G. J., Hu, C., Wang, J., et al., Implications of Infalling Fe II-Emitting Clouds in Active Galactic Nuclei: Anisotropic Properties. 2009, *ApJL*, **707**, L82, `DOI:10.1088/0004-637X/707/1/L82`

Ferland, G. J. & Persson, S. E., Implications of CA II emission for physical conditions in the broad-line region of active galactic nuclei. 1989, *ApJ*, **347**, 656, `DOI:10.1086/168156`

Fraix-Burnet, D., Marziani, P., D'Onofrio, M., & Dultzin, D., The Phylogeny of Quasars and the Ontogeny of Their Central Black Holes. 2017, *Frontiers in Astronomy and Space Sciences*, **4**, 1, `DOI:10.3389/fspas.2017.00001`

Garnica, K., Dultzin, D., Marziani, P., & Panda, S., The spectral energy distribution of extreme population A quasars. 2025, *MNRAS*, **540**, 3289, `DOI:10.1093/mnras/staf862`

Gaskell, C. M., Galactic mergers, starburst galaxies, quasar activity and massive binary black holes. 1985, *Nature*, **315**, 386, `DOI:10.1038/315386a0`

Giustini, M. & Proga, D., A global view of the inner accretion and ejection flow around super massive black holes. Radiation-driven accretion disk winds in a physical context. 2019, *A&Ap*, **630**, A94, `DOI:10.1051/0004-6361/201833810`

Goad, M. R., Korista, K. T., & Ruff, A. J., The broad emission-line region: the confluence of the outer accretion disc with the inner edge of the dusty torus. 2012, *MNRAS*, **426**, 3086, `DOI:10.1111/j.1365-2966.2012.21808.x`

Homayouni, Y., Sturm, M. R., Trump, J. R., et al., The Sloan Digital Sky Survey Reverberation Mapping Project: UV-Optical Accretion Disk Measurements with the Hubble Space Telescope. 2022, *ApJ*, **926**, 225, `DOI:10.3847/1538-4357/ac478b`

Homayouni, Y., Trump, J. R., Grier, C. J., et al., The Sloan Digital Sky Survey Reverberation Mapping Project: Mg II Lag Results from Four Years of Monitoring. 2020, *ApJ*, **901**, 55, `DOI:10.3847/1538-4357/ababa9`

Jin, C., Ward, M., Done, C., & Gelbord, J., A combined optical and X-ray study of unobscured type 1 active galactic nuclei - I. Optical spectra and spectral energy distribution modelling. 2012, *MNRAS*, **420**, 1825, DOI:10.1111/j.1365-2966.2011.19805.x

Kaspi, S., Brandt, W. N., Maoz, D., et al., Taking a Long Look: A Two-Decade Reverberation Mapping Study of High-Luminosity Quasars. 2021, *arXiv e-prints*, arXiv:2106.00691

Khadka, N., Yu, Z., Zajaček, M., et al., Standardizing reverberation-measured Mg II time-lag quasars, by using the radius-luminosity relation, and constraining cosmological model parameters. 2021, *MNRAS*, **508**, 4722, DOI:10.1093/mnras/stab2807

Laor, A. & Brandt, W. N., The Luminosity Dependence of Ultraviolet Absorption in Active Galactic Nuclei. 2002, *ApJ*, **569**, 641, DOI:10.1086/339476

Leighly, K. M. & Moore, J. R., Hubble Space Telescope STIS Ultraviolet Spectral Evidence of Outflow in Extreme Narrow-Line Seyfert 1 Galaxies. I. Data and Analysis. 2004, *ApJ*, **611**, 107, DOI:10.1086/422088

Marziani, P., Accretion/Ejection Phenomena and Emission-Line Profile (A)symmetries in Type-1 Active Galactic Nuclei. 2023, *Symmetry*, **15**, 1859, DOI:10.3390/sym15101859

Marziani, P., Deconto-Machado, A., & Del Olmo, A., Isolating an Outflow Component in Single-Epoch Spectra of Quasars. 2022a, *Galaxies*, **10**, 54, DOI:10.3390/galaxies10020054

Marziani, P., del Olmo, A., D'Onofrio, M., et al., Narrow-line Seyfert 1s: what is wrong in a name? 2018a, in Proceedings of Science, Vol. **PoS(NLS1-2018)**, *Revisiting narrow-line Seyfert 1 galaxies and their place in the Universe. 9-13 April 2018. Padova Botanical Garden, Italy. Online at ¡A href="https://pos.sissa.it/cgi-bin/reader/conf.cgi?confid=328"¿https://pos.sissa.it/cgi-bin/reader/conf.cgi?confid=328¡/A¿, id.2* (SISSA/ISAS), 002

Marziani, P., Dultzin, D., Sulentic, J. W., et al., A main sequence for quasars. 2018b, *Frontiers in Astronomy and Space Sciences*, **5**, 6, DOI:10.3389/fspas.2018.00006

Marziani, P., Garnica Luna, K., Floris, A., et al., Super-Eddington Accretion in Quasars. 2025, *Universe*, **11**, 69, DOI:10.3390/universe11020069

Marziani, P., Martínez Carballo, M. A., Sulentic, J. W., et al., The most powerful quasar outflows as revealed by the Civ λ1549 resonance line. 2016, *ApSS*, **361**, 29, DOI:10.1007/s10509-015-2611-1

Marziani, P., Olmo, A. d., Negrete, C. A., et al., The Intermediate-ionization Lines as Virial Broadening Estimators for Population A Quasars. 2022b, *ApJS*, **261**, 30, DOI:10.3847/1538-4365/ac6fd6

Marziani, P. & Sulentic, J. W., Highly accreting quasars: sample definition and possible cosmological implications. 2014, *MNRAS*, **442**, 1211, DOI:10.1093/mnras/stu951

Marziani, P., Sulentic, J. W., Dultzin-Hacyan, D., Calvani, M., & Moles, M., Comparative Analysis of the High- and Low-Ionization Lines in the Broad-Line Region of Active Galactic Nuclei. 1996, *ApJS*, **104**, 37, DOI:10.1086/192291

Marziani, P., Sulentic, J. W., Negrete, C. A., et al., Broad-line region physical conditions along the quasar eigenvector 1 sequence. 2010, *MNRAS*, **409**, 1033, `DOI:10.1111/j.1365-2966.2010.17357.x`

Marziani, P., Sulentic, J. W., Plauchu-Frayn, I., & del Olmo, A., Is Mg II 2800 a Reliable Virial Broadening Estimator for Quasars? 2013a, *AAp*, **555**, 89, 16pp

Marziani, P., Sulentic, J. W., Plauchu-Frayn, I., & del Olmo, A., Low-Ionization Outflows in High Eddington Ratio Quasars. 2013b, *ApJ*, **764**

Marziani, P., Sulentic, J. W., Stirpe, G. M., Zamfir, S., & Calvani, M., VLT/ISAAC spectra of the Hβ region in intermediate-redshift quasars. III. Hβ broad-line profile analysis and inferences about BLR structure. 2009, *A&Ap*, **495**, 83, `DOI:10.1051/0004-6361:200810764`

Marziani, P., Sulentic, J. W., Zwitter, T., Dultzin-Hacyan, D., & Calvani, M., Searching for the Physical Drivers of the Eigenvector 1 Correlation Space. 2001, *ApJ*, **558**, 553, `DOI:10.1086/322286`

Murray, N., Chiang, J., Grossman, S. A., & Voit, G. M., Accretion Disk Winds from Active Galactic Nuclei. 1995, *ApJ*, **451**, 498, `DOI:10.1086/176238`

Naddaf, M. H., Martínez-Aldama, M. L., Marziani, P., Czerny, B., & Hutsemékers, D., Quasar main sequence unfolded by 2.5D FRADO: Natural expression of Eddington ratio, black hole mass, and inclination. 2025, *A&Ap*, **702**, L13, `DOI:10.1051/0004-6361/202556852`

Netzer, H. & Marziani, P., The Effect of Radiation Pressure on Emission-line Profiles and Black Hole Mass Determination in Active Galactic Nuclei. 2010, *ApJ*, **724**, 318, `DOI:10.1088/0004-637X/724/1/318`

Panda, S., The CaFe project: Optical Fe II and near-infrared Ca II triplet emission in active galaxies: simulated EWs and the co-dependence of cloud size and metal content. 2021, *A&Ap*, **650**, A154, `DOI:10.1051/0004-6361/202140393`

Panda, S., Unveiling the quasar main sequence: illuminating the complexity of active galactic nuclei and their evolution. 2024, *Frontiers in Astronomy and Space Sciences*, **11**, 1479874, `DOI:10.3389/fspas.2024.1479874`

Panda, S., Małek, K., Śniegowska, M., & Czerny, B., Strong FeII emission in NLS1s: An unsolved mystery. 2020, in IAU Symposium, Vol. **341**, *Panchromatic Modelling with Next Generation Facilities*, ed. M. Boquien, E. Lusso, C. Gruppioni, & P. Tissera, 297–298

Panda, S. & Marziani, P., High Eddington quasars as discovery tools: current state and challenges. 2023, *Frontiers in Astronomy and Space Sciences*, **10**, 1130103, `DOI:10.3389/fspas.2023.1130103`

Panda, S., Marziani, P., & Czerny, B., The Quasar Main Sequence Explained by the Combination of Eddington Ratio, Metallicity, and Orientation. 2019, *ApJ*, **882**, 79, `DOI:10.3847/1538-4357/ab3292`

Popović, L. Č., Kovačević-Dojčinović, J., & Marčeta-Mand ić, S., The structure of the Mg II broad line emitting region in Type 1 AGNs. 2019, *MNRAS*, **484**, 3180, `DOI:10.1093/mnras/stz157`

Prince, R., Zajaček, M., Panda, S., et al., Wavelength-resolved reverberation mapping of intermediate-redshift quasars HE 0413-4031 and HE 0435-4312: Dissecting Mg II, optical Fe II, and UV Fe II emission regions. 2023, *A&Ap*, **678**, A189, DOI:10.1051/0004-6361/202346738

Proga, D., Dynamics of Accretion Flows Irradiated by a Quasar. 2007a, *ApJ*, **661**, 693, DOI:10.1086/515389

Proga, D., Theory of Winds in AGNs. 2007b, in Astronomical Society of the Pacific Conference Series, Vol. **373**, *The Central Engine of Active Galactic Nuclei*, ed. L. C. Ho & J.-W. Wang, 267

Rakshit, S., Stalin, C. S., & Kotilainen, J., Spectral Properties of Quasars from Sloan Digital Sky Survey Data Release 14: The Catalog. 2020, *ApJS*, **249**, 17, DOI:10.3847/1538-4365/ab99c5

Richards, G. T., Kruczek, N. E., Gallagher, S. C., et al., Unification of Luminous Type 1 Quasars through C IV Emission. 2011, *AJ*, **141**, 167, DOI:10.1088/0004-6256/141/5/167

Shen, Y., Grier, C. J., Horne, K., et al., The Sloan Digital Sky Survey Reverberation Mapping Project: Key Results. 2024, *ApJS*, **272**, 26, DOI:10.3847/1538-4365/ad3936

Shen, Y. & Ho, L. C., The diversity of quasars unified by accretion and orientation. 2014, *Nature*, **513**, 210, DOI:10.1038/nature13712

Sulentic, J., Marziani, P., & Zamfir, S., The Case for Two Quasar Populations. 2011, *Baltic Astronomy*, **20**, 427

Sulentic, J. W., Bachev, R., Marziani, P., Negrete, C. A., & Dultzin, D., C IV λ1549 as an Eigenvector 1 Parameter for Active Galactic Nuclei. 2007, *ApJ*, **666**, 757, DOI:10.1086/519916

Sulentic, J. W., del Olmo, A., Marziani, P., et al., What does CIVλ1549 tell us about the physical driver of the Eigenvector quasar sequence? 2017, *A&Ap*, **608**, A122, DOI:10.1051/0004-6361/201630309

Sulentic, J. W., Marziani, P., & Dultzin-Hacyan, D., Phenomenology of Broad Emission Lines in Active Galactic Nuclei. 2000a, *ARA&A*, **38**, 521, DOI:10.1146/annurev.astro.38.1.521

Sulentic, J. W., Marziani, P., Zamanov, R., et al., Average Quasar Spectra in the Context of Eigenvector 1. 2002, *ApJL*, **566**, L71, DOI:10.1086/339594

Sulentic, J. W., Marziani, P., Zwitter, T., Dultzin-Hacyan, D., & Calvani, M., The Demise of the Classical Broad-Line Region in the Luminous Quasar PG 1416-129. 2000b, *ApJL*, **545**, L15, DOI:10.1086/317330

Sulentic, J. W., Zwitter, T., Marziani, P., & Dultzin-Hacyan, D., Eigenvector 1: An Optimal Correlation Space for Active Galactic Nuclei. 2000c, *ApJL*, **536**, L5, DOI:10.1086/312717

Sun, J. & Shen, Y., Dissecting the Quasar Main Sequence: Insight from Host Galaxy Properties. 2015, *ApJL*, **804**, L15, DOI:10.1088/2041-8205/804/1/L15

Trakhtenbrot, B. & Netzer, H., Black hole growth to z = 2 - I. Improved virial methods for measuring M_{BH} and L/L_{Edd}. 2012, *MNRAS*, **427**, 3081, DOI:10.1111/j.1365-2966.2012.22056.x

Wang, J.-M., Du, P., Valls-Gabaud, D., Hu, C., & Netzer, H., Super-Eddington Accreting Massive Black Holes as Long-Lived Cosmological Standards. 2013, *Physical Review Letters*, **110**, 081301, DOI:10.1103/PhysRevLett.110.081301

Wu, Q. & Shen, Y., A Catalog of Quasar Properties from Sloan Digital Sky Survey Data Release 16. 2022, *ApJS*, **263**, 42, DOI:10.3847/1538-4365/ac9ead

York, D. G., Adelman, J., Anderson, John E., J., et al., The Sloan Digital Sky Survey: Technical Summary. 2000, *AJ*, **120**, 1579, DOI:10.1086/301513

Zamfir, S., Sulentic, J. W., Marziani, P., & Dultzin, D., Detailed characterization of Hβ emission line profile in low-z SDSS quasars. 2010, *MNRAS*, **403**, 1759, DOI:10.1111/j.1365-2966.2009.16236.x

Contrib. Astron. Obs. Skalnaté Pleso **56/1**, 102 – 111, (2026)
https://doi.org/10.31577/caosp.2026.56.1.102

Ca II and O I as precision probes of the broad-line region in AGN

M.W. Ochmann[1], **M.A. Probst**[1], **W. Kollatschny**[1], **L. Diehl**[1], **E.M. Cackett**[2], **D. Chelouche**[3,4], **R. Chini**,[5,6], **D. Grupe**[7], **M. Haas**[5], **K. Horne**[8], **S. Kaspi**[9] and **S. Komossa**[10]

[1] *Institut für Astrophysik und Geophysik, Universität Göttingen, Friedrich-Hund-Platz 1, 37077 Göttingen, Germany (E-mail: martin.ochmann@uni-goettingen.de)*

[2] *Department of Physics and Astronomy, Wayne State University, 666 W. Hancock Street, Detroit, MI 48201, USA*

[3] *Department of Physics, Faculty of Natural Sciences, University of Haifa, Haifa 3498838, Israel*

[4] *Haifa Research Center for Theoretical Physics and Astrophysics, University of Haifa, Haifa 3498838, Israel*

[5] *Ruhr University Bochum, Faculty of Physics and Astronomy, Astronomical Institute (AIRUB), 44780 Bochum, Germany*

[6] *Nicolaus Copernicus Astronomical Center, Polish Academy of Sciences, Bartycka 18, 00-716 Warszawa, Poland*

[7] *Department of Physics, Geology, and Engineering Technology, Northern Kentucky University, 1 Nunn Drive, Highland Heights, KY 41099, USA*

[8] *SUPA Physics and Astronomy, University of St. Andrews, Fife, KY16 9SS, United Kingdom*

[9] *School of Physics & Astronomy and the Wise Observatory, The Raymond and Beverly Sackler Faculty of Exact Sciences, Tel-Aviv University, Tel-Aviv 6997801, Israel*

[10] *Max-Planck-Institut für Radioastronomie, Auf dem Hügel 69, 53121 Bonn, Germany*

Received: October 1, 2025; Accepted: October 25, 2025

Abstract. Ca II and O I emission lines in active galactic nuclei (AGN) have been used as powerful diagnostic probes of the broad-line region (BLR) for the past 40 years. In particular, line ratio diagnostics have been used to constrain the physical conditions in the low-ionization phase of the BLR, while line width measurements have provided rough constraints on the location of the emission region relative to the Balmer-emitting phase of the BLR. However, due to limited observational capabilities, detailed line-profile studies of these lines—directly linking Ca II and O I with structural BLR models—have only become possible very recently. Here, we present an overview of our most recent study that has enabled investigations of Ca II and O I emission lines in unprecedented detail, directly linking Ca II triplet emission profiles to the kinematics of a rotating disk. We focus on our results for NGC 4593, but we also provide an outlook on how Ca II and O I open up a new observational window to probe the low-ionization part of the BLR in general.

Key words: NGC 4593 – active galactic nuclei – broad-line region – double-peaked emitter – reverberation mapping

1. Introduction

The O I emission lines and the Ca II triplet ($\lambda\lambda 8498, 8542, 8662$) have long been recognized as powerful diagnostic tools of the physical conditions and excitation mechanisms in active galactic nuclei (AGN). Early foundational works include studies by Grandi (1980, 1983), Persson & McGregor (1985); Persson (1988), Ferland & Persson (1989), and Joly (1989). Strong similarities between the emission-line profiles of these species have been firmly established (Persson, 1988; Rodríguez-Ardila et al., 2002a; Matsuoka et al., 2007) and are interpreted as evidence that the Ca II and O I emitting regions are largely co-spatial and share similar physical conditions. Later studies have adopted a unified view of the two species (e.g., Matsuoka et al., 2008; Marziani et al., 2013; Martínez-Aldama et al., 2015, 2021).

Given the inferred similarity in the physical conditions for Ca II and O I, a central question is where within the BLR these low-ionization lines are emitted. Answers to this question were already given in the earliest studies of Ca II in AGN: Persson (1988) noted that if Ca II triplet emission is observed in AGN, the triplet ratio is usually 1:1:1, indicating that the emission region is optically thick in Ca II. Model calculations later confirmed this conclusion by means of photoionization calculations that placed the emitting region in a cool and dense gas with temperatures of $T \leq 8000\,\mathrm{K}$, densities of $n_H \simeq 10^{12}\,\mathrm{cm}^{-3}$, and column densities of $N_H \geq 10^{23}\,\mathrm{cm}^{-2}$ (Ferland & Persson, 1989; Joly, 1989; Matsuoka et al., 2007). Such physical conditions are characteristic of an outer, cold accretion disk, with Ferland & Persson (1989) and later Dultzin-Hacyan et al. (1999) linking the Ca II emission to a wind or corona above the disk.

However, despite evidence that Ca II emission—and O I emission, for that matter—is closely tied to the atmosphere of an outer accretion disk, disk-line profiles (Chen & Halpern, 1989; Eracleous et al., 1995, 2009) of these species had remained elusive until very recently. Dias dos Santos et al. (2023) reported, for the first time, the detection of a double-peaked O I profile—that of O I λ11287—in the near-infrared spectrum of III Zw 002. Shortly after, Ochmann et al. (2024) reported the detection of double-peaked O I λ8446 as well as of double-peaked near-infrared Ca II triplet profiles in a transient spectrum of NGC 1566. This detection was followed by the detection of double-peaked O I λ8446 and Ca II triplet emission in a non-transient spectrum of NGC 4593 (Ochmann et al., 2025). Here, we summarize the key results of Ochmann et al. (2025) and discuss how future studies of O I and Ca II emission could help to advance our understanding of the BLR.

2. Observations of NGC 4593

NGC 4593 is a local ($z = 0.008312$) face-on Seyfert galaxy, which has been extensively studied in past variability campaigns (e.g., Dietrich et al., 1994; Santos-Lleo et al., 1995; Kollatschny & Dietrich, 1997; Denney et al., 2006; Barth et al., 2015; McHardy et al., 2018; Cackett et al., 2018). The detection of double-peaked O I and Ca II in NGC 4593 was made from a spectrum obtained with VLT/MUSE (Multi Unit Spectroscopic Explorer; Bacon et al., 2010, 2014) IFU spectrograph as part of the ESO program 0103.B-0908 (PI: Knud Jahnke) on 2019 April 28, with a total exposure time of 4800 s. Further details on the observations and data reduction are provided in Ochmann et al. (2025).

3. Results

We analyzed the VLT/MUSE spectrum of NGC 4593 and identified, for the first time, double-peaked profiles in both O I λ8446 and the Ca II triplet. We performed a detailed decomposition of the near-infrared O I λ8446 and Ca II triplet blend in the MUSE spectrum. We assumed identical line profiles of the Ca II triplet lines and used the unblended red wing of the Ca II λ8662 profile as a template for the red wing of Ca II λ8542. In this way, we were able to reconstruct a clean Ca II λ8662 profile, which was used for the final decomposition of the line blend shown in Fig. 1, resulting in a clean, unblended O I λ8446 profile.

The extracted line profiles of O I and Ca II are double-peaked with a full width at half maximum (FWHM) of $\sim 3700\,\mathrm{km\,s^{-1}}$. They exhibit a redward asymmetry with a red-to-blue peak ratio of 4:3. The intensity ratio of the Ca II lines is 1:1:1, suggesting a high-density emission zone in the BLR. The Ca II emission lines show no evidence of a central narrow or intermediate-width component. The profiles of Ca II and O I are remarkably similar, and we especially note the particular similarity in the red wings of both lines. Overall, the similarity between the O I λ8446 and Ca II lines suggests a very similar, overlapping emission region for both line species.

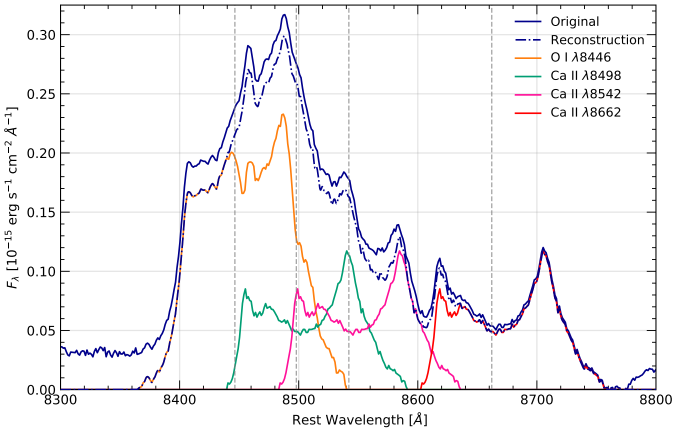

Figure 1. Decomposition of the blended O I λ8446 and Ca II triplet emission lines using the reconstructed Ca II λ8662 profile as a template for all Ca II lines. The difference between original spectrum and reconstructed blend is due to the subtraction of a linear pseudo-continuum beneath each emission line. The central wavelengths of the emission lines are indicated by dashed lines. Data taken from Ochmann et al. (2025).

To test how well the observed double-peaked Ca II profile agrees with predictions from line-emitting, non-axisymmetric accretion disk models, we fitted the profile with the elliptical disk-line model of Eracleous et al. (1995), which has seven free parameters: the inner and outer pericenter distance ξ_1 and ξ_2, the inclination angle i, the major axis orientation ϕ_0, the broadening parameter σ, the disk eccentricity e, and the emissivity power-law index q. The best-fit results are given in Table 1. For details on the fitting procedure see Ochmann et al. (2025).

Table 1. Best-fit parameters for the Ca II λ8662 profile obtained by applying the elliptical line-emitting accretion disk model.

Profile	ξ_1 [r_g]	ξ_2 [r_g]	i [deg]	ϕ_0 [deg]	σ [$\mathrm{km\,s^{-1}}$]	e	q
Ca II λ8662	320^{+9}_{-10}	1103^{+29}_{-33}	$10.8^{+0.1}_{-0.1}$	$57.1^{+1.6}_{-1.1}$	65^{+11}_{-8}	$0.22^{+0.01}_{-0.01}$	$-1.27^{+0.05}_{-0.05}$

We find that the double-peaked Ca II λ8662 profile is in good agreement with emission from a non-axisymmetric disk with an eccentricity of $e \sim 0.22$, confined within $\sim 320 - 1100\,\mathrm{r_g}$, and with an inclination of $\sim 11°$. We particularly point out the remarkably low internal turbulence of only $\sigma \sim 65\,\mathrm{km\,s^{-1}}$. This is the lowest value reported for an AGN emission line to date and is significantly lower than typical values obtained for Balmer lines in other sources (e.g., Strateva et al., 2003; Ward et al., 2024).

4. Conclusions from Ochmann et al. (2025)

The emission-line profiles of the Ca II triplet can be well reproduced with the elliptical line-emitting accretion disk model, yielding a rather sharply defined disk (between $\sim 320 - 1100\,\mathrm{r_g}$) with a small eccentricity of $e \sim 0.22$. This is only the second time—after the case of NGC 1566, for which the first double-peaked profiles of the Ca II triplet were reported by Ochmann et al. (2024)—that double-peaked profiles of Ca II have been found[1], linking the Ca II-emitting region directly to the kinematics of a rotating disk, thus bridging the gap to predictions from photoionization calculations (Ferland & Persson, 1989; Joly, 1989) that place this region in the wind or corona of an outer accretion disk. We especially point out the low internal turbulence in Ca II observed for both NGC 4593 and NGC 1566, consistent with high kinematic ordering close to the mid-plane of the disk. This suggests that line broadening in Ca II is primarily due to Keplerian rotation with only minor contributions from turbulence, making these emission lines a valuable tool for studying the BLR by being able to directly trace its kinematics. Such an undisturbed view of BLR dynamics offers great potential for refining BLR models and testing scenarios of complex gas motion, including, for instance, supermassive black hole binaries (SMBHBs) (e.g., Popović, 2012). Obtaining and modeling such high-fidelity line profiles, however, requires data of the highest quality—i.e., with sufficient signal-to-noise ratio, spectral resolution, and a small enough aperture to avoid host-galaxy absorption affecting the Ca II profiles—in order to recover clean line profiles of Ca II and O I.

5. Outlook & Future Prospects

The first detections of clean disk-line profiles in Ca II $\lambda\lambda 8498, 8542, 8662$ and O I $\lambda 8446$ demonstrate the potential of detailed line-profile studies of these low-ionization lines. Further high-quality observations of Ca II and O I emission in additional sources are strongly encouraged to establish these transitions as a novel probe of BLR structure and geometry in AGN. We stress that complex Ca II and O I emission features are already visible in published data (e.g., Persson, 1988; Garcia-Rissmann et al., 2005; Landt et al., 2008), which motivates a closer reinspection of archival spectra to search for further signatures of disk-line or complex emitters.

---

[1] We note that the double-peaked feature in the Ca II triplet is also discernible in spectra of NGC 4593 already presented by Garcia-Rissmann et al. (2005) and Landt et al. (2008), but had not been recognized until now.

A particularly valuable next step would be reverberation mapping (RM) campaigns of Ca II and O I, especially in AGN exhibiting disk-line profiles (Ochmann et al., submitted). Although RM campaigns exist for other low-ionization lines such as the Balmer series or Mg II λ2800 (e.g., Shen et al., 2016; Czerny et al., 2019), there are so far no dedicated monitoring programs for Ca II or O I. Measuring their lags and velocity-resolved responses would directly link the double-peaked profiles to the size and geometry of the emitting region, thereby testing a disk-plane origin and possible vertical stratification within the BLR through comparison with the RM signatures of other lines.

Notably, Lyβ pumping is assumed to be the dominant excitation mechanism of O I λ8446 in many AGN (e.g., Rudy et al., 1989; Rodríguez-Ardila et al., 2002b; Landt et al., 2008). Therefore, if a variable signal in O I were detected in a source where Lyβ pumping dominates, its variability would likely be causally linked to changes in the Lyβ flux.[2] We propose that this could be utilized in future campaigns to study the structure of the BLR, in particular its vertical stratification: For large enough BLRs, differences between the delay chains from the continuum → Lyα/Lyβ → O I and that from the continuum → Hα/Hβ in light-travel time may become measurable, provided that the different excitation channels operate on spatial scales comparable to the observational cadence. In this framework, the Lyβ line effectively acts as an intermediate reprocessor, introducing an additional delay channel beyond the direct continuum response and thereby allowing a new diagnostic handle on vertical BLR geometry. More precisely, if the bulk of the Lyα/Lyβ emission is generated at some distance from the ionizing source, but not directly along the line of sight to O I or Hα/Hβ, which “see” the ionizing continuum, then the light-travel path from the continuum source via Lyα/Lyβ to O I or Hα is longer than the direct path from the continuum source to O I or Hα. The basic principle of this reverberation mapping utilizing two different, spatially offset drivers, namely the ionizing continuum and the pumping line, is shown in Fig. 2 for a planar BLR geometry with an assumed vertical stratification.

We emphasize that this is a rather simplified picture—for instance, it does not account for the spatial extent of the Lyα/Lyβ-emitting region or the covering factors of the individual BLR phases—but we propose that, depending on the exact geometry, such an approach could convey information about the scale-height-dependent BLR structure.

Acknowledgements. We are grateful to Peter M. Weilbacher for reducing the VLT/MUSE observations of NGC 4593. MWO acknowledges the support of the German Aerospace Center (DLR) within the framework of the “Verbundforschung Astronomie und Astrophysik” through grant 50OR2305 with funds from the BMWK. PMW was partially supported by the BMBF through the ErUM program (VLT-BlueMUSE 05A23BAC). EMC gratefully acknowledges support for program number

---

[2] In practice, Lyα may serve as a useful proxy for Lyβ, as Lyβ is observationally more challenging to access.

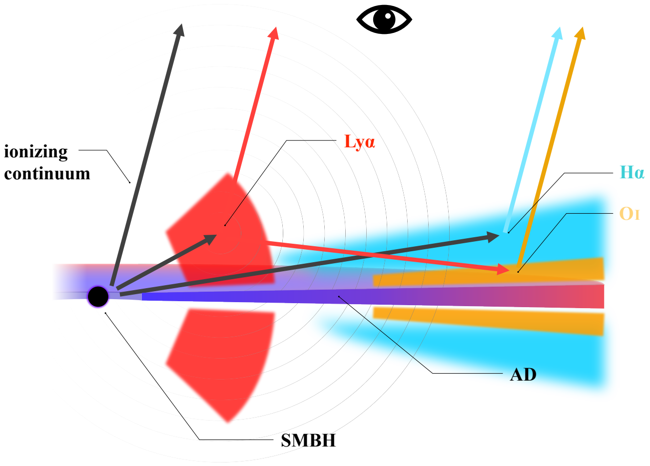

Figure 2. The basic principle of reverberation mapping of a Lyα/Lyβ-pumped emission line such as O I λ8446 for an almost planar BLR geometry with assumed vertical stratification. See text for details. The individual components are not to scale.

14121 provided by NASA through a grant from the Space Telescope Science Institute, which is operated by the Association of Universities for Research in Astronomy, Incorporated, under NASA contract NAS5-26555. Research by DC is partly supported by the Israeli Science Foundation (1650/23). The authors greatly acknowledge support by the DFG grants KO 857/35-1, KO 857/35-2 and CH 71/34-3.

References

Bacon, R., Accardo, M., Adjali, L., et al., The MUSE second-generation VLT instrument. 2010, in Society of Photo-Optical Instrumentation Engineers (SPIE) Conference Series, Vol. **7735**, *Ground-based and Airborne Instrumentation for Astronomy III*, 773508

Bacon, R., Vernet, J., Borisova, E., et al., MUSE Commissioning. 2014, *The Messenger*, **157**, 13

Barth, A. J., Bennert, V. N., Canalizo, G., et al., The Lick AGN Monitoring Project 2011: Spectroscopic Campaign and Emission-line Light Curves. 2015, *Astrophysical Journal, Supplement*, **217**, 26, `DOI:10.1088/0067-0049/217/2/26`

Cackett, E. M., Chiang, C.-Y., McHardy, I., et al., Accretion Disk Reverberation with Hubble Space Telescope Observations of NGC 4593: Evidence for Diffuse Continuum Lags. 2018, *Astrophysical Journal*, **857**, 53, `DOI:10.3847/1538-4357/aab4f7`

Chen, K. & Halpern, J. P., Structure of Line-emitting Accretion Disks in Active Galactic Nuclei: ARP 102B. 1989, *Astrophysical Journal*, **344**, 115, `DOI:10.1086/167782`

Czerny, B., Olejak, A., Rałowski, M., et al., Time Delay Measurement of Mg II Line in CTS C30.10 with SALT. 2019, *Astrophysical Journal*, **880**, 46, `DOI:10.3847/1538-4357/ab2913`

Denney, K. D., Bentz, M. C., Peterson, B. M., et al., The Mass of the Black Hole in the Seyfert 1 Galaxy NGC 4593 from Reverberation Mapping. 2006, *Astrophysical Journal*, **653**, 152, `DOI:10.1086/508533`

Dias dos Santos, D., Rodríguez-Ardila, A., Panda, S., & Marinello, M., First Observation of a Double-peaked O I Emission in the Near-infrared Spectrum of an Active Galaxy. 2023, *Astrophysical Journal, Letters*, **953**, L3, `DOI:10.3847/2041-8213/ace974`

Dietrich, M., Kollatschny, W., Alloin, D., et al., Monitoring of active galactic nuclei. IV. The Seyfert 1 galaxy NGC 4593. 1994, *Astronomy and Astrophysics*, **284**, 33

Dultzin-Hacyan, D., Taniguchi, Y., & Uranga, L., Where is the Ca II Triplet Emitting Region in AGN? 1999, in Astronomical Society of the Pacific Conference Series, Vol. **175**, *Structure and Kinematics of Quasar Broad Line Regions*, 303

Eracleous, M., Lewis, K. T., & Flohic, H. M. L. G., Double-peaked emission lines as a probe of the broad-line regions of active galactic nuclei. 2009, *New Astronomy Review*, **53**, 133, `DOI:10.1016/j.newar.2009.07.005`

Eracleous, M., Livio, M., Halpern, J. P., & Storchi-Bergmann, T., Elliptical Accretion Disks in Active Galactic Nuclei. 1995, *Astrophysical Journal*, **438**, 610, `DOI:10.1086/175104`

Ferland, G. J. & Persson, S. E., Implications of CA II Emission for Physical Conditions in the Broad-Line Region of Active Galactic Nuclei. 1989, *Astrophysical Journal*, **347**, 656, `DOI:10.1086/168156`

Garcia-Rissmann, A., Vega, L. R., Asari, N. V., et al., An atlas of calcium triplet spectra of active galaxies. 2005, *Monthly Notices of the RAS*, **359**, 765, `DOI:10.1111/j.1365-2966.2005.08957.x`

Grandi, S. A., O I λ8446 emission in Seyfert 1 galaxies. 1980, *Astrophysical Journal*, **238**, 10, `DOI:10.1086/157952`

Grandi, S. A., Reddening indicators for quasars and Seyfert 1 galaxies. 1983, *Astrophysical Journal*, **268**, 591, `DOI:10.1086/160982`

Joly, M., Formation of CA II lines in active galactic nuclei. 1989, *Astronomy and Astrophysics*, **208**, 47

Kollatschny, W. & Dietrich, M., Balmer emission-line profile variations in NGC 4593. 1997, *Astronomy and Astrophysics*, **323**, 5

Landt, H., Bentz, M. C., Ward, M. J., et al., The Near-Infrared Broad Emission Line Region of Active Galactic Nuclei. I. The Observations. 2008, *Astrophysical Journal, Supplement*, **174**, 282, `DOI:10.1086/522373`

Martínez-Aldama, M. L., Dultzin, D., Marziani, P., et al., O I and Ca II Observations in Intermediate Redshift Quasars. 2015, *Astrophysical Journal, Supplement*, **217**, 3, `DOI:10.1088/0067-0049/217/1/3`

Martínez-Aldama, M. L., Panda, S., Czerny, B., et al., The CaFe Project: Optical Fe II and Near-infrared Ca II Triplet Emission in Active Galaxies. II. The Driver(s) of the Ca II and Fe II and Its Potential Use as a Chemical Clock. 2021, *Astrophysical Journal*, **918**, 29, DOI:10.3847/1538-4357/ac03b6

Marziani, P., Martínez-Aldama, M. L., Dultzin, D., & Sulentic, J. W., Low Ionization Emission Lines in Quasars. 2013, *The Astronomical Review*, **8**, 26, DOI:10.1080/21672857.2013.11519727

Matsuoka, Y., Kawara, K., & Oyabu, S., Low-Ionization Emission Regions in Quasars: Gas Properties Probed with Broad O I and Ca II Lines. 2008, *Astrophysical Journal*, **673**, 62, DOI:10.1086/524193

Matsuoka, Y., Oyabu, S., Tsuzuki, Y., & Kawara, K., Observations of O I and Ca II Emission Lines in Quasars: Implications for the Site of Fe II Line Emission. 2007, *Astrophysical Journal*, **663**, 781, DOI:10.1086/518399

McHardy, I. M., Connolly, S. D., Horne, K., et al., X-ray/UV/optical variability of NGC 4593 with Swift: reprocessing of X-rays by an extended reprocessor. 2018, *Monthly Notices of the RAS*, **480**, 2881, DOI:10.1093/mnras/sty1983

Ochmann, M. W., Kollatschny, W., Probst, M. A., et al., The transient event in NGC 1566 from 2017 to 2019. I. An eccentric accretion disk and a turbulent, disk-dominated broad-line region unveiled by double-peaked Ca II and O I lines. 2024, *Astronomy and Astrophysics*, **686**, A17, DOI:10.1051/0004-6361/202348559

Ochmann, M. W., Weilbacher, P. M., Probst, M. A., et al., Double-peaked Ca II traces a relativistic broad-line region disk in NGC 4593. 2025, *Astronomy and Astrophysics*, **697**, L5, DOI:10.1051/0004-6361/202554800

Ochmann, M. W. et al. 2025, submitted to A&A

Persson, S. E., Calcium Infrared Triplet Emission in Active Galactic Nuclei. 1988, *Astrophysical Journal*, **330**, 751, DOI:10.1086/166509

Persson, S. E. & McGregor, P. J., Ca II emission in I Zwicky 1. 1985, *Astrophysical Journal*, **290**, 125, DOI:10.1086/162966

Popović, L. Č., Super-massive binary black holes and emission lines in active galactic nuclei. 2012, *New Astronomy Review*, **56**, 74, DOI:10.1016/j.newar.2011.11.001

Rodríguez-Ardila, A., Viegas, S. M., Pastoriza, M. G., & Prato, L., Infrared Fe II Emission in Narrow-Line Seyfert 1 Galaxies. 2002a, *Astrophysical Journal*, **565**, 140, DOI:10.1086/324598

Rodríguez-Ardila, A., Viegas, S. M., Pastoriza, M. G., Prato, L., & Donzelli, C. J., The O I Line Emission in Active Galactic Nuclei Revisited. 2002b, *Astrophysical Journal*, **572**, 94, DOI:10.1086/340192

Rudy, R. J., Rossano, G. S., & Puetter, R. C., Detection of the O i 11287 Angstrom Line in the Seyfert 1 Galaxy I ZW 1. 1989, *Astrophysical Journal*, **342**, 235, DOI:10.1086/167587

Santos-Lleo, M., Clavel, J., Barr, P., et al., Multifrequency monitoring of the Seyfert 1 galaxy NGC 4593 - II. A small, compact nucleus? 1995, *Monthly Notices of the RAS*, **274**, 1, DOI:10.1093/mnras/274.1.1

Shen, Y., Horne, K., Grier, C. J., et al., The Sloan Digital Sky Survey Reverberation Mapping Project: First Broad-line Hβ and Mg II Lags at z 0.3 from Six-month Spectroscopy. 2016, *Astrophysical Journal*, **818**, 30, DOI:10.3847/0004-637X/818/1/30

Strateva, I. V., Strauss, M. A., Hao, L., et al., Double-peaked Low-Ionization Emission Lines in Active Galactic Nuclei. 2003, *Astronomical Journal*, **126**, 1720, DOI:10.1086/378367

Ward, C., Gezari, S., Nugent, P., et al., Panic at the ISCO: Time-varying Double-peaked Broad Lines from Evolving Accretion Disks Are Common among Optically Variable AGNs. 2024, *Astrophysical Journal*, **961**, 172, DOI:10.3847/1538-4357/ad147d

Contrib. Astron. Obs. Skalnaté Pleso **56/1**, 112 – 122, (2026)
https://doi.org/10.31577/caosp.2026.56.1.112

The Baldwin effect and the Mg II - 3000 Å luminosity relation in blazars

V.M. Patiño-Álvarez[1,2], **J.U. Guerrero-González**[1], **V. Chavushyan**[1], **D.E. Monjardin-Ward**[1], **T.G. Arshakian**[3,4,5] and **I. Cruz-González**[6]

[1] *Instituto Nacional de Astrofísica, Óptica y Electrónica, Luis Enrique Erro 1, Tonantzintla, Puebla 72840, México (E-mail: victorm.patinoa@gmail.com)*

[2] *Max-Planck-Institut für Radioastronomie, Auf dem Hügel 69, D-53121 Bonn, Germany*

[3] *I. Physikalisches Institut, Universität zu Köln, Zülpicher Strasse 77, Köln, Germany*

[4] *Byurakan Astrophysical Observatory after V.A. Ambartsumian, Aragatsotn Province 378433, Armenia*

[5] *Astrophysical Research Laboratory of Physics Institute, Yerevan State University, 1 Alek Manukyan St., Yerevan, Armenia*

[6] *Universidad Nacional Autónoma de México, Instituto de Astronomía, AP 70-264, CDMX 04510, Mexico*

Received: November 1, 2025; Accepted: November 25, 2025

Abstract. We present a re-evaluation of the relationship between the Mg II $\lambda 2798$ Å emission line and the 3000 Å continuum luminosity, including an analysis of the Baldwin Effect, using a sample of 40,685 radio-quiet quasars and 441 Flat Spectrum Radio Quasars (FSRQs). To address dispersion from AGN variability, we applied a binning technique after excluding over 3,000 radio-loud sources, resulting in a refined empirical correlation. Our findings reveal statistically significant differences in the slope of this relationship between RQ quasars and FSRQs, implying either intrinsic differences in their accretion disk spectra or a significant contribution from jet-induced continuum to the BLR ionization in FSRQs. Furthermore, our investigation of the Non-Thermal Dominance (NTD) parameter shows that a substantial fraction of both populations (43.8% of RQ quasars and 55.5% of blazars) exhibit $NTD < 1$. We interpret this in blazars as evidence that the accretion disk alone cannot power the BLR, while in RQ quasars, it may indicate BLR anomalies, continuum-line time lags, or UV continuum suppression by a strong corona. Finally, we demonstrate that the Baldwin Effect is a direct consequence of the fundamental line–continuum luminosity relationship.

Key words: Active galactic nuclei — Flat-spectrum radio quasars — Radio quiet quasars

1. Introduction

The luminosities of broad emission lines and their adjacent continua in Active Galactic Nuclei (AGN) are fundamentally linked, as the ionizing continuum powers the line emission from the Broad Line Region (BLR). A key phenomenon related to this is the Baldwin Effect (BE), an inverse correlation between the equivalent width of emission lines like C IV or Mg II and the continuum luminosity, first identified by Baldwin (1977). While various physical mechanisms have been proposed to explain the BE-including a softening of the ionizing continuum and the influence of metallicity or the Eddington ratio - a compelling empirical hypothesis by Patiño Álvarez et al. (2016) suggests the BE is a direct mathematical consequence of the underlying line–continuum luminosity relationship itself.

This study tests that hypothesis using large samples of 40,685 radio-quiet (RQ) quasars and 441 Flat Spectrum Radio Quasars (FSRQs), focusing on the Mg II λ2798 Å line and the 3000 Å continuum. A critical aspect of our work is the comparison between these two populations, as FSRQs possess powerful jets that can significantly contaminate the continuum, potentially altering the fundamental line–continuum connection. We employ a conservative radio-loudness threshold ($R = 10$) to ensure a clean RQ sample, minimizing jet contamination.

Our primary objectives are to: (1) re-evaluate the Mg II–3000 Å correlation, accounting for AGN variability; (2) test if the BE emerges from this correlation as predicted; (3) investigate differences between RQ quasars and FSRQs; and (4) use the Non-Thermal Dominance (NTD) parameter to identify sources where the accretion disk may not be the sole source of ionizing photons.

2. Sample selection

Our analysis utilizes two distinct samples to compare radio-quiet (RQ) quasars and Flat Spectrum Radio Quasars (FSRQs).

2.1. Radio-quiet quasar sample

We constructed a control sample of RQ quasars from the SDSS Quasar Catalog (Shen et al., 2011, hereafter *S11*). We extracted sources with measurements for the Mg II λ2798 Å line and the 3000 Å continuum, applying a strict cut for low measurement uncertainty (< 0.03 dex). After a meticulous visual inspection of spectra to identify and remove outliers with problematic data (e.g., cropped or misidentified lines), our final RQ sample contained 43,756 quasars.

An initial fit to the Mg II–3000 Å relation confirmed the parameters from *S11*. However, we found the fit to be statistically unreliable (p-value $\simeq 1$), a result we attribute to significant scatter introduced by AGN variability. Since the single-epoch SDSS observations capture objects in random activity states, the intrinsic relationship is obscured. To mitigate this, we developed a binning technique, detailed in Section 3, which groups sources by luminosity to average out variability effects.

2.2. FSRQ blazar sample

Our FSRQ sample was drawn from the 5th Roma-BZCAT blazar catalog(Massaro et al., 2015). We cross-matched these sources with the SDSS Data Release 16 (DR16, Ahumada et al., 2020) and selected those with a redshift ($0.34 < z < 2.41$) that places the Mg II $\lambda2798$ Å line within the SDSS spectral window. This process yielded a final sample of 441 FSRQs with measurable Mg II and continuum luminosities.

2.3. Spectral analysis and measurement

To ensure a consistent comparison with the RQ sample, all FSRQ spectra were shifted to the rest frame, corrected for Galactic extinction, and trimmed to the 2500–3100 Å range.

We performed a simultaneous spectral decomposition of the continuum, Fe II emission, and the Mg II $\lambda2798$ Å line using the IRAF *specfit* task. The continuum was modeled with a power law, the Fe II emission with a template from Vestergaard & Wilkes (2001), and the Mg II line with one or two Gaussian components. This method accounts for the covariance between the continuum and line fluxes. An example of this decomposition is shown in Fig. 1.

The continuum flux at 3000 Å was measured directly from the Fe II- and line-subtracted spectrum. The total uncertainty combines the spectral noise and the SDSS calibration error. Mg II Line Flux: The line flux was obtained by integrating the spectrum over 2700–2900 Å after subtracting the continuum and Fe II emission. We rigorously estimated the uncertainty by combining three sources in quadrature: Fe II subtraction, spectral signal-to-noise, and flux calibration. Luminosities for both the line and continuum were calculated using standard cosmology. The equivalent width (EW) was computed as in Eq. 1 from the integrated line and continuum fluxes, with uncertainties propagated accordingly.

$$EW = \int_{\lambda_1}^{\lambda_2} \frac{F_\lambda - F_c}{F_c} d\lambda \qquad (1)$$

To ensure that it is valid to compare our measurements to those of *S11*, we cross-matched 183 FSRQs also present in the SDSS Quasar Catalog. The parameters (continuum and line luminosities, EW) derived from our method showed excellent agreement (average differences < 0.04 dex) with the catalog values, confirming consistency. We also note that our uncertainty estimates are more comprehensive and generally larger than those in the catalog, suggesting previous uncertainties may have been underestimated.

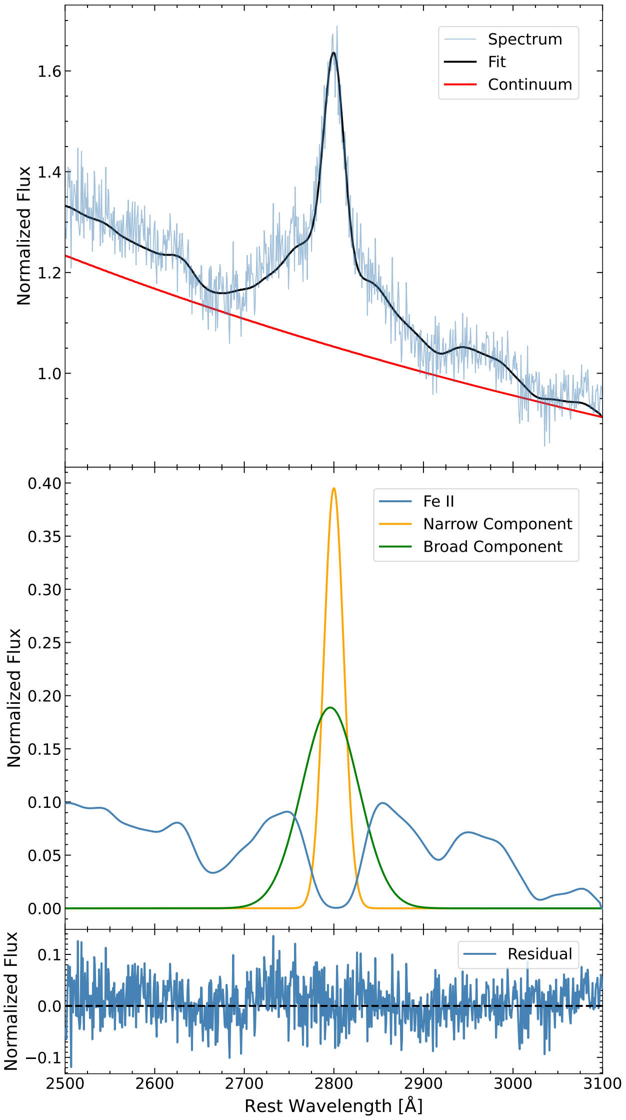

Figure 1. Example of the fitting procedure for the spectra of the FSRQ sample. The source is 5BZQ J1520+0732 (SDSS J152045.54+073230.5). Top panel: The observed spectra (blue), the final fit (black), and the power-law continuum (red). Middle panel: Spectral components fitted (excluding the continuum), including the broad Gaussian component (green), the narrow Gaussian component (orange), and the fitted Fe II emission (blue). Bottom panel: Residuals from the fit.

3. Results: line–continuum relation and the Baldwin effect

3.1. Fits to the unbinned data

We began by investigating the relationship between the Mg II line and 3000 Å continuum luminosities for our unbinned sample using three standard regression algorithms: the Bisector, Ordinary Least Squares (Y|X), and Orthogonal Distance Regression (ODR). In all three cases, the resulting linear fits yielded a p-value indistinguishable from 1.0.

A p-value of this magnitude indicates that the simple linear model does not provide a statistically significant description of the unbinned data. The model fails to reduce the residual variance meaningfully beyond the sample mean, rendering it unsuitable for its intended use in the literature: predicting one luminosity from the other for individual objects (e.g. NTD, the scaling relations of *S11*, among others). The parameters for these fits are presented in Table 1.

Table 1. Linear regression parameters for the unbinned data, following the form $\log \mathrm{L}_{\mathrm{MgII}} = a + b \log \lambda \mathrm{L}_{\lambda 3000}$. The high p-value ($\sim 1$) for all methods indicates the models have no significant predictive power for individual sources.

Method	Slope (b)	Intercept (a)	Scatter (dex)
Bisector	0.874 ± 0.036	3.900 ± 1.671	0.2506
Y|X	0.703 ± 0.034	11.825 ± 0.767	0.2464
ODR	0.887 ± 0.019	3.266 ± 0.882	0.2530

Note. While the Y|X fit exhibits the lowest formal scatter, it assumes the independent variable ($\log \lambda \mathrm{L}_{\lambda 3000}$) is error-free and provides a non-symmetrical relation, making it less generally applicable than the Bisector or ODR methods.

The profound lack of predictive power is a direct consequence of the large intrinsic scatter in the data, which we attribute primarily to AGN variability inherent in non-simultaneous, archival observations. This finding motivates the need for an alternative approach to derive a robust relation.

3.2. Mitigating variability with binning

To address the scatter introduced by AGN variability, which rendered the linear fit on unbinned data of *S11* statistically unreliable (p-value $\simeq 1$), we applied a binning technique to both our samples. For the final sample of 40,685 Radio-Quiet (RQ) quasars, this method yielded a highly significant correlation between the Mg II and 3000 Å continuum luminosities (p-value $\simeq 0$, $r = 0.998$), as shown in the right panel of Fig. 2, and in Eq. 2. The same technique applied to the

441 FSRQs also produced a strong, statistically significant correlation (p-value $= 2.3 \times 10^{-6}$, $r = 0.986$).

$$\log L_{MgII} = (0.826 \pm 0.025) \log \lambda L_{\lambda 3000} + (6.057 \pm 0.164) \tag{2}$$

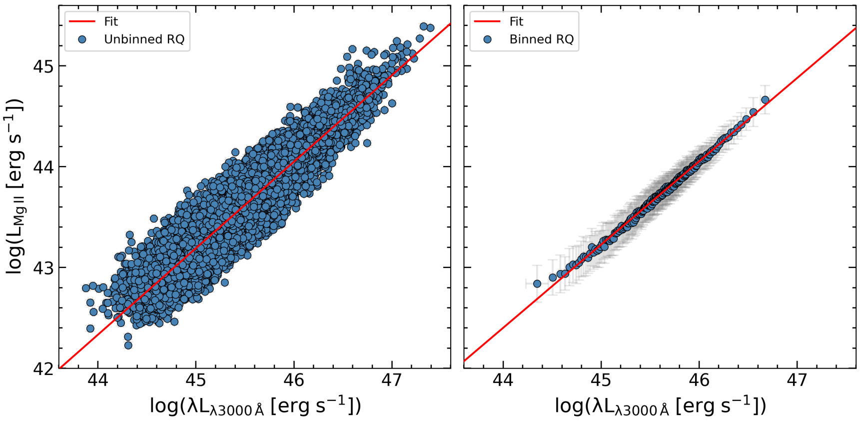

Figure 2. The relationship between the 3000 Å continuum luminosity and the Mg II λ2798 Å emission line luminosity for the RQ control sample is shown, with the unbinned data in the left panel and the binned data in the right panel. The red solid line represents the fitted relation for each data set. In the right panel, the fitted line corresponds to the relationship presented in Eq. 2.

When applying binning to the Baldwin Effect relationship for both samples, it also yields strong correlations; a Pearson correlation coefficient of -0.948, with a p-value of 10^{-101} for the RQ quasars, and a Pearson correlation coefficient of -0.913, and a corresponding p-value of 7×10^{-9} for the FSRQ sample.

3.3. A statistically significant difference in slopes

In order to statistically compare the slopes of the luminosity relations for the radio-quiet and FSRQ samples, we performed an extra sum of squares F-test. This involved comparing a model where the two samples were constrained to have a common slope against a model where they were allowed independent slopes. The test indicated that the difference in slopes was statistically significant (F = 104.3264, p = 1.1102×10^{-16}).

This discrepancy cannot be explained by variability alone. We conclude that the most plausible explanation is an intrinsic difference in the source of ionization: in FSRQs, the relativistic jet likely contributes to ionizing the Broad

Line Region, thereby altering the fundamental relationship between the disk continuum and the emission lines.

4. The non-thermal dominance parameter

To quantify the jet's contribution to the continuum, we employed the Non-Thermal Dominance (NTD) parameter. The NTD compares the observed 3000 Å continuum luminosity (L_{obs}) to the luminosity predicted (L_p) by the empirical Mg II–3000 Å relation established from our RQ quasar sample. This relation defines the expected behavior for a purely disk-ionized BLR.

Based on the assumption that $L_p \simeq L_{disk}$, we can distinguish 3 clear regimes:

- $NTD > 2$: Indicates a jet-dominated continuum.
- $1 < NTD < 2$: Consistent with a disk-dominated continuum.
- $NTD < 1$: The observed continuum is fainter than predicted from the line luminosity.

Our analysis revealed a significant population of sources with $NTD < 1$ in both samples: 43.8% of RQ quasars and 55.5% of FSRQs. This result is robust, persisting even when measurement uncertainties are considered.

4.1. Interpretation of $NTD < 1$

The physical interpretation of a suppressed continuum ($NTD < 1$) differs between the two populations:

- In FSRQs (Blazars): The most plausible explanation is that the jet itself contributes to ionizing the Broad Line Region. The observed Mg II line is strengthened by this additional, non-thermal ionizing source, leading to an over-prediction of the pure-disk continuum luminosity (L_p) and resulting in $NTD < 1$. This is supported by growing observational evidence of jet-BLR interaction in individual blazars (e.g., 3C 454.3: León-Tavares et al. (2013); Isler et al. (2013); Amaya-Almazán et al. (2021); CTA 102: Chavushyan et al. (2020); B2 1633+382: Amaya-Almazán et al. (2022); Ton 599: Hallum et al. (2022)).
- In Radio-Quiet Quasars: Since significant jet ionization is unlikely, $NTD < 1$ points to intrinsic properties of the disk-BLR system. Potential explanations include: 1) Internal extinction dust in the torus or host galaxy that preferentially reddens and suppresses the UV continuum relative to the broad emission lines; 2) Anomalies in BLR structure (e.g., outflows/inflows) altering its efficiency (e.g. Popović et al., 2019); 3) Time lags between continuum variations and the BLR's response; or 4) A strong corona that diverts accretion power, suppressing the UV continuum relative to the total ionizing

flux that powers the lines (e.g. Haardt & Maraschi, 1991; Risaliti & Lusso, 2019).

5. The origin of the Baldwin effect

We tested the hypothesis that the Baldwin Effect (BE) arises naturally from the empirical relationship between the Mg II line luminosity and the 3000 Å continuum luminosity (Patiño Álvarez et al., 2016). Mathematically, the BE can be derived directly from the line-continuum relation through a change of variables, which predicts a specific link between their slopes: $B - \beta = 1$, where B is the slope of the line-continuum relation and β is the slope of the BE.

Our analysis of both the RQ and FSRQ samples confirms this prediction. The measured slopes satisfy the $B - \beta \simeq 1$ condition within uncertainties. This result demonstrates that the Baldwin Effect is an inherent feature of the line-continuum connection and does not require a separate physical explanation for its origin.

Regarding the physical origin of the non-linear line-continuum relation itself ($B \neq 1$), we identify two key factors:

1. The 3000 Å continuum as a proxy: The Mg II line responds to the ionizing continuum at $\lambda \lesssim 1621$ Å(corresponding to the 7.64624 eV ionization energy), while we observe the non-ionizing 3000 Å continuum as a practical proxy. Differences in spectral shape and variability amplitude between these bands naturally produce a non-linear relationship.
2. Time delays and BLR physics: The finite size of the Broad Line Region introduces light-travel time delays between continuum and line variations. Combined with the complex responsivity of the BLR gas, this can modify the effective slope of the relationship from the expected linear case.

These well-established AGN properties provide the physical basis for the observed non-linearity, from which the Baldwin Effect emerges mathematically.

6. Conclusions

Our analysis of the Mg II λ2798 Å line and 3000 Å continuum in 40,685 radio-quiet quasars and 441 FSRQs yields the following key conclusions:

1. A Refined Empirical Relation: By applying a binning technique to mitigate AGN variability, we have derived a robust, new empirical relation between the Mg II line and 3000 Å continuum luminosities for radio-quiet quasars, which accurately describes the underlying correlation.
2. A Fundamental Difference Between RQ Quasars and FSRQs: We find a statistically significant difference in the slopes of the line–continuum luminosity relation (and the associated Baldwin Effect) between RQ quasars and

FSRQs. This points to a fundamental physical distinction, most plausibly explained by the relativistic jet in FSRQs contributing to the ionization of the Broad Line Region.

3. The Diagnostic Power of $NTD < 1$: The Non-Thermal Dominance parameter reveals that a substantial fraction of both RQ quasars (43.8%) and FSRQs (55.5%) exhibit a continuum fainter than predicted ($NTD < 1$). In FSRQs, this signals jet ionization of the BLR. In RQ quasars, it indicates complex disk-BLR-corona physics, such as BLR anomalies, continuum-line time lags, or UV suppression by a strong corona.

4. The Origin of the Baldwin Effect: We confirm that the Baldwin Effect for the Mg II line is a direct mathematical consequence of the line–continuum luminosity relationship, requiring no separate physical mechanism to explain its existence.

Acknowledgements. J.U.G.-G. and D.E.M.-W. acknowledge support from the the CONAHCYT (Consejo Nacional de Humanidades, Ciencia y Tecnología) program for Ph.D. and M.Sc. studies, respectively. Additionally, this work was supported by the Max Plank Institute for Radioastronomy (MPIfR) - Mexico Max Planck Partner Group led by V.M.P.-A. ICG acknowledge financial support from DGAPA-UNAM grant IN-119123 and CONAHCYT grant CF-2023-G-100. This research was supported by the YSU, in the frames of the internal grant.

Funding for the Sloan Digital Sky Survey IV has been provided by the Alfred P. Sloan Foundation, the U.S. Department of Energy Office of Science, and the Participating Institutions.

SDSS-IV acknowledges support and resources from the Center for High Performance Computing at the University of Utah. The SDSS website is www.sdss4.org.

SDSS-IV is managed by the Astrophysical Research Consortium for the Participating Institutions of the SDSS Collaboration including the Brazilian Participation Group, the Carnegie Institution for Science, Carnegie Mellon University, Center for Astrophysics — Harvard & Smithsonian, the Chilean Participation Group, the French Participation Group, Instituto de Astrofísica de Canarias, The Johns Hopkins University, Kavli Institute for the Physics and Mathematics of the Universe (IPMU) / University of Tokyo, the Korean Participation Group, Lawrence Berkeley National Laboratory, Leibniz Institut für Astrophysik Potsdam (AIP), Max-Planck-Institut für Astronomie (MPIA Heidelberg), Max-Planck-Institut für Astrophysik (MPA Garching), Max-Planck-Institut für Extraterrestrische Physik (MPE), National Astronomical Observatories of China, New Mexico State University, New York University, University of Notre Dame, Observatório Nacional / MCTI, The Ohio State University, Pennsylvania State University, Shanghai Astronomical Observatory, United Kingdom Participation Group, Universidad Nacional Autónoma de México, University of Arizona, University of Colorado Boulder, University of Oxford, University of Portsmouth, University of Utah, University of Virginia, University of Washington, University of Wisconsin, Vanderbilt University, and Yale University.

References

Ahumada, R., Prieto, C. A., Almeida, A., et al., The 16th Data Release of the Sloan Digital Sky Surveys: First Release from the APOGEE-2 Southern Survey and Full Release of eBOSS Spectra. 2020, *Astrophysical Journal, Supplement*, **249**, 3, DOI:10.3847/1538-4365/ab929e

Amaya-Almazán, R. A., Chavushyan, V., & Patiño-Álvarez, V. M., Multiwavelength Analysis and the Difference in the Behavior of the Spectral Features during the 2010 and 2014 Flaring Periods of the Blazar 3C 454.3. 2021, *Astrophysical Journal*, **906**, 5, DOI:10.3847/1538-4357/abc689

Amaya-Almazán, R. A., Chavushyan, V., & Patiño-Álvarez, V. M., Multiwavelength Analysis and the C IV λ1549 Å Emission Line Behavior From 2008 to 2020 of FSRQ B2 1633+382. 2022, *Astrophysical Journal*, **929**, 14, DOI:10.3847/1538-4357/ac5741

Baldwin, J. A., Luminosity Indicators in the Spectra of Quasi-Stellar Objects. 1977, *ApJ*, **214**, 679, DOI:10.1086/155294

Chavushyan, V., Patiño-Álvarez, V. M., Amaya-Almazán, R. A., & Carrasco, L., Flare-like Variability of the Mg II λ2798 Å Emission Line and UV Fe II Band in the Blazar CTA 102. 2020, *Astrophysical Journal*, **891**, 68, DOI:10.3847/1538-4357/ab6ef6

Haardt, F. & Maraschi, L., A Two-Phase Model for the X-Ray Emission from Seyfert Galaxies. 1991, *Astrophysical Journal, Letters*, **380**, L51, DOI:10.1086/186171

Hallum, M. K., Jorstad, S. G., Larionov, V. M., et al., Emission-line Variability during a Nonthermal Outburst in the Gamma-Ray Bright Quasar 1156+295. 2022, *Astrophysical Journal*, **926**, 180, DOI:10.3847/1538-4357/ac4710

Isler, J. C., Urry, C. M., Coppi, P., et al., A Time-resolved Study of the Broad-line Region in Blazar 3C 454.3. 2013, *ApJ*, **779**, 100, DOI:10.1088/0004-637X/779/2/100

León-Tavares, J., Chavushyan, V., Patiño-Álvarez, V., et al., Flare-like Variability of the Mg II λ2800 Emission Line in the Γ-Ray Blazar 3C 454.3. 2013, *ApJL*, **763**, L36, DOI:10.1088/2041-8205/763/2/L36

Massaro, E., Maselli, A., Leto, C., et al., The 5th edition of the Roma-BZCAT. A short presentation. 2015, *Astrophysics and Space Science*, **357**, 75, DOI:10.1007/s10509-015-2254-2

Patiño Álvarez, V., Torrealba, J., Chavushyan, V., et al., Baldwin Effect and Additional BLR Component in AGN with Superluminal Jets. 2016, *Frontiers in Astronomy and Space Sciences*, **3**, 19, DOI:10.3389/fspas.2016.00019

Popović, L. Č., Kovačević-Dojčinović, J., & Marčeta-Mandić, S., The structure of the Mg II broad line emitting region in Type 1 AGNs. 2019, *Monthly Notices of the RAS*, **484**, 3180, DOI:10.1093/mnras/stz157

Risaliti, G. & Lusso, E., Cosmological Constraints from the Hubble Diagram of Quasars at High Redshifts. 2019, *Nature Astronomy*, **3**, 272, DOI:10.1038/s41550-018-0657-z

Shen, Y., Richards, G. T., Strauss, M. A., et al., A Catalog of Quasar Properties from Sloan Digital Sky Survey Data Release 7. 2011, *ApJS*, **194**, 45, `DOI:10.1088/0067-0049/194/2/45`

Vestergaard, M. & Wilkes, B. J., An Empirical Ultraviolet Template for Iron Emission in Quasars as Derived from I Zwicky 1. 2001, *ApJS*, **134**, 1, `DOI:10.1086/320357`

Contrib. Astron. Obs. Skalnaté Pleso **56/1**, 123 – 130, (2026)
https://doi.org/10.31577/caosp.2026.56.1.123

Advancing computational spectroscopy: machine learning approaches for reconstructing incomplete spectroscopic and collisional datasets

N.M. Sakan[1], **V.A. Srećković**[1] and **V. Vujčić**[2]

[1] *University of Belgrade, Institute of Physics Belgrade, PO Box 57, (E-mail: nsakan@ipb.ac.rs, vlada@ipb.ac.rs)*

[2] *Astronomical Observatory, Volgina 7, 11060 Belgrade, Serbia (E-mail: veljko@aob.rs)*

Received: September 29, 2025; Accepted: October 31, 2025

Abstract. Spectroscopy remains a cornerstone of modern physics and chemistry, providing critical insights into molecular structures and interstellar phenomena. Accurate interpretation of interstellar line spectra through radiative transfer modeling relies heavily on two essential types of molecular input data: spectroscopic information (including energy levels, transition probabilities, and statistical weights) and collisional data. However, the completeness and precision of these datasets are often limited, constraining the reliability of astrophysical models. This work explores the application of machine learning (ML) and artificial neural networks (ANNs) for predicting and reconstructing missing spectroscopic/collisional data. We analyze their potential to enhance spectral databases, thereby improving stellar spectral analyses and the determination of fundamental stellar parameters. The study also addresses key challenges, methodological limitations, and validation issues inherent to data-driven approaches. Finally, we discuss current progress, share practical experiences, and outline future prospects and research needs in the rapidly evolving field of computational spectroscopy.

Key words: astrophysical plasma – optical characteristics – modeling – stellar atmospheres – ML – ANNs – A&M data

1. Introduction

Spectroscopy has played a fundamental role in advancing our understanding of both physical and chemical processes (Mihajlov et al., 2011a; Mihajlov et al., 2011b; Srećković et al., 2018; Dimitrijević et al., 2018). The analysis of interstellar spectral lines through radiative transfer modeling typically depends on two key types of molecular data: spectroscopic information (including energy levels, transition probabilities, and statistical weights) and collisional data (see e.g. Pop et al., 2021; Mihajlov et al., 2015, 2016; Srećković et al., 2017; Iacob, 2014; Iacob et al., 2022). It is both highly relevant and tempting to examine the application of machine learning (ML) and artificial neural networks (ANNs), particularly in their role of predicting or reconstructing missing spectroscopic and collisional data, while also identifying the existing limitations and challenges associated with these methods (Fig.1).

Spectral libraries constitute the foundation of stellar astrophysics and galactic research. They serve as templates for stellar population synthesis, automated parameterization processes for extensive surveys such as SDSS Ahumada et al. (2020), GAIA, and LAMOST, as well as for the investigation of stellar evolution. These libraries may be empirical (derived from observed spectra) or theoretical (generated from model atmospheres and radiative transfer codes). Theoretical libraries need to solve computationally demanding radiative transfer equations for millions of spectral lines, whereas empirical libraries might be observationally costly and contain gaps in parameter space. Both types of libraries confront substantial obstacles. In order to get beyond these restrictions, machine learning provides a strong set of techniques that can generate accurate and efficient spectral data by learning the intricate mapping between stellar properties and the resulting spectra.

Deep generative models are at the forefront of creating entirely novel, yet physically plausible, stellar spectra. A primary application is using Generative Adversarial Networks (GANs) Goodfellow et al. (2014) and Variational Autoencoders (VAEs) Kingma & Welling (2013). These models are trained on existing spectral libraries (e.g., PHOENIX Husser et al. (2013), Kurucz Kurucz (1993)). Once trained, they can generate a spectrum for any arbitrary combination of fundamental parameters (T_{eff}, $\log g$, [Fe/H], [α/Fe]) within the trained parameter range, effectively filling in the gaps of sparse empirical grids or creating a smooth, continuous library from a discrete theoretical one (Sharma et al., 2020).

In high-dimensional spectral space, standard interpolation methods like linear and cubic spline don't work good enough because the relationships between parameters and flux values are not linear. Deep neural networks and other machine learning models are usually very good at this. You can teach them how to use a set of parameters to make a full-spectrum, accurate prediction. You can also make models that do spectral super-resolution, this is very helpful for comparing data from different surveys (Bai et al., 2018).

It can take anywhere from a few minutes to a few hours to figure out one synthetic spectrum using codes like SYNTHE or SME. A well-trained ML model can make a spectrum of the same quality in just a few milliseconds. This approach, that involves creating a large but manageable training dataset from standard synthesis code, and using it in training a neural network in order to produce the results with smallest possible error. This creates a "surrogate model" that is very similar to the real code and speeds up the process by a lot (Tsalmantza & Hogg, 2012).

This paper focuses on the use of ML and ANNs for predicting or reconstructing missing spectroscopic and collisional datasets, as well as discussing the inherent challenges and limitations of such approaches. Furthermore, we

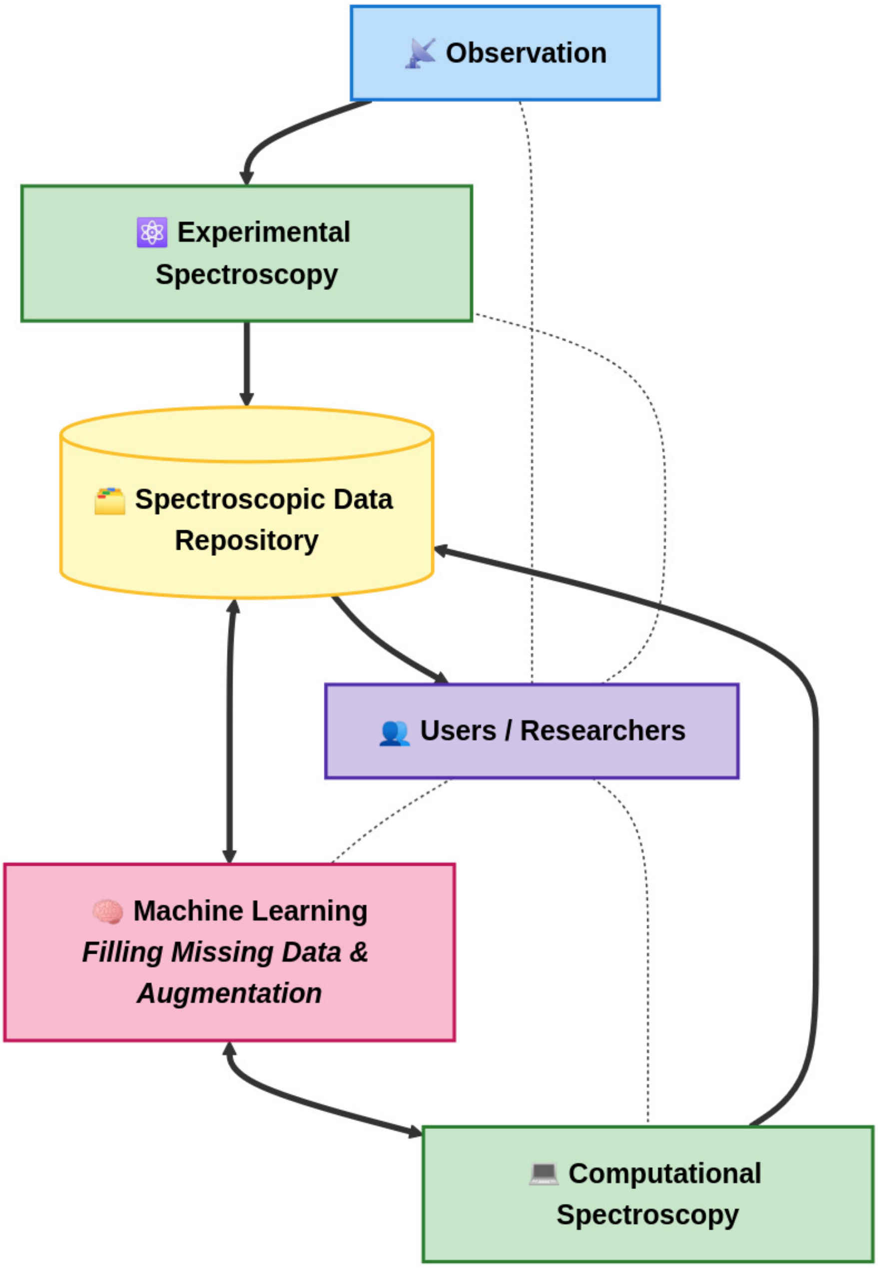

Figure 1. Collaborative flow of spectroscopic data environment

share our insights, experiences, and encountered difficulties, and provide an outlook on the future directions, needs, and developments in this emerging field of computational spectroscopy.

2. Neural network approaches to spectroscopic and collisional modeling

2.1. Data augmentation and domain adaptation

Tasks such as forecasting stellar properties using data-driven models requires an extensive dataset that could vary a parameters and complete the generation of the spectra as soon as possible. Machine learning-generated spectra can augment empirical datasets by providing supplementary examples of rare star types or by producing a more equitable training set. Moreover, generative models can facilitate domain adaptation by translating spectra from one survey's instrumental system (e.g., resolution, wavelength coverage) to another's, hence enhancing the consistency of cross-survey studies Li et al. (2024).

Notwithstanding its potential, the application of machine learning for spectrum creation presents some challenges:

Physical Plausibility: Machine learning models may occasionally generate "hallucinated" features that appear plausible yet lack any physical foundation. It is essential to regularize and validate the model in accordance with physical principles. When using a ML models for generating a stellar spectrum it is essential to bare in mind that a created spectrum must exhibit physical consistency, so it must be compared to existing measured or generated spectra whenever possible.

Training Data Limitations: The machine learning algorithm will absorb and mimic the biases and flaws present in the original dataset, so the generated data is inherently limited by the quality and comprehensiveness of the training data.

Interpretability: Deep learning models are most closely described as "black boxes". This complicates the understanding of the principles behind the generation of specific spectral features. Thus, a challenge for adequate astrophysical interpretation and validation of the generated spectra is present.

Extrapolation: Machine learning models typically exhibit inadequate performance when extending beyond the parameter space included by their training data. Having this in mind it could be concluded that application of ML is most reliable for interpolation, but always should be careful when new features are included.

2.2. Problem statement

In order to interpolate and augentate the molecular cross-section data ($\sigma_{J,v}(\lambda)$) for various molecular ions the appropriate artificial neural network (ANN) is needed. It needs to input the wavelength (λ) [nm], the vibrational quantum number (v), the rotational quantum number (J), and the Molecule type. The output is a cross-section, known in theory Srećković et al. (2020) and given as follows:

$$\sigma_{J,v}(\lambda) = \frac{8\pi^3}{3\lambda}\left[\frac{J+1}{2J+1}\left|D_{J,v;J+1,E'_{imp}}\right|^2 + \frac{J}{2J+1}\left|D_{J,v;J-1,E'_{imp}}\right|^2\right] \qquad (1)$$

Although the problem seems to be well defined, a complication in applying a simple neural network emerged.

2.3. Neural network design

The input s implemented in ANN are wavelength (λ) [nm] as a primary input, vibrational quantum number (v) as a one-hot categorical/discrete input, rotational quantum number (J) also as a categorical/discrete, one-hot, and molecule type one-hot encoded for the 7 molecular ions that have been analyzed.
The output is a simple cross-section value (σ) [cm^2].

The data preprocessing was applied, the scale wavelength to range [0,1] is used, the range is divide by max wavelength, the one-hot encode molecule type (7 categories), that selects the ANN for the particular molecular type. Quantum numbers were used as-is (one-hot), the log-transform of cross-section values is applied in order to cover wider range of data more precisely.

2.4. Training considerations

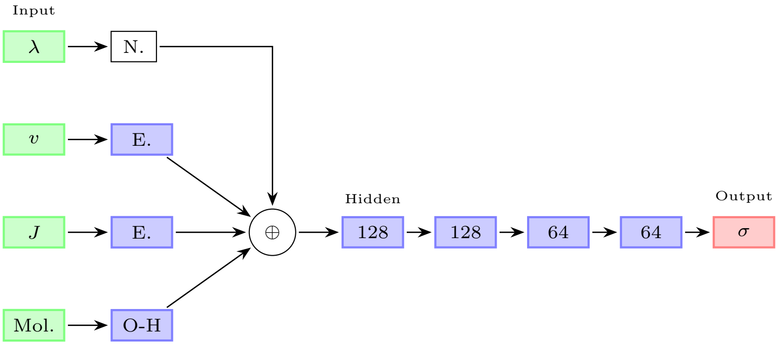

Figure 2. Deep neural network architecture for molecular cross-section interpolation. N. = Normalization, E. = Embedding, O-H = One-Hot, Mol. = Molecule.

The metrics introduced for the determining a quality of the fit was a mean squared logarithmic error (MSLE). Since the goal was a interpolation and augenation of the existing data the entire data set was used. Each of seven molecules had a separate ANN. In order to realize a genetic algorithm the 0.2 dropout rate is introduced and dropout layers were defined.

Also a physics-informed (PINNs) enhancements for perceptron where used and the resulting ANN was trained separately as well as using a genetic algorithm. The physically involved layer did not give any significant improvement. It included s $1/\lambda$ as additional input, features like $\frac{J}{2J+1}$ and $\frac{J+1}{2J+1}$, custom loss to penalize deviations from expected functional form.

The best performing deep ANN network, not the PINN, where more thorough research should be carried out, is given in Fig 2.

2.5. Final remarks and future work

This paper focuses on the use of ML (see e.g. Sakan et al., 2022; Lemishko et al., 2024, and references therein) and ANNs for predicting or reconstructing missing spectroscopic and collisional datasets, as well as discussing the inherent challenges and limitations of such approaches. Furthermore, we share our insights, experiences, and encountered difficulties, and provide an outlook on the future directions, needs, and developments in this emerging field of computational spectroscopy. The findings and their analysis demonstrate the applications' interdisciplinary nature.

3. Conclusion

Machine learning is revolutionizing the way we generate and work with stellar spectral data. By acting as a powerful interpolator and ultra-fast emulator of physical models, ML is enabling the creation of vast, high-fidelity, and continuous spectral libraries that were previously computationally prohibitive. This eases and enhances the ability to analyze the data from current and next-generation astronomical surveys. It should be noted that challenges remain regarding physical consistency and interoperability. Since the application of simple perceptron neural networks as well as physically informed perceptron networks, and after applying a genetic algorithm to have the best fitted solution, we did not produce a trained ANN good enough for applicable solution. The work is still in progress, and the focus should be onto GANs and VAEs. From all mentioned above, it is obvious that the synergy between machine learning and traditional astrophysical modeling is creating a new paradigm for data-driven discovery in astronomy and this approach could only gain momentum by the growth of the available computational power.

Acknowledgements. This research was supported by the Ministry of Science, Technological Development and Innovation of the Republic of Serbia (MSTDIRS) through contract no. 451-03-66/2024-03/200002 made with Astronomical Observatory (Belgrade), 451-03-47/2023-01/200024 made with Institute of physics Belgrade. We also appreciate the networking opportunities facilitated by the COST Actions CA21101 (Confined Molecular Systems: From a New Generation of Materials to the Stars – COSY).

References

Ahumada, R., Prieto, C. A., Almeida, A., & et al., The 16th Data Release of the Sloan Digital Sky Surveys: First Release from the APOGEE-2 Southern Survey and Full Release of eBOSS Spectra. 2020, *ApJS*, **249**, 3, `DOI:10.3847/1538-4365/ab929e`

Bai, Y., Liu, J.-F., & Wang, S., Machine learning classification of Gaia Data Release 2. 2018, *Research in Astronomy and Astrophysics*, **18**, 118, `DOI:10.1088/1674-4527/18/10/118`

Dimitrijević, M. S., Srećković, V. A., Sakan, N. M., Bezuglov, N. N., & Klyucharev, A. N., Free-Free Absorption in Solar Atmosphere. 2018, *Geomagn. Aeron.*, **58**, 1067, `DOI:10.1134/S0016793218080054`

Goodfellow, I. J., Pouget-Abadie, J., Mirza, M., et al., Generative Adversarial Networks. 2014, *arXiv e-prints*, arXiv:1406.2661, `DOI:10.48550/arXiv.1406.2661`

Husser, T.-O., Wende-von Berg, S., Dreizler, S., et al., A new extensive library of PHOENIX stellar atmospheres and synthetic spectra. 2013, *A&A*, **553**, A6, `DOI:10.1051/0004-6361/201219058`

Iacob, F., Spectral characterization of hydrogen-like atoms confined by oscillating systems. 2014, *CEJP*, **12**, 628, `DOI:10.2478/s11534-014-0496-1`

Iacob, F., Meltzer, T., Mezei, J. Z., Schneider, I. F., & Tennyson, J., Study of bound and resonant states of NS molecule in the R-matrix approach. 2022, *J.Phys.B*, **55**, 235202, `DOI:10.1088/1361-6455/ac9cae`

Kingma, D. P. & Welling, M., Auto-Encoding Variational Bayes. 2013, *arXiv e-prints*, arXiv:1312.6114, `DOI:10.48550/arXiv.1312.6114`

Kurucz, R., ATLAS9 Stellar Atmosphere Programs and 2 km/s grid. 1993, *Robert Kurucz CD-ROM*, **13**

Lemishko, K., Armstrong, G. S. J., Mohr, S., et al., Machine learning-based estimator for electron impact ionization fragmentation patterns. 2024, *J.Phys.D*, `DOI:10.1088/1361-6463/ada37e`

Li, H., Zhao, Q., Zhang, C., et al., DSRL: A low-resolution stellar spectral of LAMOST automatic classification method based on discrete wavelet transform and deep learning methods. 2024, *Experimental Astronomy*, **57**, 20, `DOI:10.1007/s10686-024-09940-0`

Mihajlov, A., Srećković, V., & Sakan, N., Inverse Bremsstrahlung in Astrophysical Plasmas: The Absorption Coefficients and Gaunt Factors. 2015, *Journal of Astrophysics and Astronomy*, **36**, 635 – 642, `DOI:10.1007/s12036-015-9350-0`

Mihajlov, A., Srećković, V., Ignjatović, L., & Dimitrijević, M., Atom-Rydberg-atom chemi-ionization processes in solar and DB white-dwarf atmospheres in the presence of (n - n')-mixing channels. 2016, *MNRAS*, **458**, 2215 – 2220, `DOI:10.1093/mnras/stw308`

Mihajlov, A. A., Sakan, N. M., Srećković, V. A., & Vitel, Y., Modeling of continuous absorption of electromagnetic radiation in dense partially ionized plasmas. 2011a, *J. Phys. A*, **44**, 095502, `DOI:10.1088/1751-8113/44/9/095502`

Mihajlov, A. A., Sakan, N. M., Srećković, V. A., & Vitel, Y., Modeling of the Continuous Absorption of Electromagnetic Radiation in Dense Hydrogen Plasma. 2011b, *Baltic Astronomy*, **20**, 604, `DOI:10.1515/astro-2017-0345`

Pop, N., Iacob, F., Niyonzima, S., et al., Reactive collisions between electrons and BeT+: Complete set of thermal rate coefficients up to 5000 K. 2021, *Atomic Data and Nuclear Data Tables*, **139**, 101414, `DOI:10.1016/j.adt.2021.101414`

Sakan, N. M., Traparić, I., Srećković, V. A., & Ivković, M., The usage of perceptron, feed and deep feed forward artificial neural networks on the spectroscopy data: astrophysical & fusion plasmas. 2022, *CAOSP*, **52**, 97, `DOI:10.31577/caosp.2022.52.3.97`

Sharma, K., Singh, H. P., Gupta, R., et al., Stellar spectral interpolation using machine learning. 2020, *MNRAS*, **496**, 5002, `DOI:10.1093/mnras/staa1809`

Srećković, V. A., Ignjatović, L. M., & Dimitrijević, M. S., Photodestruction of diatomic molecular ions: Laboratory and astrophysical application. 2020, *Molecules*, **26**, 151, `DOI:10.3390/molecules26010151`

Srećković, V. A., Sakan, N., Šulić, D., et al., Free–free absorption coefficients and Gaunt factors for dense hydrogen-like stellar plasma. 2018, *MNRAS*, **475**, 1131, `DOI:10.1093/mnras/stx3237`

Srećković, V. A., Šulić, D. M., Ignjatović, L. M., & Dimitrijević, M. S., A study of high-frequency properties of plasma and the influence of electromagnetic radiation from IR to XUV. 2017, *Nucl. Techn. & Rad. Protect.*, **32**, 222, `DOI:10.2298/NTRP1703222S`

Tsalmantza, P. & Hogg, D. W., A Data-driven Model for Spectra: Finding Double Redshifts in the Sloan Digital Sky Survey. 2012, *Astrophysical Journal*, **753**, 122, `DOI:10.1088/0004-637X/753/2/122`

Contrib. Astron. Obs. Skalnaté Pleso **56/1**, 131 – 139, (2026)
https://doi.org/10.31577/caosp.2026.56.1.131

Collisional data for the study of laboratory and space plasmas

V.A. Srećković[1], **L.M. Ignjatović**[1] and **M.S. Dimitrijević**[2]

[1] *Institute of Physics Belgrade, University of Belgrade, Pregrevica 118, 11080 Belgrade, Serbia, (E-mail: vlada@ipb.ac.rs)*

[2] *Astronomical Observatory Belgrade, Volgina 7, 11000 Belgrade, Republic of Serbia (E-mail: mdimitrijevic@aob.rs)*

Received: November 3, 2025; Accepted: November 29, 2025

Abstract. This paper highlights the importance of collisional processes in astrophysical environments, including the interstellar medium, planetary atmospheres, and laboratory studies. We emphasize the critical roles of heavy-particle ionization and dissociative recombination, underscoring the need for accurate cross-section data. Our research focuses on calculations of cross sections and rate coefficients needed for modeling. We also discuss future research directions.

Key words: atomic and molecular datasets – laboratory and astrophysical plasma – collisional peocesses – astrochemistry – modeling

1. Introduction

We are living in an era of big data, where unprecedented volumes of information demand reduction and analysis on scales far beyond human capability (Škoda & Adam, 2020; Garofalo et al., 2017). This has driven the adoption of artificial intelligence (AI) and machine learning (ML). Effective interpretation also requires complementary datasets for example, spectroscopic data for telescope spectra or collisional data for plasma modeling (Ivezić et al., 2017; Sen et al., 2022; Srećković et al., 2017; Srećković et al., 2018). As a result, growing emphasis is placed on systematic collections of atomic and molecular data, including collisional and photo-absorption studies, some now produced or refined with AI/ML methods (Anirudh et al., 2023; Trieschmann et al., 2023).

The need for reliable datasets has long been recognized, leading to the creation of dedicated databases. A notable example is the Virtual Atomic and Molecular Data Centre (VAMDC) Albert et al. (2020), which pioneered distributed databases accessible through a unified portal, initially for astronomy. Some initiatives like Europlanet related to testing and research in laboratories should also be mentioned here. Europlanet has a special program called Europlanet 2024 Research Infrastructure. It provides transnational access to unique labs where scientists can simulate planetary conditions.

This paper highlights challenges in collisional data collection and modeling fundamental to both astrophysical environments (e.g., interstellar medium, planetary atmospheres) and laboratory plasmas. A schematic presentation illustrating the connections between collisional processes, astrophysical environment modeling, and laboratory investigations is shown in Figure 1.

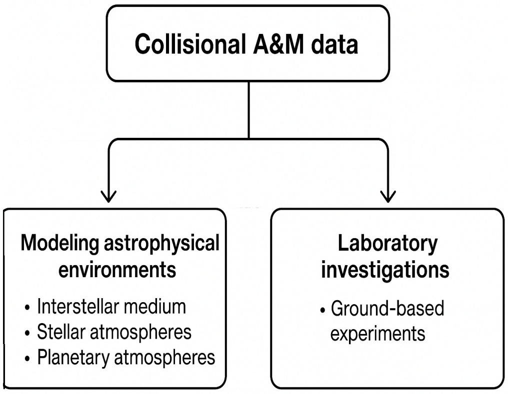

Figure 1. Schematic presentation with connection of collisional processes and modeling astrophysical environments and laboratory investigations.

Planetary atmospheres are generally weakly ionized gases, where ionization originates from diverse sources such as galactic cosmic rays, solar UV radiation, magnetospheric particles, and radioactive decay (Atreya, 1999). One of the most striking manifestations of atmospheric electrification is lightning, a transient high-current discharge that can act as a natural particle accelerator and has been observed not only on Earth but also on Jupiter, Saturn, and possibly other planets. In addition, electron impact ionization and related collisional processes, including associative ionization, chemi-ionization, and photoionization, play a central role in governing the conductivity and discharge phenomena of both terrestrial and extraterrestrial atmospheres (see e.g. Fox et al., 2008; Yair et al., 2008).

2. Collisional processes

2.1. Heavy particle ionization

Exciting an atom into a *Rydberg state* with a high principal quantum number n makes it highly sensitive to inelastic thermal collisions, which may lead to ionization. This process, known as *chemi-ionization* (CI), can proceed through different channels depending on the reaction outcome:

$$B^*(n) + B \rightarrow B + B^+ + e, \tag{1}$$

i.e. non-associative ionization and

$$B^*(n) + B \rightarrow B_2^+ + e, \tag{2}$$

known as associative ionization.

In these expressions, B represents atoms in the ground state, B^+ the corresponding ions, $B^*(n)$ Rydberg atoms with $n \gg 1$, B_2^+ molecular ions in the ground electronic state, and e the free electron.

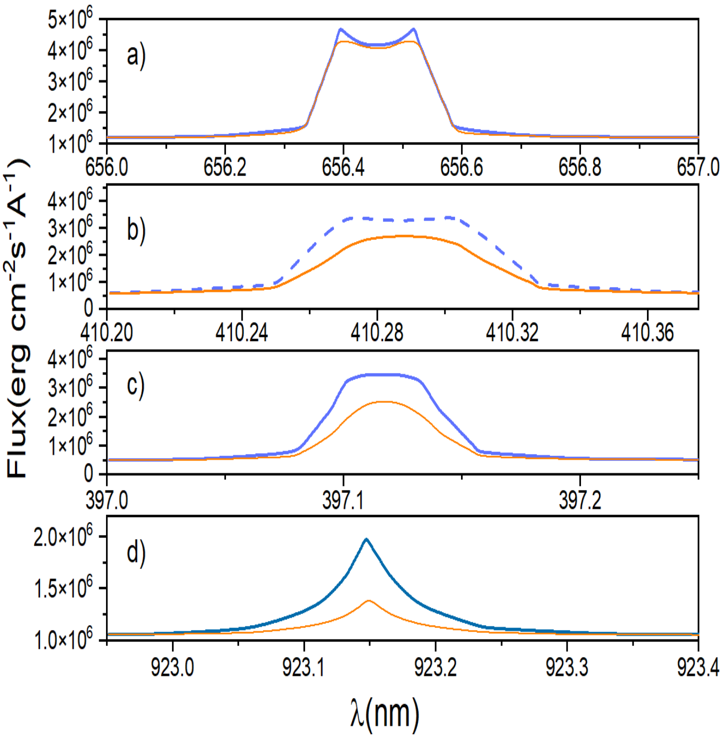

Figure 2. Profiles of hydrogen lines (a) Hα, (b) Hδ, (c) Hϵ, and (d) Paϵ in the atmospheres of late-type (M) stars. The blue curves correspond to profiles without CI processes, while the yellow curves include the contribution of CI processes.

These collisional CI mechanisms significantly affect the ionization balance and excited-state populations in weakly ionized laboratory plasmas (Ignjatović et al., 2019; Mihajlov et al., 2016; Hörnquist et al., 2023; Falcinelli et al., 2021). In astrophysical contexts, the processes (1) and (2), such as those involving hydrogen, are particularly important (Gnedin et al., 2009; Barklem, 2007). Results from Srećković et al. (2022) demonstrate that CI reactions can strongly modify the optical properties of the solar photosphere compared to electron–atom impact ionization, and therefore must be included in non-local thermodynamic equilibrium (non-LTE) modeling of the solar atmosphere (see e.g. Fig. 2).

Furthermore, atom-Rydberg atom CI processes have been proposed as useful tools for modeling and diagnosing dense, partially ionized regions in the broad-line regions (BLRs) of active galactic nuclei (AGN) (Srećković et al., 2018). Srećković et al. (2020) showed that when neutral hydrogen densities exceed 10^{12} cm^{-3}, CI reactions dominate over electron-atom collisions, thus exerting a major influence on the optical properties of these regions.

The associative channel of CI has also been suggested to contribute to the formation of molecular ions in interstellar gas (Dalgarno & Black, 1976). To model interstellar cloud chemistry, reliable cross sections and rate coefficients for such processes are required. Studies on helium, lithium, and alkali atoms Klyucharev et al. (2007); Srećković et al. (2018); Srećković et al. (2023) have further connected CI to astrophysical and planetary phenomena, including Io's atmosphere, Li-rich stars, and various geo-cosmical plasmas.

Finally, excitation and de-excitation in atom–Rydberg atom collisions can impact the efficiency of the ionization processes (1) and (2) (Barklem, 2007; Dimitrijević et al., 2020, 2021; Srećković et al., 2023). Such effects are especially relevant for the solar photosphere, the interstellar medium, DB-type white dwarf atmospheres, and AGN BLRs.

2.2. Electron driven collisional processes

Over recent decades, computational methods have become central to studying the dynamics and interactions of molecules embedded in larger structures (Reis et al., 2022; Iacob, 2020; Pop et al., 2021). Despite their massive scale, interstellar clouds remain poorly understood as confined systems. Deep within molecular clouds, molecules are shielded from photodissociation and photoionization by absorption and scattering of interstellar radiation (Puzzarini & Barone, 2020; Guerrero-Méndez et al., 2023). To model such environments, it is essential to consider not only radiative but also collisional processes, especially electron-driven reactions involving molecular ions such as dissociation.

Dissociative rate coefficients, defined as the change in molecular cation concentration over time, provide critical insight into the abundance of molecular ions. For instance, ions such as HeH^+, H_2^+, and He_2^+ have been detected in stellar media, with receiving particular attention due to its importance at relatively low temperatures (see e.g. Augustovičová et al., 2013; Guberman, 2012). The destruction of H_2^+ is a crucial step in the chemical network that leads to water formation in protoplanetary disks. The reactions that destroy H_2^+ actually

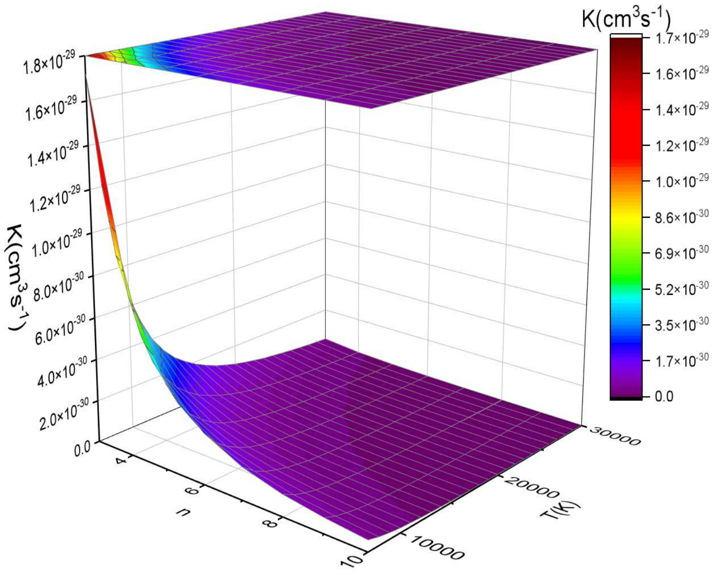

Figure 3. Three-dimensional plot of the dissociative rate coefficients for the He_2^+ system, based on data from the ACol database.

initiate the production of key intermediates such as OH^+, H_2O^+, and H_3O^+. The He_2^+ molecular ion has notable diagnostic value in astrophysics. It forms transiently under strong ionizing radiation and serves as a tracer of high-energy processes in environments such as protoplanetary disks and planetary atmospheres. Although short-lived and chemically inert, He_2^+ provides insight into the ionization state and radiation conditions that influence the evolution of these systems.

Access to reliable datasets and recommended values remains crucial for the modeling community (Marinković et al., 2017; Anirudh et al., 2023).

Dissociative recombination (DR), a dominant electron-driven destruction process, can be written as

$$e + M_2^+ \Longrightarrow M^*(n) + M, \tag{3}$$

where M and $M^*(n)$ are ground and Rydberg atoms, and M_2^+ is a molecular ion in its ground state.

These reactions are often explained through the dipole resonant mechanism, where the dipole component of the electron–ion interaction drives recombination, and may be analyzed using the decay approximation (Mihajlov et al., 2012). Figure 3 shows DR rate coefficients for He_2^+ from the ACol database, across $7000 \leq T \leq 30000$ K and $3 \leq n \leq 10$. The probability of DR increases with smaller n and lower T, confirming electron-driven collisions as a primary channel for Rydberg atom formation under such plasma conditions.

Since these processes influence both excited-state populations and free-electron densities, they also affect spectral line shapes, not only in molecular clouds and the interstellar medium but also in weakly ionized stellar atmospheres (Gnedin et al., 2009; Beuc & Pichler, 2020).

3. Summary

In this paper, we have highlighted the significance of collisional processes in the study of the astrophysical environments such as interstellar medium, planetary atmospheres, and laboratory experiments. We have emphasized the critical role of processes such as heavy-particle ionization and dissociative recombination, as well as the necessity for accurate cross-section data.

With regard to data resources, numerous comprehensive databases provide atomic and molecular information for spectroscopic studies of atmospheres and the interstellar medium like BASECOL, KIDA, etc. Despite the availability of these individual databases, we believe that the approach promoted by the VAMDC consortium, linking distributed databases through a single unified portal, represents the future standard for providing researchers with streamlined access to scientific data.

As a future step, we intend participation of ML models to produce i.e., to fast predict new A&M data. We are currently in the process of preparation for training and testing datasets for development of advanced models.

Acknowledgements. We gratefully acknowledge the networking opportunities provided by COST Actions CA21101 (COSY) and CA22133 (PLANETS), supported by COST (European Cooperation in Science and Technology). The authors also recognize the support of the Institute of Physics Belgrade and the Astronomical Observatory, funded by the Ministry of Science, Technological Development, and Innovations of the Republic of Serbia. V.A.S. acknowledges the support of the Science Fund of the Republic of Serbia through Grant No. 6821, Atoms and (bio)molecules – dynamics and collisional processes on short time scales (ATMOLCOL).

References

Albert, D., Antony, B. K., Ba, Y. A., et al., A Decade with VAMDC: Results and Ambitions. 2020, *Atoms*, **8**, 76, `DOI:10.3390/atoms8040076`

Anirudh, R., Archibald, R., Asif, M. S., et al., 2022 Review of Data-Driven Plasma Science. 2023, *IEEE Transactions on Plasma Science*, **51**, 1750, `DOI:10.1109/TPS.2023.3268170`

Atreya, S. K., Photochemistry of planetary atmospheres. 1999, *EOS Transactions*, **80**, 320, `DOI:10.1029/99EO00240`

Augustovičová, L., Špirko, V., Kraemer, W. P., & Soldán, P., Radiative association of He_2^+ revisited. 2013, *Astron. Astrophys.*, **553**, A42, DOI:10.1051/0004-6361/201220957

Barklem, P. S., Non-LTE Balmer line formation in late-type spectra: effects of atomic processes involving hydrogen atoms. 2007, *Astronomy and Astrophysics*, **466**, 327, DOI:10.1051/0004-6361:20066686

Beuc, R. & Pichler, G., High-Temperature Optical Spectra of Diatomic Molecules: Influence of the Avoided Level Crossing. 2020, *Atoms*, **8**, 28, DOI:10.3390/atoms8020028

Dalgarno, A. & Black, J. H., REVIEW: Molecule formation in the interstellar gas. 1976, *Reports on Progress in Physics*, **39**, 573, DOI:10.1088/0034-4885/39/6/002

Dimitrijević, M. S., Srećković, V. A., & Ignjatović, L. M., Influence of the (n-n')-mixing processes on the optical properties of the hydrogen clouds in the broad-line region of AGNs. 2020, *Contributions of the Astronomical Observatory Skalnate Pleso*, **50**, 179, DOI:10.31577/caosp.2020.50.1.179

Dimitrijević, M. S., Srećković, V. A., Ignjatović, L. M., & Marinković, B. P., The role of some collisional processes in AGNs: Rate coefficients needed for modeling. 2021, *New Astronomy*, **84**, 101529, DOI:10.1016/j.newast.2020.101529

Falcinelli, S., Vecchiocattivi, F., Farrar, J. M., & Pirani, F., Chemi-Ionization Reactions and Basic Stereodynamical Effects in Collisions of Atom-Molecule Reagents. 2021, *Journal of Physical Chemistry A*, **125**, 3307, DOI:10.1021/acs.jpca.1c00688

Fox, J. L., Galand, M. I., & Johnson, R. E., Energy deposition in planetary atmospheres by charged particles and solar photons. 2008, *Space Science Reviews*, **139**, 3

Garofalo, M., Botta, A., & Ventre, G., Astrophysics and Big Data: Challenges, Methods, and Tools. 2017, in IAU Symposium, Vol. **325**, *Astroinformatics*, ed. M. Brescia, S. G. Djorgovski, E. D. Feigelson, G. Longo, & S. Cavuoti, 345–348

Gnedin, Y. N., Mihajlov, A. A., Ignjatović, L. M., et al., Rydberg atoms in astrophysics. 2009, *New Astron. Rev.*, **53**, 259, DOI:10.1016/j.newar.2009.07.003

Guberman, S. L. 2012, *Dissociative recombination of molecular ions with electrons* (Springer Science & Business Media), 1–473, DOI:10.1007/978-1-4615-0083-4, ISBN: 978-0-306-47765-2

Guerrero-Méndez, L., Lema-Saavedra, A., Jiménez, E., Fernández-Ramos, A., & Martínez-Núñez, E., Gas-phase formation of glycolonitrile in the interstellar medium. 2023, *Physical Chemistry Chemical Physics*, **25**, 20988, DOI:10.1039/D3CP02379F

Hörnquist, J., Hedvall, P., Orel, A. E., & Larson, Å., Associative ionization in collisions of H^++H^- and H (1 s)+H (n s). 2023, *Physical Review A*, **108**, 052811, DOI:10.1103/PhysRevA.108.052811

Iacob, F., On the geometric quantization of the ro-vibrational motion of homonuclear diatomic molecules. 2020, *Physics Letters A*, **384**, 126888, DOI:10.1016/j.physleta.2020.126888

Ignjatović, L. M., Srećković, V. A., & Dimitrijević, M. S., The collisional atomic processes of Rydberg alkali atoms in geo-cosmical plasmas. 2019, *MNRAS*, **483**, 4202, DOI:10.1093/mnras/sty3294

Ivezić, Ž., Connolly, A. J., & Jurić, M., Everything we'd like to do with LSST data, but we don't know (yet) how. 2017, in IAU Symposium, Vol. **325**, *Astroinformatics*, ed. M. Brescia, S. G. Djorgovski, E. D. Feigelson, G. Longo, & S. Cavuoti, 93–102

Klyucharev, A. N., Bezuglov, N. N., Matveev, A. A., et al., Rate coefficients for the chemi-ionization processes in sodium- and other alkali-metal geocosmical plasmas. 2007, *New Astronomy Reviews*, **51**, 547, DOI:10.1016/j.newar.2007.05.001

Marinković, B. P., Jevremović, D., Srećković, V. A., et al., BEAMDB and MolD - databases for atomic and molecular collisional and radiative processes: Belgrade nodes of VAMDC. 2017, *European Physical Journal D*, **71**, 158, DOI:10.1140/epjd/e2017-70814-6

Mihajlov, A., Srećković, V., Ignjatović, L. M., & Klyucharev, A., The Chemi-Ionization Processes in Slow Collisions of Rydberg Atoms with Ground State Atoms: Mechanism and Applications. 2012, *J. Clust. Sci.*, **23**, 47, DOI:10.1007/s10876-011-0438-7

Mihajlov, A. A., Srećković, V. A., Ignjatović, L. M., & Dimitrijević, M. S., Atom-Rydberg-atom chemi-ionization processes in solar and DB white-dwarf atmospheres in the presence of (n - n')-mixing channels. 2016, *Monthly Notices of the Royal Astronomical Society*, **458**, 2215, DOI:10.1093/mnras/stw308

Pop, N., Iacob, F., Niyonzima, S., et al., Reactive collisions between electrons and BeT+: Complete set of thermal rate coefficients up to 5000 K. 2021, *At. Data Nucl. Data Tables*, **139**, 101414, DOI:10.1016/j.adt.2021.101414

Puzzarini, C. & Barone, V., A never-ending story in the sky: The secrets of chemical evolution. 2020, *Phys. Life Rev.*, **32**, 59, DOI:10.1016/j.plrev.2019.07.001

Reis, H., Żuchowski, P., & Grubišić, S., Computational Methods for the Description of Intermolecular Interactions and Molecular Motion in Confining Environments. 2022, *Front. Chem.*, **10**, 941269, DOI:10.3389/fchem.2022.941269

Sen, S., Agarwal, S., Chakraborty, P., & Singh, K. P., Astronomical big data processing using machine learning: A comprehensive review. 2022, *Experimental Astronomy*, **53**, 1, DOI:10.1007/s10686-021-09827-4

Srećković, V., Ignjatović, L., Jevremović, D., Vujčić, V., & Dimitrijević, M., Radiative and Collisional Molecular Data and Virtual Laboratory Astrophysics. 2017, *Atoms*, **5**, 31, DOI:10.3390/atoms5030031

Srećković, V. A., Dimitrijević, M. S., & Ignjatović, L. M., The influence of collisional-ionization and recombination processes on spectral line shapes in stellar atmospheres and in the hydrogen clouds in broad-line region of AGNs. 2020, *Contributions of the Astronomical Observatory Skalnate Pleso*, **50**, 171, DOI:10.31577/caosp.2020.50.1.171

Srećković, V. A., Dimitrijević, M. S., & Ignjatović, L. M., Absorption caused by potassium molecules in astrophysical plasmas: Data needed for modeling. 2023, *Adv. Space Res.*, **71**, 1252, DOI:10.1016/j.asr.2022.07.084

Srećković, V. A., Dimitrijević, M. S., Ignjatović, L. M., Bezuglov, N. N., & Klyucharev, A. N., The collisional atomic processes of rydberg hydrogen and helium atoms: Astrophysical relevance. 2018, *Galaxies*, **6**, DOI:10.3390/galaxies6030072

Srećković, V. A., Ignjatović, L. M., & Dimitrijević, M. S., Electron-impact processes involving small molecular ions relevant for the astrochemistry. 2022, *Contributions of the Astronomical Observatory Skalnate Pleso*, **52**, 90, DOI:10.31577/caosp.2022.52.3.90

Srećković, V. A., Dimitrijević, M. S., & Ignjatović, L. M., Atom–Rydberg atom chemi-ionization/recombination processes in the hydrogen clouds in broad-line region of AGNs. 2018, *Mon. Not. R. Astron. Soc.*, **480**, 5078, DOI:10.1093/mnras/sty2256

Trieschmann, J., Vialetto, L., & Gergs, T., Machine learning for advancing low-temperature plasma modeling and simulation. 2023, *arXiv e-prints*, arXiv:2307.00131, DOI:10.48550/arXiv.2307.00131

Škoda, P. & Adam, F. 2020, *Knowledge Discovery in Big Data from Astronomy and Earth Observation* (Elsevier), DOI:10.1016/C2018-0-02187-8

Yair, Y., Fischer, G., Simões, F., Renno, N., & Zarka, P., Updated Review of Planetary Atmospheric Electricity. 2008, *Space Science Reviews*, **137**, 29, DOI:10.1007/s11214-008-9349-9

Contrib. Astron. Obs. Skalnaté Pleso **56/1**, 140 – 148, (2026)
https://doi.org/10.31577/caosp.2026.56.1.140

Molecular ion reaction rates for planetary atmospheres and the interstellar medium

V.A. Srećković[1], **Lj.M. Ignjatović**[1], **M. Langović**[1] and **V.Vujčić**[2]

[1] *University of Belgrade, Institute of Physics Belgrade, PO Box 57, (E-mail: vlada@ipb.ac.rs, ljuba@ipb.ac.rs)*

[2] *Astronomical Observatory, Volgina 7, 11060 Belgrade, Serbia (E-mail: veljko@aob.rs)*

Received: September 10, 2025; Accepted: October 22, 2024

Abstract. Planetary systems are formed in dense interstellar clouds where chemistry is driven by complex ion–molecule processes. To improve astrochemical models, we present theoretically calculated datasets of cross sections and rate coefficients for important molecular ions under astrophysical conditions. The results provide a dataset relevant to protoplanetary disks and laboratory plasmas, and support the development of a user-friendly platform for data dissemination within the Virtual Atomic and Molecular Data Center (VAMDC) and the Serbian Virtual Observatory (SerVO).

Key words: databases – molecules – collisions – astrochemistry – modeling – planets – atmosphere

1. Introduction

Planetary systems originate from dense clouds of interstellar gas and dust, where gravitational forces interplay with thermal pressure, turbulence, and magnetic fields to drive collapse and disk formation (van Dishoeck et al., 2023; Walsh et al., 2012). To interpret the complex chemistry observed in these environments, astrochemical models - rooted in interstellar medium (ISM) chemistry while evolving into diverse transformations - are employed to refine our understanding of planetary formation processes. These models are supported by advances in astrochemical databases such as UMIST (Millar et al., 2024), KIDA (Wakelam et al., 2024), and the A&M VAMDC initiative (Albert et al., 2020), which enhance the accuracy of reaction rate coefficients (see Fig.1). A critical aspect of these models involves examining reaction rates that reveal the presence and behavior of various molecular species, particularly small molecular ions (Öberg et al., 2023; Bae et al., 2022). Consequently, it is important to investigate not only radiative processes but also non-radiative mechanisms, such as electron-driven reactions including dissociative recombination.

Observations, including those from ALMA, of ions such as N_2H^+ provide insights into midplane conditions within protoplanetary disks-regions where planetesimals are believed to form. Additional ions, such as NS^+, may also influence ion-driven chemistry, contribute to cooling processes, and impact the physical and chemical evolution of star-forming regions.

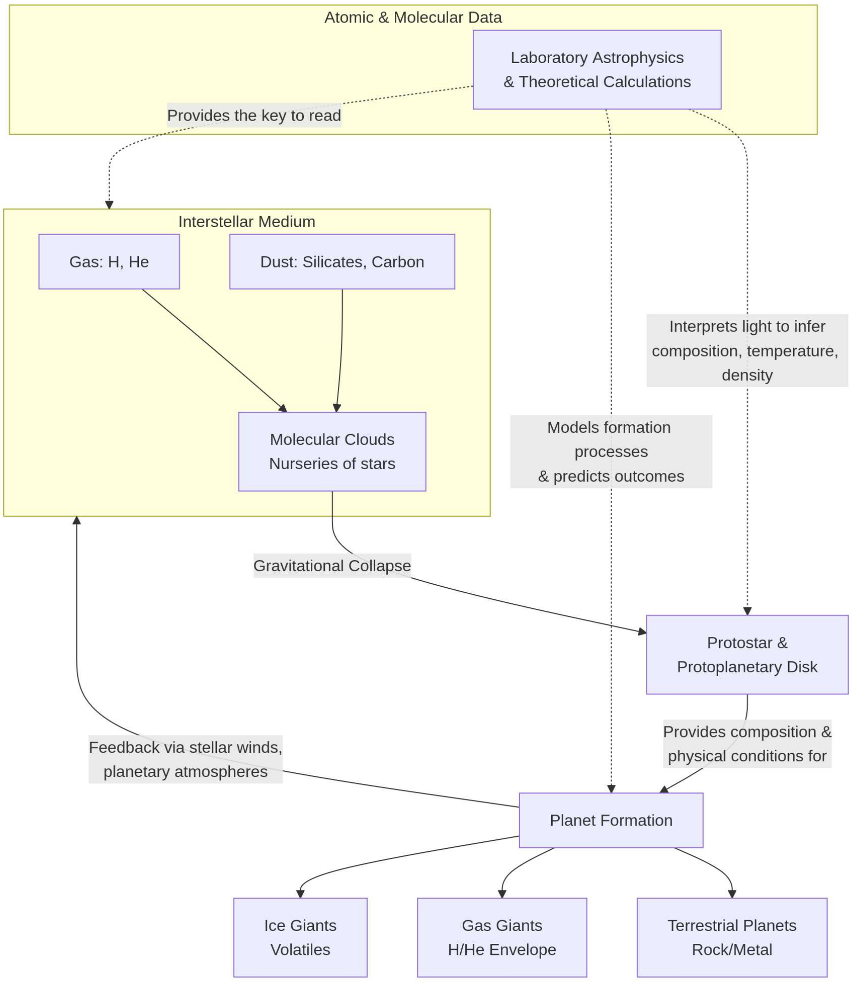

Figure 1. A&M data and its astro importance.

Accurate molecular ion data are essential for modeling astrophysical environments, from protoplanetary disks to planetary atmospheres. Recent studies of dissociative recombination and resonance structures in NS+ systems provide benchmarks for cation chemistry (Hassaine et al., 2024; Iacob et al., 2022). From a theoretical perspective, solvable potential models such as relativistic pseudo-Gaussian oscillators extend the family of exactly or approximately tractable systems, offering valuable tools for understanding confinement and spectral properties in hydrogen-like and molecular systems (Iacob, 2010; Iacob et al., 2019; Pop et al., 2021)

This paper aims to conduct theoretical studies involving the calculation, comparison, and analysis of cross sections and rate coefficients for molecular ions such as H_2^+, SiH^+, He_2^+, HeH^+, etc. under astrophysically relevant conditions. The intended outcome is a comprehensive dataset applicable to astrochemical environments as well as laboratory plasmas. Moreover, we aim to contribute to the broader scientific infrastructure by developing a user-friendly, extensible, and searchable e-platform for data dissemination and integration-aligned with existing frameworks such as VAMDC (Dubernet et al., 2024).

2. Data and databases

The databases are important for modeling laboratory and stellar plasmas, as well as for studies of planet formation. The Belgrade databases include astrophysically relevant data. The Belgrade database ACol provides collisional data, while the MolD database contains photodissociation cross sections for individual rovibrational states of diatomic molecular ions.

The Belgrade nodes provide unique datasets and specialized spectroscopic data, that are not fully covered by international repositories, thereby offering complementary resources for molecular collision and astrophysical research. This complementarity emphasizes the nodes' value in filling data gaps and supporting precise modeling in astrophysics and chemical physics.

2.1. SerVO

The SerVO (`http://servo.aob.rs`) hosts the Belgrade radiative and collisional nodes MolD and ACol of the Virtual Atomic and Molecular Data Centre (VAMDC) (Albert et al., 2020). The databases MolD (`http://servo.aob.rs/mold`) and ACol (`http://servo.aob.rs/acol`) include astrophysically relevant data. Furthermore, the data and its analysis demonstrate their interdisciplinary character and applications, such as in physics, astrophysics, and chemistry. One can see on the left side of the SerVO web page are links to BG Nodes (MolD, ACol). In the middle are links to the photo plate archive as well as new information related to scientific meetings, etc.

The MolD and ACol Belgrade A&M databases have been linked with the VAMDC project (`http://vamdc.eu`) since their early phases of development

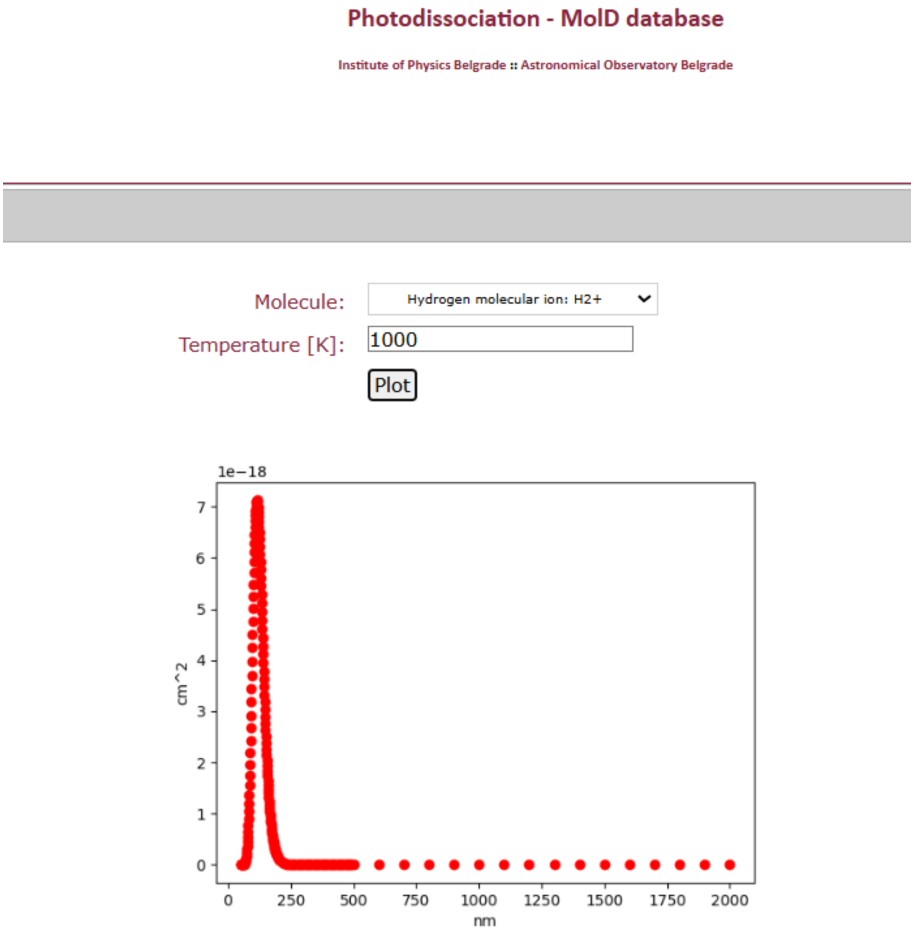

Photodissociation - MolD database

Institute of Physics Belgrade :: Astronomical Observatory Belgrade

Molecule: Hydrogen molecular ion: H2+

Temperature [K]: 1000

Figure 2. Snapshot of the MolD database (`http://servo.aob.rs/mold`): Photodissociation of the H_2^+ molecular ion for selected parameters. The SerVO (`http://servo.aob.rs`) hosts the Belgrade radiative and collisional nodes MolD

(see e.g. Vujčič et al., 2015). The VAMDC project Albert et al. (2020) intends to bring together numerous current databases under a common standard, creating a centralized platform for accessing atomic and molecular data. Users can download A&M data in a consistent format using the XML Schema for Atoms, Molecules, and Solids (XSAMS) (Jevremović et al., 2020; Albert et al., 2020; Marinković et al., 2017). Technically, the data models were updated to effortlessly transition to the VAMDC's tree-structured serialization schema, XSAMS. All databases are stored on a MariaDB server (an open-source relational database management system based on MySQL) and backed up on a regular basis.

The Belgrade nodes of the VAMDC offer practical accessibility for external researchers through standardized web services and user-friendly query tools. These platforms execute queries locally and transmit data in the VAMDC-specified XSAMS format, ensuring compatibility with VAMDC standards. The web interfaces allow researchers to perform searches and retrieve data without complex programming, and while detailed API documentation is explicitly provided, adherence to VAMDC standards enables programmatic access using standard protocols.

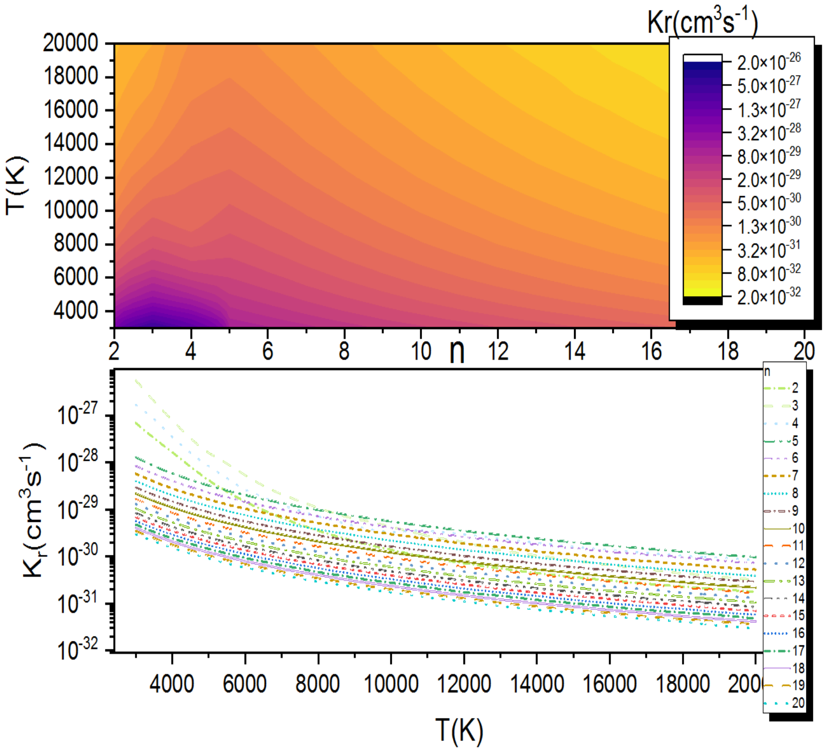

Figure 3. Figures created using data from the ACol database (http://servo.aob.rs/acol).

2.2. The MolD photodissociation database

The MolD database provides information on numerous molecular species and their excited states (see e.g. Srećković et al., 2017a; Vujčić et al., 2023). As a radiative database, it contains averaged thermal photodissociation cross sections as well as state-resolved data for the ro-vibrational levels of diatomic molecular ions (see Fig. 2).

The database has undergone several development phases and is maintained by the Astronomical Observatory in Belgrade. It is widely used in astronomy for investigating diverse astrophysical processes and modeling (Mihajlov et al., 2011; Srećković et al., 2014; Coppola et al., 2013), while its data also support studies of plasma chemistry and laboratory experiments (Srećković et al., 2021, 2022).

2.3. The ACol database for collisional processes

The ACol database provides cross sections and rate coefficients for collisional processes, including excitation, de-excitation, ionization, and recombination in hydrogen, helium, and alkali (see e.g. Srećković et al., 2022; Srećković et al., 2017b; Vujčić et al., 2023, and references therein). It represents the newest BG VAMDC node and is hosted by SerVO. Queries are processed locally, with results delivered in the VAMDC-standard XSAMS format through an AJAX-based interface. The database is applicable to laboratory studies as well as to modeling interstellar gas, weakly ionized atmospheric layers, and low-temperature plasmas. (see Fig. 3)

3. Summary

Emergence of planetary systems starts with the gravitational collapse of dense interstellar clouds, in a process where turbulence, pressure, and magnetic fields result in formation. Understanding the complex chemistry relies on astrochemical models, supported by specialized databases/data ecosystems such as UMIST, KIDA, and VAMDC, which provide essential reaction rate data. A key focus is the study of molecular ion reaction rates, including both radiative and electron-driven non-radiative processes like dissociative recombination.

In this work, we present an overview of the MolD and ACol databases - hosted within the VAMDC and SerVO frameworks - designed to support both astrophysical and laboratory research. Reliable maintenance and curation require not only adherence to established principles but also continuous alignment with rapid developments in information technology. Future improvements and standards should involve regular updates of Node software, including Python and Django, alongside enhancements to the web interface with AJAX-based queries, new visualizations, and additional extensions. Equally important is the expansion of datasets to include newly calculated or measured radiative and collisional processes. Another direction is the integration of machine learning techniques to accelerate the prediction of atomic and molecular data, supported by ongoing efforts to prepare training and testing datasets for the development of advanced models. Although machine learning approaches can speed up data generation, their predictions may lack precision. Therefore, results obtained through such models should be interpreted with caution.

Acknowledgements. This work has been supported by the Institute of Physics Belgrade and Astronomical Observatory, through funds from the Ministry of Science, Technological Development and Innovations of the Republic of Serbia. The authors acknowledge the networking opportunities from COST Actions: CA21101 (COSY), CA22133 (PLANETS) supported by COST (European Cooperation in Science and Technology). VAS is grateful for the hospitality of West University Timisoara. BPM. acknowledges support of the Science Fund of the Republic of Serbia, Grant No. 6821, Atoms and (bio)molecules - dynamics and collisional processes on short time scale – ATMOLCOL.

References

Albert, D., Antony, B. K., Ba, Y. A., et al., A Decade with VAMDC: Results and Ambitions. 2020, *Atoms*, **8**, 76, `DOI:10.3390/atoms8040076`

Bae, J. et al., Molecules with ALMA at Planet-forming Scales (MAPS): A Circumplanetary Disk Candidate in Molecular-line Emission in the AS 209 Disk. 2022, *Astrophysical Journal Letters*, **934**, L20, `DOI:10.3847/2041-8213/ac7fa1`

Coppola, C. M., Galli, D., Palla, F., Longo, S., & Chluba, J., Non-thermal photons and H_2 formation in the early Universe. 2013, *MNRAS*, **434**, 114, `DOI:10.1093/mnras/stt1007`

Dubernet, M. L., Boursier, C., Denis-Alpizar, O., et al., BASECOL2023 scientific content. 2024, *Astronomy and Astrophysics*, **683**, A40, `DOI:10.1051/0004-6361/202348233`

Hassaine, R., Gauchet, F., Iacob, F., et al., Dissociative recombination of NS^+ in collision with slow electrons. 2024, *Journal of Physics B Atomic Molecular Physics*, **57**, 165201, `DOI:10.1088/1361-6455/ad5e20`

Iacob, F., Relativistic pseudo-Gaussian oscillators. 2010, *Physics Letters A*, **374**, 1332, `DOI:10.1016/j.physleta.2009.10.048`

Iacob, F., Meltzer, T., Mezei, J. Z., Schneider, I. F., & Tennyson, J., Study of bound and resonant states of NS molecule in the R-matrix approach. 2022, *Journal of Physics B Atomic Molecular Physics*, **55**, 235202, `DOI:10.1088/1361-6455/ac9cae`

Iacob, F., Pop, N., Mezei, J. Z., et al., Recombination and excitation of molecular cations with electrons: Application to, H_2^+ BeD^+ and BeT^+. 2019, in American Institute of Physics Conference Series, Vol. **2071**, *Tim 18 Physics Conference*, 020007

Jevremović, D., Srećković, V. A., Marinković, B. P., & Vujčić, V., Databases for collisional and radiative processes in small molecules needed for spectroscopy use in astrophysics. 2020, *Contributions of the Astronomical Observatory Skalnate Pleso*, **50**, 44, DOI:10.31577/caosp.2020.50.1.44

Marinković, B. P., Jevremović, D., Srećković, V. A., et al., BEAMDB and MolD - databases for atomic and molecular collisional and radiative processes: Belgrade nodes of VAMDC. 2017, *European Physical Journal D*, **71**, 158, DOI:10.1140/epjd/e2017-70814-6

Mihajlov, A. A., Ignjatović, L. M., Srećković, V. A., & Dimitrijević, M. S., Chemi-ionization in Solar Photosphere: Influence on the Hydrogen Atom Excited States Population. 2011, *Astrophys. J., Suppl. Ser.*, **193**, 2, DOI:10.1088/0067-0049/193/1/2

Millar, T. J., Walsh, C., Van de Sande, M., & Markwick, A. J., The UMIST database for astrochemistry 2022. 2024, *Astronomy & Astrophysics*, **682**, A109, DOI:10.1051/0004-6361/202347057

Öberg, K. I., Facchini, S., & Anderson, D. E., Protoplanetary Disk Chemistry. 2023, *Annual Review of Astronomy and Astrophysics*, **61**, 287, DOI:10.1146/annurev-astro-022823-040844

Pop, N., Iacob, F., Niyonzima, S., et al., Reactive collisions between electrons and BeT+: Complete set of thermal rate coefficients up to 5000 K. 2021, *At. Data Nucl. Data Tables*, **139**, 101414, DOI:10.1016/j.adt.2021.101414

Srećković, V., Ignjatović, L., Jevremović, D., Vujčić, V., & Dimitrijević, M., Radiative and Collisional Molecular Data and Virtual Laboratory Astrophysics. 2017a, *Atoms*, **5**, 31, DOI:10.3390/atoms5030031

Srećković, V. A., Jevremović, D., Vujčić, V., et al., Mol-D a database and a web service within the Serbian virtual observatory and the virtual atomic and molecular data centre. 2017b, *Proceedings of the International Astronomical Union*, **12**, 393, DOI:10.1017/S1743921316012643

Srećković, V. A., Mihajlov, A. A., Ignjatović, L. M., & Dimitrijević, M. S., Ion-atom radiative processes in the solar atmosphere: quiet Sun and sunspots. 2014, *Advances in Space Research*, **54**, 1264, DOI:10.1016/j.asr.2013.11.017

Srećković, V. A., Ignjatović, L. M., & Dimitrijević, M. S., Photodestruction of Diatomic Molecular Ions: Laboratory and Astrophysical Application. 2021, *Molecules*, **26**, DOI:10.3390/molecules26010151

Srećković, V. A., Ignjatović, L. M., Kolarski, A., et al., Data for Photodissociation of Some Small Molecular Ions Relevant for Astrochemistry and Laboratory Investigation. 2022, *Data*, **7**, DOI:10.3390/data7090129

van Dishoeck, E. F. et al., The diverse chemistry of protoplanetary disks as revealed by JWST. 2023, *Faraday Discussions*, **245**, 52, DOI:10.1039/D2FD00134F

Vujčić, V., Marinković, B. P., Srećković, V. A., et al., Current stage and future development of Belgrade collisional and radiative databases/datasets of importance for molecular dynamics. 2023, *Physical Chemistry Chemical Physics*, **25**, 26972, DOI:10.1039/D3CP03752E

Vujčič, V., Jevremović, D., Mihajlov, A. A., et al., MOL-D: A Collisional Database and Web Service within the Virtual Atomic and Molecular Data Center. 2015, *Journal of Astrophysics and Astronomy*, **36**, 693, DOI:10.1007/s12036-015-9344-y

Wakelam, V., Gratier, P., Loison, J. C., et al., The 2024 KIDA network for interstellar chemistry. 2024, *Astronomy & Astrophysics*, **689**, A63, DOI:10.1051/0004-6361/202347934

Walsh, C., Nomura, H., Millar, T. J., & Aikawa, Y., Chemical processes in protoplanetary disks. II. On the importance of photochemistry and X-ray ionization. 2012, *Astrophysical Journal*, **747**, 114, DOI:10.1088/0004-637X/747/2/114

Contrib. Astron. Obs. Skalnaté Pleso **56/1**, 149 – 155, (2026)
https://doi.org/10.31577/caosp.2026.56.1.149

Photodissociation data for small molecular ions of astrochemical interest

V.A. Srećković[1], L.M. Ignjatović[1], M. Langović[1], V. Petrović[2] and H. Delibašić[2]

[1] *Institute of Physics Belgrade, University of Belgrade, Pregrevica 118, 11080 Belgrade, Serbia, (E-mail: vlada@ipb.ac.rs)*

[2] *Faculty of Science, Department of Physics, University of Kragujevac, Serbia (E-mail: violeta.petrovic@pmf.kg.ac.rs)*

Received: September 13, 2025; Accepted: October 28, 2025

Abstract. This study examines radiative processes, with a focus on photodissociation, in non-symmetric hydrogen–silicon molecular systems. for the wide range of parameters. The results provide essential input for photochemical modeling in both laboratory plasmas and astrophysical contexts.

Key words: atomic and molecular datasets – laboratory and astrophysical plasma – optical characteristics – absorption – photodissociation – non-symmetric systems – modeling

1. Introduction

Atomic and molecular (A&M) data are vital for advancing spectroscopy, supporting theoretical models, and guiding experiments in molecular physics and astrochemistry (Hauschildt & Baron, 2010; Ferland et al., 2017; Albert et al., 2020; Mihajlov et al., 2011; Srećković et al., 2017; Srećković et al., 2021). Optical properties of small molecules, particularly molecular ions, remain of high interest for applications in astrochemistry, precision spectroscopy, and searches for interstellar species (Ignjatović et al., 2014; Vázquez-Carson et al., 2022; Mihajlov et al., 2011; Iacob, 2020; Srećković et al., 2022; Quitián-Lara et al., 2024).

Photodissociation governs molecular fragmentation in interstellar clouds and must be accurately modeled to predict abundances across environments such as protoplanetary disks, stellar envelopes, and galactic molecular clouds (Heays et al., 2017; Öberg, 2016). Among these, silicon-bearing molecules are notable, representing nearly 10% of known interstellar species (McCarthy et al., 2003). SiH and SiH^+, in particular, have astrophysical importance as components of interstellar clouds and stellar atmospheres (Singh & Vanlandingham, 1978; Stancil et al., 1997; van der Tak et al., 2020). Recent experiments confirmed SiH^+ production and provided benchmark data for astrochemical modeling (Mosnier et al., 2016).

Photodissociation cross-sections can be incorporated into astrophysical modeling tools such as CLOUDY, PDR Toolbox, or UCL-PDR to simulate the chemical and thermal balance of interstellar and circumstellar environments (see e.g. Ferland et al., 1998). These cross-sections are used to calculate wavelength-dependent photodissociation rates, which determine the destruction efficiencies of molecules under varying radiation fields. By integrating the cross-section data into the chemical reaction networks, the models can more accurately predict molecular abundances, emission features, and the evolution of photodissociation regions (PDRs) exposed to ultraviolet or X-ray radiation.

Here, we focus on spectroscopic properties of hydrogen–silicon systems, with emphasis on SiH^+ molecular ions, which are relevant to both astrophysical and fundamental studies (Yang et al., 2025). We present calculated absorption coefficients e.g. cross-sections in the EUV and UV ranges, applicable to synchrotron experiments and broader areas such as plasma modeling, ultrafast laser research, and astrophysical simulations (Mosnier et al., 2016; Doménech et al., 2017). Section 2 outlines the theoretical framework, Section 3 discusses findings in laboratory and astrophysical contexts, and Section 4 concludes with perspectives for future work.

2. Theory

This work examines how radiative processes influence the optical behavior of weakly ionized plasmas in both laboratory and astrophysical environments, with emphasis on bound–free photodissociation in strongly non-symmetric systems.

We shall investigate the processes that can be described as non-symmetric

$$\varepsilon_\lambda + AM^+ \Rightarrow A^+ + M. \tag{1}$$

M is a silicon atom (Si), and A=H. Molecular-ion in the ground electronic state SiH^+ is represented by the symbol AM^+.

For the species under investigation, the mean thermal photodissociation cross-section $\sigma^{(bf)}(\lambda, T)$ can be represented in the form given by Srećković et al. (2017); Srećković et al. (2021)

$$\sigma^{(bf)}(\lambda, T) = \frac{\sum\limits_{J,v}(2J+1)e^{\frac{-E_{J,v}}{kT}} \cdot \sigma^{(bf)}_{J,v}(\lambda)}{\sum\limits_{J,v}(2J+1)e^{\frac{-E_{J,v}}{kT}}}. \tag{2}$$

Here, $\sigma^{(bf)}_{J,v}(\lambda)$ represents the partial photodissociation cross-section for the ro-vibrational states characterized by the quantum numbers v and J, while $E_{J,v}$ denotes the energies of these states relative to the ground ro-vibrational state. In the given expression, $E_{J,v} = E_{dis} + \epsilon_{J,v}$, where E_{dis} is the dissociation energy of the molecular ion, and the energies $\epsilon_{J,v} < 0$ are determined as described in Srećković et al. (2017). Under the dipole approximation, the partial cross-sections $\sigma^{(bf)}_{J,v}(\lambda)$ can be defined by the expression from (Srećković et al., 2021)

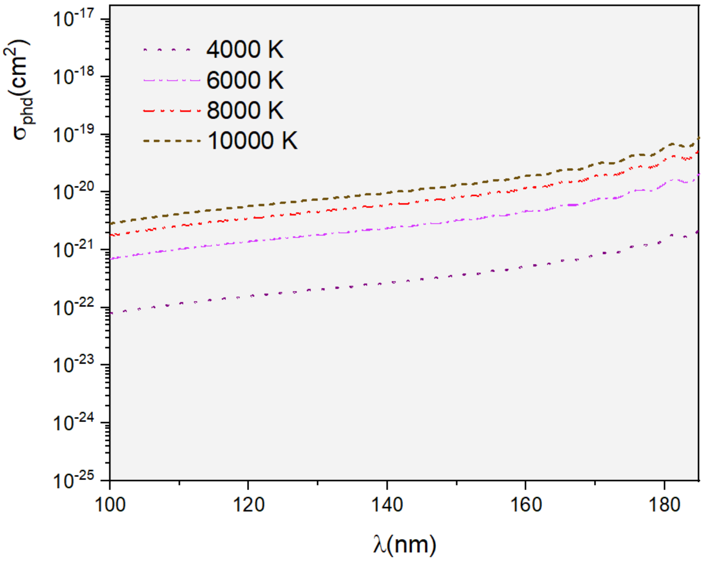

Figure 1. Calculated A&M data i.e. the mean thermal photodissociation cross-section for molecular-ion SiH^+.

3. Results and discussion

3.1. Astrophysical and laboratory relevance

Many astronomical software packages rely on photo-dissociation data (see e.g. Hauschildt & Baron, 2010, and references therein). In interstellar and circumstellar environments, UV photons strongly influence chemistry: atomic and molecular abundances in diffuse clouds are largely controlled by photodissociation and photoionization (Heays et al., 2017). In cometary comae, small molecules originate from UV-driven photodissociation of parent species (Irvine et al., 1998). These processes are essential for modeling diverse astrophysical regions, from dense star-forming clouds and protoplanetary disks to stellar envelopes and galactic molecular clouds (van Dishoeck et al., 2008). Such environments, where molecular destruction is dominated by photodissociation, are known as photon-dominated regions.

SiH^+, like other small molecular ions such as CH^+, OH^+, and NH^+, plays a important role in astrochemical networks and plasma environments, where its formation and destruction influence the chemistry of hydrogen- and silicon-bearing species. Comparable dissociation studies on ions such as BeT^+ and NS^+ highlight that accurate photodissociation data across diverse molecular systems are essential for reliably modeling molecular lifetimes and reaction pathways in both astrophysical and fusion plasmas (Hassaine et al., 2024; Iacob et al., 2022, 2020; Iacob, 2014, 2010).

Photodissociation of the SiH^+ ion is significant in plasma physics, spectroscopy, and semiconductor research (Zhao & Zeng, 2014). Silicon molecules occur in plasma environments such as etching and thin-film deposition, where understanding dissociation and ionization dynamics supports optimization of plasma-enhanced chemical vapor deposition (Gabriel et al., 2014). Laboratory measurements of photodissociation and photoionization cross-sections provide benchmark data for astrophysical and plasma modeling (Mosnier et al., 2016). Studies of VUV and EUV photon interactions with silicon ions further clarify bond strengths and reaction pathways.

3.2. The obtained quantities

The dataset spans the ultraviolet region and covers temperatures up to 10,000 K. These results are relevant for laboratory plasma diagnostics, astrophysical applications, and industrial plasma modeling.

Figure 1 shows the calculated average thermal photodissociation cross-section, $\sigma^{(bf)}_{\mathrm{SiH}^+}(\lambda; T)$, of the silicon hydride ion over a wide temperature range (up tp 10,000 K) and wavelengths from 100 to 190 nm. The plot highlights a complex dependence on both variables, with pronounced maxima near 180–190 nm.

The calculated SiH^+ photodissociation cross-sections are generally consistent with previous theoretical data, including Stancil et al. (1997) and later MRCI studies (see e.g. McMillan et al., 2016), with minor resonance deviations. A conservative uncertainty is adopted, and these cross-sections are expected to refine SiH^+ photodissociation rates by up to an order of magnitude under typical interstellar and circumstellar radiation fields, improving predictions of silicon-bearing molecular abundances and emission. In the absence of experimental measurements, this semi-quantitative agreement with independent theoretical results supports the reliability of the present data.

4. Summary

This study investigates the photodissociation of non-symmetric molecular ions, focusing on the averaged cross-sections of SiH^+ across the EUV–UV range and temperatures up to 10,000 K. The resulting cross-sections enable more accurate modeling of SiH^+ destruction, directly influencing predicted silicon-bearing molecular abundances, emission features, and chemical evolution in UV-irradiated interstellar and circumstellar environments. These findings are relevant for both laboratory and astrophysical applications, including spectroscopy, synchrotron-based experiments, and simulations of weakly ionized stellar and interstellar plasmas. SiH^+ plays a important role in interstellar chemistry, and its attosecond-scale photodynamics provide valuable insights for modeling space environments, laser-driven plasmas, and processes involving interstellar dust.

Acknowledgements. We express our gratitude for the support provided by the Science Fund of the Republic of Serbia under Grant No. 6821, titled Atoms and (bio)molecules – Dynamics and Collisional Processes on Short Time Scales (ATMOLCOL). We thank the Institute of Physics Belgrade, University of Belgrade, for funds provided by the Republic of Serbia's Ministry of Science, Technological Development, and Innovations. We also appreciate the networking opportunities facilitated by the COST Actions CA21101 (Confined Molecular Systems: From a New Generation of Materials to the Stars – COSY).

References

Albert, D., Antony, B. K., Ba, Y. A., et al., A Decade with VAMDC: Results and Ambitions. 2020, *Atoms*, **8**, 76, `DOI:10.3390/atoms8040076`

Doménech, J. L., Schlemmer, S., & Asvany, O., Accurate Frequency Determination of Vibration-Rotation and Rotational Transitions of SiH^+. 2017, *Astrophys. J.*, **849**, 60, `DOI:10.3847/1538-4357/aa8fca`

Ferland, G., Korista, K., Verner, D., et al., CLOUDY 90: numerical simulation of plasmas and their spectra. 1998, *Publications of the Astronomical Society of the Pacific*, **110**, 761

Ferland, G. J., Chatzikos, M., Guzmán, F., et al., The 2017 Release Cloudy. 2017, *Rev. Mex. Astron. Astrofís.*, **53**, 385, `DOI:10.48550/arXiv.1705.10877`

Gabriel, O., Kirner, S., Klick, M., Stannowski, B., & Schlatmann, R., Plasma monitoring and PECVD process control in thin film silicon-based solar cell manufacturing. 2014, *EPJ Photovolt.*, **5**, 55202, `DOI:10.1051/epjpv/2013028`

Hassaine, R., Gauchet, F., Iacob, F., et al., Dissociative recombination of NS^+ in collision with slow electrons. 2024, *Journal of Physics B Atomic Molecular Physics*, **57**, 165201, `DOI:10.1088/1361-6455/ad5e20`

Hauschildt, P. H. & Baron, E., A 3D radiative transfer framework. VI. PHOENIX/3D example applications. 2010, *Astron. Astrophys.*, **509**, A36, `DOI:10.1051/0004-6361/200913064`

Heays, A. N., Bosman, A. D., & van Dishoeck, E. F., Photodissociation and photoionisation of atoms and molecules of astrophysical interest. 2017, *Astron. Astrophys.*, **602**, A105, `DOI:10.1051/0004-6361/201628742`

Iacob, F., Relativistic pseudo-Gaussian oscillators. 2010, *Physics Letters A*, **374**, 1332, `DOI:10.1016/j.physleta.2009.10.048`

Iacob, F., Spectral characterization of hydrogen-like atoms confined by oscillating systems. 2014, *Central European Journal of Physics*, **12**, 628, DOI:10.2478/s11534-014-0496-1

Iacob, F., On the geometric quantization of the ro-vibrational motion of homonuclear diatomic molecules. 2020, *Phys. Lett. A*, **384**, 126888, DOI:10.1016/j.physleta.2020.126888

Iacob, F., Meltzer, T., Mezei, J. Z., Schneider, I. F., & Tennyson, J., Study of bound and resonant states of NS molecule in the R-matrix approach. 2022, *Journal of Physics B Atomic Molecular Physics*, **55**, 235202, DOI:10.1088/1361-6455/ac9cae

Iacob, F., Pop, N., Mezei, J. Z., et al., Reactive collisions between electrons and BeT^+. 2020, in American Institute of Physics Conference Series, Vol. **2218**, *American Institute of Physics Conference Series* (AIP), 050010

Ignjatović, L. M., Mihajlov, A. A., Srećković, V. A., & Dimitrijević, M. S., The ion-atom absorption processes as one of the factors of the influence on the sunspot opacity. 2014, *Mon. Not. R. Astron. Soc.*, **441**, 1504, DOI:10.1093/mnras/stu638

Irvine, W. M., Dickens, J. E., Lovell, A. J., et al., Chemistry in cometary comae. 1998, *Faraday Discuss.*, **109**, 475, DOI:10.1039/a709289j

McCarthy, M. C., Gottlieb, C. A., & Thaddeus, P., Silicon molecules in space and in the laboratory. 2003, *Mol. Phys.*, **101**, 697, DOI:10.1080/0026897021000035197

McMillan, E. C., Shen, G., McCann, J. F., McLaughlin, B. M., & Stancil, P. C., Rovibrationally resolved photodissociation of SH+. 2016, *Journal of Physics B: Atomic, Molecular and Optical Physics*, **49**, 084001, DOI:10.1088/0953-4075/49/8/084001

Mihajlov, A. A., Sakan, N. M., Srećković, V. A., & Vitel, Y., Modeling of continuous absorption of electromagnetic radiation in dense partially ionized plasmas. 2011, *J. Phys. A*, **44**, 095502, DOI:10.1088/1751-8113/44/9/095502

Mosnier, J. P., Kennedy, E. T., van Kampen, P., et al., Inner-shell photoexcitations as probes of the molecular ions CH^+, OH^+, and SiH^+: Measurements and theory. 2016, *Phys. Rev. A*, **93**, 061401, DOI:10.1103/PhysRevA.93.061401

Quitián-Lara, H. M., Fantuzzi, F., Mason, N. J., & Boechat-Roberty, H. M., Decoding the molecular complexity of the solar-type protostar NGC 1333 IRAS 4A. 2024, *Mon. Not. R. Astron. Soc.*, **527**, 10294, DOI:10.1093/mnras/stad3873

Singh, P. D. & Vanlandingham, F. G., Line positions and oscillator strengths of rotation-vibration band of possible interstellar SiH and SiH^+. 1978, *Astron. Astrophys.*, **66**, 87

Srećković, V., Ignjatović, L., Jevremović, D., Vujčić, V., & Dimitrijević, M., Radiative and Collisional Molecular Data and Virtual Laboratory Astrophysics. 2017, *Atoms*, **5**, 31, DOI:10.3390/atoms5030031

Srećković, V. A., Ignjatović, L. M., & Dimitrijević, M. S., Photodestruction of Diatomic Molecular Ions: Laboratory and Astrophysical Application. 2021, *Molecules*, **26**, DOI:10.3390/molecules26010151

Srećković, V. A., Ignjatović, L. M., Kolarski, A., et al., Data for Photodissociation of Some Small Molecular Ions Relevant for Astrochemistry and Laboratory Investigation. 2022, *Data*, **7**, DOI:10.3390/data7090129

Stancil, P. C., Kirby, K., Sannigrahi, A. B., et al., The Photodissociation of SiH^+ in Interstellar Clouds and Stellar Atmospheres. 1997, *Astrophys. J.*, **486**, 574, DOI:10.1086/304520

van der Tak, F. F. S., Lique, F., Faure, A., Black, J. H., & van Dishoeck, E. F., The Leiden Atomic and Molecular Database (LAMDA): Current Status, Recent Updates, and Future Plans. 2020, *Atoms*, **8**, 15, DOI:10.3390/atoms8020015

van Dishoeck, E. F., Jonkheid, B., & van Hemert, M. C., Photoprocesses in protoplanetary disks. 2008, *arXiv e-prints*, arXiv:0806.0088, DOI:10.48550/arXiv.0806.0088

Vázquez-Carson, S. F., Sun, Q., Dai, J., Mitra, D., & Zelevinsky, T., Direct laser cooling of calcium monohydride molecules. 2022, *New J. Phys.*, **24**, 083006, DOI:10.1088/1367-2630/ac806c

Yang, Y. K., Su, X. G., Wang, K., et al., Photodissociation dynamics of : Rovibrationally resolved Feshbach resonances mediated by coupled excited states in the ultraviolet region. 2025, *Phys. Rev. A*, **111**, 013118, DOI:10.1103/PhysRevA.111.013118

Zhao, J. & Zeng, H., Study on the spectroscopic data and vibrational levels of the ground SiH+ molecular ion. 2014, *Spectrosc. Spect. Anal.*, **34**, 3192, DOI:10.3964/j.issn.1000-0593(2014)12-3192-05

Öberg, K. I., Photochemistry and Astrochemistry: Photochemical Pathways to Interstellar Complex Organic Molecules. 2016, *Chem. Rev.*, **116**, 9631–9663, DOI:10.1021/acs.chemrev.5b00694

Contrib. Astron. Obs. Skalnaté Pleso **56/1**, 156 – 185, (2026)
https://doi.org/10.31577/caosp.2026.56.1.156

Feeding frenzy in the mighty black holes: what we could learn from them

S. Panda[1], **H. Benati Gonçalves**[2], **T. Storchi-Bergmann**[2], **M. Śniegowska**[3], **B. Czerny**[4], **E. Bon**[5], **P. Marziani**[6], **N. Bon**[5], **A. Rodríguez Ardila**[7], **D. May**[1], **M.A. Fonseca Faría**[8], **L. Fraga**[8], **F. Pozo Nuñez**[9], **E. Bañados**[10], **J. Heidt**[11], **K. Garnica**[12] **and D. Dultzin**[12]

[1] *International Gemini Observatory/NSF NOIRLab, Casilla 603, La Serena, Chile, (E-mail: swayamtrupta.panda@noirlab.edu)*
[2] *Departamento de Astronomia, Instituto de Física, Universidade Federal do Rio Grande do Sul, CP 15051, 91501-970, Porto Alegre, RS, Brazil*
[3] *School of Physics and Astronomy, Tel Aviv University, Tel Aviv 69978, Israel*
[4] *Center for Theoretical Physics, Polish Academy of Sciences, Al. Lotników 32/46, 02-668 Warsaw, Poland*
[5] *Astronomical Observatory Belgrade, Volgina 7, 11060 Belgrade, Serbia*
[6] *INAF-Astronomical Observatory of Padova, Vicolo dell'Osservatorio, 5, 35122 Padova PD, Italy*
[7] *Observatório Nacional, Rua José Cristino, 77, São Cristovão, 20921-400, Rio de Janeiro, RJ, Brasil*
[8] *Laboratório Nacional de Astrofísica (LNA), Rua dos Estados Unidos 154, Bairro das Nações, Minas Gerais, Brazil*
[9] *Astroinformatics, Heidelberg Institute for Theoretical Studies, Schloss-Wolfsbrunnenweg 35, 69118 Heidelberg, Germany*
[10] *Max-Planck Institut für Astronomie, Königstuhl 17 Heidelberg, Germany*
[11] *Landessternwarte, Zentrum für Astronomie der Universität Heidelberg, Königstuhl 12, 69117 Heidelberg, Germany*
[12] *Universidad Nacional Autónoma de México, Instituto de Astronomía, AP 70-264, 04510, CDMX, Mexico*

Received: October 1, 2025; Accepted: November 20, 2025

Abstract. Eddington ratio ($\lambda_{\rm Edd}$) is a paramount parameter governing the accretion history and life cycles of Active Galactic Nuclei (AGNs). This short review presents a multi-faceted view of the importance of the Eddington ratio spanning varied AGN studies. We find that $\lambda_{\rm Edd}$ is crucial for standardizing the Radius-Luminosity (R-L) relation - a necessary step for employing quasars

(QSOs) as standardizable cosmological probes to help clarify the standing of the Hubble tension. In this data-driven era, we consolidated disparate aspects by developing novel relations borne out of large datasets, such as the robust, nearly *universal anti-correlation* between fractional variability ($F_{\rm var}$) and $\lambda_{\rm Edd}$ derived from Zwicky Transient Facility (ZTF) data, which is vital for interpreting forthcoming high-cadence surveys like Rubin Observatory's LSST. Addressing the conundrum where JWST results suggest an overabundance of massive high-redshift black holes, we demonstrate that local AGNs offer clarification: Changing-Look AGNs (CLAGNs), driven by rapid $\lambda_{\rm Edd}$ shifts, cluster in the low-accretion regime ($\lambda_{\rm Edd} \sim 0.01$), a rate independently confirmed by our integral field spectroscopy and photoionization modeling of a well-known Seyfert 2 galaxy, rich in high-ionization, forbidden, coronal lines. Conversely, for the high-redshift, high-luminosity population where traditional reverberation mapping (RM) is highly impractical, photometric reverberation mapping (PRM) offers a rapid alternative to constrain accretion disk sizes, enabling efficient estimates of black hole masses ($M_{\rm BH}$) and $\lambda_{\rm Edd}$. Finally, we developed tailored semi-empirical spectral energy distributions (SEDs) for extremely high-accretion quasars, successfully validating their characteristic extreme physical conditions.

Key words: supermassive black holes (1663) – active galactic nuclei (16) – quasars (1319) – spectroscopy (1558) – photometry (1234) – scaling relations (2031) – spectral energy distribution (2129) – photoionization (2060)

1. Accretion rate - a key parameter in AGN studies

The Black Hole Accretion Rate (BHAR) is among the fundamental properties that help define the state and activity of the central supermassive black hole (SMBH) residing at the very centers of galaxies. The BHAR or an equivalent parameter, the Eddington ratio, is the ratio of the net bolometric output from the active galactic nuclei (AGN) relative to the Eddington limit[1]. Coupled with the knowledge of the mass of the SMBH, the Eddington ratio enables an understanding of the accretion history and life cycles of AGNs (Netzer, 2015; Padovani et al., 2017; Alexander et al., 2025; Marziani et al., 2025). The applications of the Eddington ratio are far-fetched, from studying the temporal modulation of radiative output from individual AGNs to constraining the bulk-statistical growth of AGNs across cosmic time. It has been found to be a direct correlate to explain the dispersion in the well-known broad-line region (BLR) radius - AGN luminosity (R-L) relation (Martínez-Aldama et al., 2019; Du & Wang, 2019; Panda & Marziani, 2023). The R-L relation is an empirical scaling relation, where the BLR radius is estimated using the reverberation mapping (RM) technique, where one can estimate the excess in the light travel time between photons that directly arrive from the source of ionizing radiation (in the case of the SMBH, this is the accretion disk - a flattened disk-like structure arising

---

[1] $L_{\rm Edd} \approx 1.26 \times 10^{38} \left(\frac{M_{\rm BH}}{M_\odot}\right)$ erg s^{-1}.

from the loss of angular momentum as the matter accretes onto the SMBH), and those that get intervened by gaseous media in-between accretion disk and the distant observer before eventually making their way to the observer. This offset in the light travel time between the two (photon) paths helps determine how far the intervening, line-emitting media is from the source of the radiation. This intervening medium, in our case, is the broad-line region (BLR), which produces the bulk of the emission lines that we observe in an AGN spectrum due to a variety of radiative processes, e.g., recombination, collisional excitation, and fluorescence (Osterbrock & Ferland, 2006). We note, however, that the reverberation mapping technique has also been used to determine the sizes of the accretion disk itself (using the continuum reverberation mapping, Edelson et al. 2015), the sizes of the dusty regions (dust reverberation, Suganuma et al. 2006), and to map the further-out narrow-line region (NLR, Peterson et al. 2013).

Coming back to the R-L relation, having known the BLR radius, we now require the AGN luminosity. The general approach involves extracting the continuum flux from the AGN spectrum, wherein we look for narrow, line-free, continuum windows, and with an assumed cosmology, which gives us the luminosity distance, we can estimate the AGN luminosity. Therefore, having the AGN luminosity, for example, from a single-epoch spectrum, and with the aid of the R-L relation, we can infer the black hole masses using well-known scaling relations based on the virial theorem[2] and extends to the creation of large quasar catalogs (Marziani et al., 2003a; Vestergaard & Peterson, 2006; Shen et al., 2011; Panda et al., 2024a). This, then, allows us to get insight into the black hole mass distribution over a range of redshift and infer their activity with the combined knowledge of the black hole mass and the net bolometric output. Another advantage of the R-L relation has been to utilize it as, cosmologically speaking, a standardizable relation to infer the cosmology using quasars (Watson et al., 2011; Haas et al., 2011; Czerny et al., 2013). Here, we get the continuum flux as before, either through single epoch spectroscopy or carefully optimized photometry - either by a systematic modeling of the contaminants all except the accretion disk (Pozo Nuñez et al., 2023; Jaiswal et al., 2024), or through the usage of medium/narrow-band filters to avoid regions where such contributions from contaminants dominate (Chelouche et al., 2019; Panda et al., 2024b; Pozo Nuñez et al., 2025). Instead of assuming a cosmological model, we then perform the reverberation mapping to extract the size of the emitting region, here R_{BLR}, and infer the AGN luminosity using the R-L relation (Blandford & McKee, 1982; Peterson et al., 2004; Bentz et al., 2013; Panda et al., 2019a; Cackett et al., 2021). Having uniquely determined the continuum flux and the

---

[2] Here, the virial theorem requires the knowledge of the velocity dispersion (or FWHM) of a prominent emission line, its location (R_{BLR}) from the central gravitational potential, i.e., the SMBH, and the assumption of the geometry and distribution of the emitting gas around the SMBH. This latter term is usually referred to as the virial factor or f-factor (Collin et al., 2006; Panda et al., 2019b).

luminosity from independent methods, we can then derive the luminosity distance for each of these objects[3], and populate the Hubble-Lemaitre diagram and constrain the existing cosmological models. With the aid of quasars, we are well-poised to bridge the gap between the local and early Universe cosmological probes and help clarify the stance on the Hubble tension (Czerny et al., 2023a; Panda & Marziani, 2023; Di Valentino et al., 2025). However, to infer the Hubble constant, we aggregate the RM AGNs with other cosmological probes, e.g., Type-1 Supernovae, chronometric measurements of the Universe expansion, baryon acoustic oscillation data, quasar angular sizes, H II starburst galaxies, and Amati-correlated gamma-ray burst data (Cao et al., 2022; Czerny et al., 2023a). On the other hand, to get to the Hubble constant directly from AGNs alone, we need the aid of standard candles or standard rulers, e.g., the sizes of the accretion disks allow us to characterize the angular sizes of the AGNs, in conjunction with the redshift-independent luminosity distances (see e.g., Jaiswal et al., 2024).

A fundamental issue using the R-L relation has been the realization of the highly-accreting AGNs and their location on the R-L relation (Du et al., 2016; Grier et al., 2017; Du et al., 2018; Martínez-Aldama et al., 2019). When the R-L relation was first established, the scaling relation was built using multi-epoch, ground-based, and space-based spectrophotometric observations of well-known nearby Seyfert galaxies (Kaspi et al., 2000; Bentz et al., 2009). The slope of the relation was found to be close to the expectation from the standard photoionization theory, i.e., ∼0.5, especially after careful host subtraction (Wandel et al., 1999; Negrete et al., 2013; Panda, 2022). Fast forward to mid-2015, newer reverberation mapping (RM) campaigns, with luminous sources accreting at relatively higher rates albeit with lower variability amplitudes, started to populate a region in the R-L parameter space which demonstrated a significant dispersion from the existing R-L relation, thus giving rise to studies to understand what made these sources inherently different from their local counterparts (Du et al., 2018; Martínez-Aldama et al., 2019; Panda et al., 2019a). Later, in Martínez-Aldama et al. (2019), we found the key reason for the dispersion was directly connected to the Eddington ratio - the higher the value, the more the source deviates from the scaling relation, especially in the direction where the inferred $\mathrm{R_{BLR}}$ is shorter than expected. The problem, however, with the Eddington ratio in this context, is the way it is derived - the bolometric luminosity is derived from the continuum luminosity, and so is the black hole mass. This is the same luminosity that is the 'L' in the R-L relation, thus creating a circular loop. We need an independent observable that could trace the Eddington ratio. Many studies have pointed to the strength of the Fe II emission (or, $\mathrm{R_{Fe}}$) to be a viable surrogate to the Eddington ratio through carefully statistical

---

[3] Given, $\mathrm{R_{BLR}} \propto \mathrm{L}^{0.5}$ from photoionization theory and the empirical R-L relation, and the AGN flux, $\mathrm{F} = \mathrm{L}/\ 4\pi \mathrm{d}_{\mathrm{L}}^{2}$, we can re-write luminosity distance, $\mathrm{d_L} \propto \mathrm{R_{BLR}}/\sqrt{4\pi \mathrm{F}}$.

and theoretically-motivated studies (Sulentic et al., 2000; Marziani et al., 2003b; Marziani & Sulentic, 2014; Shen & Ho, 2014; Marziani et al., 2018; Panda et al., 2019b; Martínez-Aldama et al., 2021); c.f. Panda (2024) for a recent overview. Du & Wang (2019) (see also, Panda & Marziani 2023) eventually made the breakthrough, and provided us with an R_{Fe}-corrected R-L relation which not only solved the circularity problem, but brought the scatter in the newfound R-L to a measly 0.19 dex, re-instating the R-L relation as a standardizable relation for use in cosmology.

This is just one of the many highlights of the Eddington ratio and how it has come to the rescue. In later sections of this short contribution, we demonstrate a few recent studies that involve this key parameter and how it has helped improve our understanding of AGNs, and set the stage for the ongoing and upcoming, exciting studies with state-of-the-art facilities and observatories, e.g., JWST (Gardner et al., 2006), Dark Energy Spectroscopic Instrument (DESI, DESI Collaboration et al., 2025), and Rubin-LSST (Ivezić et al., 2019; Pozo Nuñez et al., 2023; Czerny et al., 2023b). In the following sections, we will summarize a few recent advancements that have allowed us to unravel the connection between the black hole activity and the mass of the SMBH, and in turn, the Eddington ratio, as well as the novel relations we have found. That would not be possible without the use of spectrophotometric observations of AGNs using a multitude of telescope facilities - targeted and survey-mode, single-epoch and monitoring campaigns, archival and new observations, covering the two hemispheres.

2. Getting ready for LSST: Photo-variability reveals a nearly Universal scaling relation

We have all been greeted with the *first look* of Rubin[4] and the potential it will have in the coming decade upon the start of its operations. We expect the Legacy Survey of Space and Time (LSST) to discover tens of millions of AGNs - a recent study of QSO number counts puts this to ∼12.2 million in i-band stretching to a 5σ median depth of 26.4 mag (Ivezić et al. 2019, Li et al., under review). The latest survey simulations (v5.0) suggest a mean cadence of nearly every half-night in *riz* bands in the Wide-Fast-Deep (WFD) mode, while this can be as high as every 3 nights for the u-band. The numbers are slightly more optimistic for the Deep-Drilling-Fields (DDFs, see e.g., Pozo Nuñez et al. 2024). The sheer amount of data that is going to be involved is nothing that we have analyzed before. Not to forget, it is going to be a daunting challenge to get a spectroscopic follow-up for all these detections, although some upcoming surveys seem promising (ESO/4MOST - de Jong et al. 2019; Frohmaier et al. 2025, Spec-S5 - Besuner et al. 2025, WST - Mainieri et al. 2024). In anticipation of the start of Rubin operations and to tackle the prospective challenge of spectra-starving,

---

[4] `https://rubinobservatory.org/gallery/collections/first-look-gallery`

we looked into the large repository of photometrically detected and monitored AGNs in the Zwicky Transient Facility (ZTF, Bellm et al., 2019; Graham et al., 2019) that led to a rather convincing discovery.

2.1. Photometric variability anti-correlates with the Eddington ratio

The paper (Benati Gonçalves et al., 2025) presents a systematic study of optical variability for 915 type-1 quasars with $0 \leq z \leq 3$, using ZTF g-band light curves and Sloan Digital Sky Survey (SDSS) DR16 spectral parameters (including black-hole masses, bolometric luminosities, and Eddington ratios). These sources were pre-selected from the All Quasar Multiepoch Spectroscopy (AQMES) MEDIUM subsample of the Black Hole Mapper project of the SDSS-V (Kollmeier et al., 2019). We computed the fractional variability amplitude ($\mathrm{F_{var}}$) via the excess-variance formalism, and after rigorous filtering ($\geq$ 100 observations, $\mathrm{F_{var}} > 0$) and correcting for minimal emission-line contributions (a few percent of the continuum flux), we arrive at a key result - a redshift-independent anti-correlation between $\mathrm{F_{var}}$ and the Eddington ratio (λ_{Edd}). The best-fit relation for the full sample is

$$\log \lambda_{\mathrm{Edd}} = (-0.71 \pm 0.06) \log(\mathrm{F_{var}}) - (1.52 \pm 0.06) \tag{1}$$

or equivalently $\mathrm{F_{var}} \approx 10^{-0.71} \lambda_{\mathrm{Edd}}^{-1.52}$ (see, e.g., Figure 1 for a revised version). This yields a Pearson coefficient r ≈ -0.31 ($p < 0.01$) for all redshifts, with the strongest anti-correlation at low-z (r ≈ -0.40) and a marginal trend in the highest bin ($2 \leq z < 3$). We present a general equation encapsulating this relationship, which appears to be almost free of redshift dependence, enabling predictions of quasar variability based on accretion parameters or vice versa, a significant enhancement to prior works (see e.g., Klimek et al., 2004). The derived relation with the Eddington ratio provides a unified framework for interpreting variability in AGNs and facilitates future studies of quasar variability using high-cadence surveys, such as the Vera C. Rubin Observatory's LSST (Ivezić et al., 2019).

Additional correlations show that $\mathrm{F_{var}}$ declines monotonically with continuum luminosities $\mathrm{L_{1350}}$, $\mathrm{L_{3000}}$, $\mathrm{L_{5100}}$, and bolometric luminosity across all redshift bins (negative Pearson r values ranging from -0.23 to -0.59), while, the $\mathrm{F_{var}}$–$\mathrm{M_{BH}}$ relationship evolves from a weak positive correlation at low-z (r ≈ 0.22) to a moderate anti-correlation at high-z (r ≈ -0.36). We discussed potential selection biases (luminosity-driven Malmquist bias, rest-frame time-baseline shortening at high-z) but demonstrate that the correlation between $\mathrm{F_{var}}$ and λ_{Edd} is largely free of any significant redshift dependence (see Benati Gonçalves et al., 2025, for more details).

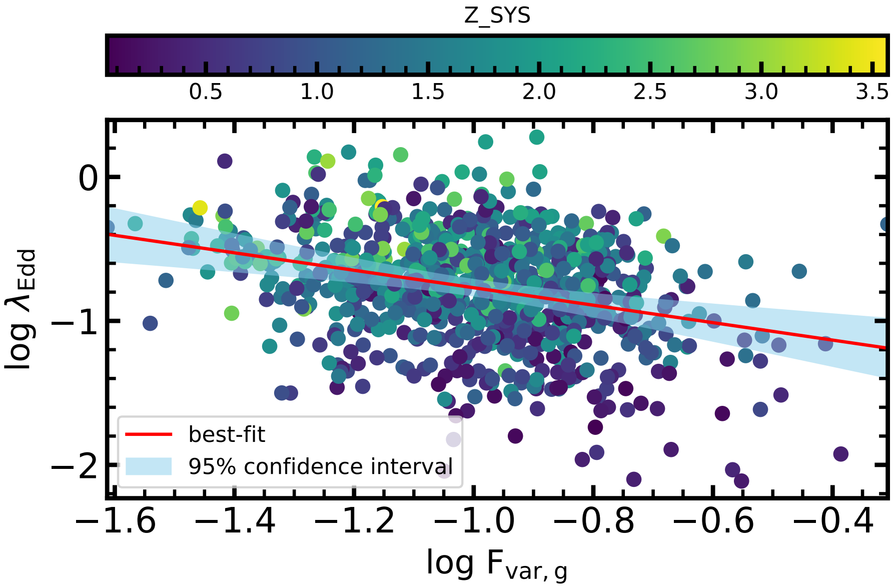

Figure 1. Distribution of the fractional variability ($F_{\rm var}$) in the g-band ZTF lightcurves for the AQMES medium field monitored within the SDSS-V, versus the Eddington ratio. The latter is taken from the SDSS DR16 QSO catalogue (Wu & Shen, 2022). The color axis depicts the distribution of redshift. The best-fit correlation after cleaning sources with insufficient $F_{\rm var}$ in g-band information: log $\lambda_{\rm Edd}$ = -0.61 log $F_{\rm var}$ - 1.38 (ρ = -0.28; p-value = 2.8E-18).

2.2. Possible biases and streamlining the parent sample

Below, we summarize some additional tests of robustness for our newfound scaling relation.

- lightcurve baseline testing: as it currently stands, the correlation involves all AGNs with at least 100 observations in overa 6-year period (mid-2017 to late-2023). The median of the number of g-band observations is 304; thus, we attempted to check the correlation for only those cases where the number of visits was $\geq$ 300. We were left with 53% of the number of AGNs (488/920). However, the correlation grew stronger: log $\lambda_{\rm Edd}$ = -0.71 log $F_{\rm var}$ - 1.50 (ρ = -0.31; p-value = 2.74E-12), almost identical to the original version as shown in Eq. 1.

- removing host-dominated sources: Given the wide range of redshift considered in the sample selection ($z \leq 3$), we decided to also check the variety in our sample with respect to the contamination induced by the presence of a strong host component. This is especially an issue for the low-z sample ($z \leq 1$), where the fitting routine in the spectral decomposition code PyQSOFit (Guo et al., 2018) - the mainstay pipeline used to derive the SDSS DR16 QSO catalog chooses whether to fit a host-galaxy component to the spectrum or not, based on a minimum number of host-galaxy pixels identified by the routine. If this criterion is not met, no host galaxy component is fit. Another way to look at this issue is that if the AGN dominates the spectrum, the resulting fit will have a negligible host-galaxy contribution. At the moment of writing, we do not have a straightforward way to filter such sources out without this information. On the other hand, for the sources with $z > 1$, no host galaxy template is incorporated (the host galaxy template fits within the rest-frame SDSS range, i.e., 3450-8000 Å). Therefore, we only rely on the Malmquist bias for this latter case. Nonetheless, we made a simple test to account for the host contribution. The QSO catalog does provide us with the fractional host contribution at 5100Å ($f_{\mathrm{host},5100}$). We plotted the distribution for $f_{\mathrm{host},5100}$ and noted a clear dichotomy at 0.4 (see Figure 2 left panel). After filtering out the sources' significant host contribution ($>$ 40%), resulting in recovery of 86% of the sample (792/920), we still recover a familiar version of the correlation between λ_{Edd} and F_{var}.

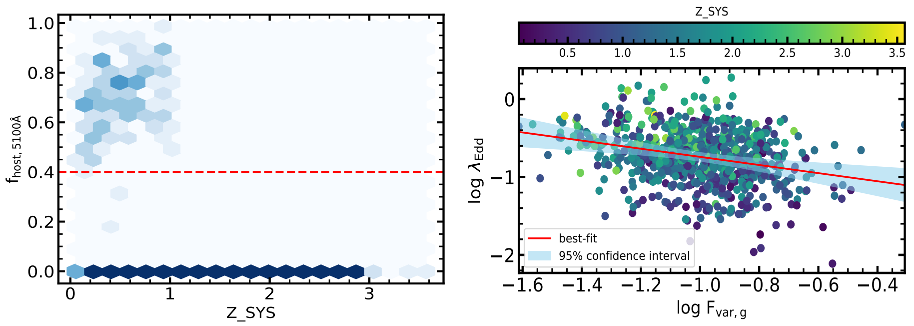

Figure 2. (Left:) Host fraction (estimated at 5100 Å) as a function of redshift for our sample. The hexagons highlight the number density of sources with a darker shade of blue corresponding to higher density. (Right:) The best-fit correlation after filtering out the sources with significant host contribution (>40%): $\log \lambda_{\mathrm{Edd}} = -0.52 \log F_{\mathrm{var}} - 1.26$ ($\rho = -0.27$; p-value = 7.1E-15).

- combining the above two cases: taking the two above cases together and making the cut, we recover a correlation similar to the original one (with 44% of the sample): $\log \lambda_{\mathrm{Edd}} = -0.62 \log F_{\mathrm{var}} - 1.37$ ($\rho = -0.3$; p-value = 9.78E-10).

- quality cut on the relative error in F_{var}: Next we capitalize on the relative error in the F_{var} itself. The $errF_{var}/F_{var}$ in the g-band has a distribution with a median around 57%. Thus, we tried a simple cut to limit to the sources with less than 50% in relative error in F_{var}. This led to a substantial reduction in the remaining sources (∼39%; 357/920). Applying this cut only, we get a stronger correlation than its original form: $\log \lambda_{Edd}$ = -0.83 $\log F_{var}$ - 1.54 (ρ = -0.32; p-value = 5.78E-10).

- dependence on the M_{BH} bins: To check the co-dependence of M_{BH} on the derived correlation, we made a test by binning the sources within 4 equal bins of M_{BH}. The M_{BH} distribution for the cleaned sample of 920 sources ranges from $10^{6.81}$ to $10^{10.32}$ $M_\odot$, with a mean $\sim 10^{8.99}$ $M_\odot$ (σ = 0.55 dex; median mass = $\sim 10^{9.09}$ $M_\odot$). We thus constructed 4 bins, each of 1 dex width, i.e., between 6.5 - 7.5, 7.5 - 8.5, 8.5 - 9.5, and 9.5 - 10.5. These bins have 14, 148, 607, and 151 sources, respectively. The correlation for each M_{BH} bin is found as follows:
  - bin-1: $\log \lambda_{Edd}$ = -0.79 $\log F_{var}$ - 1.53 (ρ = -0.1; p-value = 0.725)
  - bin-2: $\log \lambda_{Edd}$ = -1.03 $\log F_{var}$ - 1.71 (ρ = -0.47; p-value = 2.32E-09)
  - bin-3: $\log \lambda_{Edd}$ = -0.58 $\log F_{var}$ - 1.33 (ρ = -0.25; p-value = 7.97E-10)
  - bin-4: $\log \lambda_{Edd}$ = -0.65 $\log F_{var}$ - 1.54 (ρ = -0.38; p-value = 1.62E-06)

  Given that most of the sources (66%) are in bin-3, the resemblance of the correlation for this bin relative to the cleaned sample is expected. We note also the shifting range in the redshift range as we move along the M_{BH} bins, which is connected to the Malmquist bias (wherein we tend to observe the brighter targets as we transcend in redshift). Another reason is the sensitivity of our spectrograph detectors, which marks a limiting magnitude below which the detection of targets is seldom. Given the direct proportionality between the M_{BH} and luminosity, the faintness of the target could lead to the estimation of a lower M_{BH} for these sources. We, however, miss these sources as we go along the redshift. We, therefore, need better facilities (e.g., DESI; Pucha et al. 2025) to probe this low-luminosity regime, esp. in the higher z regime, to have a better handle on completeness of the sample.

  However, interestingly, the correlation for bin-2 (7.5 - 8.5) is found to be the strongest among all (ρ = -0.47 with a slope suggesting an almost 1-to-1 inverse relation between F_{var} and λ_{Edd}). The top panel of Figure 3 shows the consolidated version of each bin's performance. This reveals an interesting conclusion: the dispersion between the individual best-fits varies between ∼ 0.5 dex (for the smallest values of $\log F_{var}$) to ∼ 0.25 dex (for the largest values of $\log F_{var}$). These values are consistent with the dispersion in the M_{BH} scaling relations often adopted (e.g., the M-$\sigma_\star$ relation with a dispersion ∼0.44 dex, Prieto et al. 2022; and similarly for RM-derived M_{BH},

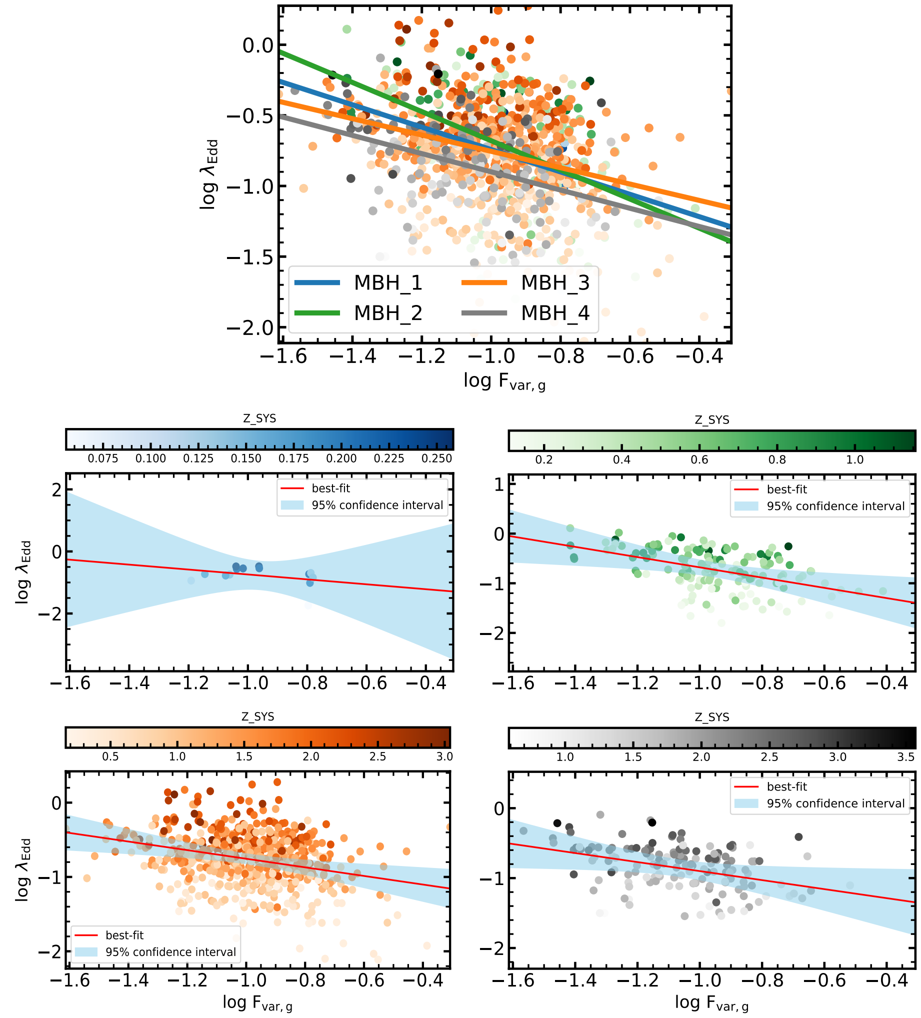

Figure 3. Correlations similar to as shown in Figure 1, but with the data binned in four separate bins of $M_{\rm BH}$ (in log-scale, in $M_\odot$ units): between 6.5 - 7.5 (blue), 7.5 - 8.5 (green), 8.5 - 9.5 (orange), and 9.5 - 10.5 (grey). The sources are colored as per their respective $M_{\rm BH}$ bins, while the gradient in color represents the corresponding range in redshift as depicted in the lower sub-panels. The best-fit per $M_{\rm BH}$ bin is shown in the top panel. Each of the lower sub-panels shows the individual best-fit to the binned data per $M_{\rm BH}$ bin. The color-axis in each of these sub-panels is the redshift corresponding to the respective bin. Note the shifting range in the redshift range as we move along the $M_{\rm BH}$ bins.

i.e., between 0.4 - 0.51 dex, Du & Wang 2019). Also, it is interesting to see that, apart from the M_{BH} bin containing the largest BH massed sources, the rest of the three relations coincide around log F_{var} ∼ -0.9 and log λ_{Edd} ∼ -0.75. This could suggest that the correlation briefly becomes independent of the M_{BH} variations within this region.

Overall, these experiments only reinforce the *almost* universality of the relation found between the fractional variability (F_{var}) and the Eddington ratio (λ_{Edd}). The derived universal F_{var}–λ_{Edd} relation, therefore, enables predictions of quasar variability from accretion parameters and vice versa, offering a powerful tool for upcoming high-cadence surveys.

3. Changing-look and how?

The last decade has seen a surge in the detections of changing-look AGNs (CLAGNs) - these sources have marked increases in their variability features compared to their counterparts, which we discussed in the previous section; thanks to massive, multiplex spectroscopic surveys such as SDSS and DESI, to name a few. Combination of intensive photometric monitoring, e.g., Catalina Real-Time Transient Survey (CRTS, Drake et al., 2009) and Zwicky Transient Facility (ZTF, Bellm et al., 2019; Graham et al., 2019) and multi-epoch spectroscopy have revealed $\geq$ 500 known CLAGNs to date (Temple et al., 2023; Wang et al., 2024; Zeltyn et al., 2024; Guo et al., 2025b). Many of these detections were serendipitous to start with, but as we prepare for Rubin LSST to start its operations, the community has become more aware of selection criteria to look for CLAGNs in massive datasets, and even forecast the changing-state of these AGNs (Graham et al., 2020; Sánchez-Sáez et al., 2021; Ricci & Trakhtenbrot, 2023). With the aid of beyond-meter class facilities, e.g., Gemini/ESO-VLT/DESI, we now peer deep into the redshift space to reveal CLAGN candidates close to the cosmic noon (Ross et al., 2020; Guo et al., 2025a). Understanding the nature of this special class of AGNs in contrast to the general variable nature of AGNs is vital to our understanding and perhaps aids in revealing new classes of CLAGNs, e.g., the extreme variability quasars (EVQs, Ren et al., 2022).

In this direction, we (Panda & Śniegowska, 2024) made a significant stride to reveal where the population of the CLAGNs is mostly discovered through a systematic analysis of known SDSS CLAGNs. In the next sub-section, we describe our methodology and the key findings that connect again the key parameter - Eddington ratio (see left panel in Figure 4).

3.1. Eddington ratio distribution as a proxy to catch Changing-Look AGNs

The paper by Panda & Śniegowska (2024) presents a homogeneous spectroscopic analysis of 93 CLAGNs compiled from the SDSS, BOSS, and eBOSS archives. Multi-epoch spectra are processed with the PyQSOFit pipeline (Guo et al., 2018), delivering epoch-resolved measurements of the AGN continuum, broad-line parameters, black-hole mass (M_{BH}), and Eddington ratio (λ_{Edd}). The sample was assembled by cross-matching existing CLAGN catalogs and retrieving all available SDSS spectra, ensuring at least two epochs with detectable broad Hβ emission profiles. Spectral decomposition follows the standard PyQSOFit methodology, incorporating a power-law continuum, Fe II emission templates, and host-galaxy eigenspectra when required. Each epoch is placed on the optical Eigenvector 1 (EV1) plane, i.e, the optical plane between the broad FWHM(Hβ) versus the strength of the optical Fe II emission, i.e., the parameter R_{Fe}. This is the canonical quasar main-sequence diagram (Boroson & Green, 1992; Sulentic et al., 2000; Marziani et al., 2001, 2018; Panda et al., 2019b; Panda, 2024). The majority of CL-AGNs evolve within Population-B (FWHM Hβ > 4000 km/s), with only a few exhibiting inter-population transitions (A $\rightleftharpoons$ B). Turn-on events are accompanied by systematic shifts toward lower M_{BH} and, therefore, higher λ_{Edd}, supporting accretion-rate modulation as the primary driver of the phenomenon. We then classified the sources as "Turn-On", "Turn-Off" or mixed "On-Off" cycles; and found that the distribution is dominated by simple monotonic transitions, echoing earlier reports that turn-off events are more frequently observed (Shen & Burke, 2021). Balmer-decrement (Hα/Hβ) variability is examined for 32 objects with at least 3 epochs. The ratios display diverse temporal behavior, often deviating from the case-B value ($\sim$3.1, Osterbrock & Ferland 2006), implying a complex interplay among dust extinction, BLR density, and ionizing-continuum changes. The resulting database furnishes a comprehensive resource for probing the physical mechanisms behind AGN spectral variability. The systematic migration of CLAGNs on the EV1 and M_{BH} - λ_{Edd} planes bolsters models in which rapid accretion-rate fluctuations dominate the changing-look phenomenon (Noda & Done, 2018; Sniegowska et al., 2020), while heterogeneous Balmer-decrement trends suggest additional BLR structural evolution.

The main finding from this study was the realization of the Eddington ratio distribution of these CLAGNs. We specifically consider the spectral epochs as widely separated in time and with the most variation in the continuum and emission line characteristics to reveal that the CLAGNs dominate the low-accretion regime ($\lambda_{Edd} \sim 0.01$), dominated by sources in the Population B (FWHM Hβ $\geq$ 4000 km s^{-1}), in contrast to the high accretors that dominate the Population A parameter space (Du et al., 2018; Panda et al., 2019b; Śniegowska et al., 2021; Garnica et al., 2022).

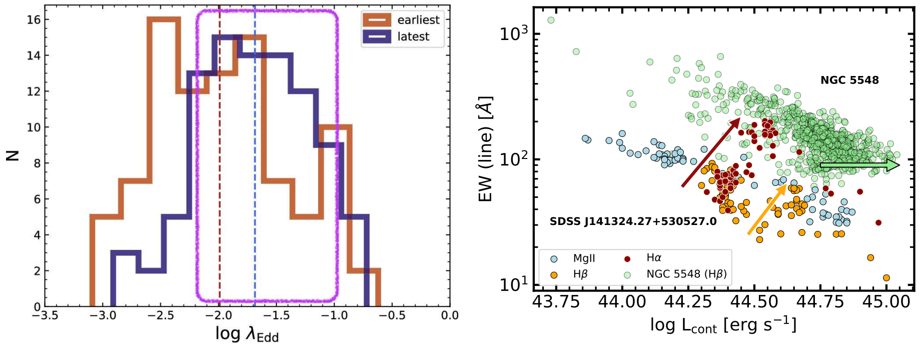

Figure 4. (*Left:*) Distribution of Eddington ratios in the sample from Panda & Śniegowska (2024). We show the distributions for the earliest (in brown) and the latest (in purple) epochs for the sources in our sample. The median values for the two distributions (red = -1.99, blue = -1.685) are marked with vertical dashed lines. The magenta box marks the range of the Eddington ratio for NGC 5548, i.e., log $\lambda_{\rm Edd}$ = [-2.2, -1]. (*Right:*) The distribution of the emission line EW versus the AGN continuum luminosity. Here, we demonstrate the trend for two sources: SDSS J141324.27+530527.0 (Wang et al., 2018) with 72 spectral epochs over ∼15 years (5527 days), and NGC 5548 (Bon et al., 2018; Panda et al., 2022, 2023) with more than 750 spectral epochs over ∼25 years (9624 days). For the former source (SDSS J141324.27+530527.0), we have taken the spectral data from the homogeneous fitting in Panda & Śniegowska (2024), which includes the MgII, Hβ, and Hα emission lines and the corresponding AGN continua nearest to these lines (at 3000Å, 5100Å, and 6000Å), as shown in the panel. For NGC 5548, we show the dataset from Panda et al. (in prep.), which is an updated version of the dataset provided in Bon et al. (2018), where the authors analyzed the Hβ region. The SDSS source shows a clear rise from a deep minimum to a high state in both Balmer lines. However, the MgII shows a rather flat behavior - reminiscent of the Baldwin effect, suggesting the difference in ionization and response to the changing continuum levels. NGC 5548 data has a wealth of data, but the change in the source is rather gradual, and hence, a clear spike in the trend is not that prominent.

3.2. Population studies vs. tracking the changes in an individual source

Going back to the BLR structural evolution, it would be great if we could capitalize on single-object studies over longer temporal baselines to reveal and distinguish between short, intermediate, and long-term variations in these AGNs. We are fortunate to have such rich datasets focused on single AGN spectrophotometric monitoring, notably of the prototypical Population B source - NGC 5548. Taking advantage of $\geq$ 30 years of data compiled from $\sim$ 17 individual observing campaigns - including the AGN Watch and AGN STORM projects (Peterson et al., 2002; Shapovalova et al., 2004; De Rosa et al., 2015; Fausnaugh et al., 2016; Pei et al., 2017), we (Panda et al., 2022, 2023) re-discovered the saturation of the Hβ emission with growing AGN continuum luminosity, also known as the Pronik-Chuvaev effect (Pronik & Chuvaev, 1972). NGC 5548 has telltale signatures of being a CLAGN, and this anomalous behavior of the Hβ with changing continuum luminosity (Gaskell et al., 2021) has opened new avenues for us to improve our spectral models to not only reveal the inner working of the AGN, but to use this source as a laboratory to better understand the CLAGN behavior. For instance, in the right panel of Figure 4, we demonstrate the trend between the EW(Hβ) with increasing AGN luminosity, the well-known Baldwin effect (Wandel, 1999; Martínez-Aldama et al., 2021) - however, we see a flattened behavior at the extreme high end of the luminosity. This is the Pronik-Chuvaev effect. We try to check whether the CLAGNs that were studied in Panda & Śniegowska (2024) show a similar behavior to NGC 5548. To this end, we consider our best case - SDSS J141324.27+530527.0 (Wang et al., 2018), an object with 72 spectral epochs spanning over ∼15 years (5527 days). Another interesting thing with the latter source is the availability of EW information for Mg II, and Hα, in addition to Hβ for all epochs. We overlay the EW for these three emission lines in the same figure as NGC 5548. To be consistent, we utilize the continuum closest to each line. For Mg II this continuum was extracted at 3000Å while for Hβ and Hα, we use the continua at 5100Å and 6000Å respectively. We see a clear flattening behavior in Hβ in the SDSS source at higher luminosities; however, we note a rise-and-fall effect in the Balmer lines - Hα rises first, followed by Hβ. Whereas, the Mg II doesn't show any such prominent change along the luminosity trend. Not so surprisingly, the SDSS source, during its 72 epochs, modulated in Eddington ratio between (in log-scale) -0.75 to -2.5. This range is not so different from NGC 5548, which has been observed to vary in Eddington ratio between (in log-scale) -1 to -2.2. Is this a coincidence, or are we onto something? This definitely needs further investigation.

Looking into the future, we are now well-poised to utilize these findings to pre-select changing-look (and changing-state) candidates in large datasets and up-and-coming high-fidelity surveys, in conjunction with variability statistics, color-color diagrams, and marked flux variations (Shen & Burke, 2021; Ricci & Trakhtenbrot, 2023).

4. Resolving and revealing: highlights from SOAR/SIFS

Continuing our venture in the low-accretion regime, AGN spectral energy distributions (SEDs) provide a powerful diagnostic to probe the dominant ionization mechanism, test against high-quality observations, and assess the true accretion state of the AGN. In this context, we present a salient case that combines state-of-the-art photoionization modeling with one of the first high-angular-resolution integral field unit (IFU) observations obtained with the 4m SOAR telescope. This study, focused on the nearby Seyfert 2 galaxy ESO 138-G001, directly contests earlier interpretations based on HST imaging (see Figure 5). We confirm that the observed spectra are unequivocally AGN-dominated and further demonstrate that peripheral emission structures arise from filtered radiation originating from the nucleus. Using a quantitative, iterative technique, we successfully generated synthetic spectra in remarkable agreement with both nuclear and off-nuclear observations, reinforcing the AGN-driven photoionization of this low-accreting Type-2 AGN extending beyond a few hundred parsecs from the nucleus.

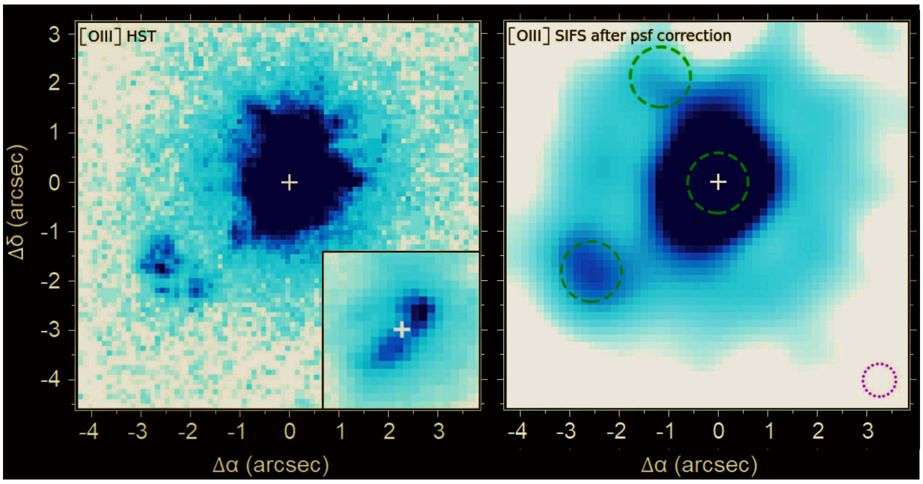

Figure 5. (*Left:*)[O III]λ5007 emission image of ESO 138-G001 from the HST/WFPC2 (Ferruit et al., 2000) with a small inset showing the details of the central part, where the nucleus is marked with a plus sign; (*Right:*) [O III]λ5007 emission image from SIFS after data treatment involving spatial re-sampling with quadratic interpolation followed by the Richardson-Lucy PSF deconvolution (see Rodríguez-Ardila et al., 2024, for more details). The green circles – with an aperture radius of 0.6 arcsec – denote the extraction regions of the spectra for the North-East (NE) knot (top left), the South-East (SE) blob (bottom left), and the nuclear region. The red circle denotes the PSF FWHM of 0.71 arcsec.

In Rodríguez-Ardila et al. (2024), we investigated the inner ~600 pc of ESO 138-G001 using the SOAR Integral Field Spectrograph[5] (SIFS; Lepine et al. (2003)). ESO 138-G001 is the nearest known Coronal Line Forest (CLiF) AGN

---

[5] The SIFS IFU employs a lenslet–fiber array with 1300 elements, yielding 1300 simultaneous spectra across a 15 × 7.8 arcsec^2 field of view at a spatial sampling of 0.30 arcsec per fiber. The data span 4200–7000 Å with $R \sim 4200$.

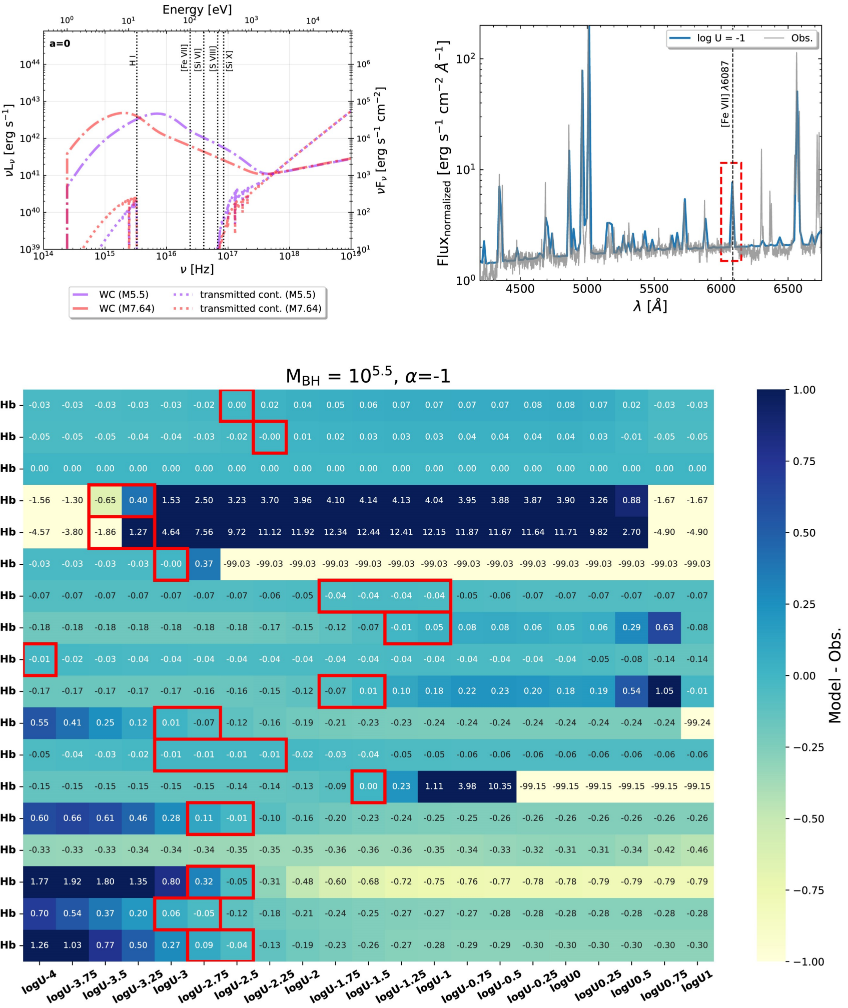

$M_{BH} = 10^{5.5}$, α=-1

	logU-4	logU-3.75	logU-3.5	logU-3.25	logU-3	logU-2.75	logU-2.5	logU-2.25	logU-2	logU-1.75	logU-1.5	logU-1.25	logU-1	logU-0.75	logU-0.5	logU-0.25	logU0	logU0.25	logU0.5	logU0.75	logU1
Ar4a/Hb	-0.03	-0.03	-0.03	-0.03	-0.03	-0.02	0.00	0.02	0.04	0.05	0.06	0.07	0.07	0.07	0.07	0.08	0.08	0.07	0.02	-0.03	-0.03
Ar4b/Hb	-0.05	-0.05	-0.05	-0.04	-0.04	-0.03	-0.02	-0.00	0.01	0.02	0.03	0.03	0.03	0.04	0.04	0.04	0.04	0.03	-0.01	-0.05	-0.05
Hb/Hb	0.00	0.00	0.00	0.00	0.00	0.00	0.00	0.00	0.00	0.00	0.00	0.00	0.00	0.00	0.00	0.00	0.00	0.00	0.00	0.00	0.00
O3a/Hb	-1.56	-1.30	-0.65	0.40	1.53	2.50	3.23	3.70	3.96	4.10	4.14	4.13	4.04	3.95	3.88	3.87	3.90	3.26	0.88	-1.67	-1.67
O3b/Hb	-4.57	-3.80	-1.86	1.27	4.64	7.56	9.72	11.12	11.92	12.34	12.44	12.41	12.15	11.87	11.67	11.64	11.71	9.82	2.70	-4.90	-4.90
Fe14/Hb	-0.03	-0.03	-0.03	-0.03	-0.00	0.37	-99.03	-99.03	-99.03	-99.03	-99.03	-99.03	-99.03	-99.03	-99.03	-99.03	-99.03	-99.03	-99.03	-99.03	-99.03
Ca5/Hb	-0.07	-0.07	-0.07	-0.07	-0.07	-0.07	-0.07	-0.06	-0.05	-0.04	-0.04	-0.04	-0.04	-0.05	-0.06	-0.07	-0.07	-0.07	-0.07	-0.07	-0.07
Fe7a/Hb	-0.18	-0.18	-0.18	-0.18	-0.18	-0.18	-0.18	-0.17	-0.15	-0.12	-0.07	-0.01	0.05	0.08	0.08	0.06	0.05	0.06	0.29	0.63	-0.08
He1/Hb	-0.01	-0.02	-0.03	-0.04	-0.04	-0.04	-0.04	-0.04	-0.04	-0.04	-0.04	-0.04	-0.04	-0.04	-0.04	-0.04	-0.04	-0.05	-0.08	-0.14	-0.14
Fe7b/Hb	-0.17	-0.17	-0.17	-0.17	-0.17	-0.16	-0.16	-0.15	-0.12	-0.07	0.01	0.10	0.18	0.22	0.23	0.20	0.18	0.19	0.54	1.05	-0.01
O1/Hb	0.55	0.41	0.25	0.12	0.01	-0.07	-0.12	-0.16	-0.19	-0.21	-0.23	-0.23	-0.24	-0.24	-0.24	-0.24	-0.24	-0.24	-0.24	-0.24	-99.24
S3/Hb	-0.05	-0.04	-0.03	-0.02	-0.01	-0.01	-0.01	-0.01	-0.02	-0.03	-0.04	-0.05	-0.05	-0.06	-0.06	-0.06	-0.06	-0.06	-0.06	-0.06	-0.06
Fe10/Hb	-0.15	-0.15	-0.15	-0.15	-0.15	-0.15	-0.14	-0.14	-0.13	-0.09	0.00	0.23	1.11	3.98	10.35	-99.15	-99.15	-99.15	-99.15	-99.15	-99.15
N2a/Hb	0.60	0.66	0.61	0.46	0.28	0.11	-0.01	-0.10	-0.16	-0.20	-0.23	-0.24	-0.25	-0.25	-0.26	-0.26	-0.26	-0.26	-0.26	-0.26	-0.26
Ha/Hb	-0.33	-0.33	-0.33	-0.34	-0.34	-0.34	-0.35	-0.35	-0.35	-0.36	-0.36	-0.36	-0.35	-0.34	-0.33	-0.32	-0.31	-0.31	-0.34	-0.42	-0.46
N2b/Hb	1.77	1.92	1.80	1.35	0.80	0.32	-0.05	-0.31	-0.48	-0.60	-0.68	-0.72	-0.75	-0.76	-0.77	-0.78	-0.78	-0.79	-0.79	-0.79	-0.79
S2a/Hb	0.70	0.54	0.37	0.20	0.06	-0.05	-0.12	-0.18	-0.21	-0.24	-0.25	-0.27	-0.27	-0.27	-0.28	-0.28	-0.28	-0.28	-0.28	-0.28	-0.28
S2b/Hb	1.26	1.03	0.77	0.50	0.27	0.09	-0.04	-0.13	-0.19	-0.23	-0.26	-0.27	-0.28	-0.29	-0.29	-0.30	-0.30	-0.30	-0.30	-0.30	-0.30

Figure 6. (*Top left:*) Incident SEDs generated for our photoionization modeling. The incident continua for the two black hole mass cases are shown in dot–dashed. These are used for the modeling of the nuclear region. The corresponding transmitted continua from these models are shown in dotted lines. These latter distributions are used as incident continua for the SE blob. These SEDs have been made assuming a non-spinning black hole. The IPs for notable coronal lines along with the hydrogen ionization front at 13.6 eV are marked with vertical lines; (*Top right:*) Synthetic spectrum (blue) comparison with observed spectrum (in grey), for the nuclear region, generated for the SED corresponding to the $M_{BH} = 10^{5.5}$ $M_\odot$, and ionization parameter, log U = -1. (*Bottom:*) Heatmap for the same BH mass case, $M_{BH} = 10^{5.5}$ $M_\odot$, for the density law slope, α = -1, for the nuclear region. Each of the considered emission lines is normalized to the Hβ emission line. The x-axis represents the range of ionization parameters considered in our models in each panel. The cases of ionization parameters for each line ratio that have the smallest residuals (modeled ratio–observed ratio) are highlighted with red boxes. Courtesy: Rodríguez-Ardila et al. (2024).

(Rose et al., 2015), characterized by unusually strong high-ionization lines (IP $\geq$ 100 eV) compared to typical AGN. This makes it an ideal laboratory to investigate the physics of coronal line emission. Earlier long-slit optical and near-infrared studies by Cerqueira-Campos et al. (2021) revealed a hidden broad-line region and a rich set of coronal lines, extending up to [Fe XIII] (IP = 330.8 eV) in the NIR.

From multiple, strong, narrow emission lines, we obtained $z = 0.00914$, corresponding to a physical scale of ~146 pc arcsec^{-1}. ESO 138-G001 is notable for its compact and intense coronal line emission, as well as a bright high-excitation blob ~3 arcsec southeast of the nucleus. The spatial resolution of SIFS enabled us to show that the coronal line forest emission is confined to a ~0.8 arcsec region centered on the nucleus and is powered by the AGN continuum. Radiative transfer modeling further established that the AGN spectrum is filtered by circumnuclear gas within a few tens of parsecs, such that the ionization cone and the SE blob are illuminated by a modified SED dominated by low- to mid-ionization lines, with no evidence for coronal lines (Figure 6).

Photoionization modeling with `cloudy` (Ferland et al., 2017) reproduced the observed coronal line spectrum and implied a black hole mass of $\sim 3.2 \times 10^5$ $M_\odot$, consistent with the value obtained from prior X-ray variability estimates from XMM-Newton (Hernández-García et al., 2015). The inferred accretion rate is ~1% of the Eddington limit. Our models recovered nearly all observed permitted and forbidden transitions, providing strong validation of the approach.

The incident SEDs were generated using the AGNSED three-component framework (disk, warm corona, hot corona; Kubota & Done 2018), which has proven effective for modeling coronal line emission across a wide range of AGN properties (Prieto et al., 2022). Applying this framework to ESO 138-G001, we leveraged its known redshift, black hole mass, and Eddington ratio to construct ionizing continua tailored to the source. While archival studies suggested discrepant mass estimates ($\log M_{\rm BH} = 5.5$ vs. 7.64; in units of $M_\odot$), our iterative spectral synthesis confirmed the lower value, consistent with the X-ray results, and an accretion rate of $\lambda_{\rm Edd} \approx 0.01$.

Kinematic analysis revealed broad Gaussian components in the brightest nuclear lines (e.g., [O III], Hα, [Fe VII]) with FWHM ~450–600 km s^{-1}, indicative of a nuclear outflow confined within the central arcsecond. Electron densities span 10^{3-4} cm^{-3}, reaching $\sim 5.7 \times 10^3$ cm^{-3} at the nucleus, while [O III] ratios imply $T_e \sim 2.1 \times 10^4$ K. The SE blob, at ~2.6 arcsec from the nucleus, displays only low- to mid-ionization lines and no coronal emission, consistent with photoionization by a filtered AGN continuum. The NE knot, in contrast, shows disturbed kinematics suggestive of interaction with a radio jet.

Taken together, these results establish ESO 138-G001 as a prototype CLiF AGN hosting a highly compact coronal line region, a modest nuclear outflow, and an ionization-cone geometry in which the SE blob and NE knot delineate the cone edges. The detailed interplay of coronal line emission, filtered radiation, and outflow/jet dynamics provides one of the clearest demonstrations to date of how AGN SEDs govern line emission in the low-accretion regime.

5. A faster, efficient way to derive masses of supermassive black holes

Let us shift gears and look into the other end of the redshift/luminosity - the high redshift, high luminosity end, which fittingly brings us to the high-Eddington sources with a relatively small increase in the black hole masses. Reverberation mapping (RM) at high redshift is notoriously time-intensive, often requiring monitoring campaigns that span decades. Landmark studies such as Lira et al. (2018) and Kaspi et al. (2021) demonstrated this challenge, as luminous quasars at $z \sim 2$–3, while ideal for RM due to their high accretion rates and massive black holes, demand prohibitively long temporal baselines. Even with decade-long surveys like LSST, obtaining reliable BLR lags for these sources remains a formidable task.

To address this, we utilized the photometric reverberation mapping (PRM) technique as a rapid, cost-effective alternative to spectroscopic RM for measuring accretion-disk (AD) sizes in high-redshift quasars via the C IV emission line (Panda et al., 2024b). Using carefully chosen medium-band filters that isolate line-free continuum regions (with $\leq$2% BLR contamination), a high-cadence monitoring campaign at the meter-class telescopes recovered rest-frame AD time delays with 10–15% precision. This method proved $\sim$166 times faster than traditional BLR-based RM (Figure 7).

Simulations based on thin-disk reprocessing ($\tau \propto \lambda^{4/3}$) coupled with high signal-to-noise ratios ($\sim$100) observations, demonstrate that modest-aperture facilities can deliver robust PRM results. The analysis yielded a radius–luminosity ($\mathrm{R_{AD}}$–$\mathrm{L_{1350}}$) relation with $\beta \approx 0.5$, consistent with photoionization theory. By calibrating a scaling relation between AD and BLR sizes, black-hole masses can be estimated with $\sim$23% uncertainty - an efficient alternative where direct BLR reverberation is impractical.

Building on this, Pozo Nuñez et al. (2025) demonstrated the technique during a six-month campaign of QSO J0455–4216 ($z = 2.662$), mapping an accretion disk beyond the cosmic noon for the first time. The recovered delay spectrum followed the expectations of a Shakura–Sunyaev thin disk (Shakura & Sunyaev, 1973) irradiated in a lamp-post geometry, yielding a mean emissivity radius of

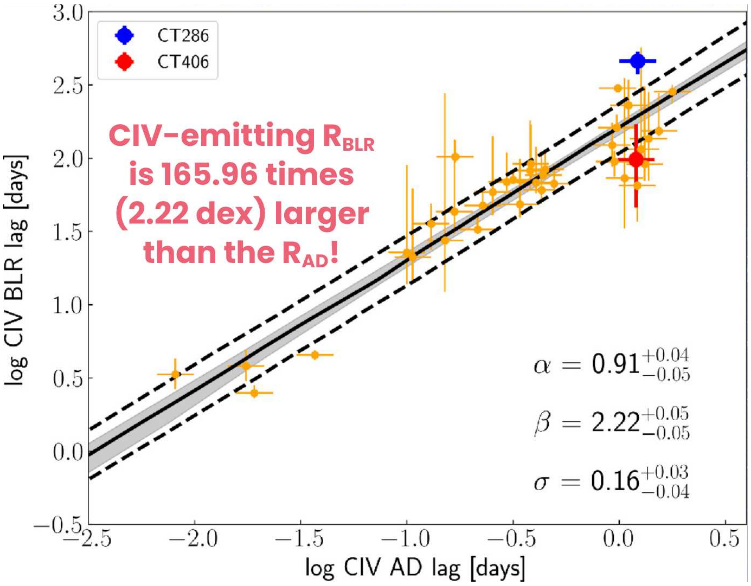

Figure 7. Recovered $R_{\rm BLR}$–$R_{\rm AD}$ relation; Courtesy: Panda et al. (2024b). The solid black line represents the mean of the posterior probability distributions, while the shaded region denotes the corresponding 1σ confidence interval. The best-fit slope (α), intercept (β), and intrinsic scatter (σ) are reported together with their 1σ uncertainties. The dashed lines indicate the mean model predictions at the upper and lower bounds when the intrinsic scatter is incorporated. The positions of the two studied sources, CT286 and CT406, which belong to the class of high-accreting sources, are marked by the blue and red circles, respectively.

$4.75^{+1.12}_{-1.05}$ light-days in the observer's frame (1.29 light-days rest frame) and implying a black hole mass of $\sim$9 $\times 10^8$ M$\odot$.

In summary, traditional C IV-based BLR lags at $z \sim$ 2–3 required nearly two decades of monitoring and revealed BLR sizes corresponding to $\sim$16-year lags. In contrast, PRM can constrain AD sizes with only 4–5 months of dense monitoring, scale these to BLR sizes, and, with the aid of single-epoch spectroscopy and the virial relation, estimate black hole masses and Eddington ratios. This approach transforms the feasibility of high-redshift RM: small ground-based telescopes equipped with medium- and narrow-band filters can now probe accretion disks and black hole growth for hundreds to thousands of quasars across cosmic time, opening a rewarding avenue for future studies.

6. Why we should care about accretion-dependent SEDs and closing remarks

BHAR is straightforward to estimate; however, it depends crucially on the determination of the net bolometric output, or bolometric luminosity (L_{bol}). The estimation of the L_{bol} is not trivial and requires estimating the area under the broad-band spectral energy distribution (SED), although a crude estimate can be derived assuming a constant scaling (Richards et al., 2006) or a parametric 'bolometric correction' (Netzer, 2019) based on mean SEDs derived from composite AGN spectra. However, the overabundance of overly massive black holes at high-z (Mezcua et al., 2024; Habouzit, 2025) and them suggested to accrete at super-Eddington limits (Panda & Marziani, 2023; Marziani et al., 2025) is closely tied to our reliance on scaling relations and mean SEDs built from local samples, the latter being limited and originally made from the general population of quasars. Therefore, not only do we need accretion-dependent SEDs, but to infer bulk statistical properties of these highly-accreting AGNs and their neighborhood, we are in dire need to update our AGN SED databases, especially at higher redshifts - as we push forth to spatially resolve BLR in quasars at z=4 (GRAVITY+ Collaboration et al., 2025).

To this end, Garnica et al. (2025) presented semi-empirical spectral energy distributions (SEDs) tailored to extreme, high-accretion (xA) quasars. By integrating extensive optical survey data with multi-frequency archival data, we constructed median SEDs that capitalize on the pronounced spectral homogeneity observed among super-Eddington candidates (Panda & Marziani, 2023). The SED construction is performed in three spectral regimes - radio to NIR, optical-UV dominated by the accretion-disk, and in X-ray - each normalized at 5100Å to facilitate direct comparison with conventional templates. A systematic juxtaposition with the canonical Mathews & Ferland (MF87) SED underscores substantive divergences, particularly in the high-energy domain (see Figure 8). To evaluate the ramifications for broad-line region (BLR) diagnostics and how these SEDs affect the emitting regions, we employed `cloudy` photoionization simulations, demonstrating that the newly derived SED reproduces the extreme BLR conditions characteristic of xA quasars: markedly low ionization parameters, elevated gas densities, and supersolar metallicities. These physical conditions naturally account for the observed suppression of C IV relative to Hβ and the pronounced Fe II emission. In summary, the work delivers a data-driven, semi-empirical xA SED that diverges from traditional quasar templates and validates its influence on BLR physical-parameter determinations.

We provide `cloudy`-ready template median SED (q2) for the RQ extreme population A (drawn from the systematic analysis of 139 R_{Fe}-rich sources), along with the first and third quartiles (q1 and q3) for the community. (Garnica et al., 2025) suggests that for these xA SEDs characterized by high-to-super accretion

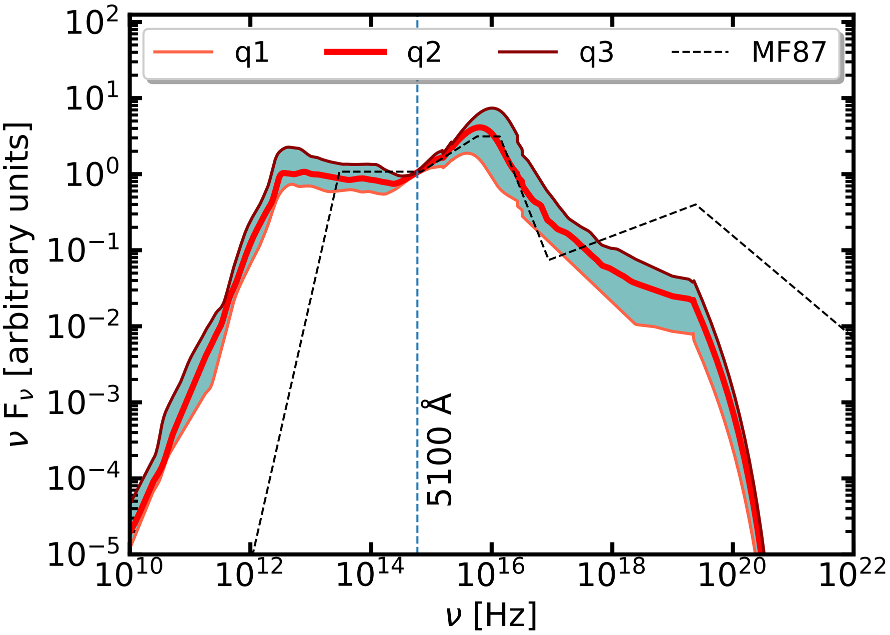

Figure 8. Spectral Energy Distributions (SEDs) from Garnica et al. (2025) for high--Eddington accreting (xA) quasars. The median SED (q2) and the inter-quartile range defined by the lower (q1) and higher (q3) SEDs are also highlighted. For reference, the often used AGN SED from Mathews & Ferland (1987) is also shown, demonstrating the variations in the broad-band SED shape relative to the Fe II strength-based SEDs.

mode, the bolometric output is more pronounced relative to the mean quasar SED from Richards et al. (2006), between 1.2 - 1.7 times higher[6].

In summary, we see that the Eddington ratio has come to our rescue in more than one way, and with the growing interest over the last decades and coming years promising more advancements and challenges, we are well-poised for many more interesting AGN-related discoveries.

Acknowledgements. S.P. is supported by the international Gemini Observatory, a program of NSF NOIRLab, which is managed by the Association of Universities for Research in Astronomy (AURA) under a cooperative agreement with the U.S. National Science Foundation, on behalf of the Gemini partnership of Argentina, Brazil, Canada, Chile, the Republic of Korea, and the United States of America. SP acknowledges the

---

[6] The bolometric corrections for the q1, q2 and q3 SEDs (luminosity based) are 11.16, 15.70, and 11.00, respectively.

entire organizing committee of the 15th Serbian Conference on Spectral Line Shapes in Astrophysics, for their invitation to this memorable conference. S.P. acknowledges Michael Eracleous and Ed Cackett for their helpful contributions and feedback. M.S. acknowledges support from the European Research Council (ERC) under the European Union's Horizon 2020 research and innovation program (grant agreement number 950533), and the Israel Science Foundation (grant number 1849/19). F.P.N. gratefully acknowledges the generous and invaluable support of the Klaus Tschira Foundation and funding from the European Research Council (ERC) under the European Union's Horizon 2020 research and innovation program (grant agreement No 951549).

References

Alexander, D. M., Hickox, R. C., Aird, J., et al., What drives the growth of black holes: A decade of progress. 2025, *New Astronomy Review*, **101**, 101733, `DOI:10.1016/j.newar.2025.101733`

Bellm, E. C., Kulkarni, S. R., Graham, M. J., et al., The Zwicky Transient Facility: System Overview, Performance, and First Results. 2019, *Publications of the ASP*, **131**, 018002, `DOI:10.1088/1538-3873/aaecbe`

Benati Gonçalves, H., Panda, S., Storchi Bergmann, T., Cackett, E. M., & Eracleous, M., Exploring Quasar Variability with ZTF at $0 < z < 3$: A Universal Relation with the Eddington Ratio. 2025, *Astrophysical Journal*, **988**, 27, `DOI:10.3847/1538-4357/addec0`

Bentz, M. C., Denney, K. D., Grier, C. J., et al., The Low-luminosity End of the Radius-Luminosity Relationship for Active Galactic Nuclei. 2013, *Astrophysical Journal*, **767**, 149, `DOI:10.1088/0004-637X/767/2/149`

Bentz, M. C., Peterson, B. M., Netzer, H., Pogge, R. W., & Vestergaard, M., The Radius-Luminosity Relationship for Active Galactic Nuclei: The Effect of Host-Galaxy Starlight on Luminosity Measurements. II. The Full Sample of Reverberation-Mapped AGNs. 2009, *Astrophysical Journal*, **697**, 160, `DOI:10.1088/0004-637X/697/1/160`

Besuner, R., Dey, A., Drlica-Wagner, A., et al., The Spectroscopic Stage-5 Experiment. 2025, *arXiv e-prints*, arXiv:2503.07923, `DOI:10.48550/arXiv.2503.07923`

Blandford, R. D. & McKee, C. F., Reverberation mapping of the emission line regions of Seyfert galaxies and quasars. 1982, *Astrophysical Journal*, **255**, 419, `DOI:10.1086/159843`

Bon, N., Bon, E., & Marziani, P., AGN Broad Line Region variability in the context of Eigenvector 1: case of NGC 5548. 2018, *Frontiers in Astronomy and Space Sciences*, **5**, 3, `DOI:10.3389/fspas.2018.00003`

Boroson, T. A. & Green, R. F., The Emission-Line Properties of Low-Redshift Quasi-stellar Objects. 1992, *Astrophysical Journal, Supplement*, **80**, 109, `DOI:10.1086/191661`

Cackett, E. M., Bentz, M. C., & Kara, E., Reverberation mapping of active galactic nuclei: from X-ray corona to dusty torus. 2021, *iScience*, **24**, 102557, `DOI:10.1016/j.isci.2021.102557`

Cao, S., Zajaček, M., Panda, S., et al., Standardizing reverberation-measured C IV time-lag quasars, and using them with standardized Mg II quasars to constrain cosmological parameters. 2022, *Monthly Notices of the RAS*, **516**, 1721, DOI:10.1093/mnras/stac2325

Cerqueira-Campos, F. C., Rodríguez-Ardila, A., Riffel, R., et al., Coronal-line forest active galactic nuclei - I. Physical properties of the emission-line regions. 2021, *Monthly Notices of the RAS*, **500**, 2666, DOI:10.1093/mnras/staa3320

Chelouche, D., Pozo Nuñez, F., & Kaspi, S., Direct evidence of non-disk optical continuum emission around an active black hole. 2019, *Nature Astronomy*, **3**, 251, DOI:10.1038/s41550-018-0659-x

Collin, S., Kawaguchi, T., Peterson, B. M., & Vestergaard, M., Systematic effects in measurement of black hole masses by emission-line reverberation of active galactic nuclei: Eddington ratio and inclination. 2006, *Astronomy and Astrophysics*, **456**, 75, DOI:10.1051/0004-6361:20064878

Czerny, B., Cao, S., Jaiswal, V. K., et al., Accretion disks, quasars and cosmology: meandering towards understanding. 2023a, *Astrophysics and Space Science*, **368**, 8, DOI:10.1007/s10509-023-04165-7

Czerny, B., Hryniewicz, K., Maity, I., et al., Towards equation of state of dark energy from quasar monitoring: Reverberation strategy. 2013, *Astronomy and Astrophysics*, **556**, A97, DOI:10.1051/0004-6361/201220832

Czerny, B., Panda, S., Prince, R., et al., Expectations for time-delay measurements in active galactic nuclei with the Vera Rubin Observatory. 2023b, *Astronomy and Astrophysics*, **675**, A163, DOI:10.1051/0004-6361/202345844

de Jong, R. S., Agertz, O., Berbel, A. A., et al., 4MOST: Project overview and information for the First Call for Proposals. 2019, *The Messenger*, **175**, 3, DOI:10.18727/0722-6691/5117

De Rosa, G., Peterson, B. M., Ely, J., et al., Space Telescope and Optical Reverberation Mapping Project.I. Ultraviolet Observations of the Seyfert 1 Galaxy NGC 5548 with the Cosmic Origins Spectrograph on Hubble Space Telescope. 2015, *Astrophysical Journal*, **806**, 128, DOI:10.1088/0004-637X/806/1/128

DESI Collaboration, Abdul-Karim, M., Adame, A. G., et al., Data Release 1 of the Dark Energy Spectroscopic Instrument. 2025, *arXiv e-prints*, arXiv:2503.14745, DOI:10.48550/arXiv.2503.14745

Di Valentino, E., Said, J. L., Riess, A., et al., The CosmoVerse White Paper: Addressing observational tensions in cosmology with systematics and fundamental physics. 2025, *Physics of the Dark Universe*, **49**, 101965, DOI:10.1016/j.dark.2025.101965

Drake, A. J., Djorgovski, S. G., Mahabal, A., et al., First Results from the Catalina Real-Time Transient Survey. 2009, *Astrophysical Journal*, **696**, 870, DOI:10.1088/0004-637X/696/1/870

Du, P., Lu, K.-X., Zhang, Z.-X., et al., Supermassive Black Holes with High Accretion Rates in Active Galactic Nuclei. V. A New Size-Luminosity Scaling Relation for the Broad-line Region. 2016, *Astrophysical Journal*, **825**, 126, DOI:10.3847/0004-637X/825/2/126

Du, P. & Wang, J.-M., The Radius-Luminosity Relationship Depends on Optical Spectra in Active Galactic Nuclei. 2019, *Astrophysical Journal*, **886**, 42, `DOI:10.3847/1538-4357/ab4908`

Du, P., Zhang, Z.-X., Wang, K., et al., Supermassive Black Holes with High Accretion Rates in Active Galactic Nuclei. IX. 10 New Observations of Reverberation Mapping and Shortened Hβ Lags. 2018, *Astrophysical Journal*, **856**, 6, `DOI:10.3847/1538-4357/aaae6b`

Edelson, R., Gelbord, J. M., Horne, K., et al., Space Telescope and Optical Reverberation Mapping Project. II. Swift and HST Reverberation Mapping of the Accretion Disk of NGC 5548. 2015, *Astrophysical Journal*, **806**, 129, `DOI:10.1088/0004-637X/806/1/129`

Fausnaugh, M. M., Denney, K. D., Barth, A. J., et al., Space Telescope and Optical Reverberation Mapping Project. III. Optical Continuum Emission and Broadband Time Delays in NGC 5548. 2016, *Astrophysical Journal*, **821**, 56, `DOI:10.3847/0004-637X/821/1/56`

Ferland, G. J., Chatzikos, M., Guzmán, F., et al., The 2017 Release Cloudy. 2017, *Revista Mexicana de Astronomia y Astrofisica*, **53**, 385, `DOI:10.48550/arXiv.1705.10877`

Ferruit, P., Wilson, A. S., & Mulchaey, J., Hubble Space Telescope WFPC2 Imaging of a Sample of Early-Type Seyfert Galaxies. 2000, *Astrophysical Journal, Supplement*, **128**, 139, `DOI:10.1086/313379`

Frohmaier, C., Vincenzi, M., Sullivan, M., et al., TiDES: The 4MOST Time Domain Extragalactic Survey. 2025, *arXiv e-prints*, arXiv:2501.16311, `DOI:10.48550/arXiv.2501.16311`

Gardner, J. P., Mather, J. C., Clampin, M., et al., The James Webb Space Telescope. 2006, *Space Science Reviews*, **123**, 485, `DOI:10.1007/s11214-006-8315-7`

Garnica, K., Dultzin, D., Marziani, P., & Panda, S., The spectral energy distribution of extreme population A quasars. 2025, *Monthly Notices of the RAS*, **540**, 3289, `DOI:10.1093/mnras/staf862`

Garnica, K., Negrete, C. A., Marziani, P., et al., High metal content of highly accreting quasars: Analysis of an extended sample. 2022, *Astronomy and Astrophysics*, **667**, A105, `DOI:10.1051/0004-6361/202142837`

Gaskell, C. M., Bartel, K., Deffner, J. N., & Xia, I., Anomalous broad-line region responses to continuum variability in active galactic nuclei - I. Hβ variability. 2021, *Monthly Notices of the RAS*, **508**, 6077, `DOI:10.1093/mnras/stab2443`

Graham, M. J., Kulkarni, S. R., Bellm, E. C., et al., The Zwicky Transient Facility: Science Objectives. 2019, *Publications of the ASP*, **131**, 078001, `DOI:10.1088/1538-3873/ab006c`

Graham, M. J., Ross, N. P., Stern, D., et al., Understanding extreme quasar optical variability with CRTS - II. Changing-state quasars. 2020, *Monthly Notices of the RAS*, **491**, 4925, `DOI:10.1093/mnras/stz3244`

GRAVITY+ Collaboration, El Dayem, K. A., Aimar, N., et al., Spatially resolved broad line region in a quasar at z=4: Dynamical black hole mass and prominent outflow. 2025, *arXiv e-prints*, arXiv:2509.13911, `DOI:10.48550/arXiv.2509.13911`

Grier, C. J., Trump, J. R., Shen, Y., et al., The Sloan Digital Sky Survey Reverberation Mapping Project: Hα and Hβ Reverberation Measurements from First-year Spectroscopy and Photometry. 2017, *Astrophysical Journal*, **851**, 21, `DOI:10.3847/1538-4357/aa98dc`

Guo, H., Shen, Y., & Wang, S. 2018, PyQSOFit: Python code to fit the spectrum of quasars, Astrophysics Source Code Library, record ascl:1809.008

Guo, W.-J., Pan, Z., Siudek, M., et al., The First Identification of Lyα Changing-look Quasars at High Redshift in DESI. 2025a, *Astrophysical Journal, Letters*, **981**, L8, `DOI:10.3847/2041-8213/adb426`

Guo, W.-J., Zou, H., Greenwell, C. L., et al., Changing-look Active Galactic Nuclei from the Dark Energy Spectroscopic Instrument. II. Statistical Properties from the First Data Release. 2025b, *Astrophysical Journal, Supplement*, **278**, 28, `DOI:10.3847/1538-4365/adc124`

Haas, M., Chini, R., Ramolla, M., et al., Photometric AGN reverberation mapping - an efficient tool for BLR sizes, black hole masses, and host-subtracted AGN luminosities. 2011, *Astronomy and Astrophysics*, **535**, A73, `DOI:10.1051/0004-6361/201117325`

Habouzit, M., Is the JWST detecting too many AGN candidates? 2025, *Monthly Notices of the RAS*, **537**, 2323, `DOI:10.1093/mnras/staf167`

Hernández-García, L., Masegosa, J., González-Martín, O., & Márquez, I., X-ray spectral variability of Seyfert 2 galaxies. 2015, *Astronomy and Astrophysics*, **579**, A90, `DOI:10.1051/0004-6361/201526127`

Ivezić, Ž., Kahn, S. M., Tyson, J. A., et al., LSST: From Science Drivers to Reference Design and Anticipated Data Products. 2019, *Astrophysical Journal*, **873**, 111, `DOI:10.3847/1538-4357/ab042c`

Jaiswal, V. K., Mandal, A. K., Prince, R., et al., Application of the FRADO model of BLR formation to the Seyfert galaxy NGC 5548 and the first step toward determining the Hubble constant. 2024, *arXiv e-prints*, arXiv:2410.03597, `DOI:10.48550/arXiv.2410.03597`

Kaspi, S., Brandt, W. N., Maoz, D., et al., Taking a Long Look: A Two-decade Reverberation Mapping Study of High-luminosity Quasars. 2021, *Astrophysical Journal*, **915**, 129, `DOI:10.3847/1538-4357/ac00aa`

Kaspi, S., Smith, P. S., Netzer, H., et al., Reverberation Measurements for 17 Quasars and the Size-Mass-Luminosity Relations in Active Galactic Nuclei. 2000, *Astrophysical Journal*, **533**, 631, `DOI:10.1086/308704`

Klimek, E. S., Gaskell, C. M., & Hedrick, C. H., Optical Variability of Narrow-Line Seyfert 1 Galaxies. 2004, *Astrophysical Journal*, **609**, 69, `DOI:10.1086/420809`

Kollmeier, J., Anderson, S. F., Blanc, G. A., et al., SDSS-V Pioneering Panoptic Spectroscopy. 2019, *Bulletin of the American Astronomical Society*, **51**, 274

Kubota, A. & Done, C., A physical model of the broad-band continuum of AGN and its implications for the UV/X relation and optical variability. 2018, *Monthly Notices of the RAS*, **480**, 1247, `DOI:10.1093/mnras/sty1890`

Lepine, J. R. D., de Oliveira, A. C., Figueredo, M. V., et al., SIFUS: SOAR integral field unit spectrograph. 2003, in Society of Photo-Optical Instrumentation Engineers (SPIE) Conference Series, Vol. **4841**, *Instrument Design and Performance for Optical/Infrared Ground-based Telescopes*, ed. M. Iye & A. F. M. Moorwood, 1086–1095

Lira, P., Kaspi, S., Netzer, H., et al., Reverberation Mapping of Luminous Quasars at High z. 2018, *Astrophysical Journal*, **865**, 56, `DOI:10.3847/1538-4357/aada45`

Mainieri, V., Anderson, R. I., Brinchmann, J., et al., The Wide-field Spectroscopic Telescope (WST) Science White Paper. 2024, *arXiv e-prints*, arXiv:2403.05398, `DOI:10.48550/arXiv.2403.05398`

Martínez-Aldama, M. L., Czerny, B., Kawka, D., et al., Can Reverberation-measured Quasars Be Used for Cosmology? 2019, *Astrophysical Journal*, **883**, 170, `DOI:10.3847/1538-4357/ab3728`

Martínez-Aldama, M. L., Panda, S., Czerny, B., et al., The CaFe Project: Optical Fe II and Near-infrared Ca II Triplet Emission in Active Galaxies. II. The Driver(s) of the Ca II and Fe II and Its Potential Use as a Chemical Clock. 2021, *Astrophysical Journal*, **918**, 29, `DOI:10.3847/1538-4357/ac03b6`

Marziani, P., Dultzin, D., Sulentic, J. W., et al., A main sequence for quasars. 2018, *Frontiers in Astronomy and Space Sciences*, **5**, 6, `DOI:10.3389/fspas.2018.00006`

Marziani, P., Garnica Luna, K., Floris, A., et al., Super-Eddington Accretion in Quasars. 2025, *Universe*, **11**, 69, `DOI:10.3390/universe11020069`

Marziani, P. & Sulentic, J. W., Highly accreting quasars: sample definition and possible cosmological implications. 2014, *Monthly Notices of the RAS*, **442**, 1211, `DOI:10.1093/mnras/stu951`

Marziani, P., Sulentic, J. W., Zamanov, R., et al., An Optical Spectroscopic Atlas of Low-Redshift Active Galactic Nuclei. 2003a, *Astrophysical Journal, Supplement*, **145**, 199, `DOI:10.1086/346025`

Marziani, P., Sulentic, J. W., Zwitter, T., Dultzin-Hacyan, D., & Calvani, M., Searching for the Physical Drivers of the Eigenvector 1 Correlation Space. 2001, *Astrophysical Journal*, **558**, 553, `DOI:10.1086/322286`

Marziani, P., Zamanov, R. K., Sulentic, J. W., & Calvani, M., Searching for the physical drivers of eigenvector 1: influence of black hole mass and Eddington ratio. 2003b, *Monthly Notices of the RAS*, **345**, 1133, `DOI:10.1046/j.1365-2966.2003.07033.x`

Mathews, W. G. & Ferland, G. J., What Heats the Hot Phase in Active Nuclei? 1987, *Astrophysical Journal*, **323**, 456, `DOI:10.1086/165843`

Mezcua, M., Pacucci, F., Suh, H., Siudek, M., & Natarajan, P., Overmassive Black Holes at Cosmic Noon: Linking the Local and the High-redshift Universe. 2024, *Astrophysical Journal, Letters*, **966**, L30, `DOI:10.3847/2041-8213/ad3c2a`

Negrete, C. A., Dultzin, D., Marziani, P., & Sulentic, J. W., Reverberation and Photoionization Estimates of the Broad-line Region Radius in Low-z Quasars. 2013, *Astrophysical Journal*, **771**, 31, `DOI:10.1088/0004-637X/771/1/31`

Netzer, H., Revisiting the Unified Model of Active Galactic Nuclei. 2015, *Annual Review of Astron and Astrophys*, **53**, 365, `DOI:10.1146/annurev-astro-082214-122302`

Netzer, H., Bolometric correction factors for active galactic nuclei. 2019, *Monthly Notices of the RAS*, **488**, 5185, `DOI:10.1093/mnras/stz2016`

Noda, H. & Done, C., Explaining changing-look AGN with state transition triggered by rapid mass accretion rate drop. 2018, *Monthly Notices of the RAS*, **480**, 3898, `DOI:10.1093/mnras/sty2032`

Osterbrock, D. E. & Ferland, G. J. 2006, *Astrophysics of gaseous nebulae and active galactic nuclei*

Padovani, P., Alexander, D. M., Assef, R. J., et al., Active galactic nuclei: what's in a name? 2017, *Astronomy and Astrophysics Reviews*, **25**, 2, `DOI:10.1007/s00159-017-0102-9`

Panda, S., Parameterizing the AGN Radius–Luminosity Relation from the Eigenvector 1 Viewpoint. 2022, *Frontiers in Astronomy and Space Sciences*, **9**, 850409, `DOI:10.3389/fspas.2022.850409`

Panda, S., Unveiling the quasar main sequence: illuminating the complexity of active galactic nuclei and their evolution. 2024, *Frontiers in Astronomy and Space Sciences*, **11**, 1479874, `DOI:10.3389/fspas.2024.1479874`

Panda, S., Bon, E., Marziani, P., & Bon, N., Taming the derivative: Diagnostics of the continuum and Hβ emission in a prototypical Population B active galaxy. 2022, *Astronomische Nachrichten*, **343**, e210091, `DOI:10.1002/asna.20210091`

Panda, S., Bon, E., Marziani, P., & Bon, N., Saturation of the curve: Diagnostics of the continuum and Hβ emission in Population B active galaxy NGC 5548. 2023, *Bulletin of the Astronomical Society of Brazil*, **34**, 246, `DOI:10.48550/arXiv.2308.05831`

Panda, S., Kozłowski, S., Gromadzki, M., et al., Virial Black Hole Masses for Active Galactic Nuclei behind the Magellanic Clouds. 2024a, *Astrophysical Journal, Supplement*, **272**, 11, `DOI:10.3847/1538-4365/ad3549`

Panda, S., Martínez-Aldama, M. L., & Zajaček, M., Current and future applications of Reverberation-mapped quasars in Cosmology. 2019a, *Frontiers in Astronomy and Space Sciences*, **6**, 75, `DOI:10.3389/fspas.2019.00075`

Panda, S. & Marziani, P., High Eddington quasars as discovery tools: current state and challenges. 2023, *Frontiers in Astronomy and Space Sciences*, **10**, 1130103, `DOI:10.3389/fspas.2023.1130103`

Panda, S., Marziani, P., & Czerny, B., The Quasar Main Sequence Explained by the Combination of Eddington Ratio, Metallicity, and Orientation. 2019b, *Astrophysical Journal*, **882**, 79, `DOI:10.3847/1538-4357/ab3292`

Panda, S., Pozo Nuñez, F., Bañados, E., & Heidt, J., Probing the C IV Continuum Size–Luminosity Relation in Active Galactic Nuclei with Photometric Reverberation Mapping. 2024b, *Astrophysical Journal, Letters*, **968**, L16, DOI:10.3847/2041-8213/ad5014

Panda, S. & Śniegowska, M., Changing-look Active Galactic Nuclei. I. Tracking the Transition on the Main Sequence of Quasars. 2024, *Astrophysical Journal, Supplement*, **272**, 13, DOI:10.3847/1538-4365/ad344f

Pei, L., Fausnaugh, M. M., Barth, A. J., et al., Space Telescope and Optical Reverberation Mapping Project. V. Optical Spectroscopic Campaign and Emission-line Analysis for NGC 5548. 2017, *Astrophysical Journal*, **837**, 131, DOI:10.3847/1538-4357/aa5eb1

Peterson, B. M., Berlind, P., Bertram, R., et al., Steps toward Determination of the Size and Structure of the Broad-Line Region in Active Galactic Nuclei. XVI. A 13 Year Study of Spectral Variability in NGC 5548. 2002, *Astrophysical Journal*, **581**, 197, DOI:10.1086/344197

Peterson, B. M., Denney, K. D., De Rosa, G., et al., The Size of the Narrow-line-emitting Region in the Seyfert 1 Galaxy NGC 5548 from Emission-line Variability. 2013, *Astrophysical Journal*, **779**, 109, DOI:10.1088/0004-637X/779/2/109

Peterson, B. M., Ferrarese, L., Gilbert, K. M., et al., Central Masses and Broad-Line Region Sizes of Active Galactic Nuclei. II. A Homogeneous Analysis of a Large Reverberation-Mapping Database. 2004, *Astrophysical Journal*, **613**, 682, DOI:10.1086/423269

Pozo Nuñez, F., Bañados, E., Panda, S., & Heidt, J., Accretion disc reverberation mapping in a high-redshift quasar. 2025, *Astronomy and Astrophysics*, **700**, L8, DOI:10.1051/0004-6361/202555421

Pozo Nuñez, F., Bruckmann, C., Deesamutara, S., et al., Modelling photometric reverberation mapping data for the next generation of big data surveys. Quasar accretion discs sizes with the LSST. 2023, *Monthly Notices of the RAS*, **522**, 2002, DOI:10.1093/mnras/stad286

Pozo Nuñez, F., Czerny, B., Panda, S., et al., Reevaluating LSST's Capability for Time Delay Measurements in Quasar Accretion Disks. 2024, *Research Notes of the American Astronomical Society*, **8**, 47, DOI:10.3847/2515-5172/ad284a

Prieto, A., Rodríguez-Ardila, A., Panda, S., & Marinello, M., A novel black hole mass scaling relation based on coronal gas, and its dependence with the accretion disc. 2022, *Monthly Notices of the RAS*, **510**, 1010, DOI:10.1093/mnras/stab3414

Pronik, V. I. & Chuvaev, K. K., Hydrogen lines in the spectrum of the galaxy Markaryan 6 during its activity. 1972, *Astrophysics*, **8**, 112, DOI:10.1007/BF01002159

Pucha, R., Juneau, S., Dey, A., et al., Tripling the Census of Dwarf AGN Candidates Using DESI Early Data. 2025, *Astrophysical Journal*, **982**, 10, DOI:10.3847/1538-4357/adb1dd

Ren, W., Wang, J., Cai, Z., & Guo, H., Extreme Variability Quasars in Their Various States. I. The Sample Selection and Composite SDSS Spectra. 2022, *Astrophysical Journal*, **925**, 50, DOI:10.3847/1538-4357/ac3828

Ricci, C. & Trakhtenbrot, B., Changing-look active galactic nuclei. 2023, *Nature Astronomy*, **7**, 1282, `DOI:10.1038/s41550-023-02108-4`

Richards, G. T., Lacy, M., Storrie-Lombardi, L. J., et al., Spectral Energy Distributions and Multiwavelength Selection of Type 1 Quasars. 2006, *Astrophysical Journal, Supplement*, **166**, 470, `DOI:10.1086/506525`

Rodríguez-Ardila, A., May, D., Panda, S., Fonseca-Faria, M. A., & Fraga, L., The narrow-line region properties of ESO 138-G001 unveiled by SOAR/SIFS observations. 2024, *Monthly Notices of the RAS*, **527**, 10649, `DOI:10.1093/mnras/stad3872`

Rose, M., Elvis, M., & Tadhunter, C. N., Coronal-Line Forest AGN: the best view of the inner edge of the AGN torus? 2015, *Monthly Notices of the RAS*, **448**, 2900, `DOI:10.1093/mnras/stv113`

Ross, N. P., Graham, M. J., Calderone, G., et al., The first high-redshift changing-look quasars. 2020, *Monthly Notices of the RAS*, **498**, 2339, `DOI:10.1093/mnras/staa2415`

Sánchez-Sáez, P., Lira, H., Martí, L., et al., Searching for Changing-state AGNs in Massive Data Sets. I. Applying Deep Learning and Anomaly-detection Techniques to Find AGNs with Anomalous Variability Behaviors. 2021, *Astronomical Journal*, **162**, 206, `DOI:10.3847/1538-3881/ac1426`

Shakura, N. I. & Sunyaev, R. A., Black holes in binary systems. Observational appearance. 1973, *Astronomy and Astrophysics*, **24**, 337

Shapovalova, A. I., Doroshenko, V. T., Bochkarev, N. G., et al., Profile variability of the Hα and Hβ broad emission lines in NGC 5548. 2004, *Astronomy and Astrophysics*, **422**, 925, `DOI:10.1051/0004-6361:20035652`

Shen, Y. & Burke, C. J., A Sample Bias in Quasar Variability Studies. 2021, *Astrophysical Journal, Letters*, **918**, L19, `DOI:10.3847/2041-8213/ac1e2e`

Shen, Y. & Ho, L. C., The diversity of quasars unified by accretion and orientation. 2014, *Nature*, **513**, 210, `DOI:10.1038/nature13712`

Shen, Y., Richards, G. T., Strauss, M. A., et al., A Catalog of Quasar Properties from Sloan Digital Sky Survey Data Release 7. 2011, *Astrophysical Journal, Supplement*, **194**, 45, `DOI:10.1088/0067-0049/194/2/45`

Sniegowska, M., Czerny, B., Bon, E., & Bon, N., Possible mechanism for multiple changing-look phenomena in active galactic nuclei. 2020, *Astronomy and Astrophysics*, **641**, A167, `DOI:10.1051/0004-6361/202038575`

Śniegowska, M., Marziani, P., Czerny, B., et al., High Metal Content of Highly Accreting Quasars. 2021, *Astrophysical Journal*, **910**, 115, `DOI:10.3847/1538-4357/abe1c8`

Suganuma, M., Yoshii, Y., Kobayashi, Y., et al., Reverberation Measurements of the Inner Radius of the Dust Torus in Nearby Seyfert 1 Galaxies. 2006, *Astrophysical Journal*, **639**, 46, `DOI:10.1086/499326`

Sulentic, J. W., Marziani, P., & Dultzin-Hacyan, D., Phenomenology of Broad Emission Lines in Active Galactic Nuclei. 2000, *Annual Review of Astron and Astrophys*, **38**, 521, `DOI:10.1146/annurev.astro.38.1.521`

Temple, M. J., Ricci, C., Koss, M. J., et al., BASS XXXIX: Swift-BAT AGN with changing-look optical spectra. 2023, *Monthly Notices of the RAS*, **518**, 2938, `DOI:10.1093/mnras/stac3279`

Vestergaard, M. & Peterson, B. M., Determining Central Black Hole Masses in Distant Active Galaxies and Quasars. II. Improved Optical and UV Scaling Relationships. 2006, *Astrophysical Journal*, **641**, 689, `DOI:10.1086/500572`

Wandel, A., On the Baldwin Effect in Active Galactic Nuclei. I. The Continuum-Spectrum-Mass Relationship. 1999, *Astrophysical Journal*, **527**, 649, `DOI:10.1086/308134`

Wandel, A., Peterson, B. M., & Malkan, M. A., Central Masses and Broad-Line Region Sizes of Active Galactic Nuclei. I. Comparing the Photoionization and Reverberation Techniques. 1999, *Astrophysical Journal*, **526**, 579, `DOI:10.1086/308017`

Wang, J., Xu, D. W., & Wei, J. Y., Identification of SDSS J141324.27+530527.0 as a New "Changing-look" Quasar with a "Turn-on" Transition. 2018, *Astrophysical Journal*, **858**, 49, `DOI:10.3847/1538-4357/aab88b`

Wang, S., Woo, J.-H., Gallo, E., et al., Identifying Changing-look AGNs Using Variability Characteristics. 2024, *Astrophysical Journal*, **966**, 128, `DOI:10.3847/1538-4357/ad3049`

Watson, D., Denney, K. D., Vestergaard, M., & Davis, T. M., A New Cosmological Distance Measure Using Active Galactic Nuclei. 2011, *Astrophysical Journal, Letters*, **740**, L49, `DOI:10.1088/2041-8205/740/2/L49`

Wu, Q. & Shen, Y., A Catalog of Quasar Properties from Sloan Digital Sky Survey Data Release 16. 2022, *Astrophysical Journal, Supplement*, **263**, 42, `DOI:10.3847/1538-4365/ac9ead`

Zeltyn, G., Trakhtenbrot, B., Eracleous, M., et al., Exploring Changing-look Active Galactic Nuclei with the Sloan Digital Sky Survey V: First Year Results. 2024, *Astrophysical Journal*, **966**, 85, `DOI:10.3847/1538-4357/ad2f30`

Contrib. Astron. Obs. Skalnaté Pleso **56/1**, 186 – 193, (2026)
https://doi.org/10.31577/caosp.2026.56.1.186

Alertissimo - a tool for orchestration of LSST broker streams

V. Vujčić[1], **V.A. Srećković**[2] **and S. Babarogić**[3]

[1] *Astronomical Observatory, Volgina 7, 11060 Belgrade, Serbia (E-mail: veljko@aob.rs)*

[2] *University of Belgrade, Institute of Physics Belgrade, PO Box 57, 11001 Belgrade, Serbia*

[3] *University of Belgrade, Faculty of Organizational Sciences, Jove Ilića, 11000 Belgrade, Serbia*

Received: September 25, 2025; Accepted: November 19, 2025

Abstract. The Vera C. Rubin Observatory, through its Legacy Survey of Space and Time, will soon start producing 10 million alerts on transient astronomical objects per night. Due to logistics and bandwidth, alerts will not be dispatched directly to the public but to 'brokers' i.e. tools selected by LSST to handle alert streams. Brokers offer both common, specific and micro-specific functionalities related to alert handling, analysis, representation and dissemination. In this ecosystem, potentially augmented by data streams from other astronomical sources, there is a - need demonstrated by the community - for use cases which combine features of individual brokers. In this paper we present initial efforts and a prototype of such a tool, along with a language that would allow users to define use cases / workflows in a manner tailored for the domain.

Key words: astronomical transients – large astronomical surveys – Vera C. Rubin Observatory – real time event processing – domain-specific languages – natural language processing

1. Introduction

As a new era of astronomical data science is about to kick off with Vera C. Rubin Observatory's Legacy Survey of Space and Time (Rubin/LSST) Ivezić et al. (2019) production phase, the ecosystem of tools and infrastructure dealing with transient astronomical events looks fit and (almost) ready for the data burst. It is commonly known that the LSST Alert Production pipeline (Bosch et al., 2018) will capture and process images, perform difference-image analysis and distribute alerts of every astronomical source with a signal-to-noise ratio (SNR) ratio > 5 in positive or negative flux (Graham et al., 2019a). Due to bandwidth and other considerations, alerts will not be directly available to the public but through 'brokers' - tools developed by different scientific teams worldwide, specifically made for and approved by LSST. At least six brokers (AleRCE, AMPEL, ANTARES, Fink, Lasair, Pitt-Google) will be able to ingest LSST alert stream in near-real time, analyze, classify, offer UI tools, programming APIs and more. Some of the main features of brokers overlap but they differ significantly in how they expose these features, with even greater divergence in their underlying implementations and backend technologies. (Vujčić et al., 2025).

2. Alertissimo

We introduce Alertissimo (2025) - a tool for orchestration of broker streams and potentially for a wider scope of astro-science use cases. It can be seen as a novel topic but also an extension of the work done and analyzed by the Serbian group related to astronomical stream processing and virtual observatory (Vujčić & Jevremović, 2020; Jevremović et al., 2020). This tool is conceived on two premises:
a) that there is a need for building workflows out of multiple LSST broker data streams (and potentially external sources as well);
b) that there is a need for a tool that would allow expressing such workflows in a powerful yet approachable manner.
We can roughly name these two premises as 'Broker Orchestration' and 'DSL for Transients'. We also present Alertissimo's overall architecture.

2.1. Broker orchestration

As stated above, at least 6 LSST brokers are in a mature development phase, and some of them - like Lasair, ALeRCE, ANTARES and Fink - have worked in production with Zwicky Transient Facility (ZTF) data (Graham et al. 2019b, data volume order of magnitude lower than LSST). Apart from technological choices, implementation differences and performance, brokers also vary in features (and microfeatures), and in the ways they are exposed through their UIs and APIs. There are ongoing discussions in the Transients and Variable Stars scientific collaboration (LSST-TVS) on use cases that combine features of various brokers (see the Appendix A for a use case featuring supermassive binary black hole (SMBBH) detection). There may also be availability and responsiveness considerations, in a technical sense.

Brokers offer external access to their features through APIs, most through REST[1] and Python, some through a Python interface only. Here we have a similar but non-standardized set of their exposed methods, not only related to major feature differences but also to naming conventions and microfeatures (e.g - how do they retrieve single vs multiple objects? can they handle SQL? how does output look like and can you control granulation? etc). API access control is implemented differently across brokers, typically requiring users to supply

---

[1] Representational State Transfer, an architectural style for web services which defines GET and POST methods for data retrieval

credentials - such as tokens or username/password combinations - with varying permission models and granularity.

It is a relatively easy task to write a program or a script that would pick specific methods from various brokers and perform a single use case. Alertissimo should act here as a generator of scientific scenarios - take any number of features from any broker (or other available source) and orchestrate them with one another. The primary function of Alertissimo here is one of a science-enabler, where all decisions are in control of the user[2].

Alertissimo is designed with an input-agnostic core, where user-specified workflows are first translated into intermediate representations (IR) with a well-defined structure built using Pydantic[3] models. These IR models are the product of a conceptual analysis of broker features; their design is generalized, while their implementation is specialized through a polymorphic class structure.

2.2. DSL for transients

The challenge of translating high-level user specifications into executable workflows is often addressed through Domain-Specific Languages (DSLs) and workflow systems (Gil et al., 2010). There are three main directions for Alertissimo UI development, one of them being the backbone of the others - the DSL for Transients. The two others, Natural Language Processing (NLP) Chowdhary (2020) and visual workflow builder are planned to be built once a mature DSL foundation is established. DSLs (Mernik et al., 2005) are programming languages designed for a very specific purpose and are usually of declarative nature[4]. Alertissimo's DSL for Transients acts as the semantic and syntactic backbone linking user intent with system capabilities. It exposes a structured, declarative representation of broker operations, allowing every workflow to be expressed in a consistent formalism. This provides that all interactions, no matter how informal their starting point was, ultimately resolve into a precise and testable specification. The demo version of Alertissimo featuring DSL for Transients is currently available through a github branch (`https://github.com/sambolino/alertissimo/tree/feature/dsl`). Example of DSL for Transients is found in the Appendix A.

The natural language interface in Alertissimo will enable users to describe their scientific intentions in plain terms, while maintaining expressive power.

---

[2] However, the idea persists that Alertissimo could also act in a 'light' AI-based counseling manner too, based on the knowledge of previous user experiences/success rates. This kind of development could take place in later phases.

[3] Pydantic is a Python library designed for data validation, parsing, and serialization which provides a structured way to define data schemas and ensures that incoming data conform to the specified types and constraints.

[4] Declarative programming languages are stating 'what' should be done in contrast with imperative languages which are describing 'how' it should be done. All general programming languages are imperative while more narrowly specified languages, such as SQL, rule-based languages, HTML etc are declarative.

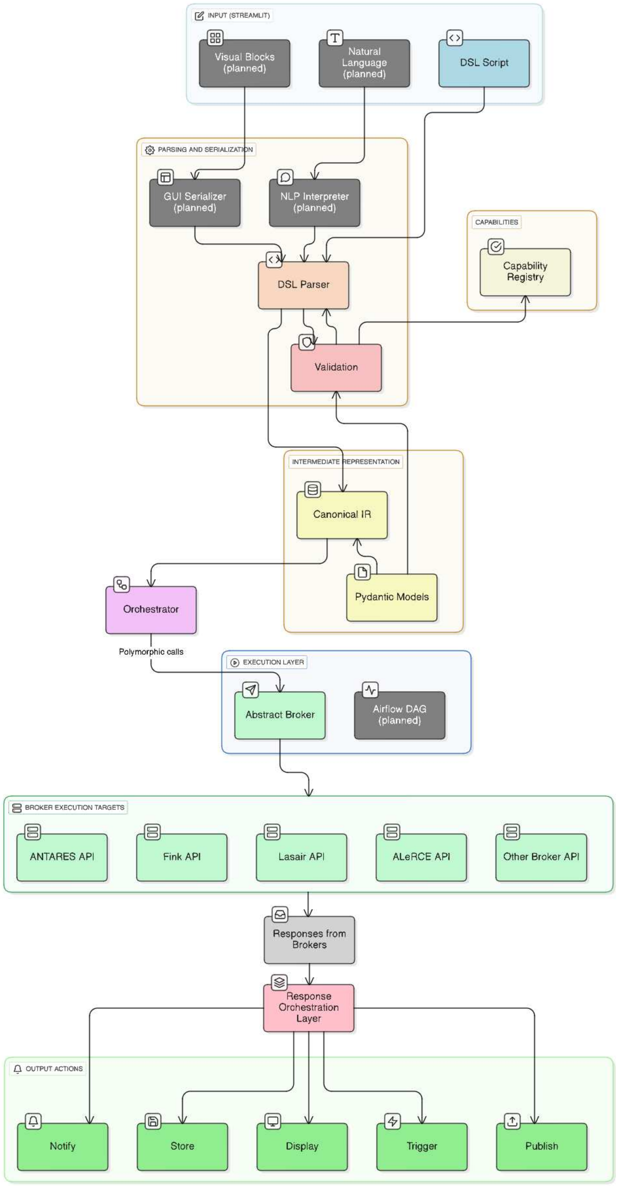

Figure 1. End to end flow diagram of Alertissimo modules illustrating the pipeline from DSL input through orchestration to broker execution. For detailed description see Subsection 2.3

The aim is to test both a pure NLP prompt, where users would describe use-cases in written English, and a chat-bot style AI dialogue which could act as an assistant providing refinement and disambiguation, even for users initially unfamiliar with broker architectures. Both the natural language and visual interfaces of Alertissimo will be developed on top of a formally defined DSL grammar. As DSL defines the valid constructs, relationships, and parameter types for workflows involving broker orchestration, it also ensures that any interface - textual, conversational, or visual - ultimately produces valid, executable specifications. This formal grammar serves as the common translation layer: natural language inputs are parsed and normalized into DSL expressions, and also the visual interface directly maps user manipulations of blocks and links into equivalent DSL statements.

From a broader perspective, this layered UI approach reflects a continuum between accessibility and expressiveness. At one end, the conversational interface empowers domain scientists to describe ideas without syntactic constraints; at the other, the DSL offers power users fine-grained control and versionable scripts suitable for integration into research pipelines. The visual interface bridges these modes, exposing the structure of the DSL while remaining approachable.

2.3. Architecture overview

The overall architecture of Alertissimo is depicted in Figure 1, with data flow and key components as follows:

1. Input Layer: Users can define their use-cases via multiple interfaces (DSL, NLP/chatbot (planned), Visual blocks - Yahoo Pipes (Pruett, 2007) style (planned)), with the DSL being the currently implemented method.

2. Parsing and Validation: User input is reduced to DSL formalism to the appropriate parser (DSL Parser, etc.). Validation is performed both in terms of grammar and broker capabilities.

3. Capabilities: Broker capabilities are defined within yaml[5] files

4. IR Generation: Valid DSL is being translated into IR models, still being execution-agnostic.

5. Orchestration and Execution: The validated IR is processed by the Orchestrator. This component manages the workflow by making polymorphic calls to the Execution Layer, which consists of an Abstract Broker interface. This design allows the system to specialize the implementation for different targets

---

[5] YAML is a human-readable data serialization language primarily used for configuration files and data storage

while maintaining a generic core. For the sake of performance/execution control, The orchestrator can also trigger a workflow coordination framework, such as an Airflow DAG (planned).

6. Response Handling and Output: Responses from brokers are collected and processed by and the system executes one or more output actions, such as to Notify a user, Store the data, Display it, Trigger a downstream process, or Publish the results.

3. Conclusion

Alertissimo is a new tool for building scientific workflows out of streams of alerts generated by Rubin/LSST. The alerts are not disseminated directly to the public, but through tools called 'brokers' - projects developed for ingestion and analysis of LSST transient alerts. Alertissimo covers all of the brokers' concepts and features and offers an integrated interface for orchestrating multiple brokers within a single workflow. On top of Alertissimo lies a domain-specific language devised to easily yet expressively represent scientific use cases. NLP/LLM/chatbot and visual workflows are planned as extensions that dependably translate and validate to the canonical DSL.

Together, these interaction paradigms establish a scalable human–machine interface strategy, ensuring that Alertissimo remains adaptable as new brokers, data modalities, and analysis paradigms emerge in astronomy and astrophysics. Our prototype demonstrates how broker interoperability and workflow definition can empower the astronomy and astrophysics community in the era of Rubin/LSST.

Acknowledgements. This research was supported by the Ministry of Science, Technological Development and Innovation of the Republic of Serbia (MSTDIRS) through contract no. 451-03-66/2024-03/200002 made with Astronomical Observatory (Belgrade), 451-03-47/2023-01/200024 made with Institute of physics Belgrade. The authors acknowledge the networking opportunities from the COST Action CA22133 - The birth of solar systems (PLANETS) supported by COST (European Cooperation in Science and Technology).

References

Alertissimo. 2025, Alertissimo, https://github.com/sambolino/alertissimo, accessed: 2025-10-29

Bosch, J., AlSayyad, Y., Armstrong, R., et al., An overview of the LSST image processing pipelines. 2018, *arXiv preprint arXiv:1812.03248*

Chowdhary, K., Natural language processing. 2020, *Fundamentals of artificial intelligence*, 603

Gil, Y., Ratnakar, V., Kim, J., et al., Wings: Intelligent workflow-based design of computational experiments. 2010, *IEEE Intelligent Systems*, **26**, 62

Graham, M., Bellm, E., Guy, L., Slater, C., & Dubois-Felsmann, G. 2019a, *LSST Alerts: Key Numbers* (DMTN-102, URL https://dmtn-102. lsst. io, LSST Data Management Technical Note)

Graham, M., Kulkarni, S., Bellm, E., et al., The Zwicky Transient Facility: Science Objectives. 2019b, *Publications of the Astronomical Society of the Pacific*, **131**, 078001, DOI:10.1088/1538-3873/ab006c

Ivezić, Ž., Kahn, S. M., Tyson, J. A., et al., LSST: From Science Drivers to Reference Design and Anticipated Data Products. 2019, *Astrophysical Journal*, **873**, 111, DOI:10.3847/1538-4357/ab042c

Jevremović, D., Srećković, V., Marinković, B., & Vujčić, V., Databases for collisional and radiative processes in small molecules needed for spectroscopy use in astrophysics. 2020, *Contributions of the Astronomical Observatory Skalnate Pleso*, **50**, 44

Komossa, S., Grupe, D., Marziani, P., et al., The extremes of AGN variability: outbursts, deep fades, changing looks, exceptional spectral states, and semi-periodicities. 2026, *Advances in Space Research*, **77**, 4041

Kovačević, A. B., Popović, L. Č., & Ilić, D., Two-dimensional correlation analysis of periodicity in active galactic nuclei time series. 2020, *Open astronomy*, **29**, 51

Mernik, M., Heering, J., & Sloane, A. M., When and how to develop domain-specific languages. 2005, *ACM computing surveys (CSUR)*, **37**, 316

Pruett, M. 2007, *Yahoo! pipes* (O'Reilly)

Vujčić, V. & Jevremović, D., Real-time stream processing in astronomy. 2020, in *Knowledge Discovery in Big Data from Astronomy and Earth Observation* (Elsevier), 173–182

Vujčić, V., Srećković, V., Babarogić, S., & Aleksić, J., An overview of astronomical transient brokers in Rubin era. 2025, *Contrib. Astron. Obs. Skalnaté Pleso*, **55**, 95

A. DSL for Transients - example code

Here is a sample code of DSL for Transients for supermassive binary black hole (SMBBH) detection, based on the use case presented on the online meeting of the LSST-TVS collaboration. The use case was proposed by prof dr Andjelka Kovačević based on longstanding research of AGN and SMBBH variability (Kovačević et al. (2020), Komossa et al. (2026)). The meeting took place on the Feb 21st 2025. Comments include original definition of the use case from the discussion.

```
# Fink+ALeRCE+Lasair+ANTARES agree on alert
# ('required' argument is added for showcase)
confirm object_id="ZTF25aazqavg" brokers=[fink, alerce, lasair, antares] required=3
# ALeRCE retrieves ZTF curves of alerted object
lightcurve broker=alerce survey="ztf"
# Lasair retrieves historical light curves from Pan-STARR of
# alerted objects, and crossmatches with IR, R, X catalogues.
# Helps identify multi-wavelength periodicity.
crossmatch broker=lasair catalog="panstarrs" filters=["ir", "radio", "xray"]
# ANTARES crossmatches alerted object with eROSITA etc for
# further confirmation of multiwavelength of periodicity origin.
crossmatch broker=antares catalog="erosita"
# Lasair provides a Kafka-based alert stream that updates in
# real-time whenever a new observation is made for a
# monitored object.
monitor broker=lasair stream="kafka"
classify method="periodicity_detection"
notify team
store db
```

PRÁCE ASTRONOMICKÉHO OBSERVATÓRIA
NA SKALNATOM PLESE
LVI, číslo 1

Zostavovatelia: Dr Milan S. Dimitrijević
Dr Paola Marziani
Dr Djordje Savić
Dr Luka Č. Popović
Výkonný redaktor: RNDr. Richard Komžík, CSc.
Vedecký redaktor: RNDr. Augustín Skopal, DrSc.
Vydal: Astronomický ústav SAV, Tatranská Lomnica
IČO vydavateľa: 00 166 529
Periodicita: 3-krát ročne
ISSN (on-line verzia): 1336-0337
CODEN: CAOPF8
Rok vydania: 2026.
Počet strán: 194

Contributions of the Astronomical Observatory Skalnaté Pleso are processed using
LaTeX 2$_\varepsilon$ CAOSP DocumentClass file 3.10 ver. 2024.